



**AFRL-RW-EG-TR-2011-053**

**A High Strain-Rate Investigation of a  
Zr-Based Bulk Metallic Glass and an  
HTPB Polymer Composite**

STINFO COPY

---

**George P. Sunny**

**Department of Mechanical and Aerospace Engineering  
Case Western Reserve University  
Cleveland, OH 44106**

**Grant No. FA8651-09-1-0006**

**March 2011**

**Final Report**

**Distribution A: Approved for public release; distribution unlimited.  
Approval Confirmation 96 ABW/PA # 96ABW-2011-0074, dated  
February 23, 2011**

STINFO COPY

**AIR FORCE RESEARCH LABORATORY, MUNITIONS DIRECTORATE**

**Air Force Materiel Command ■ United States Air Force ■ Eglin Air Force Base**

This page intentionally left blank

# NOTICE AND SIGNATURE PAGE

IN ACCORDANCE WITH ASSIGNED DISTRIBUTION S

Using Government drawings, specifications, or other data included in this document for any purpose other than Government procurement does not in any way obligate the U.S. Government. The fact that the Government formulated or supplied the drawings, specifications, or other data does not license the holder or any other person or corporation; or convey any rights or permission to manufacture, use, or sell any patented invention that may relate to them.

Qualified requestors may obtain copies of this report from the Defense Technical Information Center (DTIC) <<http://www.dtic.mil/dtic/index.html>>.

AFRL-RW-EG-TR-2011-053 HAS BEEN REVIEWED AND IS APPROVED FOR PUBLICATION  
TATEMENT.

FOR THE DIRECTOR:

//Original Signed//  
HOWARD G. WHITE, PhD  
Technical Advisor  
Ordnance Division

//Original Signed//  
JEFFREY D. KUHN, MAJ, PhD  
Branch Chief  
Energetic Materials Branch

//Original Signed//  
JENNIFERL. JORDAN, PhD  
Project Manager  
Energetic Materials Branch

This report is published in the interest of scientific and technical information exchange, and its publication does not constitute the Government's approval or disapproval of its ideas or findings.

This page intentionally left blank

# REPORT DOCUMENTATION PAGE

*Form Approved*  
OMB No. 0704-0188

Public reporting burden for this collection of information is estimated to average 1 hour per response, including the time for reviewing instructions, searching existing data sources, gathering and maintaining the data needed, and completing and reviewing this collection of information. Send comments regarding this burden estimate or any other aspect of this collection of information, including suggestions for reducing this burden to Department of Defense, Washington Headquarters Services, Directorate for Information Operations and Reports (0704-0188), 1215 Jefferson Davis Highway, Suite 1204, Arlington, VA 22202-4302. Respondents should be aware that notwithstanding any other provision of law, no person shall be subject to any penalty for failing to comply with a collection of information if it does not display a currently valid OMB control number. **PLEASE DO NOT RETURN YOUR FORM TO THE ABOVE ADDRESS.**

<b>1. REPORT DATE (DD-MM-YYYY)</b> 03-2011		<b>2. REPORT TYPE</b> Final		<b>3. DATES COVERED (From - To)</b> March 2009 – January 2011	
<b>4. TITLE AND SUBTITLE</b>  A High Strain-Rate Investigation of a Zr-Based Bulk Metallic Glass and an HTPB Polymer Composite				<b>5a. CONTRACT NUMBER</b>	
				<b>5b. GRANT NUMBER</b> FA8651-09-1-0006	
				<b>5c. PROGRAM ELEMENT NUMBER</b> 62102F	
<b>6. AUTHOR(S)</b>  George P. Sunny				<b>5d. PROJECT NUMBER</b> 2502	
				<b>5e. TASK NUMBER</b> 95	
				<b>5f. WORK UNIT NUMBER</b> 05	
<b>7. PERFORMING ORGANIZATION NAME(S) AND ADDRESS(ES)</b>  Department of Mechanical and Aerospace Engineering Case Western Reserve University Cleveland, OH 44106				<b>8. PERFORMING ORGANIZATION REPORT NUMBER</b>  AFRL-RW-EG-TR-2011-053	
<b>9. SPONSORING / MONITORING AGENCY NAME(S) AND ADDRESS(ES)</b>  Air Force Research Laboratory, Munitions Directorate Ordnance Division Energetic Materials Branch (AFRL/RWME) Eglin AFB FL 32542-5910 Technical Advisor: Dr. Jennifer L. Jordan				<b>10. SPONSOR/MONITOR'S ACRONYM(S)</b> AFRL-RW-EG	
				<b>11. SPONSOR/MONITOR'S REPORT NUMBER(S)</b> Same as Block 8	
<b>12. DISTRIBUTION / AVAILABILITY STATEMENT</b>  Distribution A: Approved for public release; distribution unlimited. Approval Confirmation 96 ABW/PA # 96ABW-2011-0074, dated February 23, 2011					
<b>13. SUPPLEMENTARY NOTES</b> DISTRIBUTION STATEMENT INDICATING AUTHORIZED ACCESS IS ON THE COVER PAGE AND BLOCK 12 OF THIS FORM. DATA RIGHTS RESTRICTIONS AND AVAILABILITY OF THIS REPORT ARE SHOWN ON THE NOTICE AND SIGNATURE PAGE.					
<b>14. ABSTRACT</b> High strain-rate tests are performed on LM-1 using a Split-Hopkinson Pressure Bar (SHPB) to investigate effects of <i>L/D</i> ratio and annealing. An ultra high-speed camera was also employed to record the deformation and failure processes of LM-1. The amorphous specimens exhibit a reduction in peak stress with reduced <i>L/D</i> ratio and failure at the specimen-insert interface, indicative of stress concentrations due to the difference in the specimen and insert diameters, while the annealed specimens exhibited extensive fragmentation.  High strain-rate compression experiments are conducted on a hydroxy-terminated polybutadiene (HTPB) polymer and its composite using another modified SHPB for testing of soft materials. Results from the experiments on HTPB polymer indicate a transition in the polymer between low and high strain-rate sensitivity at 2100/s, along with axial splitting at strain-rates above 3000/s. On the other hand, reduced rate-sensitivity is observed in the HTPB composite, most likely due to the presence of numerous interfaces between the glass beads and the polymer binder.					
<b>15. SUBJECT TERMS</b> Shear, Split-Hopkinson Pressure Bar, SHPB, explosive stimulant, metallic glass, HTPB					
<b>16. SECURITY CLASSIFICATION OF:</b>			<b>17. LIMITATION OF ABSTRACT</b>	<b>18. NUMBER OF PAGES</b>	<b>19a. NAME OF RESPONSIBLE PERSON</b>
<b>a. REPORT</b>	<b>b. ABSTRACT</b>	<b>c. THIS PAGE</b>			Jennifer M. Jordan
UNCLASSIFIED	UNCLASSIFIED	UNCLASSIFIED	UL	285	<b>19b. TELEPHONE NUMBER (include area code)</b> 850-882-8992

This page intentionally left blank

A HIGH STRAIN-RATE INVESTIGATION OF  
A ZR-BASED BULK METALLIC GLASS AND AN HTPB POLYMER COMPOSITE

by

GEORGE PADAYATIL SUNNY

Submitted in partial fulfillment of the requirements

For the degree of Doctor of Philosophy

Dissertation Advisors: Prof. Vikas Prakash, Prof. John Lewandowski, Dr. Jennifer Jordan

Department of Mechanical and Aerospace Engineering,

CASE WESTERN RESERVE UNIVERSITY

May, 2011

**CASE WESTERN RESERVE UNIVERSITY**  
**SCHOOL OF GRADUATE STUDIES**

We hereby approve the thesis/dissertation of

George Padayatil Sunny

candidate for the Doctor of Philosophy degree\*.

(signed) Vikas Prakash  
(chair of the committee)

John J. Lewandowski

Jennifer L. Jordan

Joseph Mansour

Xiong (Bill) Yu

(date) January 20, 2011

\*We also certify that written approval has been obtained for any proprietary material contained therein.

*“There are those who look at things the way they are, and ask why... I dream of things that never were, and ask why not?” – Robert F. Kennedy*

*“Some people follow their dreams. Others hunt them down and beat them mercilessly into submission.” – Neil Kendall*

## TABLE OF CONTENTS

Table of Contents	iv
List of Tables	x
List of Figures	xi
Acknowledgments	xviii
Abstract	xx
Chapter 1: BACKGROUND AND LITERATURE SURVEY OF	
METALLIC GLASSES	1
1.1 Overview of Metallic Glasses	1
1.2 The First Metallic Glasses	1
1.3 Bulk Metallic Glasses	2
1.4 Flow and Fracture of Bulk Metallic Glasses	4
1.5 Previous Results on Zr-Based BMGs	6
1.5.1 Quasi-static tests on Zr-based BMGs	7
1.5.2 Mechanical tests of Zr-based BMGs at high strain-rates	9
1.5.3 Quasi-static and Dynamic Fracture of Zr-based BMGs	12
1.6 Scope of the present investigation	16
References	19
Tables	24
Figures	25
Chapter 2: HIGH STRAIN-RATE RESPONSE OF LM-1 USING	29
CONVENTIONAL INSERTS	
2.1 Overview	29
2.2 Split-Hopkinson Pressure Bar (SHPB)	29
2.2.1 Governing Equations for the SHPB	31

2.2.2 Pulse shaping technique	35
2.3 Additional equipment for the SHPB experiment	38
2.4 Specimen preparation	38
2.5 Results	39
2.5.1 As-cast LM-1	39
2.5.2 Annealed LM-1	41
2.6 Discussion	41
2.6.1 As-cast LM-1	41
2.6.2 Annealed LM-1	43
2.7 Summary	46
References	49
Figures	53
Chapter 3: DESIGN OF NEW INSERTS AND IMPROVED EVALUATION OF HIGH STRAIN-RATE RESPONSE OF LM-1	70
3.1 Overview	70
3.2 Conditions for Valid SHPB Experiments	71
3.2.1 Equilibrium conditions	71
3.2.2 Elastic behavior of incident and transmitted bars	71
3.2.3 Minimal dispersion	72
3.2.4 Uniform and uniaxial stress state	73
3.2.5 Single loading	74
3.3 Finite Element Simulation of SHPB	74
3.4 Additional Specimen Geometries	76

3.4.1 Conical inserts	77
3.4.2 Dogbone specimen	77
3.4.3 Development of new insert design	78
3.5 Additional Considerations with New Inserts	79
3.5.1 Limitations and assumptions	79
3.5.2 Applications	80
3.6 Macroscopic Fracture Behavior of LM-1 with New Inserts	82
3.7 Measurements of Peak Stress and Strain in LM-1	84
3.7.1 Preparation of strain gage experiment	84
3.7.2 Results from strain gage experiments on LM-1	86
3.8 Discussion	87
3.8.1 Comparison of stress and strain-rate signals from gages on bar and specimen	87
3.8.2 Comparison of peak stresses with conventional inserts and new inserts	89
3.8.3 Effects of L/D and strain-rate	90
3.9 Summary	91
References	94
Tables	97
Figures	102
Chapter 4: HIGH LOADING-RATE FRACTURE OF LM-1	132
4.1 Overview	132
4.2 Background and Motivation	132

4.3 Experimental Procedure	138
4.4 Wave Propagation in the MHPB	140
4.5 Results and Discussion	142
4.6 Summary	147
References	150
Tables	154
Figures	155
Chapter 5: Literature Review of Hydroxy-Terminated Polybutadiene (HTPB)	
and HTPB-based Particulate Composites	187
5.1 Overview	187
5.2 HTPB Binder Background	189
5.2.1 HTPB pre-polymer	189
5.2.2 Isocyanates	190
5.2.3 Chain extenders and crosslinkers	190
5.2.4 Additional components	191
5.2.5 Physical properties	192
5.3 Mechanical properties of the HTPB Polymer	193
5.3.1 Low strain-rate mechanical properties	194
5.3.2 High strain-rate mechanical properties	195
5.4 Mechanical Properties of the HTPB Composites	198
5.4.1 Low strain-rate	199
5.4.2 High strain-rate	200
5.5 Scope of the Present Study	205

References	207
Figures	210
Chapter 6: HIGH STRAIN-RATE COMPRESSION OF AN HTPB POLYMER AND ITS PARTICULATE COMPOSITE	211
6.1 Overview	211
6.2 Experimental Challenges in Testing “Soft” Polymers with the SHPB	212
6.2.1 Equilibrium considerations	213
6.2.2 Stress measurements	215
6.3 Experimental Procedure	216
6.3.1 Materials and specimen preparation	216
6.3.2 Experimental technique	217
6.4 Results and Discussion	219
6.4.1 Binder study	219
6.4.2 Simulant study	223
6.5 Summary	225
References	227
Tables	232
Figures	234
Chapter 7: CONCLUSIONS AND FUTURE WORK	249
7.1 Summary and Conclusions	249
7.1.1 High strain-rate compression of LM-1	249
7.1.2 Dynamic fracture of LM-1	253

7.1.3 High strain-rate compression of HTPB polymer (binder) and its composite (simulant)	255
7.2 Future Work	256
7.2.1 Composites incorporating LM-1	256
7.2.2 Temperature rise in BMGs	257
7.2.3 Additional tests with new inserts	258
7.2.4 Failure of HTPB polymer and simulant	259
7.2.5 Effects of compression and shear in HTPB	259
References	262
Figures	264
Bibliography	266

## List of Tables

Table 1.1	Comparison of observed spall strengths for $Zr_{41.25}Ti_{13.75}Cu_{12.5}Ni_{10}Be_{22.5}$ , $Si_3N_4$ , and $\Gamma$ -Met PX	24
Table 3.1	Selected properties of the BMG, maraging steel, and tungsten carbide used in the simulations	97
Table 3.2	List of experiments conducted with tapered inserts on as-cast LM-1	98
Table 3.3	List of experiments conducted with specimens with $L/D = 2.0$	99
Table 3.4	List of experiments conducted with specimens with $L/D = 1.0$	100
Table 3.5	Summary table detailing average stresses and standard deviations for the experiments shown in Figure 3.29	101
Table 4.1	Summary of fracture experiments conducted in the present study	154
Table 6.1	Ingredients in binder and simulant	231
Table 6.2	Specimen length and diameter, along with bar velocity, for the HTPB and simulant experiments in the current study	232

## List of Figures

Figure 1.1	Plot of strength vs. elastic limit for various materials, including metallic glasses	25
Figure 1.2	Critical casting thickness of metallic glasses since 1960	26
Figure 1.3	Flow curves illustrating homogeneous and inhomogeneous flow regimes	27
Figure 1.4	Summary plot of stresses previously obtained for $Zr_{41.25}Ti_{13.75}Cu_{10}Ni_{12.5}Be_{22.5}$	28
Figure 2.1	Schematic diagram of the Split-Hopkinson Pressure Bar (SHPB)	53
Figure 2.2	Schematic drawing of the SHPB, illustrating the incident, reflected, and transmitted strain signals	54
Figure 2.3	(a) Instance in which the slopes of the incident and transmitted signals are equal; and (b) corresponding constant strain-rate region	55
Figure 2.4	Stress-strain curves for amorphous LM-1 specimens of $L/D$ ratios of (a) 2.0 and (b) 0.5	57
Figure 2.5	Graph of peak stress vs. $L/D$ ratio for the experiments considered in this study	59
Figure 2.6	Sequential high speed pictures with an interframe time of 5 $\mu s$ , showing (a) the initial specimen; (b) the shear instability during loading; (c) the formation of a fracture plane; and (d) eventual failure	60
Figure 2.7	Macroscopic view of two fragments of a specimen with $L/D$ ratio of 2.0	61

Figure 2.8	Scanning Electron Microscopy of a specimen with $L/D$ ratio of 2.0, indicating (a) the presence of a failure front in the failed specimen and (b) the failure initiation region, showing a highly stressed region near the specimen-insert interface	62
Figure 2.9	Sequential images, taken with an interframe time of 5 $\mu$ s, of a specimen ( $L/D = 0.5$ ) showing (a) the undeformed specimen, (b) shear plane formation, and (c) failure.	63
Figure 2.10	Macroscopic view of fragments for a specimen with $L/D$ ratio of 0.5	64
Figure 2.11	Comparison of stress-strain curves for annealed and amorphous LM-1 for two different $L/D$ ratios: (a) 1.0 and (b) 2.0	65
Figure 2.12	Sequential images of an annealed sample, $L/D = 1.0$ , at strain-rate 1600/s, with (a) shear plane formation and (b,c) subsequent fragmentation shown at 7 $\mu$ s intervals	67
Figure 2.13	Sequential images of annealed sample, $L/D = 2.0$ , at strain-rate 450/s and at 7 $\mu$ s intervals, with (a) undeformed sample, (b) shear plane formation, and (c) evolution of a failure “front” separating “intact” material from fragmented material	68
Figure 2.14	Comparison of (a) annealed sample to fully amorphous failed samples of (b) $L/D = 1.0$ or 2.0 and (c) $L/D = 0.5$	69
Figure 3.1	Additional specimen geometries considered in testing low-ductility materials: (a) Conical inserts, (b) Dogbone compression specimen	102

Figure 3.2	Schematic of finite element simulation setup to examine stress concentration effects	103
Figure 3.3	Axial stress contours for finite element simulations of LM-1 with cylindrical inserts for L/D ratios of (left) 0.5, (middle) 1.0, and (right) 2.0	104
Figure 3.4	Shear stress contours for finite element simulations of LM-1 with cylindrical inserts for L/D ratios of (left) 0.5, (middle) 1.0, and (right) 2.0	105
Figure 3.5	Axial stress contours for simulation with conical inserts	106
Figure 3.6	Shear stress contours for simulation with conical inserts	107
Figure 3.7	Axial stress distribution of dogbone specimen	108
Figure 3.8	Shear stress distribution of dogbone specimen	109
Figure 3.9	(a) Schematic of new insert design, (b) Actual design	110
Figure 3.10	Axial stress distribution for simulation with maraging steel inserts	111
Figure 3.11	Shear stress distribution for simulation with maraging steel inserts	112
Figure 3.12	Finite Element Simulation illustrating equilibrium of the specimen	113
Figure 3.13	Axial stress contours for simulation with tungsten carbide inserts	114
Figure 3.14	Stress-strain curve under quasi-static compression with new inserts	115
Figure 3.15	High-speed camera images of as-cast LM-1 ( $L/D = 1.0$ ) with new tapered inserts	116
Figure 3.16	High-speed camera images of as-cast LM-1 ( $L/D = 2.0$ ) with new tapered inserts	117
Figure 3.17	High-speed camera images of annealed LM-1 ( $L/D = 2.0$ )	118

	with the tapered inserts	
Figure 3.18	Specimen with strain gage attached, prior to removal of epoxy and detachment of leads	119
Figure 3.19	Wheatstone bridge employed for the strain gage experiments in this study	120
Figure 3.20	Strain history signals from the strain gages mounted on the incident bar, transmitted bar, and specimen	121
Figure 3.21	Selected strain history as determined from the strain gage in Figure 3.20	122
Figure 3.22	Stress-strain curve constructed from the specimen strain gage signal in Figure 3.20	123
Figure 3.23	Optical microscopy of as-cast specimen, $L/D = 2.0$ , after testing	124
Figure 3.24	Comparison of stress signals as determined from the transmitted bar and specimen strain gage	125
Figure 3.25	Peak stresses as determined from transmitted and specimen strain gage signals	126
Figure 3.26	Strain vs. time plots as determined from the reflected signal and from the specimen strain gage	127
Figure 3.27	Peak strain-rates as measured from reflected signal compared to constant strain-rates as measured from specimen strain gage	128
Figure 3.28	Peak strains as measured from the reflected signal and specimen strain gage	129

Figure 3.29	Peak stress achieved by as-cast LM-1 specimens with both conventional and tapered inserts.	130
Figure 3.30	Strain-rate sensitivity of LM-1 from a strain-rate of $10^{-4}/s - 10^5/s$	131
Figure 4.1	Four-point bend specimen in the present study	155
Figure 4.2	Schematic of the MHPB for dynamic four-point bending	156
Figure 4.3	Schematic of the fixture used for the dynamic four-point bending experiments	157
Figure 4.4	Schematic time-distance ( $t-x$ ) diagram for wave propagation in the MHPB	158
Figure 4.5	(a) Force-versus-time curve for experiment Frac-1, (b) corresponding force-versus-displacement curve.	159
Figure 4.6	(a) Force-versus-time curve for a typical dynamic fracture experiment, along with selected high-speed camera images, (b) corresponding force-versus-displacement curve	160
Figure 4.7	Typical fracture surfaces after a dynamic four-point bending experiment resulting in failure.	161
Figure 4.8	Side views of fracture specimen	162
Figure 4.9	Fracture surface of notched LM-1 specimen, with direction of failure propagation shown	163
Figure 4.10	Fracture surface near the notch in region B in Figure 4.9	164
Figure 4.11	Fracture surface of region C from Figure 4.9	169
Figure 4.12	Fracture surface of region D from Figure 4.9	174
Figure 4.13	Fracture surface of region E from Figure 4.9	179

Figure 4.14	Force-versus-time plot for a dynamic bending experiment in which failure did not occur	184
Figure 4.15	SEM images after an experiment in which unstable fracture did not occur	185
Figure 4.16	Results from subsequent loading of initially damaged LM-1 sample	186
Figure 5.1	Mechanism for synthesis of HTPB pre-polymer (prior to addition of isocyanates and plasticizer)	209
Figure 6.1	Schematic of one technique utilized to prepare SHPB specimens in the current study	234
Figure 6.2	Schematic of SHPB employed in experiments in the current study	235
Figure 6.3	Raw data from a representative experiment on the SHPB binder	236
Figure 6.4	Representative true stress vs. true strain and true strain-rate vs. true strain curves corresponding to the data from Figure 6.3	237
Figure 6.5	Stress-strain curves in the present study for experiments conducted on the HTPB polymer	238
Figure 6.6	Images of four post-test specimens	239
Figure 6.7	Peak stress of the HTPB polymer as a function of strain-rate in the current study, as well as in two previous studies.	240
Figure 6.8	Magnified view of Figure 6.7 to locate the approximate strain-rate from low strain-rate sensitivity to high strain-rate sensitivity at 2100/s	241
Figure 6.9	Stress-strain curves at 3000/s for HTPB from a previous study by Siviour	242

Figure 6.10	DMA traces from Siviour	243
Figure 6.11	Laser confocal microscopy of (a, b) failed HTPB polymer and (c) pristine HTPB polymer after specimen preparation	244
Figure 6.12	True stress vs. true strain curves for SHPB experiments conducted on the simulant in the present study	247
Figure 6.13	Laser confocal microscopy of simulant	248
Figure 7.1	Fracture surface of the specimen from experiment Frac-1	263

## ACKNOWLEDGMENTS

The completion of any significant research project is no solitary effort; many people contribute in various ways, either directly or indirectly. Of these people, no one helped me more than my advisors: Prof. Vikas Prakash, Prof. John Lewandowski, and Dr. Jennifer Jordan. Prof. Prakash's firm but gentle guidance and Prof. Lewandowski's relentless optimism made even the most difficult parts of this research project possible to complete. Likewise, Dr. Jordan's communication made it much easier to know what needed to be done as the research was drawing to a close. I also thank Prof. Joseph Mansour and Prof. Xiong (Bill) Yu for offering to be on my dissertation committee and for providing useful guidance throughout this project.

In addition, I am grateful for the guidance of the members of the D.K. Wright Lab and the MMC Group at Case Western Reserve University, especially from Dr. Fuping Yuan, Dr. Ali Shamimi Nouri, Dr. Joshua Caris, Nirav Parikh, Lisa Deibler, Chung-Kuo Park, Michael Bifano, and Eric Mayhew. I also gratefully acknowledge the assistance of Dr. David Hovis on patiently helping me understand how a confocal microscope works and how to interpret the data received from it. Their assistance in performing, designing, and analyzing the experiments was instrumental to the completion of this dissertation. I am also grateful for the opportunity to learn from the researchers during my internships at the Air Force Research Laboratory (AFRL) in Florida, especially from Dr. Jordan, Dr. Thomas Krawietz, Chad Rumchik, Wayne Richards, and Brian Woodworth.

I would like to thank my parents (Sunny Padayatil and Rosamma Sunny) and my brother Joseph for knowing when I needed to be encouraged and when I needed to be pushed, and all of my friends from Case Western Reserve University and Holy Rosary

Church, for challenging and comforting me during the times it was most needed. This document is as much a celebration of your assistance throughout the years.

Finally, the primary funding was provided by ONR-N0014-03-1-0205 with partial experimental support from DARPA-ARO-DAAD19-01-0525, along with additional partial funding from the Case Prime Fellowship. More recently, funding was made possible by the Science, Mathematics, and Research for Transformation (SMART) Scholarship, and the assistance of Dr. David Jeffcoat, Kathy Owens, and Janna Simons are gratefully acknowledged throughout the transition process from graduate studies to full-time research.

The supply and purchase of Zr-based materials from Liquidmetal was made possible through the Center for Mechanical Characterization of Materials. The supply of HTPB polymer and composite was received from AFRL (Eglin Air Force Base, FL).

A High Strain-Rate Investigation of a  
Zr-based Bulk Metallic Glass and an HTPB Composite

Abstract

by

GEORGE PADAYATIL SUNNY

High strain-rate tests are performed on LM-1 using a Split-Hopkinson Pressure Bar (SHPB) to investigate effects of  $L/D$  ratio and annealing. An ultra high-speed camera was also employed to record the deformation and failure processes of LM-1. The amorphous specimens exhibit a reduction in peak stress with reduced  $L/D$  ratio and failure at the specimen-insert interface, indicative of stress concentrations due to the difference in the specimen and insert diameters, while the annealed specimens exhibited extensive fragmentation.

The stress concentrations in the specimen motivated simulations using LS-DYNA to design new inserts. A tapered insert design was chosen to reduce stress concentrations on amorphous and annealed specimens. Strain gages were also attached to as-cast specimens to determine the elastic stress-strain response. As-cast and annealed specimens with tapered inserts exhibit failure in the gage section, and a comparison of the peak

stresses from quasi-static and pressure-shear plate-impact experiments to those in the current study indicate a negligible strain-rate sensitivity of LM-1.

Additional experiments are carried out using a modified SHPB to investigate the loading-rate sensitivity of notched LM-1 specimens. An ultra high-speed camera is employed to provide images synchronized with load-displacement traces from a high-bandwidth oscilloscope. No loading-rate sensitivity on the fracture toughness was observed. Experiments are also conducted to induce damage into notched LM-1 specimens without causing catastrophic failure; a damage zone is present in the specimens and slip-line fields are created which are consistent with those expected in an elastic-perfectly plastic material. Finally, experiments conducted to load previously damaged LM-1 samples indicate an increase in the fracture toughness and energy required to induce catastrophic failure.

Finally, high strain-rate compression experiments are conducted on a hydroxy-terminated polybutadiene (HTPB) polymer and its composite using another modified SHPB for testing of soft materials. Results from the experiments on HTPB polymer indicate a transition in the polymer between low and high strain-rate sensitivity at 2100/s, along with axial splitting at strain-rates above 3000/s. On the other hand, reduced rate-sensitivity is observed in the HTPB composite, most likely due to the presence of numerous interfaces between the glass beads and the polymer binder.

## ***Chapter 1 – Background and Literature Survey of Metallic Glasses***

### **1.1 Overview of Metallic Glasses**

Metallic glasses (amorphous metals) are the result of supercooling of a liquid alloy, which produces a metastable phase and prevents formation of crystals, leading to a lack of long-range periodicity. The resulting structure exhibits very high strength compared to its crystalline counterparts because the defects present in the crystalline structures, such as dislocations, are not present in the amorphous alloy. This lack of dislocations also contributes to the large elastic strain (e.g. ~2%), as seen in Figure 1.1 [1]. However, the extremely high critical cooling rates necessary for the first metallic glasses made it impossible to produce large thicknesses of the alloy and made mechanical testing of the metallic glass impractical.

In this chapter, the first metallic glasses and their methods of production will be described in Section 1.2. Next, the evolution of metallic glasses to bulk forms will be discussed in Section 1.3; the methods of mechanical characterization, flow, and fracture will be discussed in Section 1.4. Finally, some previous results for Zr-based bulk metallic glasses, a class of excellent glass formers, will be shown in Section 1.5, in order to put the scope of this part of the work, discussed in Section 1.6, into its proper context.

### **1.2 The First Metallic Glasses**

The first metallic glass,  $\text{Au}_{75}\text{Si}_{25}$ , was first produced by Klement, Willens, and Duwez at the California Institute of Technology [2]. This first metallic glass was

produced by cooling the Au-Si liquid alloy at  $10^6$  K/s through the process of splat quenching, producing an unstable metallic glass ribbon of thickness less than 0.1 mm.

About a decade after the discovery from Klement et al., other groups developed metallic glasses with reduced critical cooling rates.  $\text{Pd}_{77.5}\text{Cu}_6\text{Si}_{16.5}$  was one of these metallic glasses [3], as it exhibited a critical cooling rate between  $10^2$  and  $10^3$  K/s. A few years later, Allied Signal (now Honeywell) developed another metallic glass,  $\text{Fe}_{80}\text{B}_{20}$ , by casting the liquid alloy onto a cold, rapidly spinning wheel. However, in both of these cases, the resulting dimensions of the resulting metallic glasses meant that the glasses could only be produced in limited forms, such as ribbons, wires, and thin foils. In addition, the very small sizes of these metallic glasses made them unsuitable to conventional mechanical testing techniques.

### **1.3 Bulk Metallic Glasses (BMGs)**

The first consistent production of a BMG was by Kui, Greer, and Turnbull [4]. Cooling of  $\text{Pd}_{40}\text{Ni}_{40}\text{P}_{20}$  at approximately 10 K/s in a melted  $\text{B}_2\text{O}_3$  flux led to an amorphous alloy of minimum dimension 10 mm, and the method described produced fully amorphous specimens consistently. Unfortunately, the high cost of Pd made the production of these alloys prohibitively expensive. A decade passed while research groups investigated alternative compositions that were more cost-effective. The most successful of the early bulk glasses were primarily discovered by Inoue et al. at Tohoku University (Japan) and by Johnson et al. at the California Institute of Technology.

Inoue et al. produced three BMGs in the 1990s: La-Al-Ni [5], Zr-Cu-Ni-Al [6], and Mg-Cu-Y [7]. All three of these BMGs were produced by melt spinning or die casting, and each of them exhibited critical cooling rates on the order of 10 K/s. Such cooling rates made mechanical testing of the BMGs more practical, and tensile stresses of up to 650 MPa were recorded for the Mg-Cu-Y alloy, significantly in excess of crystalline versions of any commercially produced Mg alloy.

The glass produced by Johnson et al. at the California Institute of Technology was a pentary alloy –  $Zr_{41.25}Ti_{13.75}Cu_{10}Ni_{12.5}Be_{22.5}$  [8]. By water quenching the induction melted alloy, fully amorphous specimens of diameters up to 14 mm were produced, and the critical cooling rate for the glass specimens was found to be less than 10 K/s. The large dimensions that can be produced, because of its excellent glass forming ability, make this BMG an interesting one for mechanical testing, as will be shown later.

In all of these BMGs, there were two common characteristics: a wide supercooled liquid region, denoted by the difference between the crystallization temperature  $T_x$  and the glass transition temperature  $T_g$  (about 75-150 K), and a high value of  $T_g/T_m$  (the reduced glass transition temperature, approximately 0.65), where  $T_m$  is the melting temperature of the BMG. The maximum sample thicknesses, as shown by Inoue [9], are dependent on both the width of the supercooled liquid region and the reduced glass transition temperature; higher values of both of these quantities lead to larger maximum sample thicknesses. Advances that have led to wider supercooled liquid regions and

higher reduced glass temperatures have led to larger sample thicknesses over the past five decades, as seen in Figure 1.2 [1].

More recently, researchers have proposed empirical rules to predict alloy compositions with excellent glass forming ability. Johnson has suggested, for optimum glass forming ability, that a BMG consists of three components: one or more of the early transition metals (e.g. Zr, Ti), one or more of the late transition metals (e.g. Cu, Ni, Fe), and a simple metal (e.g. Al, Be) [10]. Inoue proposed three additional rules: at least four elements in the alloy, a wide range of atomic radii (at least 12%), and a negative heat of mixing among the components [9]. Combinations of these rules have been suggested to promote the formation of a fully amorphous system by a more efficient packing of the atoms, and this packing leads to a smaller amount of free volume in the resulting amorphous structure.

#### **1.4 Flow and Fracture Mechanisms of Metallic Glasses**

The deformation of bulk metallic glasses has been characterized by two flow regimes [11]: inhomogeneous flow, in which the plastic flow of the material manifests itself in shear bands (localized regions, less than 10 nm in width, of intense plastic deformation), and homogeneous flow, in which the plastic flow of the material is more uniform. Such behavior, as seen in Figure 1.3, appears to be dependent on both temperature and strain-rate, as quasi-static tests on metallic glasses performed at temperatures near  $T_g$  should promote large strains-to-failure, whereas at lower temperatures or higher strain-rates, catastrophic failure occurs shortly after the onset of

plastic flow. There have been three mechanisms proposed for the formation of these shear bands (i.e. inhomogeneous flow); one proposed mechanism distinguishes between the two flow regimes based on the generation and annihilation of free volume [11], where the free volume of the metallic glass corresponds to the volume that is not occupied by atoms. A second proposed mechanism suggests that small groups of atoms, called shear transformation zones (STZs) [12], arrange themselves in order to accommodate strain accumulating in the specimen. These STZs, because of their small initial size (on the order of five atom diameters), undergo intense local strain as stress is applied. The third proposed mechanism involves the local heating of the metallic glass to temperatures exceeding the glass transition temperature [11, 13]. In this mechanism, the intense localized heating leads to softening of the BMG and corresponding failure. Recent work involving coatings with both high spatial and temporal resolution [14] has shown that the magnitude of local heating is dependent on the magnitude of the shear offset in addition to the speed of the shear band and other material parameters. This work clearly indicated that while significant temperature rises may accompany final catastrophic fracture where the shear offset is large, the amount of temperature rise at the initiation of the shear band is negligible.

On a macroscopic level, the yield behavior of some metallic glasses has been characterized over a wide range of stress states by a Mohr-Coulomb criterion [15] of the form

$$\tau = \tau_0 - \alpha\sigma, \quad (1.1)$$

where  $\tau$  and  $\sigma$  are the shear and normal stresses on the plane of failure,  $\tau_0$  is the stress in pure shear, and  $\alpha$  is an experimentally determined parameter. (While the equations refer to yield behavior in the BMG, these can be used for failure in high strain-rate testing, as the small plastic strains-to-failure imply that yield and failure are almost coincident.) Such behavior has been confirmed by testing tension and compression samples with superimposed pressure, in addition to examining the fracture angle of samples tested under these conditions [16-18]. However, the degree of tension-compression asymmetry is rather small in some BMGs, so a von-Mises criterion has been suggested as well [19]. Other BMGs have been shown [20] to exhibit a modified Mohr-Coulomb behavior of the form

$$\begin{aligned}\tau_t &= \tau_0 - \alpha_t \sigma_t \\ \tau_c &= \tau_0 + \alpha_c \sigma_c, \\ \alpha_t &> \alpha_c > 0\end{aligned}\tag{1.2}$$

where the subscripts  $t$  and  $c$  refer to stresses in tension and compression, respectively. Still other metallic glasses have been shown to exhibit yield and failure in agreement with the von Mises criteria [19].

## 1.5 Previous Experiments on Zr-based BMGs

Zr-based BMGs, such as  $Zr_{41.25}Ti_{13.75}Cu_{10}Ni_{12.5}Be_{22.5}$  and  $Zr_{52.5}Cu_{17.9}Ni_{14.6}Al_{10}Ti_5$ , are considered excellent candidates for mechanical testing because of their excellent glass forming abilities. Several researchers have exploited this ability in order to characterize the compressive and shear behavior of these metallic glasses. Key experiments detailing the quasi-static behavior under compression, tension, and torsion will be discussed in 1.5.1, while the experiments detailing the high strain-rate behavior will be discussed in

1.5.2. Additional experiments detailing the quasi-static fracture behavior of Zr-based BMGs will be discussed in 1.5.3. Figure 1.4 summarizes peak stress values, as a function of strain-rate, previously determined for  $\text{Zr}_{41.25}\text{Ti}_{13.75}\text{Cu}_{10}\text{Ni}_{12.5}\text{Be}_{22.5}$  at room temperature. Most of the fully amorphous  $\text{Zr}_{41.25}\text{Ti}_{13.75}\text{Cu}_{10}\text{Ni}_{12.5}\text{Be}_{22.5}$  glass samples exhibit strengths between 1.75 GPa and 2 GPa, as seen in Figure 1.4.

### *1.5.1 Quasi-static compression, tension, and torsion of Zr-based BMGs*

The first quasi-static compression tests on  $\text{Zr}_{41.25}\text{Ti}_{13.75}\text{Cu}_{10}\text{Ni}_{12.5}\text{Be}_{22.5}$  were performed by Bruck [19]. In some of these experiments, right-circular cylindrical tabs of varying  $L/D$  (length-to-diameter) ratios of 1.5-2.0 were tested in an MTS 319.25 axial-torsional load frame under uniaxial stress conditions at strain-rates ranging from  $10^{-4}/\text{s}$  to  $10^{-3}/\text{s}$ . The material exhibited a yield strength of 1.9 GPa but less than 1% ductility for the largest diameters (7 mm rods), while slightly more ductility was exhibited for specimens with smaller diameters (2.5-3 mm). Specimens failed at  $45^\circ$  to the loading axis, consistent with the von Mises yielding criterion. Additional tests were performed to increase the stress triaxiality by reducing the  $L/D$  ratio to 0.5-0.8 and increasing the friction effects by removing grease from the specimen-load frame interfaces. In these experiments, the yield stress increased to 2.12 GPa, while the true strain-to-failure increased dramatically for the 2.5 mm diameter specimens from 4% to 29% and for the 7 mm diameter specimens from 2% to 6%.

Tensile and torsion tests were also performed by Bruck [19] to investigate the fracture processes in tension and shear, respectively. During tensile testing, the stress-

strain curve was almost completely linear to failure, with a fracture stress of 1.8 GPa and a strain-to-failure of 1.8%. Specimens failed at 55° to the loading axis, which is different from what is expected under von Mises strength criteria (45°). Scanning electron microscopy (SEM) revealed localized plasticity in shear bands, as evidenced by the vein pattern from the micrographs. Torsion tests of  $\text{Zr}_{41.25}\text{Ti}_{13.75}\text{Cu}_{10}\text{Ni}_{12.5}\text{Be}_{22.5}$  revealed a shear stress of 1.10 GPa, initiation of yield at a strain of 1.9%, and strain-to-failure of 2.1%. The fracture surface was oriented at 90° to the loading axis, again supporting the characterization of a von Mises strength criterion.

Additional quasi-static tests in tension and compression were performed in the presence of high hydrostatic pressure by Lewandowski et al. (e.g. beyond 700 MPa) [16, 18, 21].  $\text{Zr}_{41.25}\text{Ti}_{13.75}\text{Cu}_{10}\text{Ni}_{12.5}\text{Be}_{22.5}$  did not exhibit much pressure sensitivity or tension/compression asymmetry, although fracture plane angles deviated from 45°, invalidating the use of a von Mises criterion. Instead, a Mohr-Coulomb criterion was proposed for this BMG. In addition, the effects of changes in temperature and annealing on the yield strength, strain-to-failure, and fracture morphology of  $\text{Zr}_{41.25}\text{Ti}_{13.75}\text{Cu}_{10}\text{Ni}_{12.5}\text{Be}_{22.5}$  were investigated. Increasing the temperature led to a linear decrease in the yield stress for rectangular specimens of side 4 mm, whereas the use of a cylindrical specimen of 7 mm diameter led to a more rapid drop in yield stress between 500 K and 623 K ( $T_g$ ). The increase in temperature also led to more viscous flow during the failure process of the material. Annealing of the material, on the other hand, appeared to increase the compressive fracture stress, as long as the annealing was performed at temperatures not exceeding  $T_g$ . Annealing at the crystallization temperature of the

material (723 K) for 24 hours led to a decrease in strength from 1.8-1.9 GPa (fully amorphous) to 0.4-0.6 GPa. Brittle failure occurred for all specimens that were annealed for longer than 6 hours, in sharp contrast to the vein patterns more commonly exhibited on the fracture surfaces with the amorphous material.

### *1.5.2 Mechanical tests of Zr-based BMGs at high strain-rates*

The mechanical behavior of both  $\text{Zr}_{41.25}\text{Ti}_{13.75}\text{Cu}_{10}\text{Ni}_{12.5}\text{Be}_{22.5}$  and  $\text{Zr}_{52.5}\text{Cu}_{17.9}\text{Ni}_{14.6}\text{Al}_{10}\text{Ti}_5$  have not been well-characterized in either tension or torsion under high strain-rates ( $10^2/\text{s}$  and higher). However, some data exist on the behavior of both of these materials under high strain-rate compression.

The first known high strain-rate compression tests on  $\text{Zr}_{41.25}\text{Ti}_{13.75}\text{Cu}_{10}\text{Ni}_{12.5}\text{Be}_{22.5}$  were performed by Bruck [13] using a Split-Hopkinson Pressure Bar (SHPB). The failure strength was largely insensitive to the strain-rate, as the failure strength of the material at  $10^3/\text{s}$  was still about 1.8 GPa. This insensitivity to strain-rate was further confirmed by experiments performed above 3000/s in order to eliminate previously observed dispersion effects in the bulk metallic glass. Failure occurred at  $45^\circ$  to the loading axis, virtually identical to the angle found from quasi-static compression tests. In addition, a temperature increase at failure of up to 500 K after failure was detected by an infrared HgCdTe detector, supporting the claim that the high temperature rise accompanies catastrophic fracture in the BMG.

Additional compression experiments were performed by Lu [22] to investigate the effect of test temperature on the failure strength and flow behavior of  $\text{Zr}_{41.25}\text{Ti}_{13.75}\text{Cu}_{10}\text{Ni}_{12.5}\text{Be}_{22.5}$  at strain-rates between  $10^2/\text{s}$  and  $10^4/\text{s}$ . Using a specially-designed furnace around the specimen, these tests were performed at temperatures approaching and exceeding  $T_g$ . Inhomogeneous flow was exhibited in almost all of the high strain-rate tests, including the instances in which the test temperature reached over 623 K. In these cases, the failure strength was reduced from 1.8 GPa at room temperature to 1.0 GPa, while inhomogeneous flow consistently occurred for the experiments at high strain-rates. The data (both for quasi-static and dynamic experiments) were utilized to separate the flow behavior of  $\text{Zr}_{41.25}\text{Ti}_{13.75}\text{Cu}_{10}\text{Ni}_{12.5}\text{Be}_{22.5}$  into three regions, classified by flow behavior: shear localization, Newtonian flow, and non-Newtonian flow (the last of which primarily occurs at creep rates).

To investigate the high strain-rate compressive behavior at ultra-high strain-rates (above  $10^6/\text{s}$ ), experiments were performed by Zhuang et al. [23] using a powder gun plate-impact system on both  $\text{Zr}_{41.25}\text{Ti}_{13.75}\text{Cu}_{10}\text{Ni}_{12.5}\text{Be}_{22.5}$  and a  $\beta$ -composite of the metallic glass, combined with a VISAR (Velocity Interferometry System for Any Reflector) to determine the particle velocity history during the experiment. The particle velocity profiles in the experiment exhibited a surprisingly low Hugoniot elastic limit (the stress at which damage begins to occur in the material) below 100 MPa. In addition, phase changes during shock compression were suggested in the material based on the profile of the shock-velocity vs. particle velocity curve and the reduction in shear banding after very high impact velocities ( $\sim 1000$  m/s). Finally, the spall strength (resistance to

tensile failure during planar impact) of  $\text{Zr}_{41.25}\text{Ti}_{13.75}\text{Cu}_{10}\text{Ni}_{12.5}\text{Be}_{22.5}$  was measured to be 2.3 GPa, about 20% larger than quasi-static tensile yield stresses measured elsewhere [16, 17, 19]. More recent work by Yuan et al. [24] using a single-stage gas gun suggests that the spall strength is much higher than previously measured – spall strengths were found to be 2.8 GPa for an applied normal stress of 5.1 GPa and 2.3 GPa for an applied normal stress of 7.0 GPa – and that the Hugoniot Elastic Limit is approximately 6.1 GPa. Additional experiments performed in pressure-shear show a spall strength of about 2.2 GPa for a plate-impact experiment with a flyer inclined at  $12^\circ$ ; this suggests some additional damage created in the BMG due to the shear stress, but not enough to reduce the spall strength substantially. All of these values are well in excess of those reported for a variety of ceramics and advanced alloys [25, 26], as seen in Table 1.1.

Two groups of high strain-rate compression tests were performed on a similar BMG,  $\text{Zr}_{52.5}\text{Cu}_{17.9}\text{Ni}_{14.6}\text{Al}_{10}\text{Ti}_5$ , in order to characterize the behavior of the glass at strain rates of approximately  $10^3/\text{s}$ . Experiments were conducted by Hufnagel et al. [27] employing the SHPB and an ultra-high-speed camera (DRS Ultra-8) to take pictures of the deformation and failure process at  $1\ \mu\text{s}$  intervals. Peak stresses of 1.7 GPa were measured for this material with the SHPB, and after correcting for wave dispersion using the Pochhammer-Chree dispersion relations for both  $\text{Zr}_{52.5}\text{Cu}_{17.9}\text{Ni}_{14.6}\text{Al}_{10}\text{Ti}_5$  and  $\text{Zr}_{41.25}\text{Ti}_{13.75}\text{Cu}_{10}\text{Ni}_{12.5}\text{Be}_{22.5}$ , both metallic glasses were seen to exhibit negative strain-rate sensitivity; the peak stress was reduced when the strain-rate was increased. In addition, an analysis of thermal conduction and deformation, combined with pictures from the Ultra-8 camera, suggested to these authors that there was some adiabatic heating

present during the deformation, as evidenced by the presence of light emission during testing. However, the light emission is more likely due to the rapid oxidization of the highly reactive elements present, as shown in another work by Gilbert et al. [28]. The analysis by Hufnagel et al. also suggests that the thermal conductivity should be considered when determining the strain and temperature fields inside the material during loading. Additional work by Subhash [29] further supports the previous failure strength and negative strain-rate sensitivity claims for  $Zr_{52.5}Cu_{17.9}Ni_{14.6}Al_{10}Ti_5$  but also suggests that, for LM-1, the strain-rate sensitivity is negligible [30]. These claims were also found to be valid when varying amounts of Hf replaced the Zr, but the replacement of Zr with Hf increased the fracture stress from 1.4 GPa to 1.6-1.8 GPa.

### *1.5.3 Quasi-static and Dynamic Fracture of Zr-based BMGs*

A number of studies have been performed on the fracture toughness of BMGs, and the work that has been conducted has primarily focused on Zr-based BMGs (specifically LM-1), because of their excellent glass forming ability. The low critical cooling rates (e.g. 1 K/s) allow for fully amorphous specimens in excess of 1 mm in thickness, and such sample sizes are necessary to ensure plane-strain conditions during the experiment for metallic glasses that exhibit high fracture toughness. A number of studies have focused on the fracture toughness of fatigue-precracked specimens under both low (e.g. 1 MPa  $m^{1/2}/s$ ) [16, 17, 31-34] and high (e.g.  $10^6$  MPa  $m^{1/2}/s$ ) [35, 36] loading-rates, while a smaller number of studies have focused on the fracture toughness of notched specimens under quasi-static loading [17, 31-33]. Work conducted by Lewandowski et al. [37] has indicated that fracture energy is highly dependent on the

ratio of the shear modulus to the bulk modulus ( $\mu/B$ ); when this value is below 0.4, the fracture energy approaches  $100 \text{ kJ/mm}^2$ , whereas above this value, the fracture energy approaches  $0.001 \text{ kJ/mm}^2$ . (The value of  $\mu/B$  can be determined solely in terms of  $\nu$ , Poisson's ratio; the critical value of  $\nu$  in this case is approximately 0.32.)

The first notched fracture toughness experiments on LM-1 were conducted by Conner et al. [34] using two experimental setups to provide estimates of the fracture toughness. In the first setup, the LM-1 specimen was loaded under three-point bending, and the fracture toughness was calculated based on the load applied to the specimen and assuming linear elastic fracture mechanics, which is a good assumption based on the high yield strength exhibited in stress-strain curves from quasi-static experiments conducted in compression and the calculated size of the plastic zone relative to the sample dimensions [17, 19]. The second experimental setup used coherent gradient sensing (CGS), which utilizes laser light, a mirror, and two gratings in order to determine out-of-plane displacements (through the presence of fringes) which can be related directly to the fracture toughness of the specimen. Results from the experiments show consistent values of  $K_C$  (fracture toughness under mode-I loading) of about  $60 \text{ MPa m}^{1/2}$  but also the presence of some roughness in the fracture surface (approximately  $50\text{-}150 \text{ }\mu\text{m}$ ). The experiments were conducted under notched bending conditions as revealed by examination of the fracture profiles in the paper [34]. While a value for  $K_{IC}$  is given in the paper, a valid  $K_{IC}$  measurement requires the use of a fatigue precrack and the value likely overestimates the fracture toughness as shown later [17, 33].

Around the same time as the initial experiments by Conner et al., Gilbert et al. [38] conducted experiments on fatigue-precracked compact tension (CT) specimens of LM-1 as well as two annealed forms of LM-1 (633 K and 733 K). The observed fracture toughness of LM-1 was approximately  $55 \text{ MPa m}^{1/2}$ , and the annealed (633 K) and devitrified (733 K) LM-1 specimens exhibited fracture toughness of about  $1 \text{ MPa m}^{1/2}$ . While it was clear that the specimens were fatigue-precracked, it is less clear whether the dominant fracture was planar or if it had the same roughness characteristics as in the work by Conner et al. Subsequent work by Gilbert [39] showed significant out-of-plane fracture and crack front bowing, partly attributed to residual stresses induced during processing.

A few years later, additional fracture toughness experiments under low loading-rates were conducted by Lowhaphandu et al. [17, 33] also utilizing three-point bending. Results from these experiments showed a much lower fracture toughness of about  $18 \text{ MPa m}^{1/2}$ , an absence of crack front bowing, and a planar macroscopic fracture surface. More specimens were tested in this study -- the six specimens tested exhibited a scatter of less than  $2 \text{ MPa m}^{1/2}$ , indicating a high degree of confidence in the measured fracture toughness. Unlike the work performed by Conner et al., the region below the notch was observed to be largely planar; the discrepancy between the two sets of results was attributed to the thicker sample size in Lowhaphandu's work (4-7 mm, instead of 2.2 mm), along with a possible difference in the notching technique. Additional experiments using a number of notch root radii (from  $60 \mu\text{m}$  – 1 mm) show a dramatic increase in the value of the critical fracture toughness ( $K_Q$ ) from  $20 \text{ MPa m}^{1/2}$  (fatigue-precracked) to as

high as  $250 \text{ MPa m}^{1/2}$  (1 mm notch root radius) [17, 31, 32]. The large increase in the fracture toughness in the notched specimens is evidenced by the large increase in the degree of crack bifurcation in the specimens with the bluntest notches. Further experiments [31] indicate that increasing the stress-intensity rate from  $0.2 \text{ MPa m}^{1/2}/\text{s}$  to  $800 \text{ MPa m}^{1/2}/\text{s}$  had a negligible effect on the observed fracture toughness for both the fatigue-precracked and notched specimens.

Owen et al. [35] investigated dynamic fracture initiation in three-point bend specimens using a drop weight tower as well as an asymmetric impact configuration to generate mode II loading, and thus, substantial shearing in the specimen, in contrast to pure mode I conditions. The drop weight experiments indicate a large increase in the dynamic fracture toughness with loading rate, from  $60 \text{ MPa m}^{1/2}$  under quasi-static loading [34] to about  $200\text{-}250 \text{ MPa m}^{1/2}$  at crack tip loading rates of approximately  $10^7 \text{ MPa m}^{1/2}/\text{s}$ . Recent mixed-mode loading experiments have also suggested significant increases in toughness when loading is not strictly mode I [40].

Additional work has been conducted by Rittel and Rosakis [36], in which the results of dynamic three-point bend tests obtained by using two techniques – a drop-weight tower and a modified Split-Hopkinson Pressure Bar (MHPB) – were compared with those obtained by employing a short-beam dynamic fracture technique to verify its validity in testing specimens of LM-1. These results showed a large increase in the fracture toughness of LM-1 with loading-rate, from  $\sim 50 \text{ MPa m}^{1/2}$  ( $1 \text{ MPa m}^{1/2}/\text{s}$ ) to  $\sim 150 \text{ MPa m}^{1/2}$  ( $10^6 \text{ MPa m}^{1/2}/\text{s}$ ); however, substantial scatter ( $100 \text{ MPa m}^{1/2}/\text{s}$  above or

below the stated fracture toughness) was present in the results at the higher loading-rates. Any effect of notch geometry in these specimens on the fracture toughness was observed to be negligible, although the effects of mode-mixity on the toughness were not evaluated.

## **1.6 Scope of the Current Investigation on LM-1**

As noted before, there have been some differing observations of the strain-rate sensitivity of LM-1 [13, 19, 27, 30]. Knowledge of the high strain-rate behavior is key to gaining insight into the behavior of the BMG for impact applications. The previous papers mentioned did not discuss the effects of varying the  $L/D$  ratio on the strength, strain-to-failure, or fracture behavior of this BMG. In addition, annealing of this BMG has shown an increase in hardness, quasi-static compressive strength, and the potential for fragmentation, all of which may be important considerations when this material is considered for a wide variety of applications, because of its embrittlement and loss of toughness [17, 32, 37].

The high strain-rate behavior of fully amorphous and annealed LM-1 is investigated for different  $L/D$  ratios ranging from 0.5 to 2.0 in Chapter 2. A conventional SHPB was employed in order to determine the effects of changing the  $L/D$  ratio on both the peak stress and the strain-to-failure of the specimen. In addition, experiments were conducted using an ultra-high-speed camera to examine the deformation and failure process of this BMG. Finally, optical and scanning electron microscopy was conducted in order to determine the effect of  $L/D$  on the veining patterns seen on the fracture surface.

The apparent strain-rate sensitivity is discussed, and stress inhomogeneity issues due to a geometrical instability in the specimen are discussed in detail as an artifact that may have affected the results reported previously.

The results of Chapter 2 motivate the design and implementation of new inserts in Chapter 3. Finite element simulations of the stress state during SHPB compression are conducted. Previous studies have been conducted to quantify the stress concentrations that occur during SHPB experiments and are discussed in detail here. The finite element simulations are investigated to determine the effects of  $L/D$  ratio on the stress field that is present during testing. This information is utilized to rationalize some of the negative strain-rate sensitivity previously reported by other investigators [27, 29]. In addition, a new insert design has been developed to reduce stress concentrations present at the specimen-insert interface. Additional FEM simulations are conducted to confirm the homogeneous stress state and duration of equilibrium in the specimen.

Due to the new inserts, the location of failure in the specimens change, and the effects of the reduced stress concentrations on the location of failure in the specimen are explained. Significant differences in the fracture behavior of both the amorphous and annealed BMG are discussed in light of the previous simulations. Finally, to account for dispersion in the wave signals because of the new inserts, SHPB experiments in which strain gages are attached to the specimens are conducted in order to determine the stresses and strains-to-failure accurately and to provide a clearer understanding of the effects of changes in  $L/D$  on the dynamic flow and fracture behavior of LM-1. The strain-rate

effects are also discussed in light of more recent investigations [41] that provide evidence for the strain-rate sensitivity of LM-1.

In Chapter 4, high loading-rate fracture experiments are conducted on notched LM-1 samples to investigate the rate sensitivity of notched LM-1 at approximately  $10^6$  MPa m<sup>1/2</sup>/s (as opposed to the current 1 MPa m<sup>1/2</sup>/s). Dynamic fracture experiments are conducted on notched samples of amorphous LM-1 using an instrumented Modified Split-Hopkinson Pressure Bar (MHPB). The experiments were conducted using four-point bend specimens; a high-speed camera was utilized to investigate dynamic crack initiation and propagation during the loading process. In these experiments, the load-point force versus time profiles were obtained. The high-speed camera images were matched to the force-versus-time profile to examine the sequence of the failure events leading to the catastrophic fracture of the specimen. Extensive scanning electron microscopy was also conducted to examine the fracture surfaces. Finally, a series of well-controlled stress wave loading experiments were conducted to induce pre-determined sub-critical levels of damage at the notch (without causing catastrophic failure of the LM-1 specimens), so as to better understand the damage initiation mechanisms at the notch in response to the dynamic bend loading.

## References

1. Telford M. (2004) The case for bulk metallic glass. *Materials Today* **7**, 36-43.
2. Klement W., Willens R.H., Duwez P. (1960) Non-crystalline Structure in Solidified Gold-Silicon Alloys. *Nature* **187**, 869-870.
3. Chen H.S., Kimerling L.C., Poate J.M., Brown W.L. (1978) Diffusion in a Pd-Cu-Si metallic glass. *Applied Physics Letters* **32**, 461-463.
4. Kui H.W., Greer A.L., Turnbull D. (1984) Formation of bulk metallic glass by fluxing. *Applied Physics Letters* **45**, 615-616.
5. Inoue A., Zhang T., Masumoto T. (1990) Production of Amorphous Cylinder and Sheet of  $\text{La}_{55}\text{Al}_{25}\text{Ni}_{20}$  Alloy by a Metallic Mold Casting Method. *Materials Transactions JIM* **31**, 425-428.
6. Zhang T., Inoue A., Masumoto T. (1991) Amorphous Zr-Zr-Al-TM (TM=Co, Ni, Cu) Alloys with Significant Supercooled Liquid Region of over 100 K. *Materials Transactions JIM* **32**, 1005-1010.
7. Inoue A., Nakamura Y., Nishiyama N., Masumoto T. (1992) Mg-Cu-Y Bulk Amorphous Alloys with High Tensile Strength Produced by a High-Pressure Die Casting Method. *Materials Transactions JIM* **33**, 937-945.
8. Peker A., Johnson W.L. (1993) A highly processable metallic glass -  $\text{Zr}_{41.2}\text{Ti}_{13.8}\text{Cu}_{12.5}\text{Ni}_{10.0}\text{Be}_{22.5}$ . *Applied Physics Letters* **63**, 2342-2344.
9. Inoue A. (1998) *Bulk Amorphous Alloys: Preparation and Fundamental Characteristics*, Trans Tech Publications, Zurich.
10. Johnson W.L. (1996) Fundamental Aspect of Bulk Metallic Glass Formation in Multicomponent Alloys. *Materials Science Forum* **225-227**, 35-50.

11. Spaepen F. (1977) A microscopic mechanism for steady state inhomogeneous flow in metallic glasses. *Acta Metallurgica* **25**, 407-415.
12. Argon A.S. (1979) Plastic deformation in metallic glasses. *Acta Metallurgica* **27**, 47-58.
13. Bruck H.A., Rosakis A.J., Johnson W.L. (1996) The dynamic compressive behavior of Beryllium bearing bulk metallic glasses. *Journal of Materials Research* **11**, 503-511.
14. Lewandowski J.J., Greer A.L. (2006) Temperature rise at shear bands in metallic glasses. *Nat Mater* **5**, 15-18.
15. Donovan P.E. (1988) Compressive deformation of amorphous Pd<sub>40</sub>Ni<sub>40</sub>P<sub>20</sub>. *Materials Science and Engineering* **98**, 487-490.
16. Lewandowski J.J., Lowhaphandu P. (2002) Effects of hydrostatic pressure on the flow and fracture of a bulk amorphous metal. *Philosophical Magazine A* **82**, 3427-3441.
17. Lowhaphandu P., Ludrosky L.A., Montgomery S.L., Lewandowski J.J. (2000) Deformation and fracture toughness of a bulk amorphous Zr-Ti-Ni-Cu-Be alloy. *Intermetallics* **8**, 487-492.
18. Lowhaphandu P., Montgomery S.L., Lewandowski J.J. (1999) Effects of superimposed hydrostatic pressure on flow and fracture of a Zr-Ti-Ni-Cu-Be bulk amorphous alloy. *Scripta Materialia* **41**, 19-24.
19. Bruck H.A., Christman T., Rosakis A.J., Johnson W.L. (1994) Quasi-static constitutive behavior of Zr<sub>41.25</sub>Ti<sub>13.75</sub>Ni<sub>10</sub>Cu<sub>12.5</sub>Be<sub>22.5</sub> bulk amorphous alloys. *Scripta Metallurgica et Materialia* **30**, 429-434.

20. Zhang Z.F., He G., Eckert J., Schultz L. (2003) Fracture Mechanisms in Bulk Metallic Glassy Materials. *Physical Review Letters* **91**, 045505.
21. Lewandowski J.J., Lowhaphandu P. (1998) Effects of hydrostatic pressure on mechanical behavior and deformation processing of materials. *International Material Reviews* **43**, 145-187.
22. Lu J., Ravichandran G., Johnson W.L. (2003) Deformation behavior of the  $Zr_{41.2}Ti_{13.8}Cu_{12.5}Ni_{10}Be_{22.5}$  bulk metallic glass over a wide range of strain-rates and temperatures. *Acta Materialia* **51**, 3429-3443.
23. Zhuang S., Lu J., Ravichandran G. (2002) Shock wave response of a zirconium-based bulk metallic glass and its composite. *Applied Physics Letters* **80**, 4522-4524.
24. Yuan F., Prakash V., Lewandowski J.J. (2007) Spall strength and Hugoniot elastic limit of a Zirconium-based bulk metallic glass under planar shock compression. *Journal of Materials Research* **22**, 402-411.
25. Shazly M. (2005) *Dynamic Deformation and Failure of Gamma-Met PX at Room and Elevated Temperatures*. Ph.D. Thesis, Case Western Reserve University
26. Nathenson D.I. (2006) *Experimental Investigation of High-Velocity Impacts on Brittle Materials*. Ph.D. Thesis, Case Western Reserve University
27. Hufnagel T.C., Jiao T., Xing L.Q., Ramesh K.T. (2002) Deformation and failure of  $Zr_{57}Ti_5Cu_{20}Ni_8Al_{10}$  bulk metallic glass under quasi-static and dynamic compression. *Journal of Materials Research* **17**, 1441-1445.

28. Gilbert C.J., Ager Iii J.W., Schroeder V., Ritchie R.O., Lloyd J.P., Graham J.R. (1999) Light emission during fracture of a Zr--Ti--Ni--Cu--Be bulk metallic glass. *Applied Physics Letters* **74**, 3809-3811.
29. Subhash G., Zhang H., Li H. (2003) Thermodynamic and mechanical behavior of Hafnium-/Zirconium-based bulk metallic glasses. *Proceedings of the International Conference on Mechanical Behavior of Materials (ICM-9)*, Geneva, Switzerland, May 25-29, 2003.
30. Subhash G., Dowding R.J., Kecskes L.J. (2002) Characterization of uniaxial compressive response of bulk amorphous Zr-Ti-Cu-Ni-Be alloy. *Materials Science and Engineering A* **334**, 33-40.
31. Lewandowski J.J. (2001) Effects of Annealing and Changes in Stress State on Fracture Toughness of Bulk Metallic Glass. *Materials Transactions* **42**, 633-637.
32. Lewandowski J.J., Shazly M., Nouri A.S. (2006) Intrinsic and extrinsic toughening of metallic glasses. *Scripta Materialia* **54**, 337-341.
33. Lowhaphandu P., Lewandowski J.J. (1998) Fracture toughness and notched toughness of bulk amorphous alloy: Zr-Ti-Ni-Cu-Be. *Scripta Materialia* **38**, 1811-1817.
34. Conner R.D., Rosakis A.J., Johnson W.L., Owen D.M. (1997) Fracture toughness determination for a beryllium-bearing bulk metallic glass. *Scripta Materialia* **37**, 1373-1378.
35. Owen D.M., Rosakis A.J., Johnson W.L. (1999) Dynamic failure mechanisms in beryllium-bearing bulk metallic glasses. *Materials Research Society Symposium - Proceedings* **554**, 419.

36. Rittel D., Rosakis A.J. (2005) Dynamic fracture of beryllium-bearing bulk metallic glass systems: A cross-technique comparison. *Engineering Fracture Mechanics* **72**, 1905-1919.
37. Lewandowski J.J., Wang W.H., Greer A.L. (2005) Intrinsic plasticity or brittleness of metallic glasses. *Philosophical Magazine Letters* **85**, 77-87.
38. Gilbert C.J., Ritchie R.O., Johnson W.L. (1997) Fracture toughness and fatigue-crack propagation in a Zr--Ti--Ni--Cu--Be bulk metallic glass. *Applied Physics Letters* **71**, 476-478.
39. Gilbert C., Schroeder V., Ritchie R. (1999) Mechanisms for fracture and fatigue-crack propagation in a bulk metallic glass. *Metallurgical and Materials Transactions A* **30**, 1739-1753.
40. Varadarajan R., Lewandowski J. (2010) Stress-State Effects on the Fracture of a Zr-Ti-Ni-Cu-Be Bulk Amorphous Alloy. *Metallurgical and Materials Transactions A* **41**, 1758-1766.
41. Yuan F., Prakash V., Lewandowski J.J. (2010) Shear yield and flow behavior of a zirconium-based bulk metallic glass. *Mechanics of Materials* **42**, 248-255.

## Tables

Material	Impact	Applied stress (GPa)	Spall strength (GPa)	Ref.
$Zr_{41.25}Ti_{13.75}Cu_{10}Ni_{12.5}Be_{22.5}$	Normal	5.1	2.8	[24]
$Zr_{41.25}Ti_{13.75}Cu_{10}Ni_{12.5}Be_{22.5}$	Normal	7.0	2.3	[24]
$Zr_{41.25}Ti_{13.75}Cu_{10}Ni_{12.5}Be_{22.5}$	Pressure-shear, 12°	6.0	2.2	[24]
Si <sub>3</sub> N <sub>4</sub> , AS800 grade	Normal	5.0	0.81	[26]
Si <sub>3</sub> N <sub>4</sub> , AS800 grade	Normal	8.0	0.70	[26]
Γ-Met PX (TiAl alloy)	Normal	5.2	1.73	[25]

Table 1.1: Comparison of observed spall strengths for  $Zr_{41.25}Ti_{13.75}Cu_{10}Ni_{12.5}Be_{22.5}$ , Si<sub>3</sub>N<sub>4</sub>, and Γ -Met PX.

## Figures

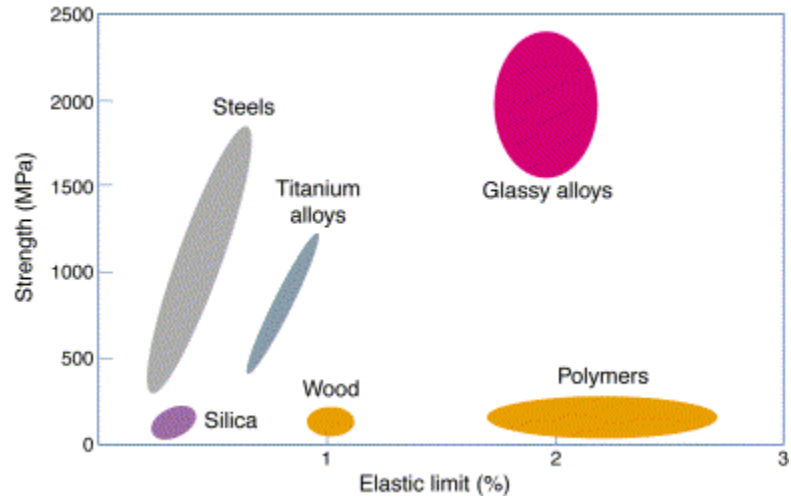


Figure 1.1: Plot of strength vs. elastic limit for various materials, including metallic glasses [1]

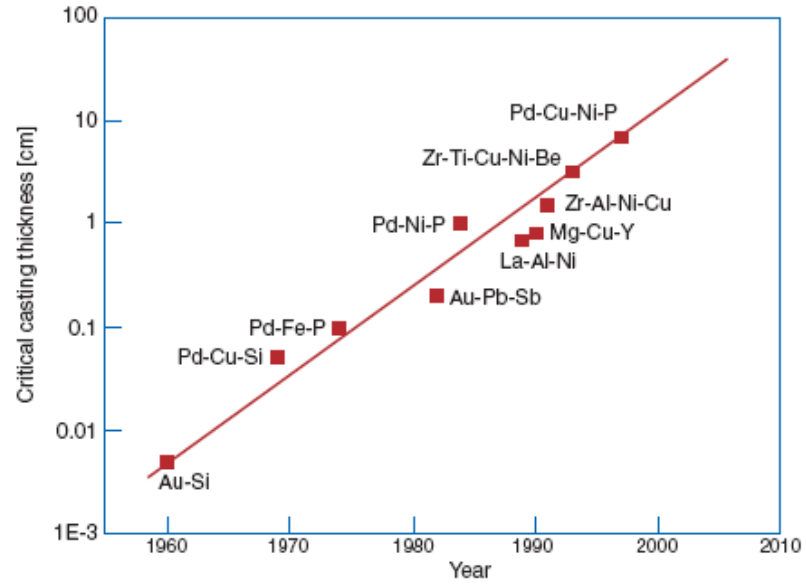


Figure 1.2: Critical casting thickness of metallic glasses since 1960 [1]

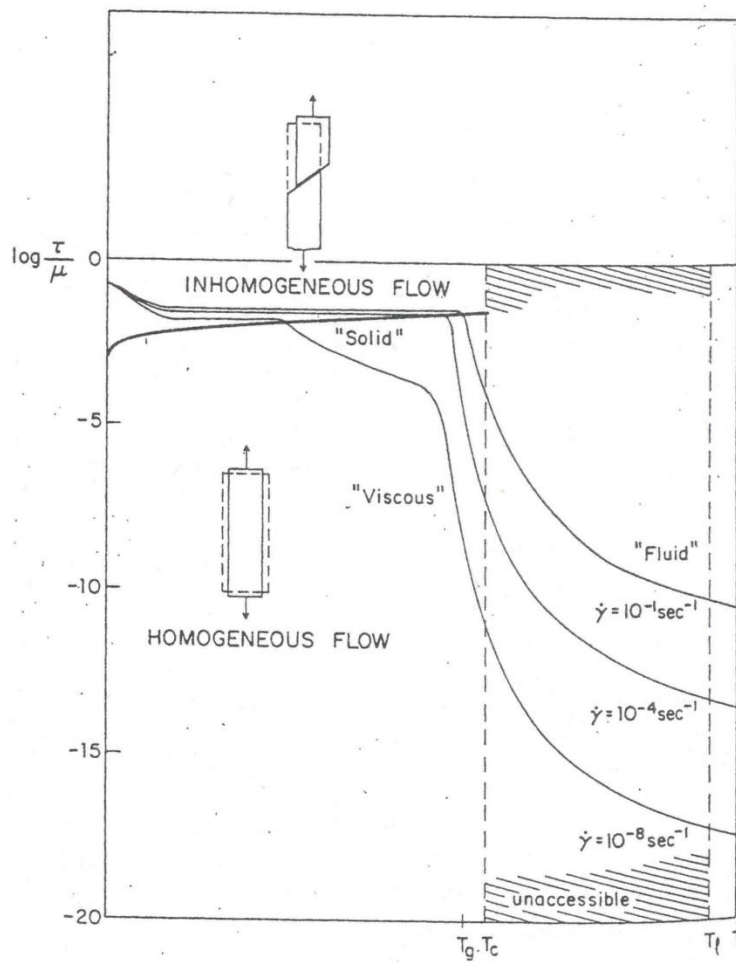


Figure 1.3: Flow curves illustrating homogeneous and inhomogeneous flow regimes [11]

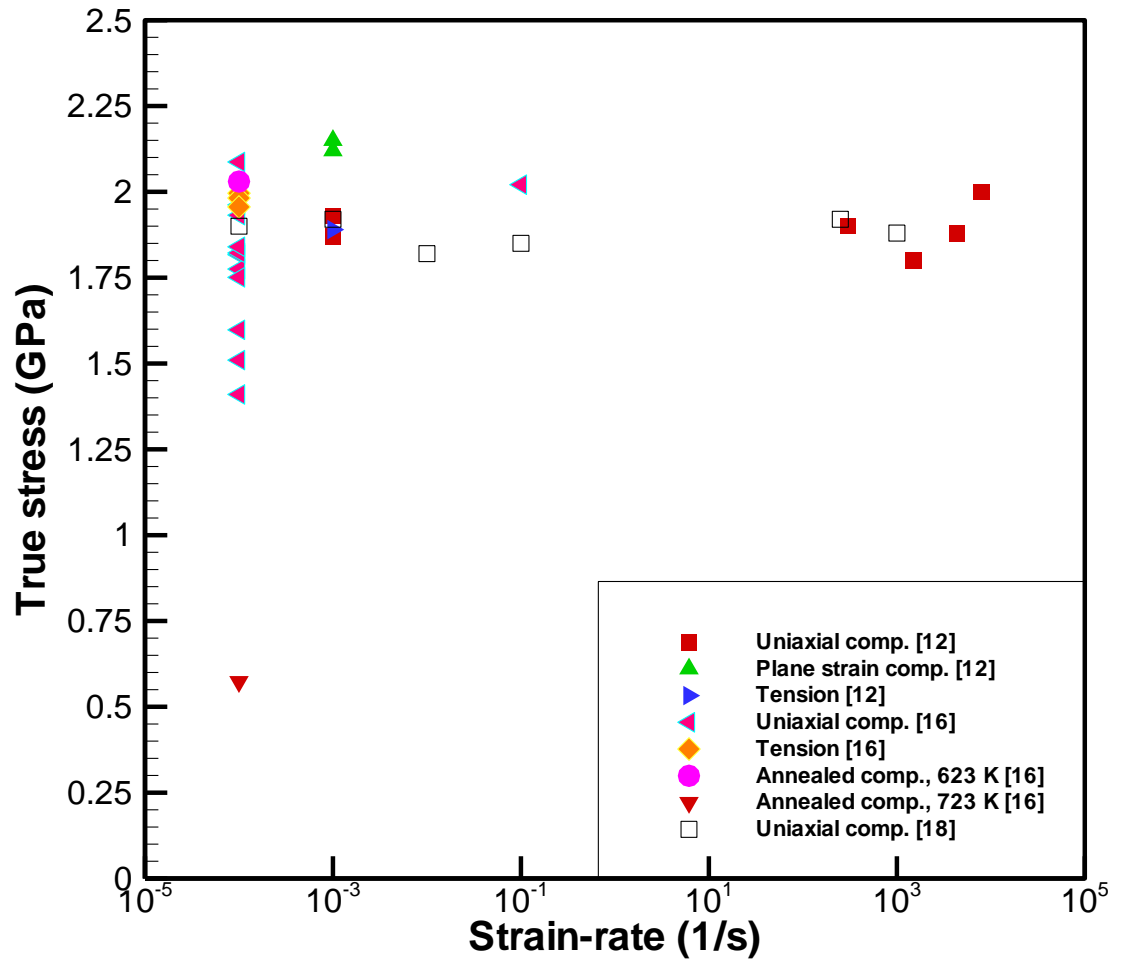


Figure 1.4: Summary plot of stresses previously obtained for  $Zr_{41.25}Ti_{13.75}Cu_{10}Ni_{12.5}Be_{22.5}$

## **Chapter 2 – High Strain-rate Response of LM-1 Using Conventional Inserts**

### **2.1 Overview**

As noted in Chapter 1, previous studies have investigated the effects of changes in the specimen's  $L/D$  ratio [1, 2] and degree of annealing [3, 4] on the mechanical behavior of amorphous LM-1 at quasi-static rates. However, neither the effects of changes in  $L/D$  ratio nor the effects of annealing have been well-characterized at high strain-rates. For strain-rates in the range of  $10^2$ - $10^4$ /s, the typical measurement technique employs a Split-Hopkinson Pressure Bar (SHPB), of which the theory and operation will be discussed in Section 2.2. Description of additional equipment, such as a high-speed camera, used to record deformation and failure events at high strain-rates, is detailed in Section 2.3. The procedures for specimen preparation and experiment execution are described in Section 2.4. The results from the SHPB experiments are analyzed in Section 2.5, and these results are placed in the context of the other recent experiments in Section 2.6, in order to gain insight into the processes governing the failure of the BMG at high strain-rates.

### **2.2 Split-Hopkinson Pressure Bar (SHPB)**

The SHPB was first employed by Hopkinson [5] in order to determine the pressure generated by explosives. However, its use in dynamic stress-strain characterization was not developed until Davies [6] and Kolsky [7] performed experiments in which two pressure bars were employed to sandwich a relatively thin specimen.

A schematic of the SHPB facility at Case Western Reserve University is shown in Figure 2.1. The SHPB consists of a pressurized gas gun and three 19.05 mm diameter maraging steel bars – a 0.2 m striker bar (propelled by the gas gun), a 1.6 m incident bar, and a 1.5 m transmitted bar. The specimen is placed between the incident and transmitted bars prior to the experiment. Upon impact of the striker bar with the incident bar, a compressive stress wave is generated inside the incident bar. This stress wave propagates along the incident bar until it reaches the specimen; after a few reverberations in the specimen, part of the incident stress wave is reflected back in the incident bar as an unloading wave, while the rest continues through to the transmitted bar. Teflon bearings and alignment fixtures ensure frictionless motion of the striker, incident, and transmitted bar while retaining precise axial alignment. Two 6 mm long, diameter-matched maraging steel inserts are placed between the incident bar and specimen and between the transmitted bar and specimen in order to prevent denting of the incident or striker bars. Vacuum grease (Dow Corning) is applied to the insert-bar interface for each of the inserts to prevent movement of the inserts during testing, and molybdenum disulfide brake grease (Sta-lube) is applied to the insert-specimen interface to reduce frictional effects at the specimen-insert interface, the presence of which may lead to barreling of the specimen. Semiconductor strain gages (Vishay Micro Measurements, model SR-4) are mounted on the incident and transmitted bars to record the strain profile histories generated by the impact; these gages are mounted diametrically opposite each other to reduce effects due to bending. The high gage-factor of the semiconductor gages minimizes the amount of amplification required. The strain gages are connected to a

Wheatstone bridge, which in turn is connected to a signal amplifier (Tektronix 5A22N); the strain signals are recorded with a high-bandwidth oscilloscope (Tektronix 680C).

### 2.2.1 Governing Equations for the SHPB

The process of determining the strains and stresses in the SHPB has been previously studied in detail by Love [8], Pochhammer [9] and Chree [10]. The second order partial differential equation,

$$\frac{\partial^2 u}{\partial x^2} = \frac{1}{c_0^2} \frac{\partial^2 u}{\partial t^2}, \text{ where } c_0^2 = \frac{E_0}{\rho_0}, \quad (2.1)$$

governs the displacement,  $u$ , due to propagation of the waves in the Hopkinson Bar as a function of position ( $x$ ) and time ( $t$ ). In Equation (2.1),  $c$  is the longitudinal wave speed of the material,  $E$  is the Young's Modulus of the material, and  $\rho$  is the density. The subscript  $_0$  denotes that the properties are of the incident and transmitted bars.

The solution to the wave equation (Equation (2.1)) is given by D'Alembert [10] as

$$u(x, t) = f(x - c_0 t) + g(x + c_0 t) = u_i + u_r, \quad (2.2)$$

where  $f(x - c_0 t)$  and  $g(x + c_0 t)$  represent the displacements in the incident and reflected pulses traveling at speed  $c_0$  to the right and left, respectively. The strain and displacement rate (i.e., velocity) are determined by taking the derivative of the displacement with respect to the position  $x$  and the time  $t$ , respectively, such that

$$\begin{aligned}\varepsilon_1 &= \frac{\partial u_1}{\partial x} = f' + g' = \varepsilon_I + \varepsilon_R, \\ \dot{u}_1 &= c_0(-f' + g') = c_0(-\varepsilon_I + \varepsilon_R)\end{aligned}\tag{2.3}$$

where  $u_1$  and  $u_2$  (will be shown later) are the displacements at the incident bar-specimen and the specimen-transmitted bar interfaces, respectively, as shown in Figure 2.2. The strains  $\varepsilon_I$ ,  $\varepsilon_R$  and  $\varepsilon_T$  (will be shown later) are the incident, reflected and transmitted engineering strain signals, respectively.

The displacement  $u_1$  (Figure 2.2) is then given by

$$u_1 = c_0 \int_0^t (-\varepsilon_I + \varepsilon_R) d\tau.\tag{2.4}$$

The transmitted wave and the displacement  $u_2$  are given by

$$u_2(x, t) = h(x - c_0 t),\tag{2.5}$$

where  $h$  is a wave traveling to the right in the transmitted bar. Similarly,

$$\varepsilon_2 = h' = \varepsilon_T,\tag{2.6}$$

and

$$\dot{u}_2 = -c_0 h' = -c_0 \varepsilon_T.\tag{2.7}$$

The displacement  $u_2$  is then given by

$$u_2 = -c_0 \int_0^t \varepsilon_T d\tau. \quad (2.8)$$

Equations (2.4) and (2.8) are true everywhere, including at the ends of the pressure bars. The engineering strain-rate in the test specimen is the difference in particle velocities of the two ends of the specimen

$$\dot{\varepsilon}_s = \frac{(\dot{u}_2 - \dot{u}_1)}{L_s} = \frac{c_0}{L_s} (-\varepsilon_T + \varepsilon_I - \varepsilon_R), \quad (2.9)$$

where  $L_s$  is the original specimen length.

The average engineering strain  $\varepsilon_s$  in the specimen is then obtained by

$$\varepsilon_s = \frac{u_2 - u_1}{L_s} = \frac{c_0}{L_s} \int_0^t (-\varepsilon_T + \varepsilon_I - \varepsilon_R) d\tau. \quad (2.10)$$

The forces  $F_1$  and  $F_2$ , corresponding to the forces on the interfaces between the specimen and the incident and transmitted sides, respectively, are given by

$$\begin{aligned} F_1 &= A_0 E_0 (\varepsilon_I + \varepsilon_R) \\ F_2 &= A_0 E_0 (\varepsilon_T) \end{aligned}, \quad (2.11)$$

where  $A_0$  is the cross-sectional area of the incident and transmitted bars and  $E_0$  is the elastic modulus of the bars, which are normally equal, because identical materials are used for the incident and transmitted pressure bars.

After an initial “ring-up” period, where the exact duration depends on the sound speed of the specimen and its geometry (particularly its length), it is assumed that wave propagation effects within the specimen can be neglected after  $\pi$  reverberations [11] and the specimen is in force equilibrium; the specimen can be assumed to be deforming uniformly after that. Under these assumptions,  $F_1=F_2$ , and therefore,  $\varepsilon_I + \varepsilon_R = \varepsilon_T$ , so that the engineering strain-rate, engineering strain, and engineering stress in the specimen are obtained as

$$\dot{\varepsilon}_s(t) = -\frac{2c_0}{L_s} \varepsilon_R, \quad (2.12)$$

$$\varepsilon_s(t) = -\frac{2c_0}{L_s} \int_0^t \varepsilon_R d\tau, \quad (2.13)$$

and

$$\sigma_s(t) = \frac{F_1}{A_s} = \frac{F_2}{A_s} = E\varepsilon_T(t), \quad (2.14)$$

where  $A_s$  is the original cross-sectional area of the specimen. When the specimen is deforming uniformly under force equilibrium, the engineering strain rate within the specimen is directly proportional to the amplitude of the reflected wave. Similarly, the engineering stress within the specimen is directly proportional to the amplitude of the transmitted wave. The above obtained engineering strain and engineering stress are thereafter converted into true strain  $e$  and true stress  $S$  with Equations (2.15) and (2.16), based on the assumption that plastic flow in metals is volume conserving [12]:

$$e_s(t) = \ln(\varepsilon_s(t) + 1), \quad (2.15)$$

and

$$S_s(t) = \sigma_s(t)(\varepsilon_s(t) + 1). \quad (2.16)$$

During the SHPB experiment, strain gages attached on the incident and transmitted bars monitor the history of the incident strain signal ( $\varepsilon_I$ ), the reflected strain signal ( $\varepsilon_R$ ), and transmitted strain signal ( $\varepsilon_T$ ). An in-house Matlab program is used to filter out the high frequency noise (above 1.5 MHz) and construct the stress-strain data from the raw data. Stress vs. strain profiles were constructed using parameters from the bars (elastic modulus, mass density, diameter), the specimen (diameter and length), and the Wheatstone bridge circuits at the strain gage stations (shunt calibrations for incident and transmitted bars).

### *2.2.2: Pulse Shaping Technique*

Equations (2.12)-(2.14) are valid after a state of force equilibrium has been obtained in the specimen. However, the force equilibrium does not occur instantaneously; it has been estimated that the time required for a uniform uniaxial stress state to be achieved within the sample is the time required for the stress pulse to reverberate  $\pi$  times within the specimen [11]. To promote dynamic stress equilibrium, and thus maintain a nearly constant strain rate over the test duration, a pulse shaping technique is routinely adopted.

For a plastically deforming solid that obeys the Taylor-von Karman theory, the time to reach force equilibrium follows the relationship [13]

$$t^2 \geq \frac{\pi^2 \rho_s l_s^2}{\partial\sigma / \partial\varepsilon}. \quad (2.17)$$

Here,  $\rho_s$  is the density of the specimen,  $l_s$  is the specimen length, and  $\partial\sigma / \partial\varepsilon$  is the work-hardening rate of the true stress/true strain curve for the material to be tested. For rise times less than that given in Equation (2.17), the sample should not be assumed to be deforming uniformly, and stress-strain data will be in error. Since use of impedance-matched materials for the striker and incident bar (i.e., a symmetric impact) yields a short rise-time pulse (approximately a square wave), one approach for achieving a uniform stress state during Split-Hopkinson pressure bar testing is to decrease the sample length so that the rise time from Equation (2.17) is as small as possible. However, in practical experiments, the decrease of the specimen length usually corresponds with a decrease in the specimen and bar diameters, increasing the machining cost and difficulty. Moreover, the small sample size may not capture the microstructural heterogeneity within the specimen with sufficient accuracy. In addition, the rise time associated with square-wave pulses generated by projectile impact is likely to be less than the minimum required equilibrium time  $t$  as predicted by Equation (2.17), regardless of changes in the sample geometry.

Because the value of  $t$  from Equation (2.17) has a practical minimum, an alternate method to facilitate stress-state equilibrium at low strains is to increase the rise time of the incident wave. In other words, the rise time of the incident wave is increased to a

value comparable with the time for the stress waves to ring up the specimen, so that the data will be valid even at small strains. Furthermore, because the highly dispersive short wavelength components arise from the leading and trailing edges in the incident wave, a longer rise-time pulse will contain fewer of these components than will a shorter rise-time pulse [13].

Experimentally, the rise time of the incident wave can be increased by placing a soft, deformable metal shim (pulse shaper) between the striker and the incident bar during impact. Copper sheets are good candidates for pulse shaping, as they are low in yield strength and exhibit significant work-hardening. However, the dimensions (particularly the thickness) of the pulse shaper are dependent on the striker bar velocity, specimen length, and the specimen material.

To produce a state of specimen equilibrium, the strain-rate (Equation (2.12)) should be constant, so that:

$$\dot{\epsilon}_R = 0 = \dot{\epsilon}_I - \dot{\epsilon}_T, \quad (2.18)$$

and that the slope of the incident and transmitted pulses are equal. Figure 2.3 shows an example in which (a) the slopes of the incident and transmitted signals are equal, which (b) leads to a large constant strain-rate region. Based on trial and error, copper sheets of thickness 0.3-0.5 mm and lateral dimensions 7 mm x 7 mm produced constant strain-rate regions similar to the ones in Figure 2.3.

### **2.3 Additional equipment for the SHPB Experiment**

To perform in-situ recording of the deformation and failure processes, an Imacon 200 ultra-high speed digital camera (DRS Technologies) was employed. For each specimen, 16 pictures were taken with interframe times of 5-7  $\mu\text{s}$ , exposure times of 0.3-1  $\mu\text{s}$ , and delay times of 225-250  $\mu\text{s}$  in order to maximize the number of frames exhibiting deformation and failure processes. To maximize the size of the pictures and produce optimal focusing conditions, a 300 mm adjustable lens was employed, and the camera was placed between 8 and 16 inches from the specimen. The camera was connected to a delay generator, which in turn was connected to the oscilloscope, and the delay generator produced a 10 ns delay to provide a precisely timed 1000 W camera flash (Photogenic Professional Lighting, model Powerlight 2500DR).

### **2.4 Specimen Preparation**

Specimens of LM-1 were prepared from rectangular plates of dimensions (90 x 63 x 5) mm, supplied by Liquidmetal, Inc. These plates were determined to be fully amorphous based on differential scanning calorimetry and X-ray diffraction in previous work [2, 3, 14]. The plates were then electrical-discharge machined to rectangular bars and subsequently ground to cylindrical bars of either 3.2 mm or 4.0 mm diameter. The long cylindrical bars were then metallographically polished to a mirror finish first using SiC grit paper (1200 grit and 2400 grit) and then diamond paste (45, 9, 3, and 1  $\mu\text{m}$ ). After polishing, the bars were placed in a brass sleeve, which was utilized to prevent damage to the LM-1 during preparation, and cut using a low-speed saw (Buehler, model 11-1180) to cylindrical tabs of  $L/D$  ratios of 0.5, 1.0, and 2.0. Flatness and parallelism

were ensured by first lapping and then polishing the faces to a 6  $\mu\text{m}$  finish using a combination of diamond paste (Lapmaster, model LAP5DIAP-M18P001) and polishing cloth (Kemet, model ASF-AW).

After lapping and polishing, the samples to be annealed were placed in a ceramic furnace (Lindbergh) at 623 K for 12 h and then air-cooled. This time and temperature, as noted in previous work [3, 14], reduced the free volume of the glass but did not induce crystallization. After annealing, the tabs were then lapped and polished once again to remove any oxide layer that may have formed during the annealing process.

## **2.5 Results**

### *2.5.1 As-cast LM-1*

Representative stress-strain curves, using the analysis provided in Section 2.2, are shown in Figure 2.4 for specimens with  $L/D$  ratios of (a) 2.0 and (b) 0.5. From the figure, it appears that specimens with a higher  $L/D$  ratio (2.0) exhibit higher stresses but lower strains-to-failure compared to the specimens with a lower  $L/D$  ratio (0.5). The peak stresses achieved by the specimens with an  $L/D$  ratio of 2.0 are between 1.7 and 1.9 GPa; these levels are within 10% of values previously determined by other researchers [15, 16]. Figure 2.5 shows a plot of peak stresses over the range of experiments covered in this study. It is apparent that, after eliminating the outlying data (circled), most (but not all) of the increase in the peak stress occurs when comparing specimens with  $L/D$  ratios of 1.0 compared to 0.5.

Figure 2.6 shows sequential images of (a) an initially undeformed specimen with an  $L/D$  ratio of 1.0, as viewed from the high-speed camera with an inter-frame time of 5  $\mu$ s. After specimen loading, (b) a shear instability forms in the specimen, as can be seen from the slight kink in the specimen. Shortly afterwards, (c) the shear instability becomes a fracture plane, and the specimen fails into two discrete pieces, which (d) slip relative to each other. Careful optical analysis of the fracture samples, such as the one shown in Figure 2.7, show that the failure of the specimen started at the specimen-insert interface with a fracture angle of approximately  $50^\circ$  to the loading axis. Additional analysis using low-magnification scanning electron microscopy (SEM), shown in Figure 2.8, confirmed the failure behavior. A failure front appears to be present in the micrographs (a), and the very bumpy surface features (b) are indicative of a high stress region near the insert-specimen interface. Also, the initial sharp angle in (b) provides further evidence of failure occurring close to the insert-specimen interface.

Sequential images were also taken for specimens with an  $L/D$  ratio of 0.5, and are shown in Figure 2.9. Due to the shorter length of the (a) initially undeformed specimen, the (b) dominant shear plane intersects both of the specimen-insert interfaces, thus inhibiting fracture along a plane that is seen in Figure 2.8. Moreover, because of the geometrical constraint, after the initial fracture (c) the specimen fragments are trapped between the inserts (loading bars). It is interesting to note that, as was the case for specimens with  $L/D = 2.0$ , the failure appears to initiate at one of the specimen-insert interfaces; however, because of the geometrical constraint, more fragmentation and crushing behavior is present, as can be seen in Figure 2.10.

### 2.5.2 Annealed LM-1

Representative stress-strain curves of the annealed and amorphous samples are shown in Figure 2.11 for  $L/D$  ratios of (a) 1.0 and (b) 2.0. As seen from the figure, the annealed material exhibits greater peak stresses than its fully amorphous counterpart, although there is some scatter in the peak stresses. In addition, annealing of the material increases the apparent strain-to-failure of the samples, particularly for samples with  $L/D$  ratios of 2.0.

Drastic changes in the deformation and failure behavior occur after annealing of the material. Figure 2.12 shows sequential images of an annealed specimen with  $L/D = 1.0$ . A shear plane (a) initiates from the specimen-insert interface (like in the fully amorphous samples), and again, this appears to be caused by a geometrical instability. After shear plane formation, the sample begins to shatter into multiple fragments (b, c) and is eventually pulverized without consolidation. Similar behavior appears to occur for a specimen with  $L/D = 2.0$  (Figure 2.13), in which an initial shear plane forms and then extensive fragmentation ensues. This particular specimen exhibits a failure front, which clearly shows the boundary between the “intact” material and the fragmented material. As can be seen in Figure 2.14, the specimen, regardless of the  $L/D$  ratio, experiences multiple fragmentation on a more extensive scale than even the fully amorphous samples with  $L/D = 0.5$ .

## 2.6 Discussion

### 2.6.1 As-cast LM-1

The results from the SHPB experiments on amorphous LM-1 using the conventional inserts, in general, are in agreement with other high strain-rate data [16, 17], which exhibit negative strain-rate sensitivity for BMGs. However, this work has examined a wider range of  $L/D$  ratios than considered in the previous studies on LM-1, and also suggests that there is perhaps a greater negative strain-rate sensitivity exhibited by specimens with smaller  $L/D$  ratios. From both comparison of the peak stresses and the flow/fracture behavior seen from high-speed photography, it is also apparent that the behavior of the bulk metallic glass can be divided into two cases by separating the specimens with the smallest  $L/D$  ratios (0.5) from all of the other specimen geometries. Such classification provides further evidence that the change in the flow/fracture behavior observed in these experiments is due to geometrical effects. In addition, it can be seen that using the conventional SHPB configuration, the failure in BMG specimens occurs away from the gage section of the specimen, thus providing evidence for the existence of non-uniform deformation conditions within the metallic glass specimens during the deformation process.

One common interpretation of the negative strain-rate sensitivity during dynamic deformation of metallic glass has been thermal softening [17-19], which has been explained because of competition between adiabatic heating and thermal conductivity [16]. Early work using infrared temperature detection [20] has suggested a local temperature increase of up to 500 K during and after specimen failure, and other authors [18, 19] have seen a temperature increase at the point of final failure. However, during typical dynamic loading processes, a large temperature rise cannot occur because failure

of the specimen occurs before any significant plastic flow can accumulate within the BMG specimen. More recent work with fusible coatings [21], providing high spatial and temporal resolution, have shown that the magnitude of the temperature rise of the specimen is associated with the magnitude of the shear offset (amount of plastic/frictional slip on the fracture/shear plane). This suggests that the drop in peak stress with increasing strain-rate is not due to the temperature rise during uniform deformation within the specimen. Moreover, recent detailed analyses further indicate that the shear banding in metallic glasses is not due to local temperature effects [21-23].

Based on the present experimental results, one of the key factors that may have contributed to the observed negative strain-rate sensitivity of peak failure stress is the stress concentration at the specimen-insert interfaces because of the difference in the diameters between the specimen and the inserts. The existence of preferential flow and failure at the specimen-insert interface suggests that such a stress concentration is indeed present in the conventional SHPB experimental setup. Such a stress concentration would violate the stress homogeneity condition, one of the five assumptions [24] that are made to derive Equations (2.12)-(2.14); numerical simulations on numerous ceramic specimen geometries have shown stress concentrations of approximately 1.4 during dynamic loading [25]. Further discussion of the stress concentration is left for Chapter 3, as the stress concentration provides the main motivation for the design of new inserts to ensure a more homogeneous stress state during dynamic loading of the BMG specimens.

### *2.6.2 Annealed LM-1*

The annealing treatment presently used clearly produces a change in the failure mechanism of LM-1. Previous work has clearly demonstrated embrittlement via significant reductions in the fracture toughness after annealing [3, 14, 26], along with slight increases in quasi-static compressive strength and hardness [3, 26]. Interestingly, it appears that the annealing treatment, under high strain-rate conditions, results in an increase in the apparent strain-to-failure of the material in addition to a slight increase in strength, when compared to the fully amorphous specimen.

The high-speed camera images clearly show that there is extensive fragmentation over the duration of the failure process, producing tiny ( $\ll 1$  mm) fragments. Furthermore, examination of the fragments failed to reveal any evidence of their consolidation, such as those present in the fully amorphous LM-1. Increasing the  $L/D$  ratio appears to increase the apparent strain-to-failure while producing a failure front that separates the intact material from the fragmented material. The increased stress to initiate flow due to the reduction in free volume promoted by annealing is consistent with the somewhat increased stress obtained in the high strain-rate tests compared to those exhibited in the fully amorphous LM-1. Based on the high-speed video recordings, the apparent increase in fracture strain appears to occur because of a transition from a shear-dominated failure to a fragmentation mechanism. Such fragmentation is often observed in brittle and semi-brittle materials like ceramics [27], particularly under high strain-rate conditions, and provides a potent energy-absorbing mechanism provided that the fragments are contained and compressed or pulverized further. Analysis of the high-speed video suggests that a similar mechanism may be present in these annealed bulk metallic

glasses, and the combination of increased strength, increased strain-to-failure, and multiple fragmentation provides for a particularly potent energy-absorbing mechanism.

Because the transition from a shear-dominated failure mechanism in fully amorphous LM-1 to a fragmentation mechanism in annealed LM-1 is due to a reduction in free volume, it is useful to consider changes in mechanical properties during annealing that might affect the failure mechanism of LM-1. Recent work by Lewandowski et al. [28] suggests that the value of  $\mu/B$ , the ratio of the shear modulus to the bulk modulus, plays a critical role in determining whether the metallic glass is tough or brittle. In addition, this ratio can change during the annealing process, leading to induced embrittlement of the metallic glass; the value of  $\mu/B$  for LM-1 increases from 0.32 to 0.38 after annealing at 623 K for 12 h and the glass experiences a reduction in fracture toughness of two orders of magnitude. Because the ratio of the value of  $\mu/B$  is dependent only on the Poisson's ratio  $\nu$ , the brittleness or toughness of the BMG can be thought of in terms of  $\nu$ , with a narrow transition zone from brittle to tough at  $\nu = 0.31-0.33$ . Control of  $\mu/B$ , and therefore,  $\nu$ , appear to be useful for controlling the failure mechanism for these metallic glasses, and the value of  $\nu$  (0.34-0.35 for fully amorphous LM-1, 0.33 for LM-1 annealed at 623 K for 12 h) implies that careful heat treatment can also be useful in controlling the failure mechanism of LM-1.

Comparisons of the high strain-rate behavior of the annealed and fully amorphous LM-1 reveal that the metallic glasses can provide extensive energy absorption via very different means. On the one hand, for specimens with sufficiently low  $L/D$ , extensive

shear banding can dissipate energy via the activation of multiple shear bands, preventing the catastrophic formation and propagation of a single shear plane. In contrast, the embrittled samples failed by multiple fragmentation, the confinement of which enables additional pulverization at higher loads and strains. Both of these mechanisms have implications in the design of layered energy-absorbing structures utilizing BMGs for one or more components. From these studies, it is apparent that the choices of layer thicknesses and properties will likely affect the tendency for shear banding or fragmentation to occur, and the constraint provided by other structures may be beneficial to the energy-absorbing characteristics of structures incorporating BMGs.

## **2.7 Summary**

In the present study, the SHPB was employed to perform high strain-rate compression tests (in the range of  $10^2$ - $10^4$ /s) on LM-1 to investigate the effect of changes in  $L/D$  ratio (from 0.5 to 2.0) and annealing on both the stress-strain behavior and the flow/fracture behavior of the metallic glass. High-speed photography, combined with optical and SEM analysis, was utilized to determine the macroscopic fracture behavior and the initiation of specimen failure. In addition, the annealed samples were compared to their fully amorphous counterparts to gain some insight into the two methods of energy absorption. Based on the results from these experiments:

1. Specimens with  $L/D$  ratios of 1.0 and 2.0, in general, achieve higher peak stresses than specimens with  $L/D$  ratios of 0.5. Annealed specimens exhibit higher peak

stresses compared to their amorphous counterparts for  $L/D$  ratios of 1.0 and 2.0. They also appear to exhibit higher strains-to-failure for  $L/D$  ratios of 2.0.

2. Specimens with  $L/D$  ratios of 1.0 and 2.0 fail by formation of a dominant shear plane. The shear fracture is followed by slip at the fracture faces relative to each other. Failure appears to begin from the specimen-insert interface, and the fracture angle of these specimens is about  $50^\circ$ .
3. Specimens with  $L/D$  ratios of 0.5 fail by formation of a dominant shear plane at the specimen-insert interface, similar to other LM-1 specimens. However, because of the small length of the specimen, crushing/consolidating behavior is more prevalent compared to specimens with larger  $L/D$  ratios.
4. Annealed specimens exhibit extensive fragmentation regardless of  $L/D$  ratio, and specimen failure again appears to initiate at the sample-insert interface. Such behavior does not include any consolidation of the fragments, unlike for the fully amorphous specimens with  $L/D = 0.5$ .
5. The increase in peak stress and the apparent increase in strain-to-failure suggest that annealing of LM-1 may provide a highly potent energy absorption mechanism, particularly if the resulting fragments are further compressed.

6. The stress concentration due to the difference in the diameters between the specimen and the insert leads to an inhomogeneous state of stress in the specimen. This assertion is also supported by the specimen failure outside the gage section of the specimen.

## References

1. Bruck H.A., Christman T., Rosakis A.J., Johnson W.L. (1994) Quasi-static constitutive behavior of  $Zr_{41.25}Ti_{13.75}Ni_{10}Cu_{12.5}Be_{22.5}$  bulk amorphous alloys. *Scripta Metallurgica et Materialia* **30**, 429-434.
2. Lewandowski J.J., Lowhaphandu P. (2002) Effects of hydrostatic pressure on the flow and fracture of a bulk amorphous metal. *Philosophical Magazine A* **82**, 3427-3441.
3. Lewandowski J.J. (2001) Effects of Annealing and Changes in Stress State on Fracture Toughness of Bulk Metallic Glass. *Materials Transactions* **42**, 633-637.
4. Lowhaphandu P., Ludrosky L.A., Montgomery S.L., Lewandowski J.J. (2000) Deformation and fracture toughness of a bulk amorphous Zr-Ti-Ni-Cu-Be alloy. *Intermetallics* **8**, 487-492.
5. Hopkinson B. (1914) A Method of Measuring the Pressure Produced in the Detonation of High Explosives or by the Impact of Bullets. *Philosophical Transactions of the Royal Society of London, Series A* **213**, 437-456.
6. Davies R.M. (1948) A critical study of the Hopkinson pressure bar. *Philosophical Transactions of the Royal Society of London, Series A* **240**, 375-457.
7. Kolsky H. (1949) An investigation of the mechanical properties of materials at very high rates of loading. *Proceedings of the Physical Society, Section B* **62**, 676-700.
8. Love A.E.H. (1927) *A Treatise on the Mathematical Theory of Elasticity*, Cambridge University Press, Cambridge, UK.

9. Pochhammer L. (1876) Über Fortplanzungsgeschwindigkeiten kleiner Schwingungen in einem unbergrenzten isotropen Kreiszyylinder (On the propagation velocities of small oscillations in an infinite isotropic circular cylinder). *Journal für der reine und angewandte Mathematick* **81**, 324-326.
10. Chree C. (1889) The Equations of an Isotropic Elastic Solid in Polar and Cylindrical Coordinates, Their Solution and Applications. *Transactions of the Cambridge Philosophical Society* **14**, 251-369.
11. Davies E.D.H., Hunter S.C. (1963) The dynamic compression testing of solids by the method of the split Hopkinson pressure bar. *Journal of the Mechanics and Physics of Solids* **11**, 155-179.
12. Dieter G.E. (1976) *Mechanical Metallurgy*, McGraw Hill, Inc., New York, NY.
13. Follansbee P.S. (1985) The Hopkinson Bar. *American Society for Materials Handbook* (2nd ed.), Materials Park, OH, 198-203
14. Lowhaphandu P., Lewandowski J.J. (1998) Fracture toughness and notched toughness of bulk amorphous alloy: Zr-Ti-Ni-Cu-Be. *Scripta Materialia* **38**, 1811-1817.
15. Lu J., Ravichandran G., Johnson W.L. (2003) Deformation behavior of the  $Zr_{41.2}Ti_{13.8}Cu_{12.5}Ni_{10}Be_{22.5}$  bulk metallic glass over a wide range of strain-rates and temperatures. *Acta Materialia* **51**, 3429-3443.
16. Hufnagel T.C., Jiao T., Xing L.Q., Ramesh K.T. (2002) Deformation and failure of  $Zr_{57}Ti_5Cu_{20}Ni_8Al_{10}$  bulk metallic glass under quasi-static and dynamic compression. *Journal of Materials Research* **17**, 1441-1445.

17. Subhash G., Zhang H., Li H. (2003) Thermodynamic and mechanical behavior of Hafnium-/Zirconium-based bulk metallic glasses. *Proceedings of the International Conference on Mechanical Behavior of Materials (ICM-9)*, Geneva, Switzerland, May 25-29, 2003.
18. Gilbert C.J., Ager Iii J.W., Schroeder V., Ritchie R.O., Lloyd J.P., Graham J.R. (1999) Light emission during fracture of a Zr--Ti--Ni--Cu--Be bulk metallic glass. *Applied Physics Letters* **74**, 3809-3811.
19. Yang B., Liu C., T., Nieh T G., Morrison M., L., Liaw P., K., Buchanan R., A. (2006) Localized heating and fracture criterion for bulk metallic glasses. *Journal of Materials Research* **21**, 915-922.
20. Bruck H.A., Rosakis A.J., Johnson W.L. (1996) The dynamic compressive behavior of Beryllium bearing bulk metallic glasses. *Journal of Materials Research* **11**, 503-511.
21. Lewandowski J.J., Greer A.L. (2006) Temperature rise at shear bands in metallic glasses. *Nat Mater* **5**, 15-18.
22. Zhang Y., Greer A.L. (2006) Thickness of shear bands in metallic glasses. *Applied Physics Letters* **89**, 071907-071903.
23. Zhang Y., Stelmashenko N.A., Barber Z.H., Wang W.H., Lewandowski J.J., Greer A.L. (2007) Local Temperature Rises during Mechanical Testing of Metallic Glasses. *Journal of Materials Research* **22**, 419-427.
24. Subhash G., Ravichandran G. (2000) Split-Hopkinson pressure bar testing of ceramics. *American Society for Materials Handbook* (8<sup>th</sup> ed.), American Society for Metals International, Materials Park, OH, 497-504

25. Chen W., Subhash G., Ravichandran G. (1994) Evaluation of ceramic specimen geometries used in split-Hopkinson pressure bar. *Dymat Journal* **1**, 193-210.
26. Gilbert C.J., Ritchie R.O., Johnson W.L. (1997) Fracture toughness and fatigue-crack propagation in a Zr--Ti--Ni--Cu--Be bulk metallic glass. *Applied Physics Letters* **71**, 476-478.
27. Zhou F., Molinari J.-F., Ramesh K.T. (2005) A cohesive model based fragmentation analysis: effects of strain rate and initial defects distribution. *International Journal of Solids and Structures* **42**, 5181-5207.
28. Lewandowski J.J., Wang W.H., Greer A.L. (2005) Intrinsic plasticity or brittleness of metallic glasses. *Philosophical Magazine Letters* **85**, 77-87.

## Figures

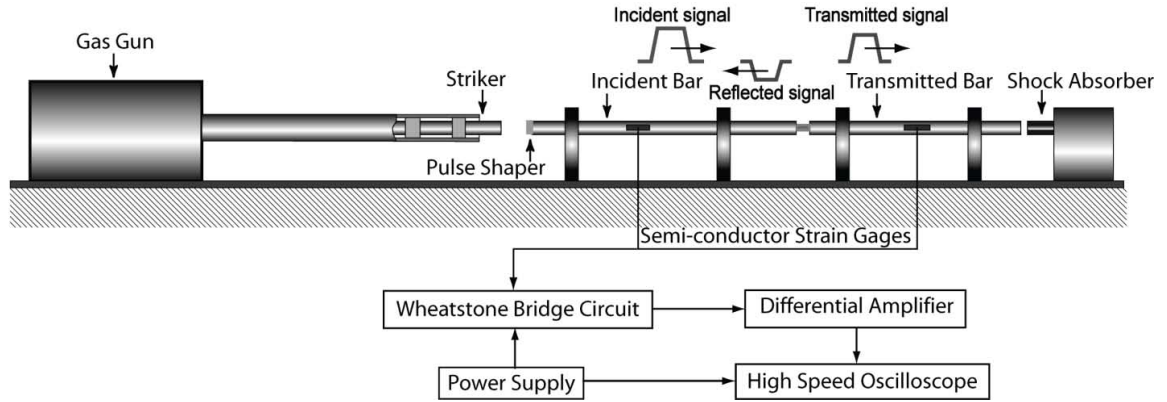


Figure 2.1 – Schematic diagram of the Split-Hopkinson Pressure Bar (SHPB)

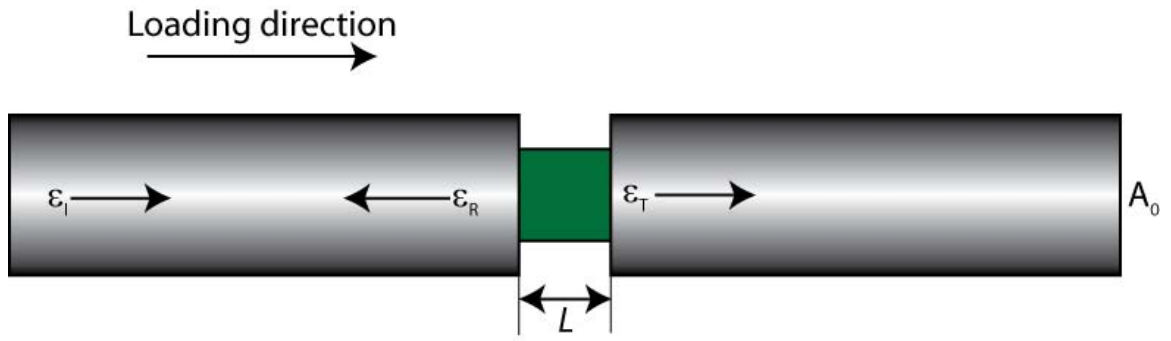
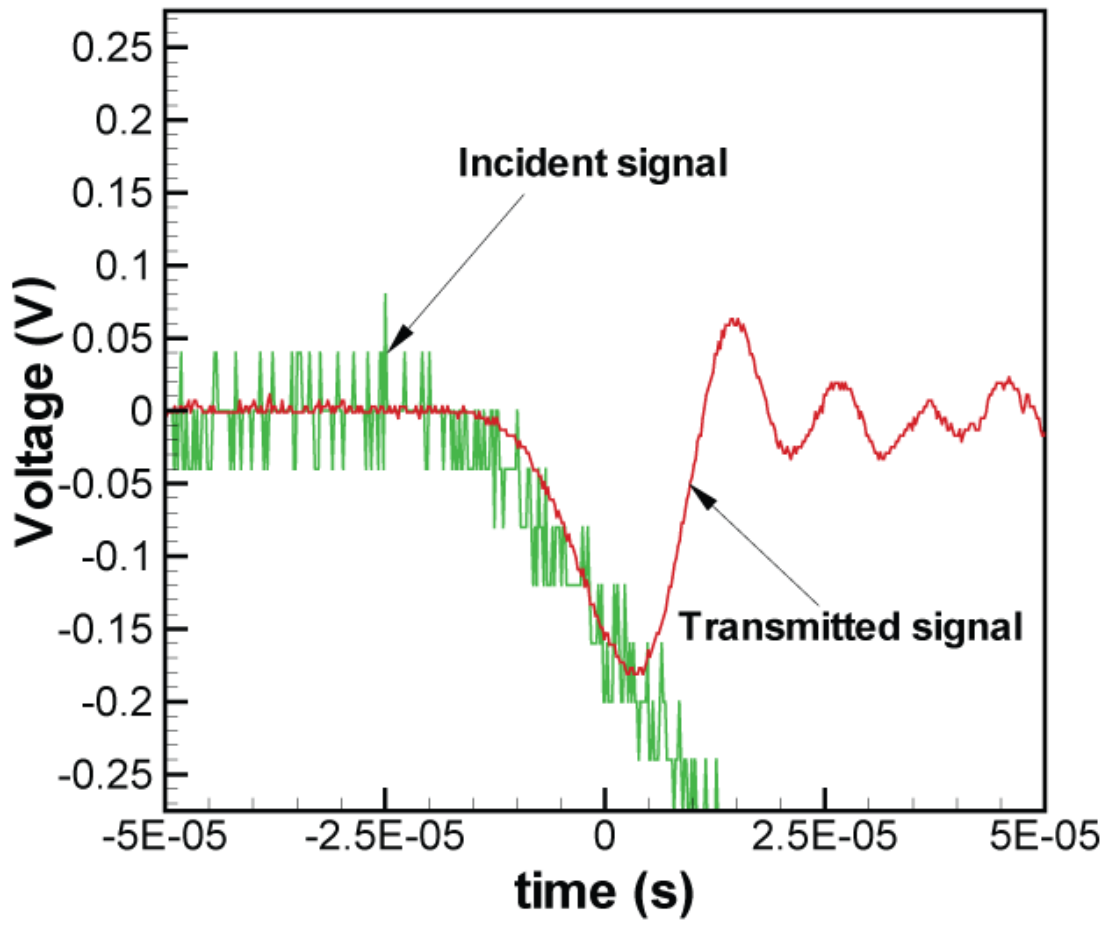
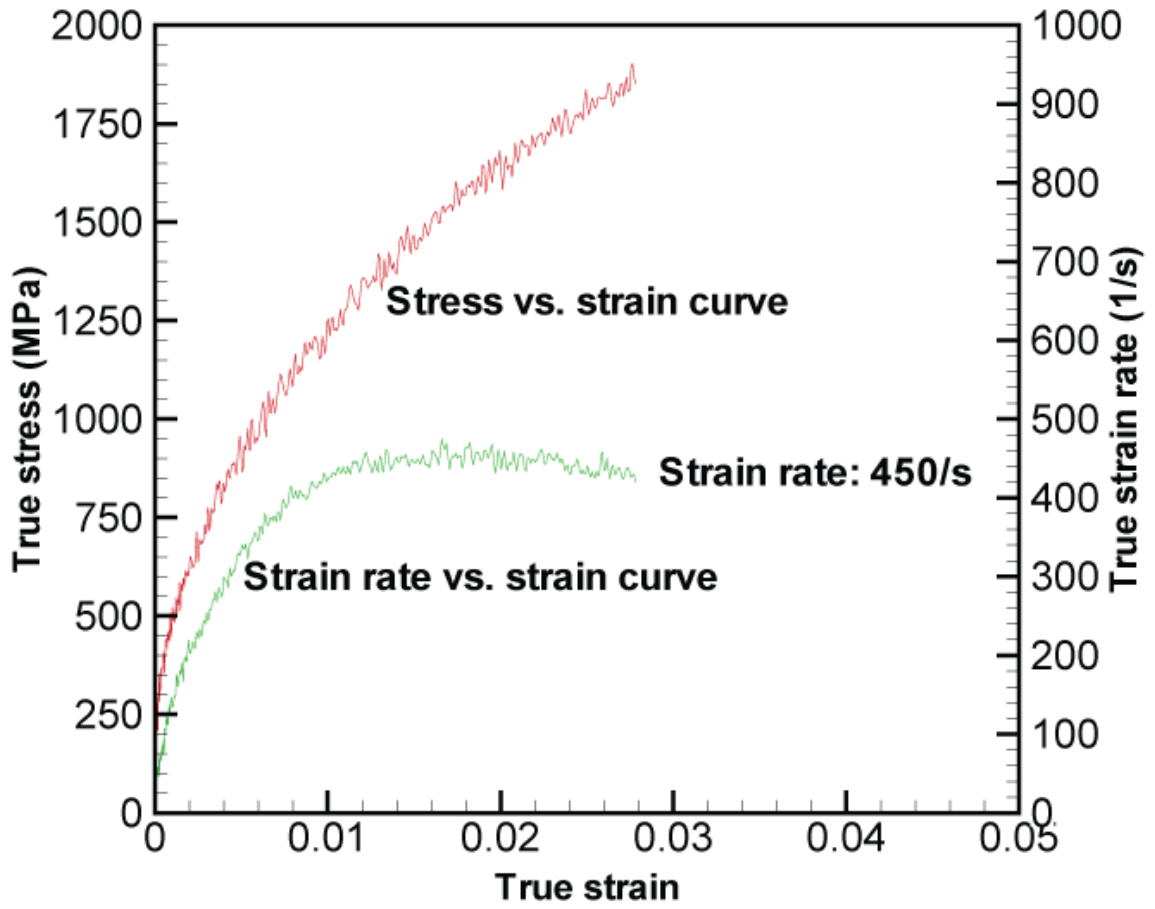


Figure 2.2 – Schematic drawing of the SHPB, illustrating the incident, reflected, and transmitted strain signals

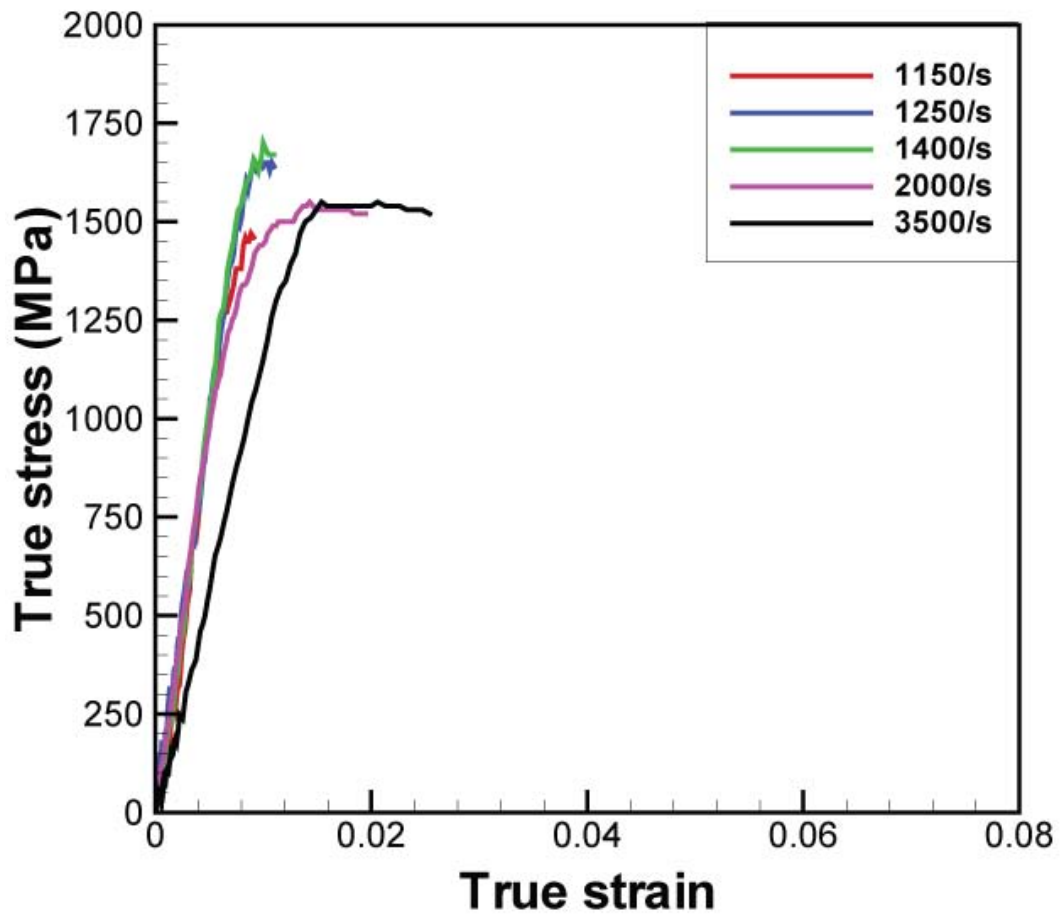


(a)

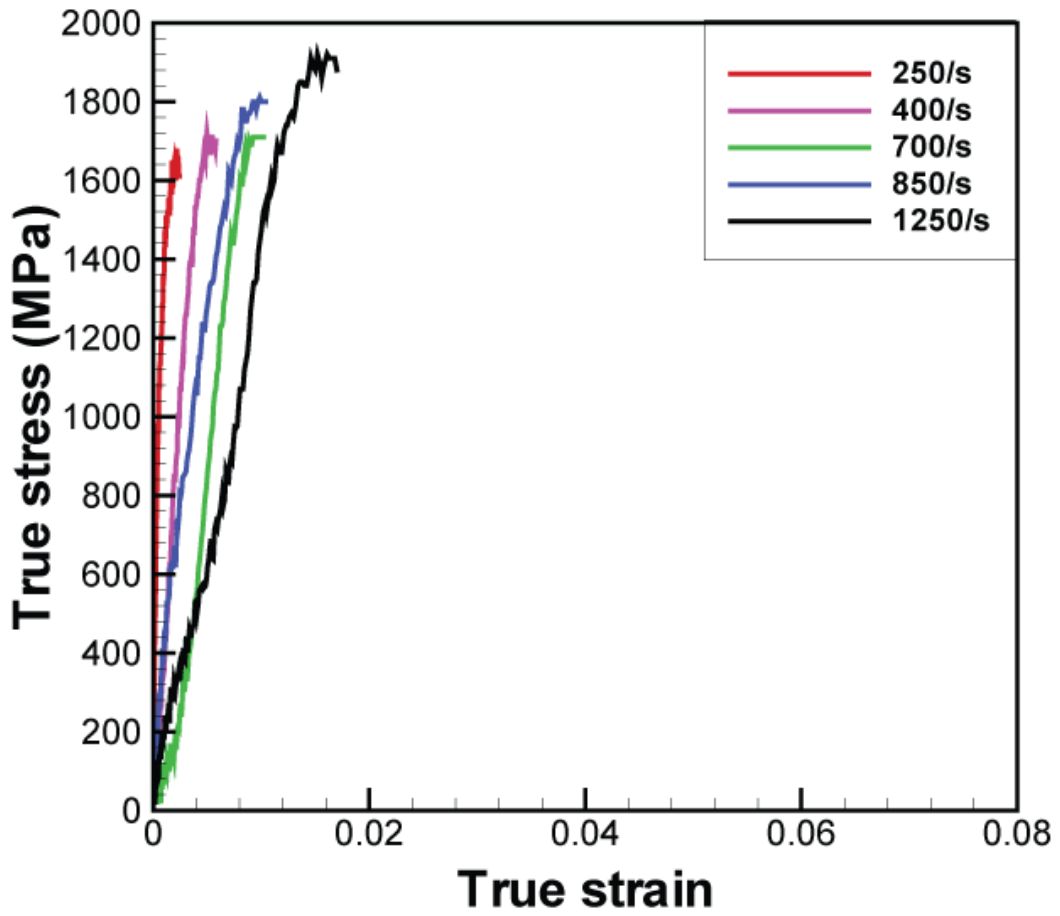


(b)

Figure 2.3 – (a) Instance in which the slopes of the incident and transmitted signals are equal; and (b) corresponding constant strain-rate region



(a)



(b)

Figure 2.4 – Stress-strain curves for amorphous LM-1 specimens of L/D ratios of (a) 2.0 and (b) 0.5

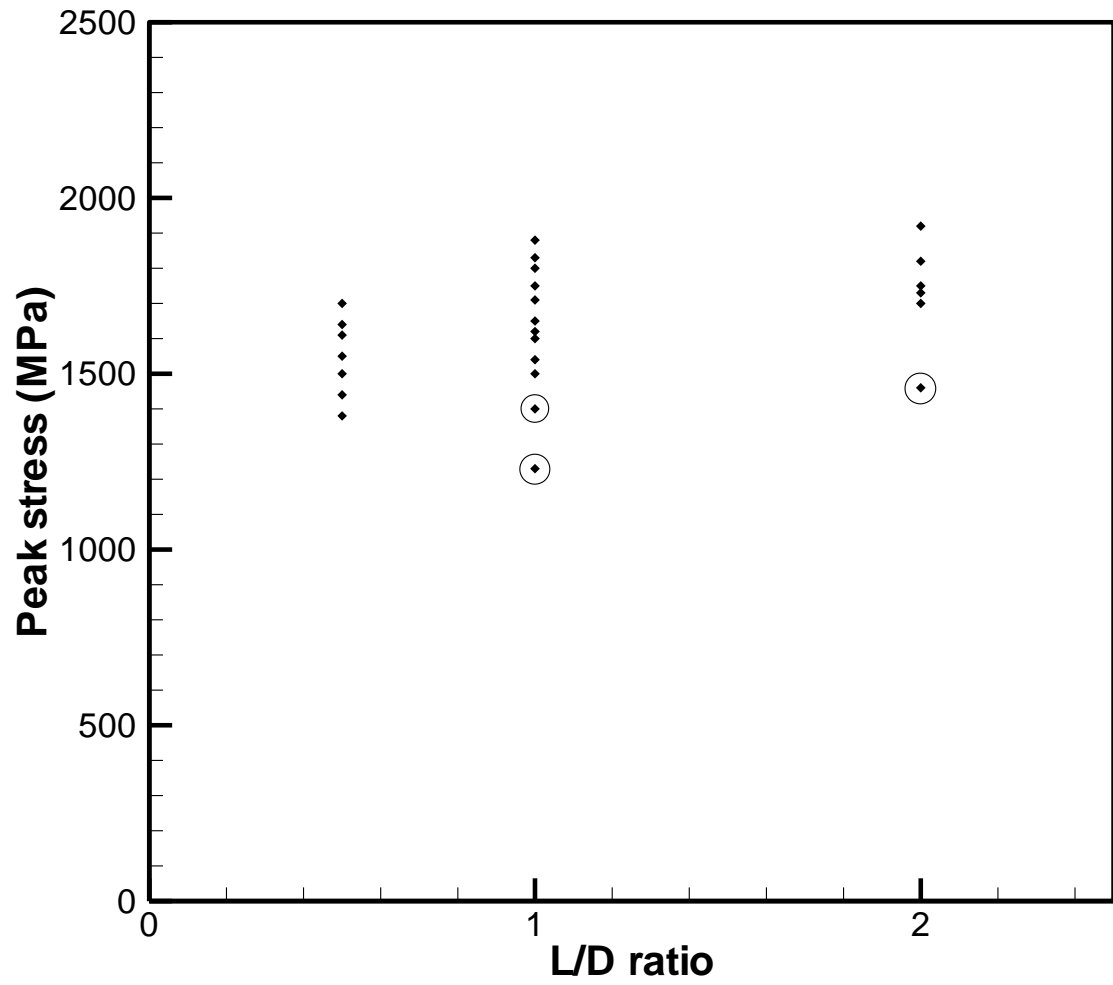


Figure 2.5 – Graph of peak stress vs.  $L/D$  ratio for the experiments considered in this study. Outlying data for this study are circled.

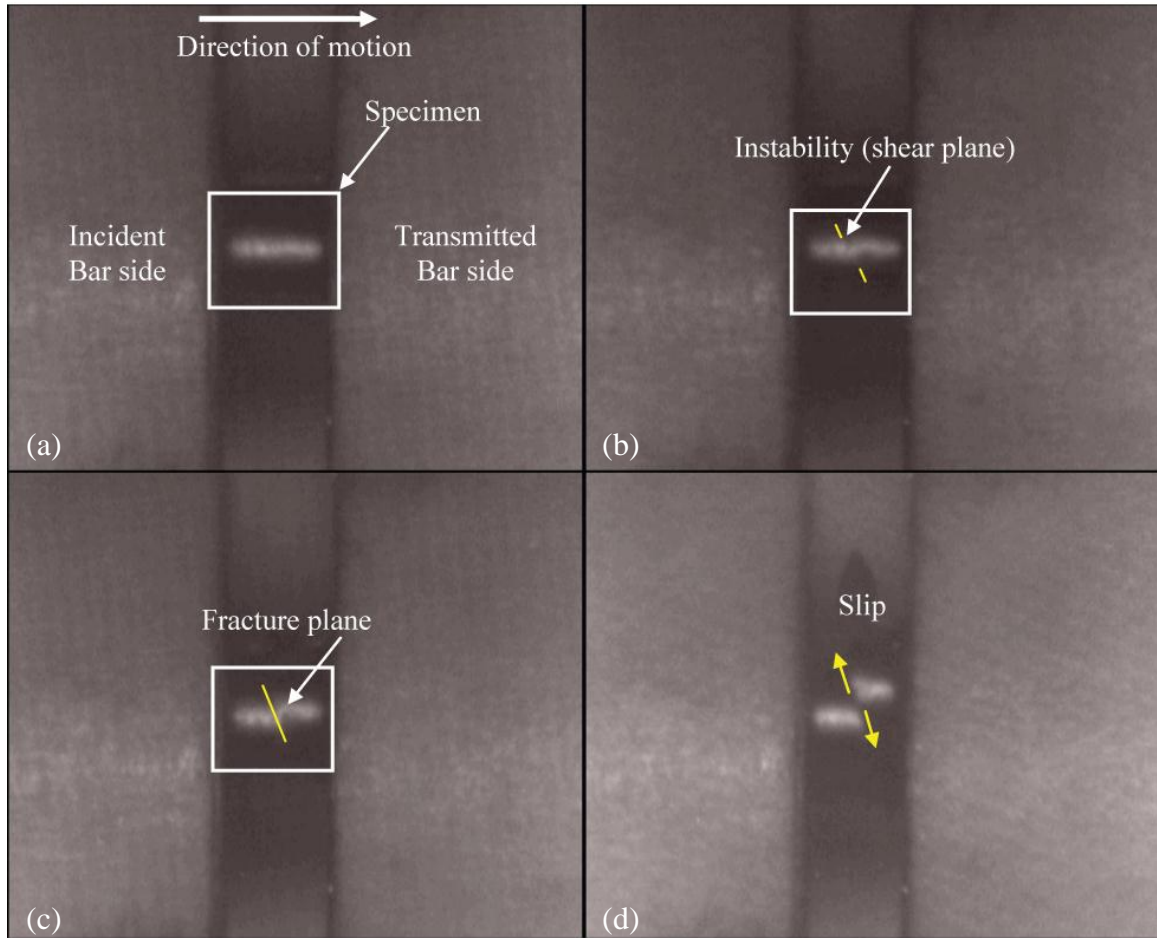


Figure 2.6 – Sequential high speed pictures with an interframe time of 5  $\mu$ s, showing (a) the initial specimen; (b) the shear instability during loading; (c) the formation of a fracture plane; and (d) eventual failure

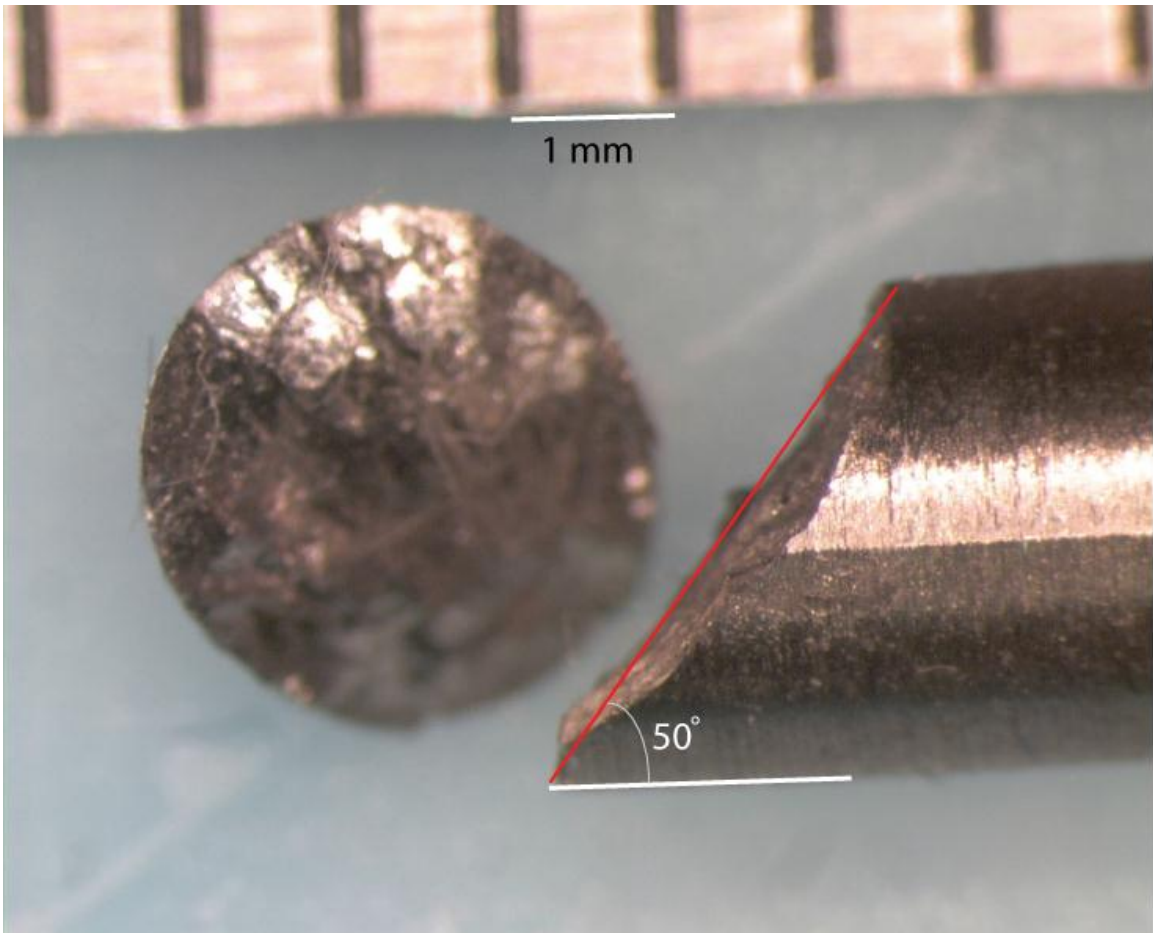


Figure 2.7 – Macroscopic view of two fragments of a specimen with  $L/D$  ratio of 2.0

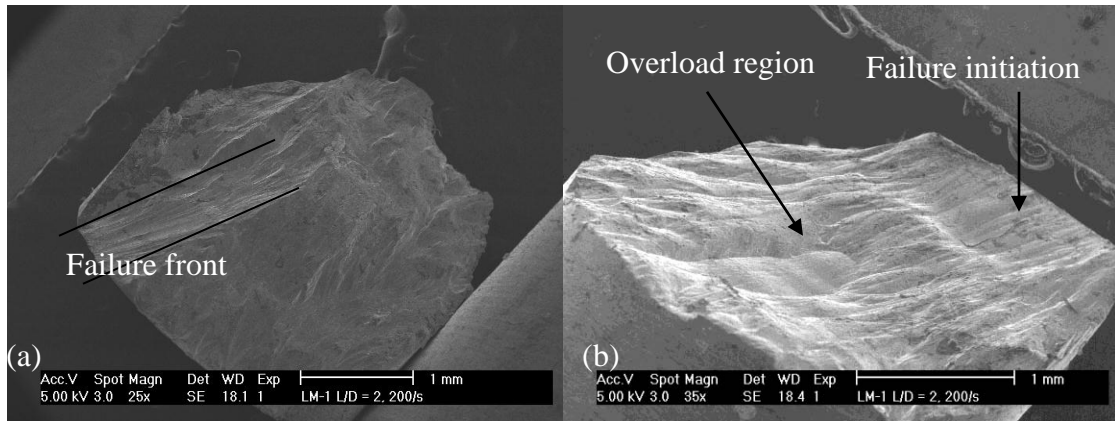


Figure 2.8 – Scanning Electron Microscopy of a specimen with  $L/D$  ratio of 2.0, indicating (a) the presence of a failure front in the failed specimen and (b) the failure initiation region, showing a highly stressed region near the specimen-insert interface

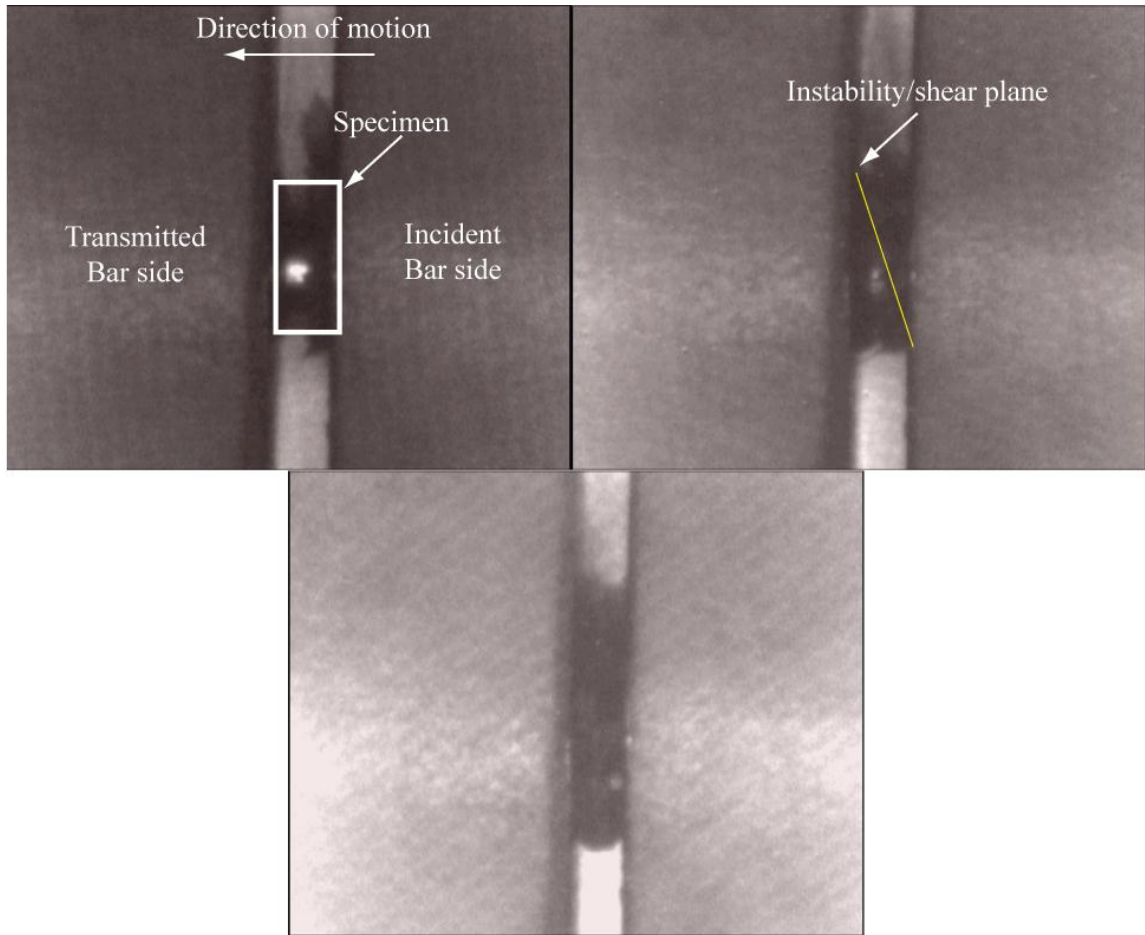


Figure 2.9 – Sequential images, taken with an interframe time of 5  $\mu$ s, of a specimen ( $L/D = 0.5$ ) showing (a) the undeformed specimen, (b) shear plane formation, and (c) failure

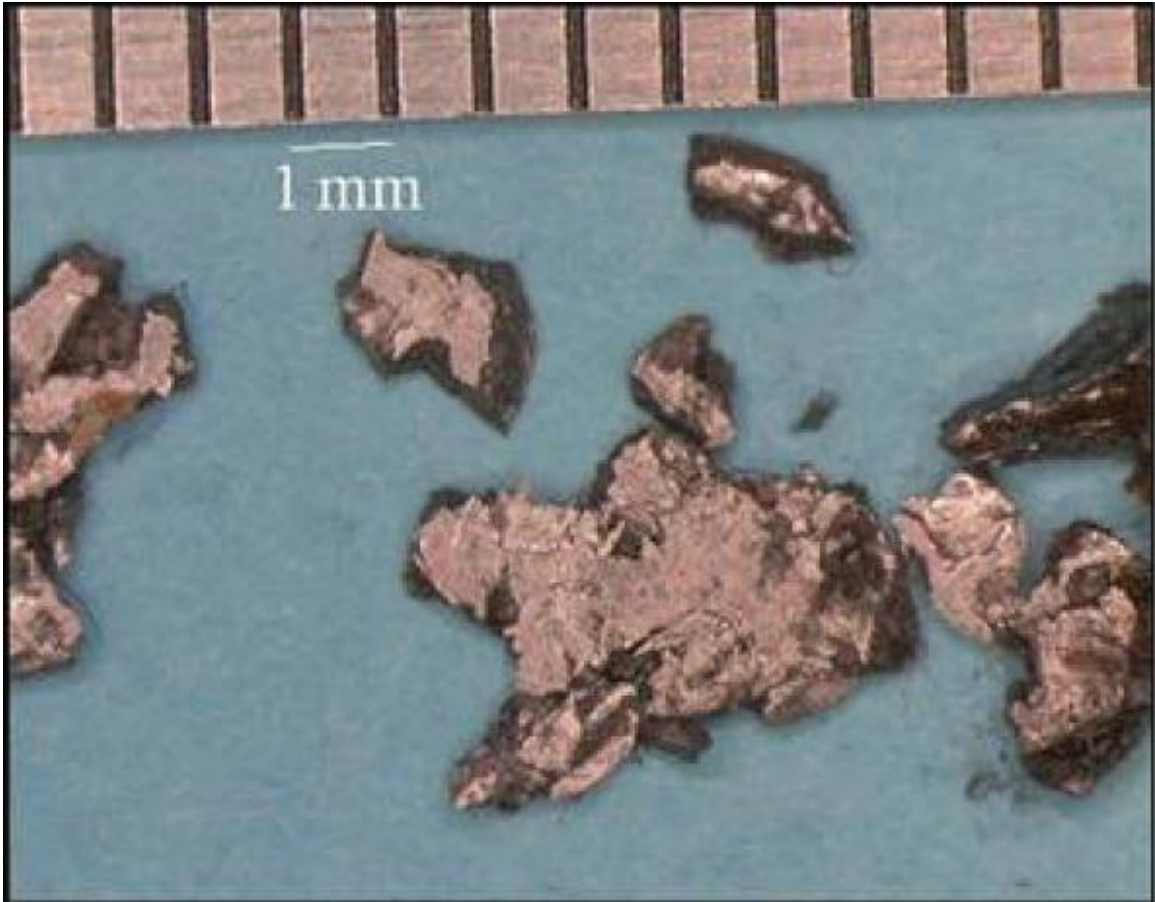
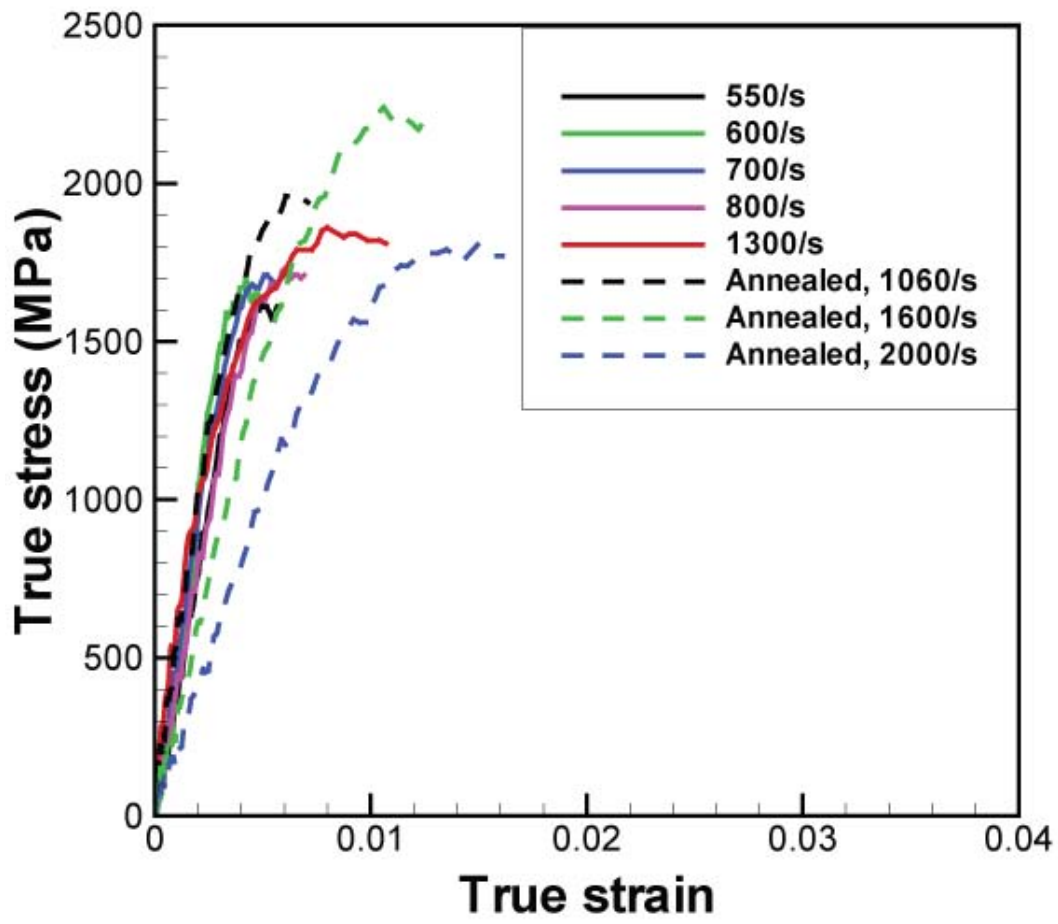
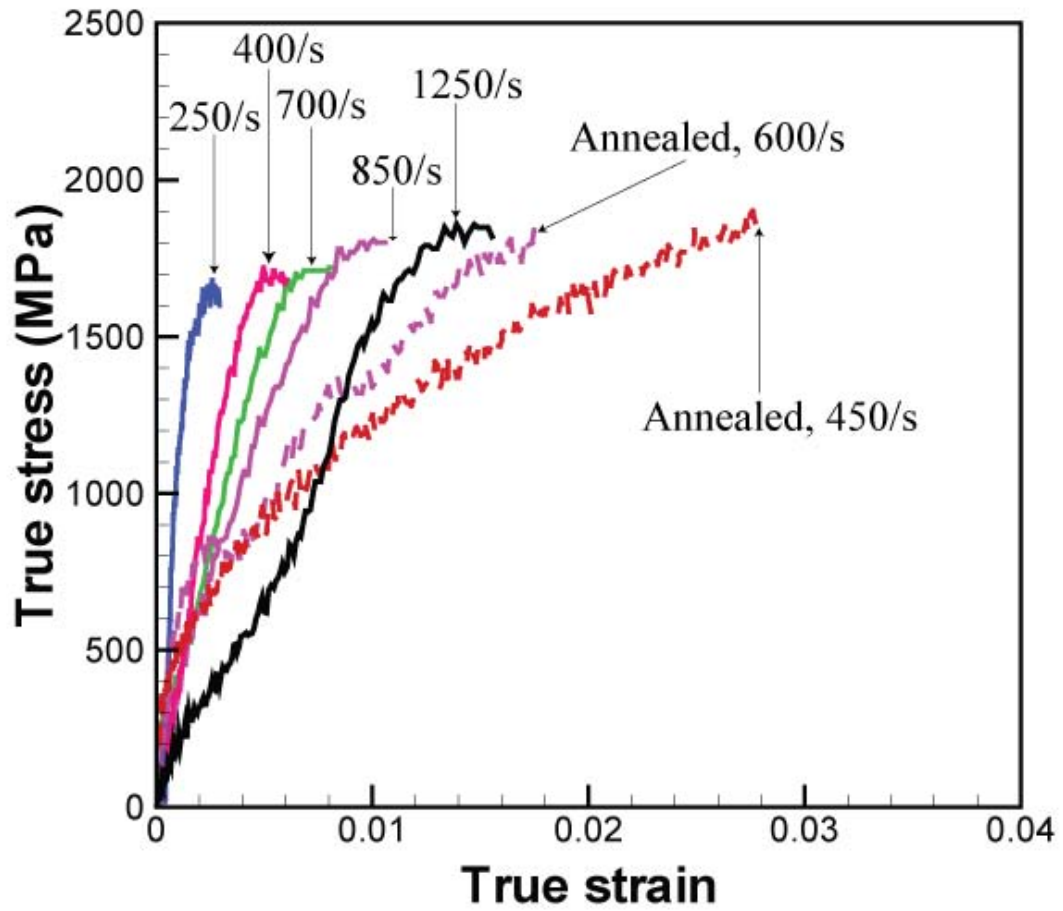


Figure 2.10 – Macroscopic view of fragments for a specimen with  $L/D$  ratio of 0.5



(a)



(b)

Figure 2.11 – Comparison of stress-strain curves for annealed and amorphous LM-1 for two different  $L/D$  ratios: (a) 1.0 and (b) 2.0

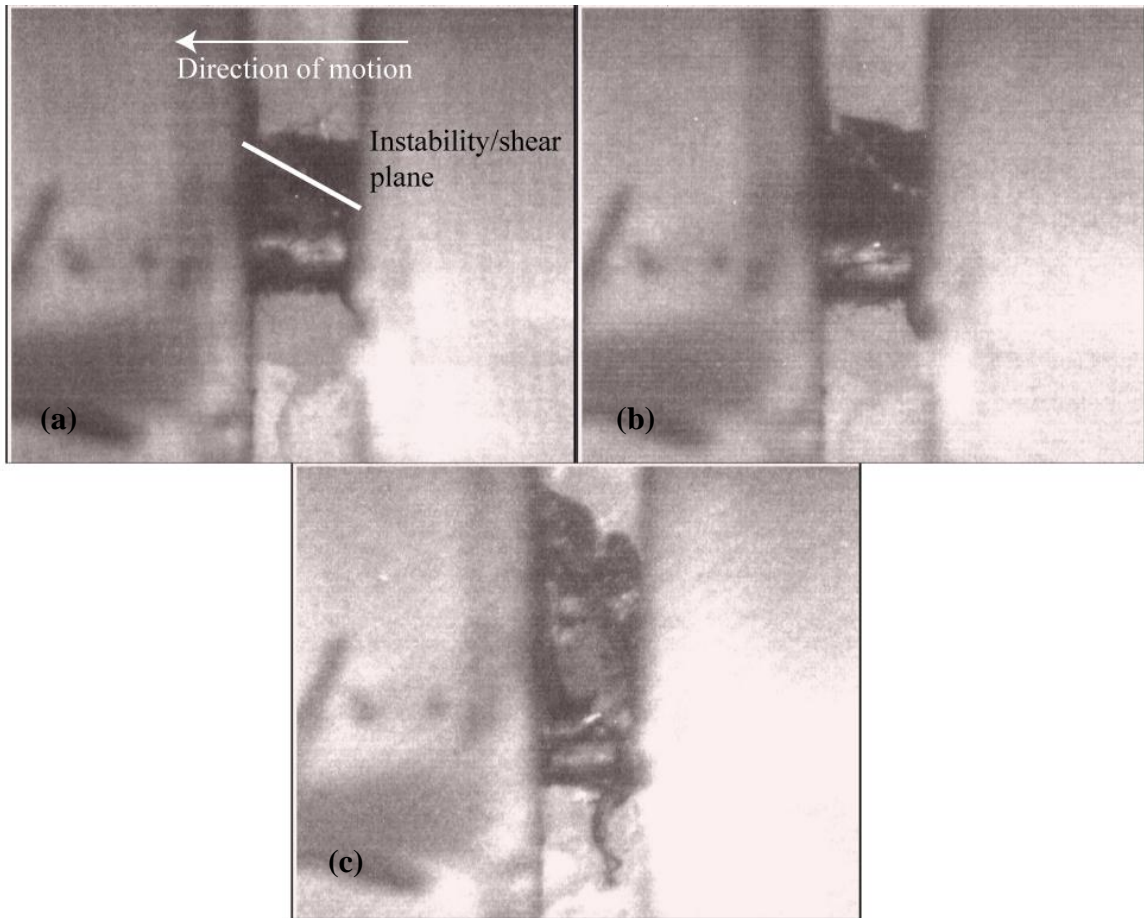


Figure 2.12 – Sequential images of an annealed sample,  $L/D = 1.0$ , at strain-rate 1600/s, with (a) shear plane formation and (b,c) subsequent fragmentation shown at 7  $\mu\text{s}$  intervals

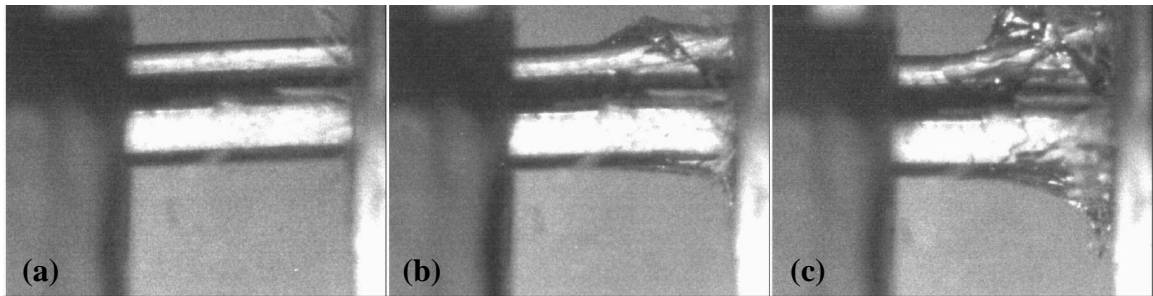
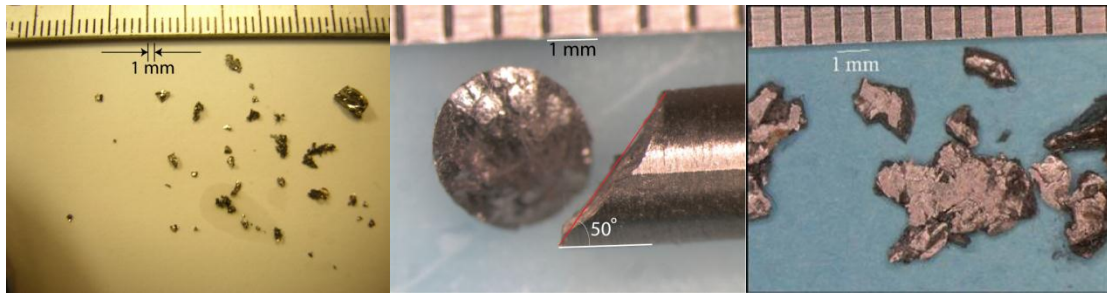


Figure 2.13 – Sequential images of annealed sample,  $L/D = 2.0$ , at strain-rate 450/s and at 7  $\mu\text{s}$  intervals, with (a) undeformed sample, (b) shear plane formation, and (c) evolution of a failure “front” separating “intact” material from fragmented material



(a)

(b)

(c)

Figure 2.14 – Comparison of (a) annealed sample to fully amorphous failed samples of  
(b)  $L/D = 1.0$  or  $2.0$  and (c)  $L/D = 0.5$

## ***Chapter 3 – Design of New Inserts and Improved Evaluation of High Strain-Rate Response of LM-1***

### **3.1 Overview**

As noted in Chapter 2, failure of the LM-1 samples initiated at the sample-insert interface, away from the gage section of the specimen. Such failure has been associated with a stress concentration that occurs because of the mismatch between the insert and sample diameters, and such a stress concentration would prevent the sample from achieving a uniform stress distribution. This rationale is the basis for the design of the new insert discussed in this chapter.

A more thorough discussion of the five conditions to achieve a valid SHPB experiment is presented in Section 3.2. The development of the finite element simulations, along with the results of the simulations clearly identifying the limitations of the cylindrical inserts, is discussed in Section 3.3. Additional candidate sample/insert geometries considered in previous papers are presented in Section 3.4 and compared to the behavior of the cylindrical insert by comparing their performance in simulations and the feasibility for machining. Examination of the behavior of these setups leads to the development of a new insert. Some limitations and applications of the insert are discussed in Section 3.5. Afterwards, high strain-rate experiments are conducted using the new inserts. The first experiments to gain an understanding of changes in the macroscopic fracture behavior in amorphous and annealed LM-1 are shown in Section 3.6, while more extensive experiments are conducted in Section 3.7 to accurately determine the stress-

strain response. A discussion of the comparison of the behavior of the new inserts to the conventional inserts, along with some new insights on the rate sensitivity of LM-1, is provided in Section 3.8 in light of the results in the current study as well as previous experiments conducted.

### **3.2 Conditions for Valid SHPB Experiments**

Work by Subhash and Ravichandran on ceramics [1] has suggested that five conditions must be satisfied to validate the SHPB experiment. Each of the conditions will be elaborated here.

#### *3.2.1 Equilibrium conditions*

As noted in Section 2.2, pulse shaping is necessary to ensure that equilibrium conditions (i.e. constant strain-rate and equal front and back stresses) are present. While effective pulse shaping will promote equilibrium conditions in the specimen, any change to the specimen or the insert will lead to a higher minimum time for force equilibrium in the specimen. This is because such a change in either the specimen or the insert will increase the wave dispersion present in the experiment, and more time will be required for the low frequency components of the wave to dissipate. Therefore, more pulse shaping (and therefore, a longer rise time) will be necessary to prevent specimen failure prior to the achievement of equilibrium conditions.

#### *3.2.2 Elastic behavior of incident and transmitted bars*

Another assumption in deriving equations (2.12) and (2.14) is that both the incident and transmitted bars remain elastic throughout the experiment and that the bars contacting the specimen remain flat and parallel. Hard specimens, such as ceramics and some metallic glasses, can cause indentation of the incident or transmitted bars, leading to both confinement stresses (which produce a nonuniform and triaxial stress state) and damage to the bars (for which the cost may be prohibitive). Typical ways to remedy this issue include the use of hard, impedance-matched, cylindrical inserts (maraging steel or tungsten carbide) in between the bars and the specimen.

Additional specimen geometries, shown in Figure 3.1, have been considered [1-8] to alleviate the issues generated by the diametral mismatch between the inserts and the specimen. Conical inserts (a) have been shown to eliminate the indentation present during experiments, but the inserts were noted to alter the reflected and transmitted signals as well, allowing dispersion effects to affect wave propagation. In addition, fabrication of tungsten carbide inserts is difficult and quite expensive because a new insert is required for each new diameter specimen. Another specimen geometry considered was the dogbone specimen (b), which, like the conical inserts, prevented indentation into the specimen. Like the conical insert, fabrication of the dogbone specimen can be prohibitively expensive because of the difficult machining necessary.

### *3.2.3 Minimal dispersion*

The third condition for a valid SHPB experiment is minimal dispersion in the incident, reflected, and transmitted signals. Dispersion in the signals will lead to different

specimen stresses and strains from those determined from the strain gage histories in the incident and transmitted bars. As noted before, one of the key reasons for effective pulse shaping is to reduce dispersion. However, any insert or specimen used that does not exhibit a constant cross-sectional area (therefore leading to an impedance mismatch throughout the insert) will increase dispersion effects. Dispersion is often remedied by application of a strain gage directly on the specimen, along with the assumption of a linear elastic stress-strain curve (a reasonable assumption for LM-1 [9-11]).

#### *3.2.4 Uniform and uniaxial stress state*

The fourth assumption made in SHPB testing is that the stress distribution in the specimen during loading is both uniform and uniaxial. Such an assumption can be violated if stress concentrations are present, such as due to indentation or because of mismatch between the insert and sample diameters. In the previous sample geometries investigated, the stress state for the specimen is not homogeneous, as the diametral mismatch between the inserts and the specimen leads to a stress concentration. For cylindrical tungsten carbide inserts, this stress concentration was seen to be approximately 1.7 [2], and a stress concentration of about 1.4 was noted for the conical inserts. Dogbone specimens, however, exhibited a small region of uniform stress where the diameter was narrowest. While the stress state was not uniform, the effect of diametral mismatch between the insert and the specimen was negligible and the simulations suggest no preferential failure at the insert-specimen interface. Such behavior would make the dogbone specimen an interesting candidate for reducing stress concentrations that have been present in the previous SHPB experiments.

### 3.2.5 Single loading

The final assumption made in derivation of the governing equations for SHPB testing is that any accumulated strain is due to one compression pulse reaching the specimen. Typically, this assumption is addressed by attaching a large rigid mass to the incident bar, effectively producing a momentum trap. After compressive loading of the specimen, a tensile pulse is introduced into the incident bar, eliminating any compressive pulses that are still present in the bar after the first compression. However, specimen failure was verified to occur after one compressive loading pulse (as seen from the high-speed camera), as the duration of the high-speed photography ( $\sim 80\text{-}100\ \mu\text{s}$ ) was much less than the time required for the compressive pulse to return ( $\sim 500\ \mu\text{s}$ ).

## 3.3 Finite Element Simulation of SHPB

In order to qualitatively determine the effects of stress concentration in the experiments conducted in Chapter 2, finite element simulations (Figure 3.2) were performed using LS-DYNA-2D to determine the stress state of the specimen during dynamic loading. To model the cylindrical tabs used in the experiments, an axisymmetric element of radius 1.6 mm was utilized, with the lengths of the elements dependent on the  $L/D$  ratio (6.4 mm, 3.2 mm, and 1.6 mm for  $L/D$  ratios of 2.0, 1.0, and 0.5, respectively). Both the incident and transmitted bars were modeled as long axisymmetric elements of radius 9.525 mm, and of sufficient length that failure in the specimen occurs by a single compressive pulse (consistent with results discussed in Chapter 2). The mesh size was 0.05 mm along the radial direction for all elements; along

the axial direction, the mesh sizes graduated from 0.05 mm (in the specimen and near the insert-specimen interface) to 1.7 mm (at the ends of the incident and transmitted bars).

To model the dynamic loading of the specimen, the stress at the free end of the incident bar was assumed to be 0, but the initial condition incorporated a pre-determined velocity (5-10 m/s) for a long enough time so that there is no unloading wave present in the incident bar prior to specimen failure. The LM-1 specimen was modeled as a bilinear elastic-plastic material; this is consistent with previous observations [9-11] showing nearly elastic-perfectly plastic behavior in both quasi-static and dynamic loading conditions. The simulations were based on the values of Young's Modulus, density, wave speed, impedance, and yield strength of the BMG, maraging steel, and tungsten carbide (to be discussed later) shown in Table 3.1.

Figure 3.3 shows the axial stress distributions of the BMG during the dynamic loading process. It is apparent from the simulations that the stress concentration that was present in Chen's work [2] is also present in the finite element simulations performed in the present study, and the magnitude of the stress concentration when  $L/D = 0.5$  is approximately the same (approximately 1.7). In addition, the magnitude of the stress concentration varies as the  $L/D$  ratio varies; for  $L/D$  ratios of 2.0, the stress concentration is slightly above 1.4. The reduction in the stress concentration with varying  $L/D$  ratio (and corresponding increase in the peak stress) appears to be consistent with Figures 2.4 and 2.5, both of which show that there is an increase in the peak stress at the  $L/D$  ratio is increased.

One explanation for the difference in the observed peak stresses may be the difference in times required for failure. The longest specimens appeared to take the greatest time for failure in both the simulations and the experiments, and this appears to lead to the greatest stress and strain accumulated in the specimen. Similar reductions in strength with increased strain-rate have been seen in other Zr-based BMGs [12, 13].

The shear stress distributions in the BMG are shown in Figure 3.4. Like for the axial stress distributions, there is a stress concentration present in the specimens which leads to elevated shear stresses. These shear stresses, however, appear to be fairly small and would likely play a role only in combination with large normal stresses. It is also apparent that the maximum shear planes are oriented approximately  $50^\circ$  from the axial surface, and this angle appears to be constant regardless of the  $L/D$  ratio. The orientation of the failure planes also suggests a cause for the change in fracture mechanisms as the  $L/D$  ratio is reduced; the first instability that forms after the initiation of failure is unable to continue through the specimen, and further shear banding can occur before the specimen completely fails.

### **3.4 Additional Specimen Geometries**

As noted in Chapter 3.2, two additional specimen geometries that are of interest are the conical insert and the dogbone specimen. The finite element simulations performed were similar to those for the cylindrical inserts (i.e. the only change in the simulation was the geometry of the specimen). Additional considerations (feasibility of

machining, stress concentrations, impedance mismatch) are also considered in this section.

#### *3.4.1 Conical inserts*

Conical inserts present several problems in SHPB testing of the BMG. Like in the cylindrical specimen, there is inhomogeneity in the axial stress state, as shown in Figure 3.5. From the stress contours, the stress concentration is approximately 1.3 (fairly consistent with work done by Chen [2]), and the peak stresses are found on the circumferential boundary, at the insert-specimen interface. In addition, there are large shear stresses at the insert-specimen interface, as shown in Figure 3.6, which could assist in premature specimen failure. Finally, as noted in Chapter 3.2, conical inserts introduce additional dispersion into the incident and transmitted signals and may be prohibitively expensive to machine from ceramics. All of these issues make conical inserts poor candidates for replacing the cylindrical inserts.

#### *3.4.2 Dogbone specimen*

Based on the axial stress contours of the dogbone specimen, shown in Figure 3.7, there does not appear to be a stress concentration in the gage area of the specimen, and so the gage area exhibits a nominally uniform stress state, as is desired. However, the shear stress contours, shown in Figure 3.8, indicate large shear stresses just outside of the gage section of the specimen. This is particularly problematic because LM-1 fails primarily due to shear, and so the large shear stresses combined with the high normal stresses may lead to failure outside the gage region of the specimen. In addition, dispersive effects

again may play a large role because of the non-uniform impedance, leading to difficulty in determining strains-to-failure and peak stresses accurately. Finally, because of both the high hardness (~ 6 GPa) and the maximum casting thickness (~10-15 mm), machining costs for the specimen may be prohibitive, and the specimen is unlikely to be completely amorphous for the necessary diameter (~19 mm).

### *3.4.3 Development of new insert design*

All three of the issues present in the dogbone specimen (high shear stresses, difficulty in machining, difficulty in processing) can be eliminated by replacing the dogbone “ends” with another material, such as maraging steel; a schematic and an actual insert are shown in Figure 3.9. To do this, part of the gage section of the specimen is made out of bulk metallic glass, and the remaining part of the experimental setup consists of contoured maraging steel (Vascomax 350) inserts. Use of the maraging steel prevents failure due to shear where the diameter is reduced because of the higher yield strength of the steel (~2.5 GPa). In addition, maraging steel can be more easily machined, as it has a much lower hardness ( $R_C = 33$ ) than LM-1 ( $R_C = 60$ ) prior to annealing, so that the reduced insert diameter can be matched to the specimen diameter. Finally, use of the maraging steel inserts no longer requires large specimens, because the inserts can be contoured to 3.2 or 4 mm diameter to match the specimens used in Chapter 2.

To validate the use of the insert design, a finite element simulation was performed using the new maraging steel inserts. All other parameters for the simulation were the same as in the previous simulations. Figure 3.10 shows the axial stress contours for the

new insert design, while Figure 3.11 shows the shear stress contours for the same simulation. In both cases, a nominally uniform state of axial stress is present in the specimen, so that the effect of the stress concentration is minimized. Also, there is very little shear stress in the specimen (less than 120 MPa, or 6% of the peak stress, based on the simulation), so premature failure is not expected at the insert-specimen interface. In addition, because the maximum axial and shear stresses in the insert (2.0 GPa and 500 MPa) are less than the yield strength (~2.5 GPa) of the insert, failure in the insert is not expected.

### **3.5 Additional Considerations with New Inserts**

#### *3.5.1 Limitations and assumptions*

While the dogbone inserts eliminate some key issues present in SHPB testing of LM-1, there are still a couple of key limitations and assumptions that must be addressed. While the simulations show that the stress state is uniform and nominally in equilibrium, there are dispersion effects because of the change of the impedance between the bars and the specimen, as well as strain in the inserts themselves. Both of these phenomena will lead to inaccurate values of the strain-to-failure and the peak stress. To determine the strain-to-failure and peak stress accurately, either a dispersion model, such as the Pochhammer-Chree relation, must be assumed, or strain gages need to be placed directly on the specimen and the signals from the strain gages compared to the incident and transmitted bar strain history signals. Use of dispersion models, particularly in complicated waveguides such as the contoured inserts, may make it impossible to obtain closed-form dispersion relations. In addition, the inserts deform during the experiment, so

any specimen strains that are measured must also take into account the deformation of the inserts. However, when strain gages are placed directly on the sample, the stress-strain curve must be assumed, which does not cause much difficulty, as the material appears to be largely linear elastic to failure [9, 10] under quasi-static conditions.

In addition, the state of equilibrium must also be established in the specimens. To facilitate this, finite element simulations illustrating the stress state are shown in Figure 3.12. It is clear from the finite element simulations that the specimen reaches and maintains equilibrium for the large majority of the experiment, as expected. This provides further confidence in the use of the inserts to provide improvements in accuracy for stress measurements.

### *3.5.2 Applications*

In addition to improvements in testing of bulk metallic glasses, such as LM-1, the use of contoured inserts holds promise in the testing of other low-ductility materials, such as ceramics. Most of the previous work has focused on using cylindrical tungsten carbide inserts or dogbone specimens in order to determine accurate peak stresses and strains-to-failure; however, as noted before, stress concentrations or large shear stresses are introduced in the specimen during testing. In addition, ceramics have high strength, so there is a possibility of insert damage before the specimen fails, which would make the results meaningless. To avoid these issues, impedance-matched contoured tungsten carbide inserts can be used in place of the maraging steel inserts to test high-strength materials without causing insert failure, as shown in Table 3.1. Figure 3.13 shows the

axial stress distribution from such a simulation. Because the tungsten carbide inserts have much greater compressive yield strengths, they can be used in place of maraging steel inserts when SHPB testing of higher strength materials is conducted.

Like in dynamic compression tests, quasi-static compression tests using large platens are influenced by stress concentrations present because of the diametral mismatch of the specimen and the platens. Such stress concentrations, which can exceed 2 at locations nearest the specimen-insert interface along the circumferential boundary [14] (with the assumptions of the material remaining elastic and the radius of the “notch” due to the change in diameter being less than 5% of the specimen diameter), may affect the yield and peak strength of the BMG, as the stress concentrations also introduce a non-uniform state of stress in the specimen. In addition, such a stress concentration may also alter the fracture angle, as seen from tension experiments conducted with a sufficiently large hydrostatic pressure to generate a negative value of the stress triaxiality [9, 15-18]. In these experiments, there still is a significant difference in the fracture angles exhibited ( $\sim 40^\circ$  in compression,  $\sim 55^\circ$  in tension).

To investigate the effect of the new insert design, tests were conducted on specimens of LM-1 with  $L/D = \sim 2.0$  (as per ASTM standards, and to ensure discrete specimen failure and plane stress conditions) and diameters of 3.2 mm at strain-rates of  $10^{-4}/s - 10^{-3}/s$ . Maraging steel inserts were utilized and were expected not to fail under the applied loads (Figure 3.10). The stress-strain curve of one of these experiments is shown in Figure 3.14; the peak stress exhibited by this specimen was 2.00 GPa, in

agreement with previous findings [9, 15-17], but the fracture angle is closer to 44°. This suggests some effect of changing the inserts utilized in quasi-static tests, but little change in the peak stress.

The Mohr-Coulomb criterion is given by

$$\tau = \tau_0 - \alpha\sigma, \quad (3.1)$$

with  $\tau$  being the critical shear stress necessary for specimen failure,  $\tau_0$  the critical shear stress under torsion,  $\alpha$  the normal stress sensitivity parameter, and  $\sigma$  the normal stress applied on the failure surface, and the expected failure angle  $\theta$  is related to  $\alpha$  by:

$$\cot(2\theta) = \alpha. \quad (3.2)$$

A fracture angle of 44° suggests of a value of  $\alpha$  of 0.035, which agrees with the previous findings [9, 15-17] and further supports the small normal stress dependence of LM-1.

### **3.6 Macroscopic Fracture Behavior of LM-1 with New Inserts**

To investigate the change in macroscopic fracture behavior (i.e. the location of initial specimen failure and the location of the shear planes) of as-cast LM-1, a series of experiments, shown in Table 3.2, were conducted using tapered inserts. All of the experiments were conducted with input (i.e. striker) bar velocities ranging from 6.7 m/s to 15.1 m/s; large pulse shapers (8 mm x 8 mm x 0.75 mm) were used to mitigate the potential effects of increased dispersion present due to the tapered inserts.

High-speed camera images (with an interframe time of 7  $\mu$ s) of an experiment conducted on as-cast LM-1 with the new inserts are shown in Figure 3.15. During this experiment, the specimen ( $L/D = 1.0$ ) is initially unstressed (Frame 1), but as the stress wave loads the specimen (Frame 9), two shear planes form in the gage region of the specimen, which leads to catastrophic failure of the specimen (Frame 10). Due to the forward momentum of the remainder of the specimen, it impacts the insert on the incident bar (Frame 16). Unlike as observed in the previous experiments, for the tapered insert geometry specimen failure occurs in the gage section; this was further confirmed using optical microscopy. Similar results were obtained with a specimen with  $L/D = 2.0$ , as shown in Figure 3.16. The intact specimen prior to loading is shown in Frame 1. An instability is clearly evident in the top half of the sample (Frame 6) which is fully contained within the gage section of the specimen. Two shear planes with different orientations are clearly seen in Frame 7, while the final separation is present in Frame 9.

Three additional tests were performed on annealed LM-1 to investigate the fracture behavior of the annealed (embrittled) LM-1 using the new tapered insert design. High-speed camera images of such a test are shown in Figure 3.17. During this experiment, the specimen ( $L/D = 2.0$ ) is initially unstressed (Frame 1), but as the stress wave loads the specimen, damage is observed to accumulate in the specimen (Frame 13). Shortly afterwards the initial failure of the specimen (Frame 14) occurs, after which the specimen continues to fracture (Frame 16 and onwards), similar to that observed in the experiments conducted without the tapered inserts. Multiple fragmentation of the sample

is exhibited in these cases, in contrast to the behavior exhibited by the as-cast LM-1, shown earlier in Figures 3.14 and 3.15.

### **3.7 Measurements of Peak Stress and Strain in LM-1**

#### *3.7.1 Preparation of strain gage experiment*

Because of the small diameter (4 mm) and length (2-8 mm) of the specimens, application of the strain gages is not a trivial process, and alignment of the strain gage can be quite difficult because the strain gage must remain stationary relative to the specimen during the curing process. To solve these issues, a new strain gage installation process was devised. The specimens were first thoroughly cleaned using acetone, and then a small amount (i.e. ~ 1 mL) of fast-curing epoxy (Hardman 04001) was placed on the surface of a glass plate. The specimen was then placed on the epoxy and allowed to cure. Cloth wipes (Kimwipes EX-L, Kimberly-Clark) were placed over the specimens to prevent dirt from settling during the curing process. After curing was completed, the top of the specimen was cleaned with acetone, followed by a conditioner and a neutralizer. The matrix of the strain gage (EA-06-031CE-350 with attached leads, Vishay Micromasurements Group) was removed, and the strain gage was then placed on the glass plate. The strain gage was placed on top of the specimen using cellophane tape and a thin film of epoxy (M-BOND 10, Vishay Micromasurements Group) was applied to the specimen-gage interface to assist in bonding. To ensure adequate pressure between the strain gage and the specimen, weights were placed on both sides of the cellophane tape and the assembly was left to cure for at least 18 hours. The resulting assembly is shown in Figure 3.18. After curing was completed, the leads of the strain gage were

disconnected from the specimen and excess epoxy was removed. The leads of the strain gage were then connected to a Wheatstone bridge by means of soldering tabs placed on the maraging steel inserts.

The Wheatstone bridge used in the experiments is shown in Figure 3.19. 350  $\Omega$  resistors are used to match the 350  $\Omega$  resistance of the strain gage. In addition, a 300  $\Omega$  resistance is connected in series to a variable resistance ( $\sim 0$ -100  $\Omega$ ) to ensure that the Wheatstone bridge can be balanced, even when small fluctuations of the other resistors occur. A shunt resistor of 130 k $\Omega$  is placed in series with a switch and in parallel with the strain gage for calibration of the Wheatstone bridge; closing the switch generates an output voltage of 5 mV between arms 2 and 3 when the input voltage is 7.5 V; the change in resistance for a gage factor of 2.06 is 0.13%. This Wheatstone bridge is connected to an amplifier (Tektronix 5A22N) with a 10x gain and is in turn connected to a high-bandwidth oscilloscope (Tektronix 420A).

Copper pulse shapers of dimensions 8 mm x 8 mm x 0.75 mm were utilized to provide a triangular pulse in the incident bar and reduce the likelihood of premature failure. The strain history signals for a representative experiment are shown in Figure 3.20. As can be seen in the figure, the incident and transmitted pulses have nominally similar slopes, but because of the dispersion in the wave profile due to the tapered inserts, the slope of the reflected signal is nonzero. However, the strain gage history on the specimen shows a linear strain vs. time profile, suggesting that the specimen is deforming at a nominally constant strain-rate. A linear fit, shown in Figure 3.21, was performed on

the strain history of the specimen to verify that the specimen is deforming at a constant strain-rate. The strain was determined using the calibration from the previous section (5 mV voltage corresponding to 0.13% strain), and linear elastic behavior of the specimen is assumed ( $E = 96$  GPa) in construction of the stress-strain curves. A stress-strain curve for this experiment is shown in Figure 3.22.

### *3.7.2 Results from strain gage experiments on LM-1*

The results of the experiments conducted on specimens with  $L/D = 2.0$  are shown in Table 3.3. Of the five specimens tested, two of them failed prior to separation of the strain gage from the specimen (shown in Figure 3.23), one did not fail during testing, and two specimens failed after the strain gage separated from the specimen (implying that the strain gage did not capture the entire strain history of the specimen). For the two specimens which failed before delamination of the strain gage, the strain measured was approximately 1.8% and 1.9%, corresponding to a peak stress range of 1.73-1.82 GPa.

The results of the experiments conducted on specimens with  $L/D = 1.0$  are shown in Table 3.3. Eight specimens were tested in this group; of the eight specimens, four failed prior to separation of the strain gage from the specimen, three specimens failed after separation of the strain gage, and one specimen did not fail during testing. For the specimens that failed prior to delamination of the specimen, the peak strain measured was between 1.7% and 2.2%, corresponding to a peak stress range of 1.63-2.00 GPa. Specimens in this group of experiments failed in a similar way to specimens tested without strain gages. Two different fracture angles are apparent in these specimens, as

shown in Figure 3.23, and these angles appear to be similar to those shown in Figure 3.18.

### **3.8 Discussion**

As can be seen from the results of the experiments conducted, the use of the new tapered inserts changes the flow and fracture behavior of as-cast LM-1. While there was a slight decrease in the peak stress with decreasing  $L/D$  in the tests conducted with the cylindrical inserts, the change in the peak stress levels attained in the tests conducted with the new inserts are less than 10%. In addition, the fracture planes of the as-cast specimens are different; instead of single shear planes in the experiments conducted with cylindrical inserts, more than one fracture angle is exhibited in these experiments. The use of the strain gages also allows a more accurate representation of the elastic stress-strain response of the specimen. This stress-strain response is useful in studying both the behavior of LM-1 and comparisons of the tests conducted with and without the new inserts, which are discussed in this section.

#### *3.8.1 Comparison of stress and strain-rate signals from gages on bar and specimen*

As noted earlier in Chapter 3, the use of the new tapered inserts causes dispersion effects, and the complicated waveguides due to the inserts may make the solution of the dispersion relation intractable. However, by testing the LM-1 specimens with the strain gages and comparing the stress and strain profiles from the specimen strain gage and the strain gages present on the incident and transmitted bars, it is possible to compare the stresses, strains, and strain-rates up to specimen failure as recorded from both the

specimen and the bar assembly. The stress vs. time curves for a representative experiment are shown in Figure 3.24, while the peak stresses (as determined from the bar and the specimen) are shown in Figure 3.25 for the six successful experiments (in which specimen failure occurred prior to separation of the strain gage from the specimen). Based on Figure 3.25, the differences in the peak stresses as determined from the transmitted bar and the specimen strain gage signals are within 10% of each other. This 10% variation in the peak stresses is a typical experimental error for tests conducted on the SHPB for materials exhibiting low strains-to-failure, as noted elsewhere [19, 20], and so the dispersion effects that are present with the new tapered inserts are not dominant when calculating peak stresses. This is an interesting result and has implications in SHPB testing of other brittle materials using the new tapered inserts.

In contrast, the differences in the strains and strain-rates as measured from the specimen strain gage and the reflected bar can be quite large. Figure 3.26 shows the strain vs. time curve for experiment SG12 as determined from both the reflected bar signal and the specimen strain gage. Compared to the strain-rate determined from the specimen strain gage (Figure 3.21, 550/s), the strain-rate determined from the reflected bar (at the time of failure) was 1200/s, more than double the actual strain-rate. In addition, Figure 3.26 also shows that the strain-rate determined from the reflected bar is not constant at the time of specimen failure, which is not the case. The strain-rates for all experiments are much lower than calculated from the reflected signal, as shown in Figure 3.27. The large difference between the strain-rates recorded from the reflected signal and from the specimen strain gage signal for specimens with  $L/D = 1.0$  produces a

large difference between the peak strains measured from the reflected signal and the specimen strain gage signal, as shown in Figure 3.28. The reason for this discrepancy is because the specimen strain gage only measures the strain (and thus the displacement) of the specimen. On the other hand, the reflected signal measures the strain in the specimen as well as in the inserts. Assuming that the constant diameter region of each of the two dogbone inserts is 4 mm in length, one can approximate the strain measured by the reflected signal by the following (for a specimen with  $L/D = 1.0$ ):

$$\varepsilon_R = \frac{\frac{4 \text{ mm}}{E_{steel}} + \frac{4 \text{ mm}}{E_{BMG}} + \frac{4 \text{ mm}}{E_{steel}}}{4 \text{ mm}}, \quad (3.3)$$

with  $E_{steel}$  and  $E_{BMG}$  as the Young's Moduli of the steel insert and the BMG, respectively (Table 3.1). Assuming Young's Moduli of 210 GPa and 96 GPa, this means that the strain-rate (and thus the strain) measured by the reflected signal would be 1.9 times as large as the specimen actually experienced. This shows that while the transmitted bar signal can be used to approximate the peak stress in these experiments, use of the reflected signal for calculating strain and strain-rate will lead to substantial errors.

### 3.8.2 Comparison of peak stresses with conventional inserts and new inserts

In Figure 3.29, the peak stresses achieved by as-cast LM-1 (in the present study) are superimposed on the peak stresses achieved with the cylindrical inserts (Figure 2.5). In addition, data from Bruck's work on LM-1 [20] is shown in this figure, and averages and standard deviations are shown in Table 5.4. Based on the figure, it is apparent that

the reduction in the stress concentration factor due to the inserts somewhat affects the peak stress in the specimen. In addition, when examining Bruck's experiments, it appears that the peak stresses from the specimen strain gages are slightly higher than from the transmitted bars. This may be because some stress triaxiality is present in the gaged samples (because of the cylindrical inserts and the small aspect ratio), but the stress state in the experiments conducted with the new tapered inserts is expected to be uniaxial.

### *3.8.3 Effects of $L/D$ and strain-rate*

Based on Figure 5.12 and the experimental error present in testing (100-200 MPa), it appears that the reduction of  $L/D$  from 2.0 to 1.0 leads to a negligible difference in the peak stress or the peak strain in the as-received BMG in the present study. In particular, the comparison of experiments SG 4 and SG 11, along with SG 5, SG 8, and SG 12 reveal negligible changes in the peak stress for a given strain-rate. Likewise, the peak strains (and therefore peak stresses) achieved by the specimens appear to be largely insensitive to the strain-rates for a given  $L/D$  ratio, in agreement with Bruck [20].

Of substantially more interest is comparing the results from the current study to other recent works in order to understand the strain-rate sensitivity of LM-1 from  $10^{-4}$ /s to  $10^5$ /s. In order to do this, the results from the current study are compared to quasi-static experiments performed previously [9] as well as high strain-rate pressure-shear plate-impact experiments conducted with a single-stage gas gun [21, 22]. The comparison of the three groups of data are done by determining the equivalent shear stress (to connect

the uniaxial stress state of the quasi-static and SHPB experiments and the uniaxial strain nature of the gas gun experiment). The data are shown in Figure 3.30 and clearly indicate that over nine orders of magnitude, the rate sensitivity of LM-1 is negligible. While this is in agreement with other investigators [10, 11, 20], up to this point, no previous studies have examined the effects of strain-rate over so wide a range.

### **3.9 Summary**

The five criteria for valid SHPB testing were discussed, along with previous numerical simulations [2] to test the assumptions of valid testing. Additional simulations are performed using LS-DYNA to justify the design of a new insert, which is then tested first to determine how the macroscopic fracture changes in LM-1 and also to determine more accurately the peak stresses and strains in the LM-1 specimens. From this study, the following conclusions can be made:

1. The present setup using cylindrical inserts appears to introduce stress concentrations of at least 1.4 that may explain the negative strain-rate sensitivity previously reported.
2. Conical inserts and dogbone specimens are judged to be poor substitutes because of high shear stresses, difficulty in machining, and large dispersion effects.
3. Replacement of the dogbone ends with maraging steel is seen to ensure a uniform stress state while ensuring that the specimens can be machined and that high shear

stresses are not present. Equilibrium is preserved in the specimen throughout a large part of the loading process.

4. While application of strain gages is necessary to get accurate strains-to-failure and peak stresses, the new insert design shows promise for SHPB testing of materials exhibiting low strains-to-failure.
5. Unlike with the conventional inserts, specimens tested with the new tapered inserts appear to fail within the gage section of the specimen. In some cases, this manifests itself in the form of self-sharpening behavior for as-cast LM-1. As-cast LM-1 samples exhibit more than one fracture plane, although the difference in the fracture angles is not as large as with the conventional inserts.
6. Annealed LM-1 samples exhibit failure in the gage section and subsequent extensive fragmentation, similar to that found with the conventional inserts.
7. A method has been successfully devised to apply strain gages directly on the specimen and therefore determine the peak stresses and peak strains experienced by the specimen under the new experimental setup.
8. Comparison of the strain gages on the specimen and the transmitted bar reveal that the peak stresses are in agreement within the experimental error. Comparison of the strain gages on the specimen and the incident bar reveal that the strain-rates

as determined from the reflected signal are much higher than actually experienced by the specimen (as shown by the strain gaged sample), leading to large discrepancies between the specimen and incident bar signals in the strain measured. This is due to the fact that the reflected signal measures the strain in both the specimen and the inserts.

9. Comparison of the peak stresses in LM-1 to earlier works investigating the peak stresses at both quasi-static strain-rates (e.g.  $10^{-4}/s$ ) and very high strain-rates (e.g.  $10^5/s$ ) indicate that the strain-rate sensitivity of LM-1 is negligible over a very wide range of strain-rates.

## References

1. Subhash G., Ravichandran G. (2000) Split-Hopkinson pressure bar testing of ceramics. *American Society for Materials Handbook* (8<sup>th</sup> ed.), American Society for Metals International, Materials Park, OH, 497-504
2. Chen W., Subhash G., Ravichandran G. (1994) Evaluation of ceramic specimen geometries used in split-Hopkinson pressure bar. *Dymat Journal* **1**, 193-210.
3. Cosculluela A., Cagnoux, J., Collombet, F. (1991) Uniaxial compression of alumina: structure, microstructure, and strain rate. *Journal de Physique IV* **1**, C3-109 - C103-116.
4. Tracy C.A. (1987) A Compression Test for High Strength Ceramics. *Journal of Testing and Evaluation* **15**, 14-19.
5. Couque H., Albertini C., Lankford J. (1993) Failure mechanisms in a unidirectional fibre-reinforced thermoplastic composite under uniaxial, in-plane biaxial and hydrostatically confined compression. *Journal of Materials Science Letters* **12**, 1953-1957.
6. Blumenthal W.R., Gray G.T., III (1989) Characterizations of shock-loaded aluminum-infiltrated boron carbide cermets. *Proceedings of the American Physical Society Topical Conference*, Albuquerque, NM, August 14-17, 1989.
7. Blumenthal W.R., Gray G.T., III (1989) Structure-property characterization of a shock-loaded boron carbide-aluminum cermet. *International conference on mechanical properties of materials at high rates of strain*, Oxford, UK, March 20, 1989.

8. Lankford J. (1977) Compressive strength and microplasticity in polycrystalline alumina. *Journal of Materials Science* **12**, 791-796.
9. Lowhaphandu P., Ludrosky L.A., Montgomery S.L., Lewandowski J.J. (2000) Deformation and fracture toughness of a bulk amorphous Zr-Ti-Ni-Cu-Be alloy. *Intermetallics* **8**, 487-492.
10. Bruck H.A., Christman T., Rosakis A.J., Johnson W.L. (1994) Quasi-static constitutive behavior of  $Zr_{41.25}Ti_{13.75}Ni_{10}Cu_{12.5}Be_{22.5}$  bulk amorphous alloys. *Scripta Metallurgica et Materialia* **30**, 429-434.
11. Lu J., Ravichandran G., Johnson W.L. (2003) Deformation behavior of the  $Zr_{41.2}Ti_{13.8}Cu_{12.5}Ni_{10}Be_{22.5}$  bulk metallic glass over a wide range of strain-rates and temperatures. *Acta Materialia* **51**, 3429-3443.
12. Hufnagel T.C., Jiao T., Xing L.Q., Ramesh K.T. (2002) Deformation and failure of  $Zr_{57}Ti_5Cu_{20}Ni_8Al_{10}$  bulk metallic glass under quasi-static and dynamic compression. *Journal of Materials Research* **17**, 1441-1445.
13. Subhash G., Zhang H., Li H. (2003) Thermodynamic and mechanical behavior of Hafnium-/Zirconium-based bulk metallic glasses. *Proceedings of the International Conference on Mechanical Behavior of Materials (ICM-9)*, Geneva, Switzerland, May 25-29, 2003.
14. Pilkey W.D. (1997) *Peterson's Stress Concentration Factors*, John Wiley and Sons, New York, NY.
15. Lewandowski J.J., Lowhaphandu P. (2002) Effects of hydrostatic pressure on the flow and fracture of a bulk amorphous metal. *Philosophical Magazine A* **82**, 3427-3441.

16. Lewandowski J.J., Shazly M., Nouri A.S. (2006) Intrinsic and extrinsic toughening of metallic glasses. *Scripta Materialia* **54**, 337-341.
17. Lowhaphandu P., Montgomery S.L., Lewandowski J.J. (1999) Effects of superimposed hydrostatic pressure on flow and fracture of a Zr-Ti-Ni-Cu-Be bulk amorphous alloy. *Scripta Materialia* **41**, 19-24.
18. Wesseling P., Lowhaphandu P., Lewandowski J. (2003) Effects of superimposed pressure on flow and fracture of two bulk metallic glass. *Mat. Res. Soc. Symp Proc.* **754**, 275-279.
19. Shazly M., Prakash V., Lerch B. (2006) *High strain-rate compression of ice*, National Aeronautics and Space Administration, Cleveland, OH.
20. Bruck H.A., Rosakis A.J., Johnson W.L. (1996) The dynamic compressive behavior of Beryllium bearing bulk metallic glasses. *Journal of Materials Research* **11**, 503-511.
21. Yuan F., Prakash V., Lewandowski J.J. (2010) Shear yield and flow behavior of a zirconium-based bulk metallic glass. *Mechanics of Materials* **42**, 248-255.
22. Sunny G., Yuan F., Prakash V., Lewandowski J. (2008) Effect of high strain rates on peak stress in a Zr-based bulk metallic glass. *Journal of Applied Physics* **104**, 093522.

## Tables

	LM-1 (BMG)	Maraging steel	Tungsten carbide
Young's Modulus	96 GPa (elastic), 9.6 GPa (plastic)	210 GPa	675 GPa
Density	6000 kg/m <sup>3</sup>	7800 kg/m <sup>3</sup>	15700 kg/m <sup>3</sup>
Wave speed	4000 m/s	5190 m/s	6560 m/s
Impedance	24 x 10 <sup>6</sup> kg/(m <sup>2</sup> s)	40.5 x 10 <sup>6</sup> kg/(m <sup>2</sup> s)	103 x 10 <sup>6</sup> kg/(m <sup>2</sup> s)
Yield strength	2.0 GPa	2.5 GPa	10 GPa
Poisson's ratio	0.33	0.30	0.20

Table 3.1 – Selected material properties of the BMG, maraging steel, and tungsten carbide used in the simulations

Exp.	<i>L/D</i>	Striker bar velocity (m/s)	Observed behavior
IN3	1	15.1	2 shear planes, self-sharpening (40°, 50°)
IN4	1	12.3	2 shear planes, self-sharpening behavior
IN5	2	11.5	2 shear planes (40°, 70°)
IN6	2	11.0	2 shear planes, failure at 90° (outlier)
IN7	1	9.2	1 shear plane
IN8	2	10.5	1 shear plane
IN9	2	13	1 shear plane
IN10	0.5	6.7	1 shear plane
IN11	0.5	8.8	2 shear planes, 30°, intersect specimen-insert interfaces
IN12	0.5	9.5	Inconclusive (grease)

Table 3.2 – List of experiments conducted with tapered inserts on as-cast LM-1. Failure initiates in gage section and shear planes are at 50° angles unless otherwise noted.

Experiment	Striker velocity (m/s)	Peak strain	Peak stress (MPa)	Specimen failed?	Strain gage separated?
SG001	7.9	1.41%	1350	Yes	Yes
SG002	8.0	1.61%	1550	Yes	Yes
SG003	7.2	1.55%	1490	No	No
SG004	8.8	1.89%	1810	Yes	No
SG005	10.3	1.83%	1750	Yes	No

Table 3.3 – List of experiments conducted with specimens with  $L/D = 2.0$

Experiment	Striker velocity (m/s)	Peak strain	Peak stress (MPa)	Specimen failed?	Strain gage separated?
SG006	8.2	1.50%	1440	Yes	Yes
SG007	7.3	0.92%	880	No	No
SG008	10.2	1.97%	1890	Yes	No
SG009	7.8	1.41%	1340	Yes	Yes
SG010	9.4	0.91%	870	Yes	Yes
SG011	8.5	1.95%	1870	Yes	No
SG012	9.0	1.70%	1630	Yes	No
SG013	8.8	2.2%	2000*	Yes	No

Table 3.4 – List of experiments conducted on specimens with  $L/D = 1.0$ . In experiment SG13, the specimen was assumed to yield prior to failure.

Experiment group (Ref)	Average stress (MPa)	Standard deviation (MPa)
L/D = 2, conventional inserts (present study)	1780	90
L/D = 1, conventional inserts (present study)	1690	130
L/D = 0.5, conventional inserts (present study)	1550	110
L/D = 2.0, new inserts with strain gage (present study)	1780	40
L/D = 1.0, new inserts with strain gage (present study)	1850	150
L/D = 1.5-2.0 [4]	1850	90
L/D = 0.7-1.0 with strain gage [4]	1960	110

Table 3.5 – Summary table detailing average stresses and standard deviations for the experiments shown in Figure 3.29.

**Figures**



Figure 3.1 – Additional specimen geometries considered in testing low-ductility materials: (a) Conical inserts, (b) Dogbone compression specimen

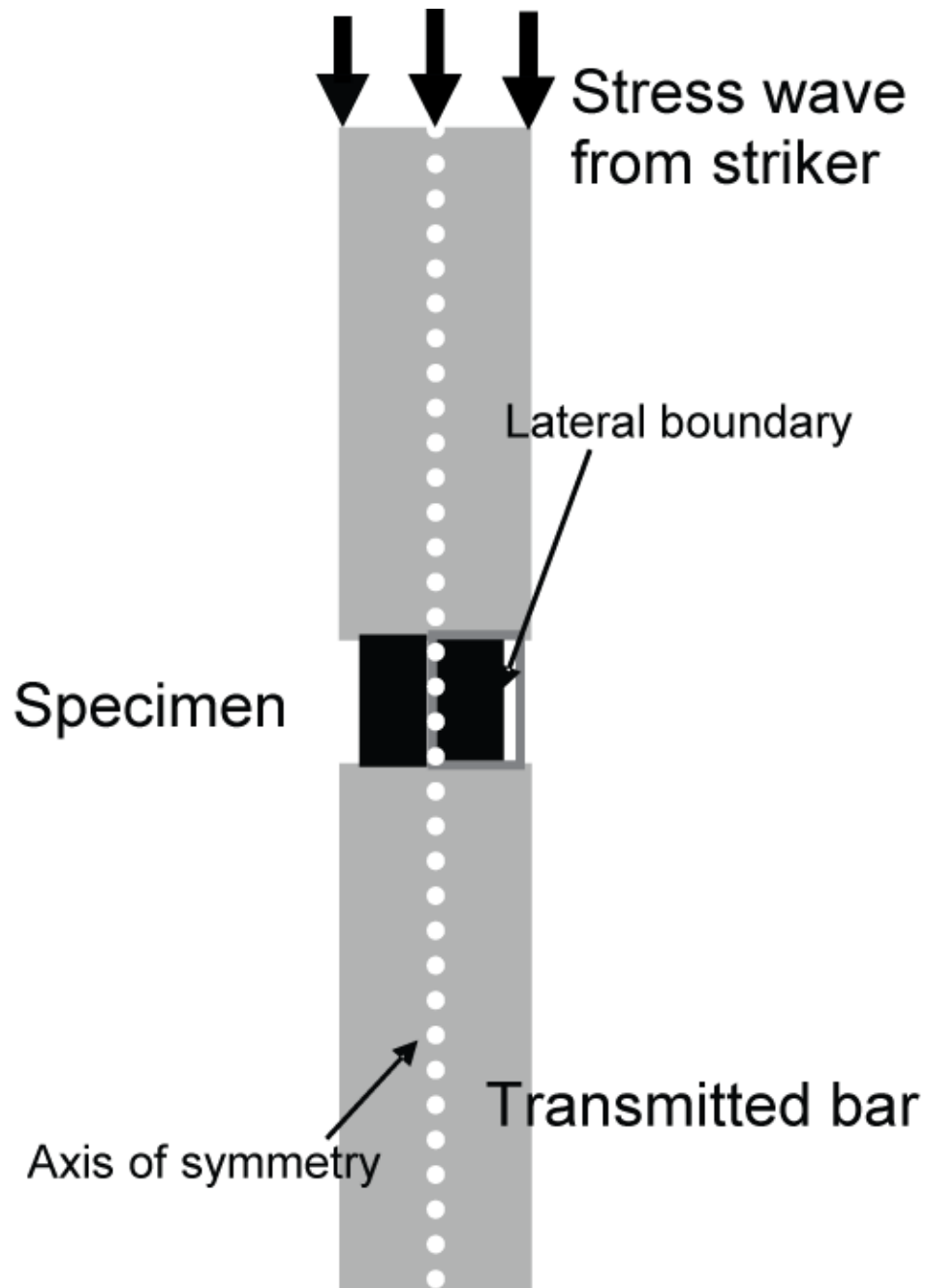


Figure 3.2 – Schematic of finite element simulation setup to examine stress concentration effects

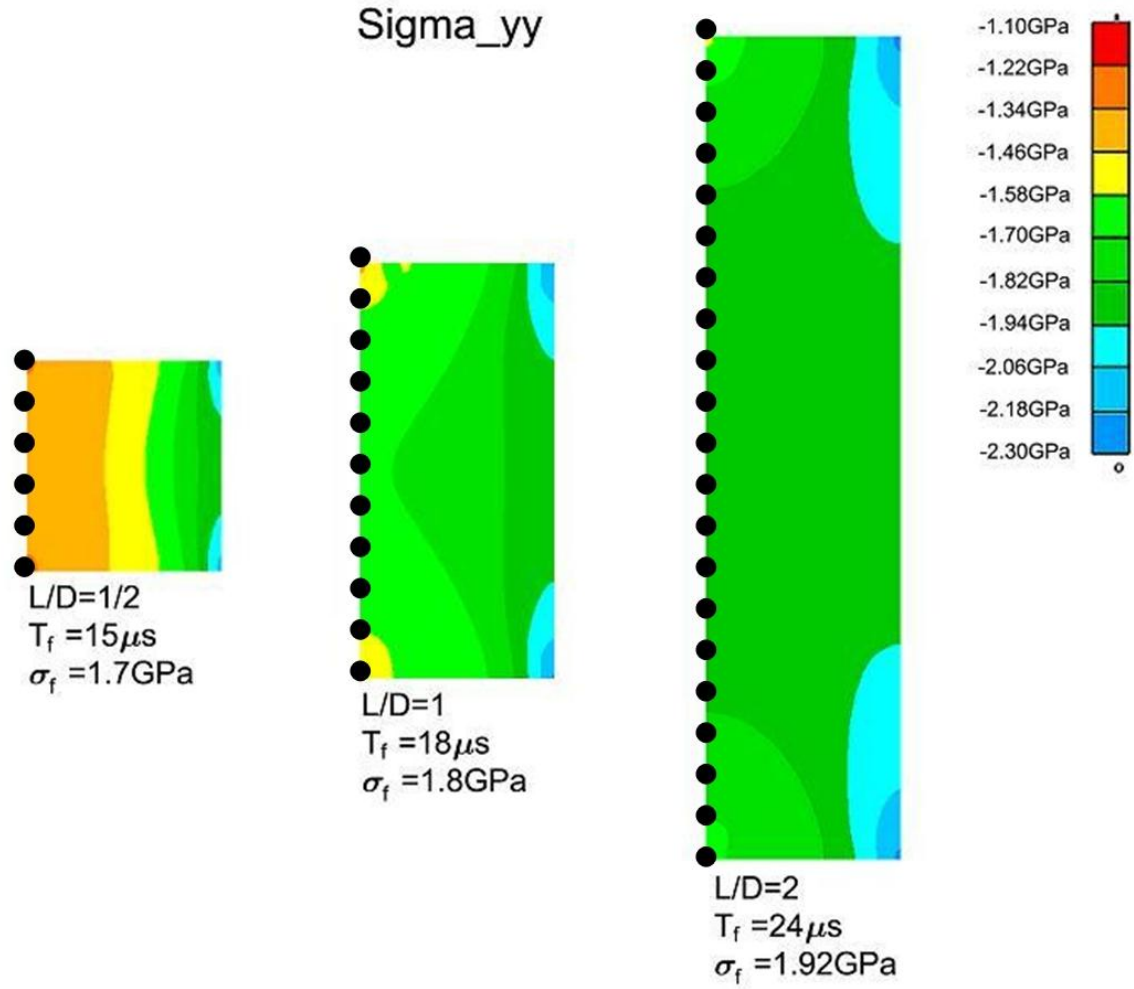


Figure 3.3: Axial stress contours for finite element simulations of LM-1 with cylindrical inserts for L/D ratios of (left) 0.5, (middle) 1.0, and (right) 2.0

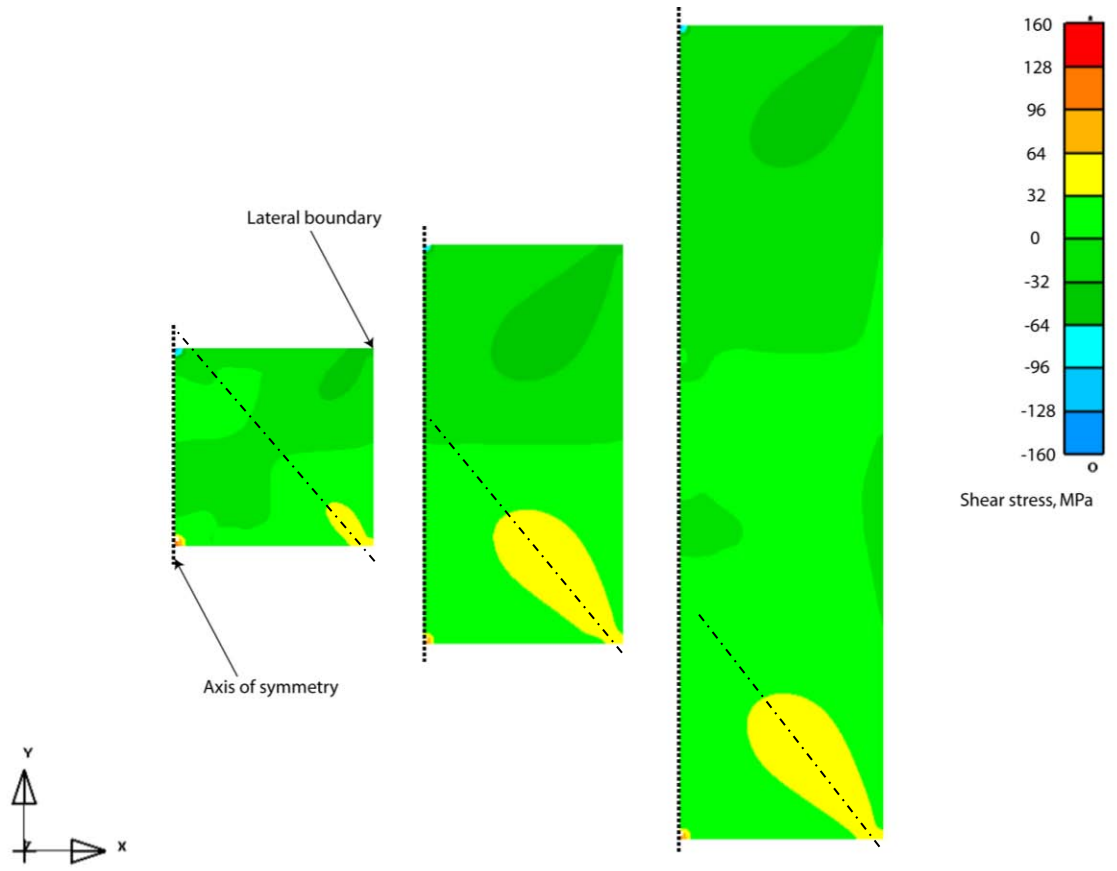


Figure 3.4: Shear stress contours for finite element simulations of LM-1 with cylindrical inserts for L/D ratios of (left) 0.5, (middle) 1.0, and (right) 2.0

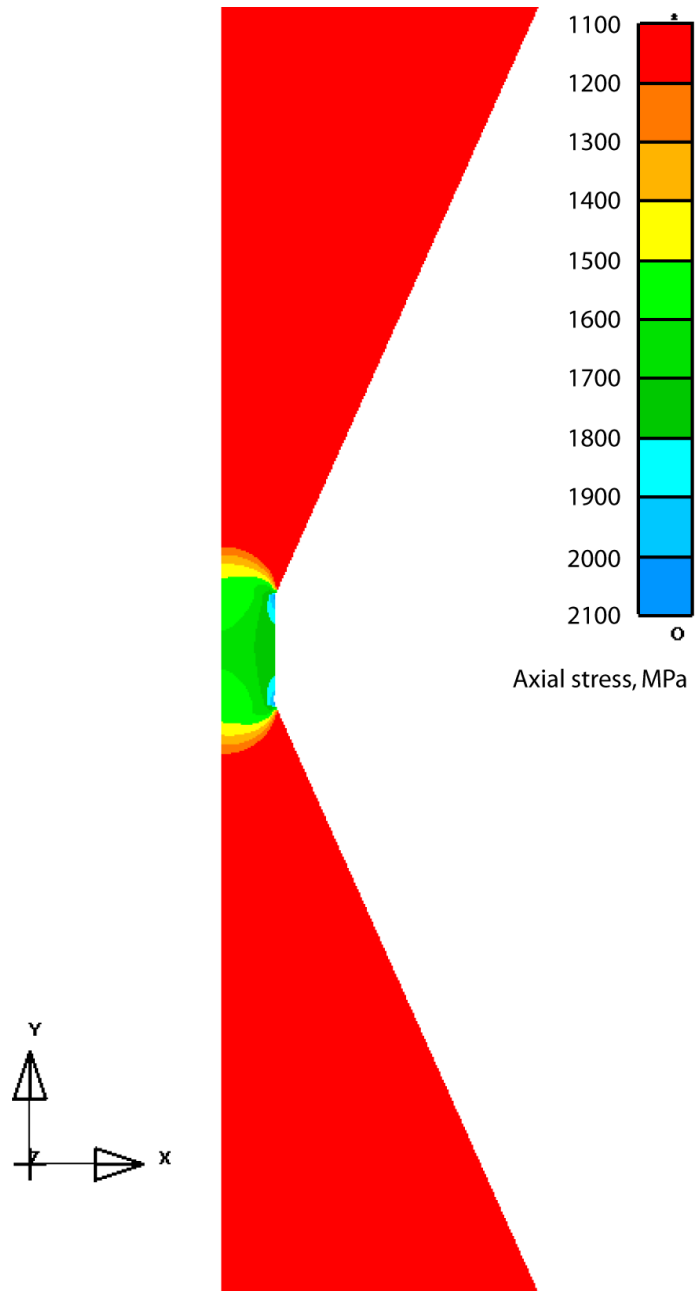


Figure 3.5: Axial stress contours for simulation with conical inserts

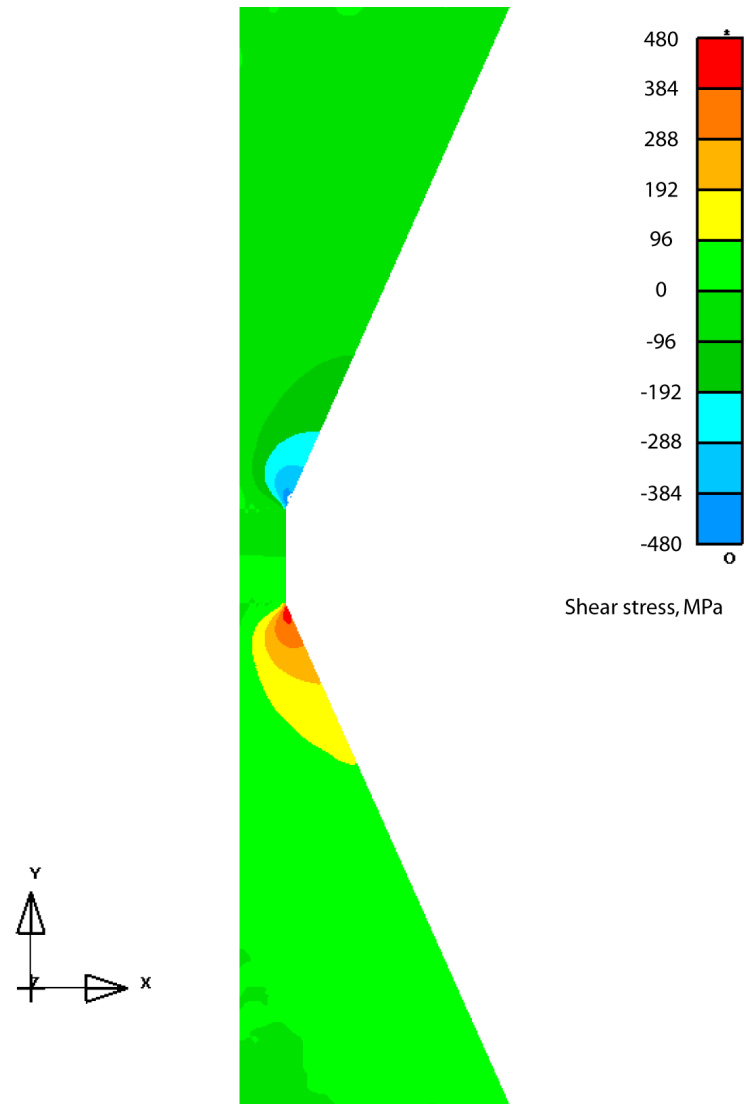


Figure 3.6: Shear stress contours for simulation with conical inserts

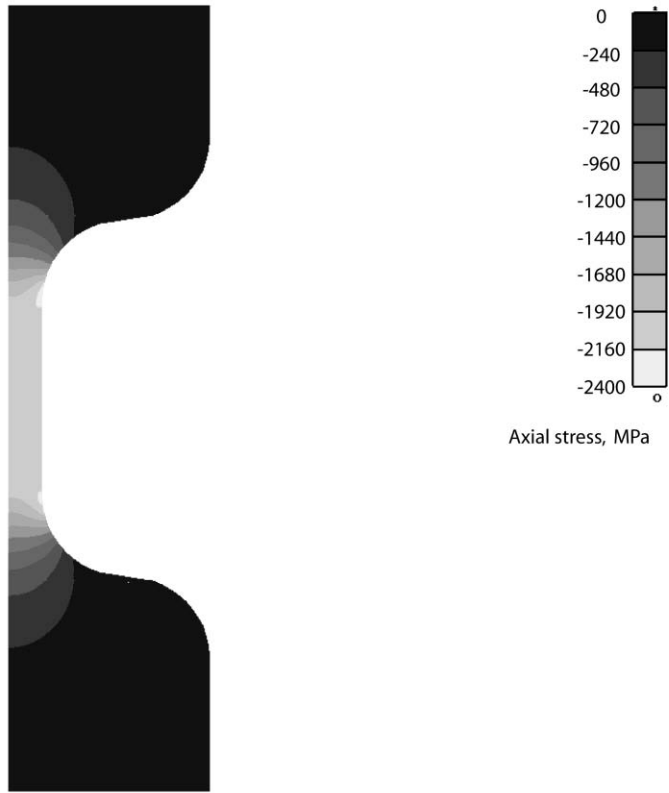


Figure 3.7: Axial stress distribution of dogbone specimen

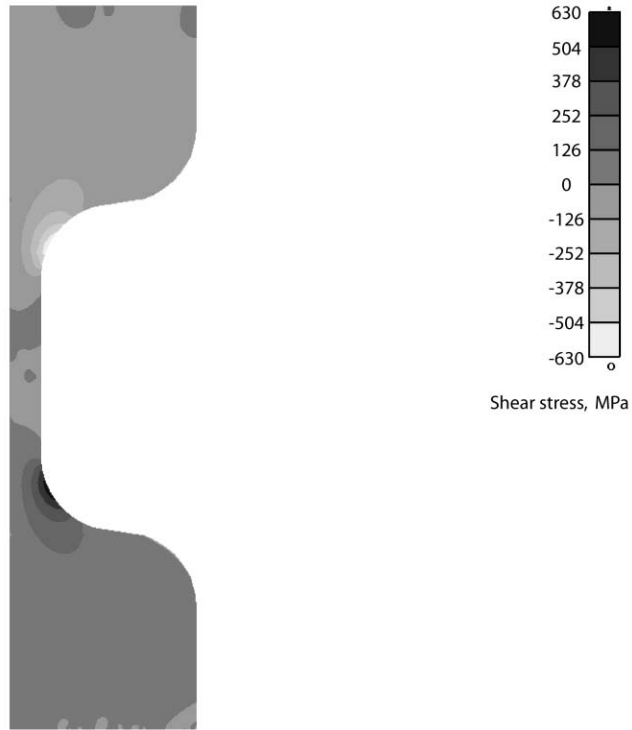
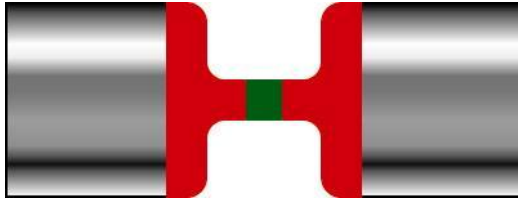


Figure 3.8: Shear stress distribution of dogbone specimen



(a)



(b)

Figure 3.9 – (a) Schematic of new insert design, (b) Actual design

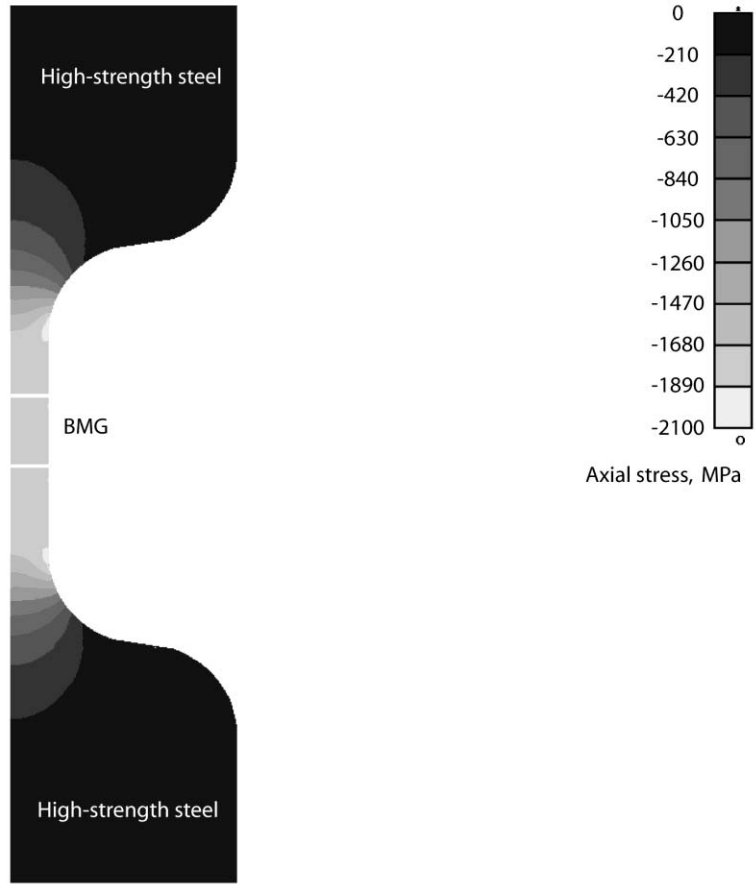


Figure 3.10 – Axial stress distribution for simulation with maraging steel inserts

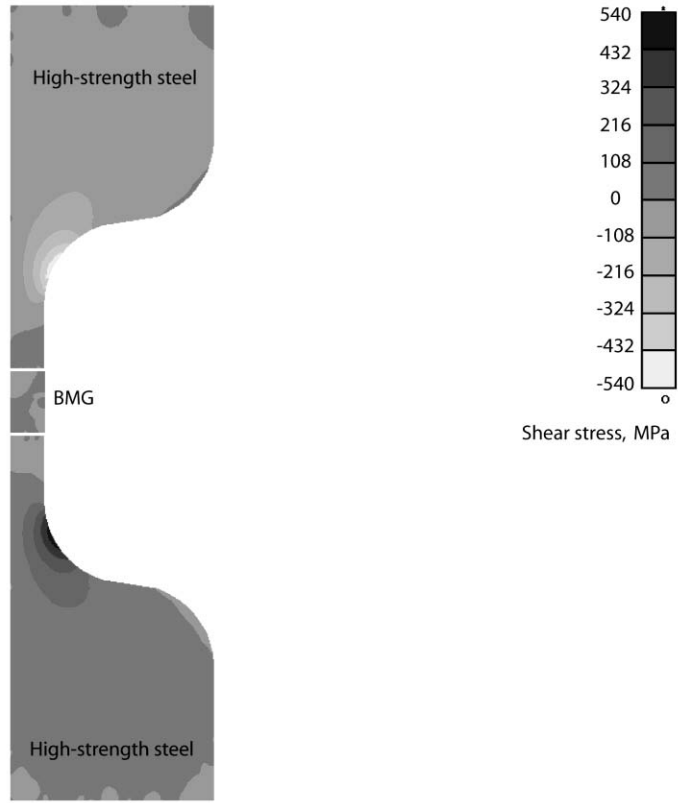


Figure 3.11 – Shear stress distribution for simulation with maraging steel inserts

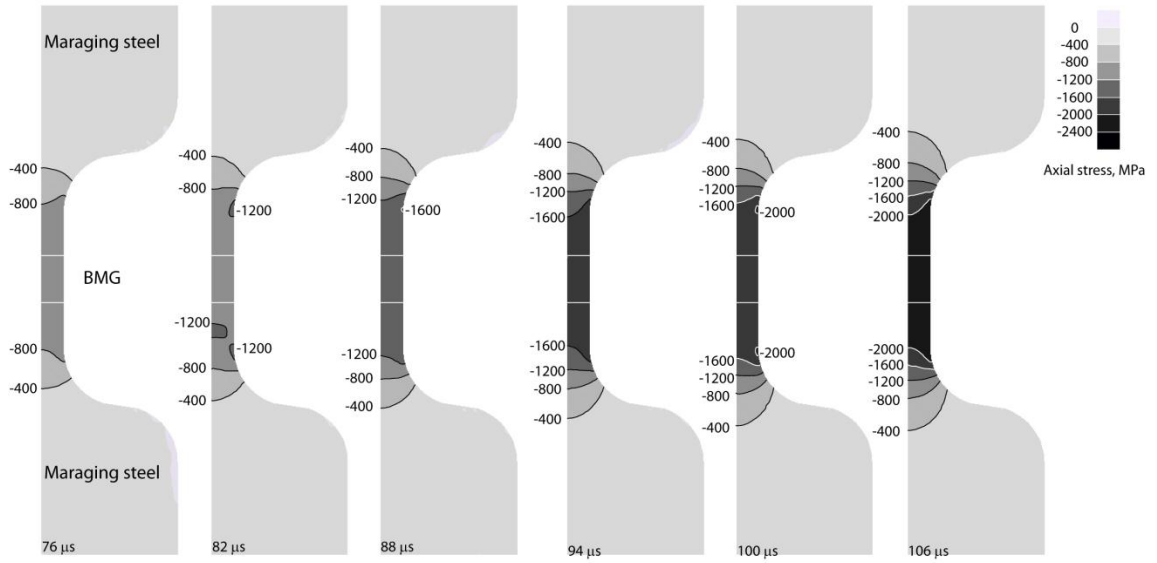


Figure 3.12 – Finite Element Simulation illustrating equilibrium of the specimen throughout the large majority of the experiment

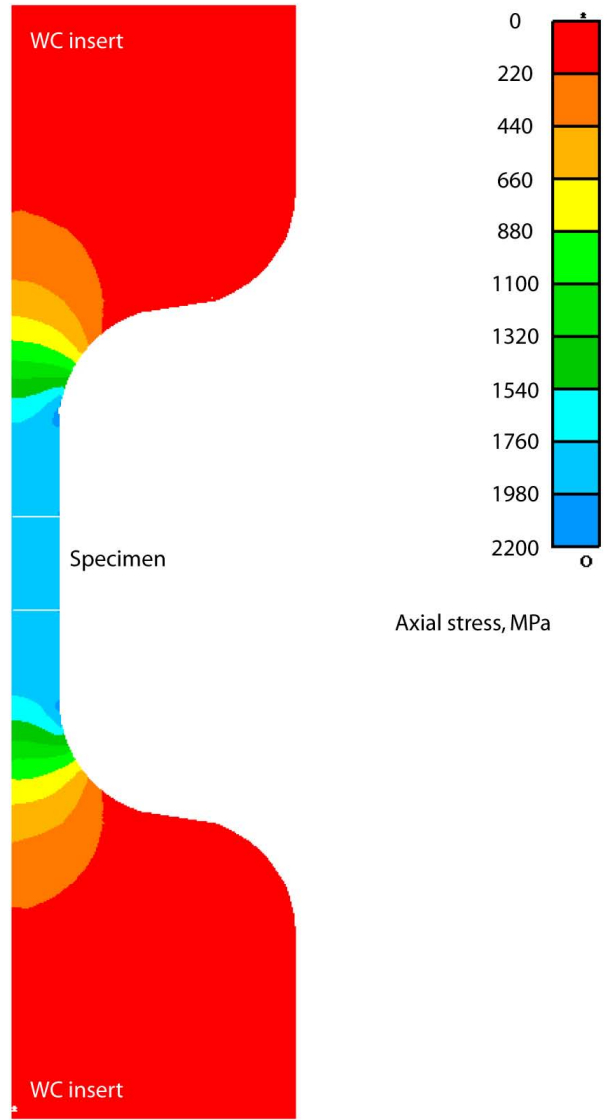


Figure 3.13 – Axial stress contours for simulation with tungsten carbide inserts

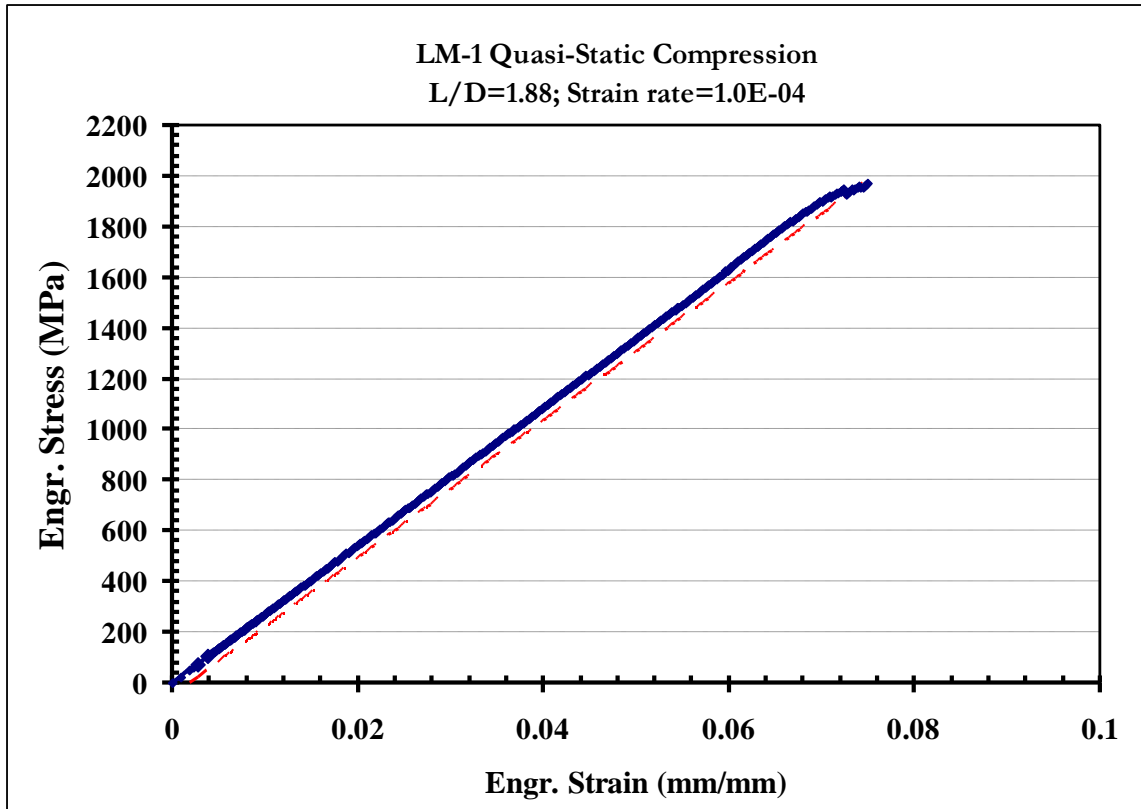


Figure 3.14 – Stress-strain curve under quasi-static compression with new inserts

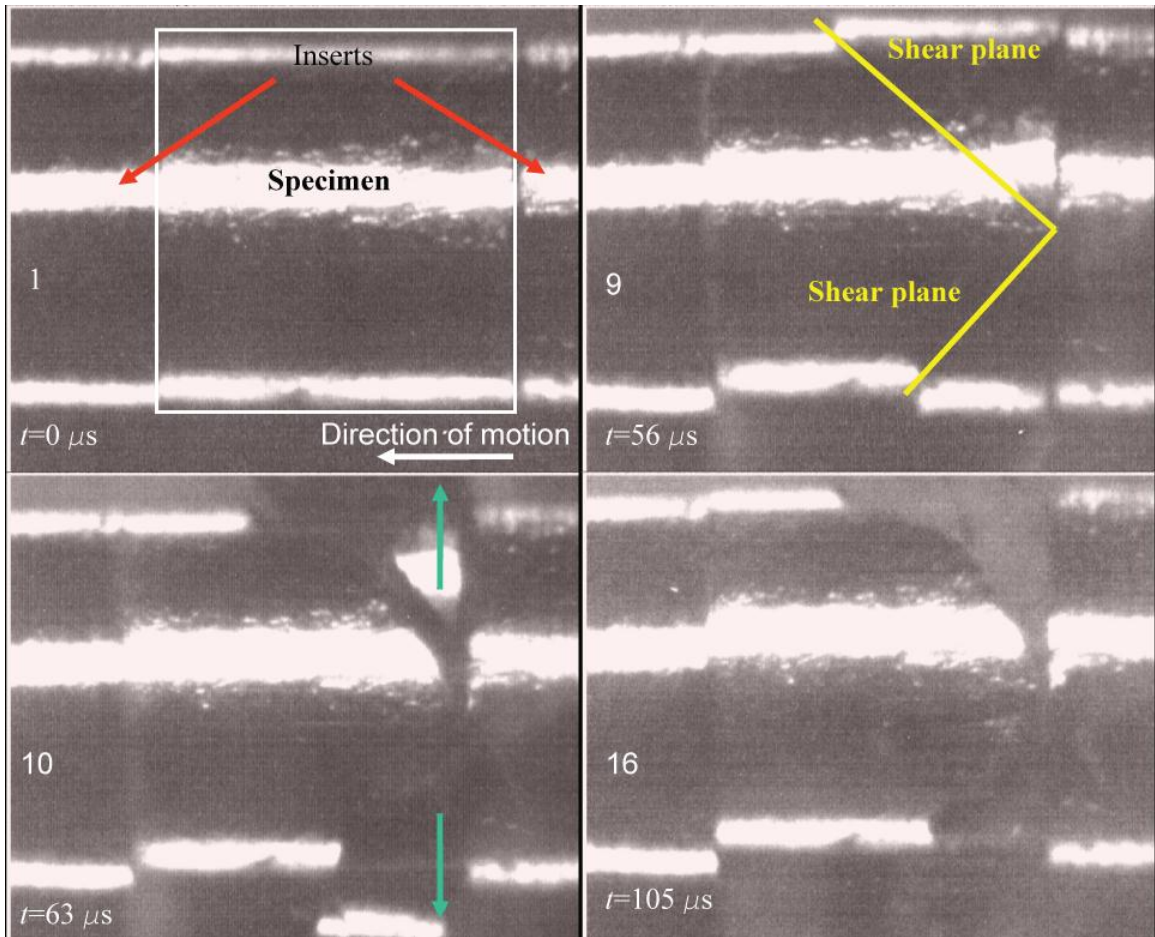


Figure 3.15 – High-speed camera images of as-cast LM-1 ( $L/D = 1.0$ ) with new tapered inserts.

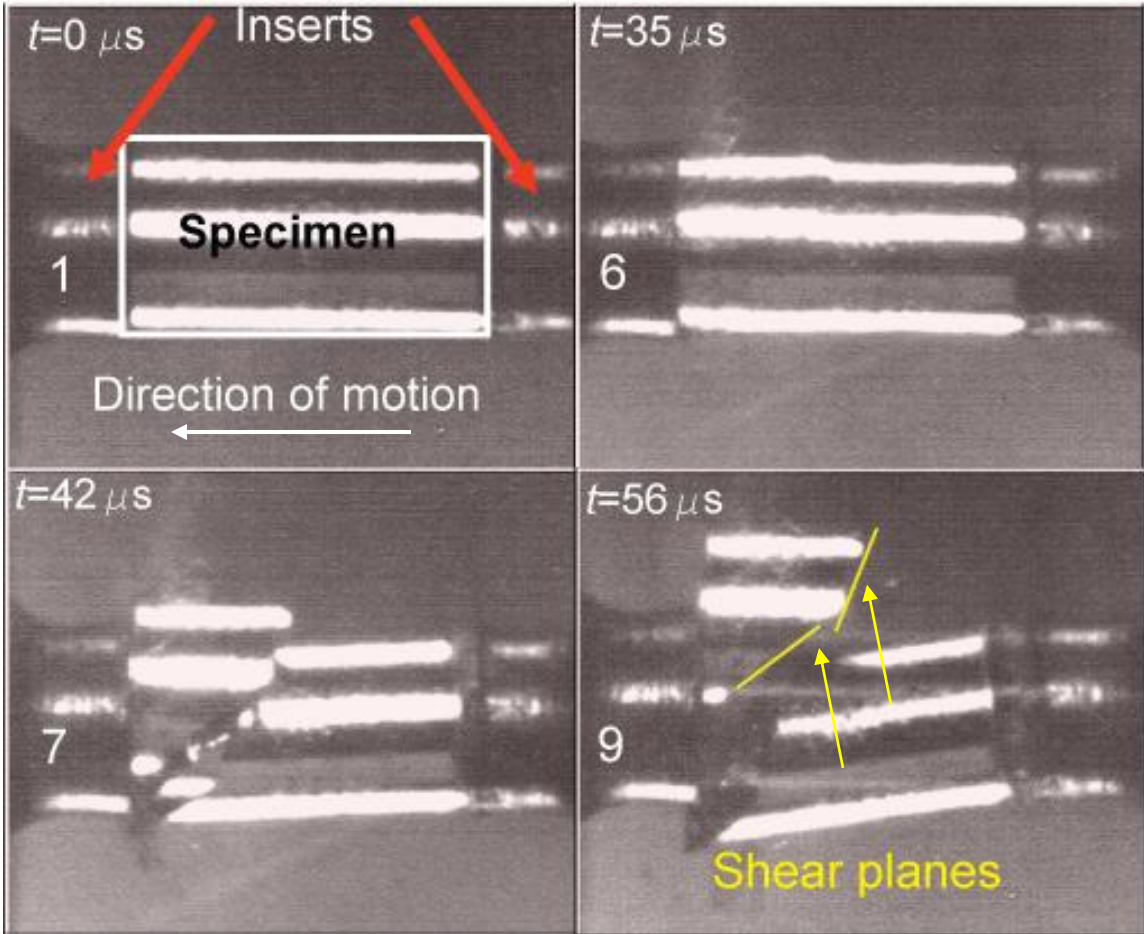


Figure 3.16 – High-speed camera images of as-cast LM-1 ( $L/D = 2.0$ ) with new tapered inserts.

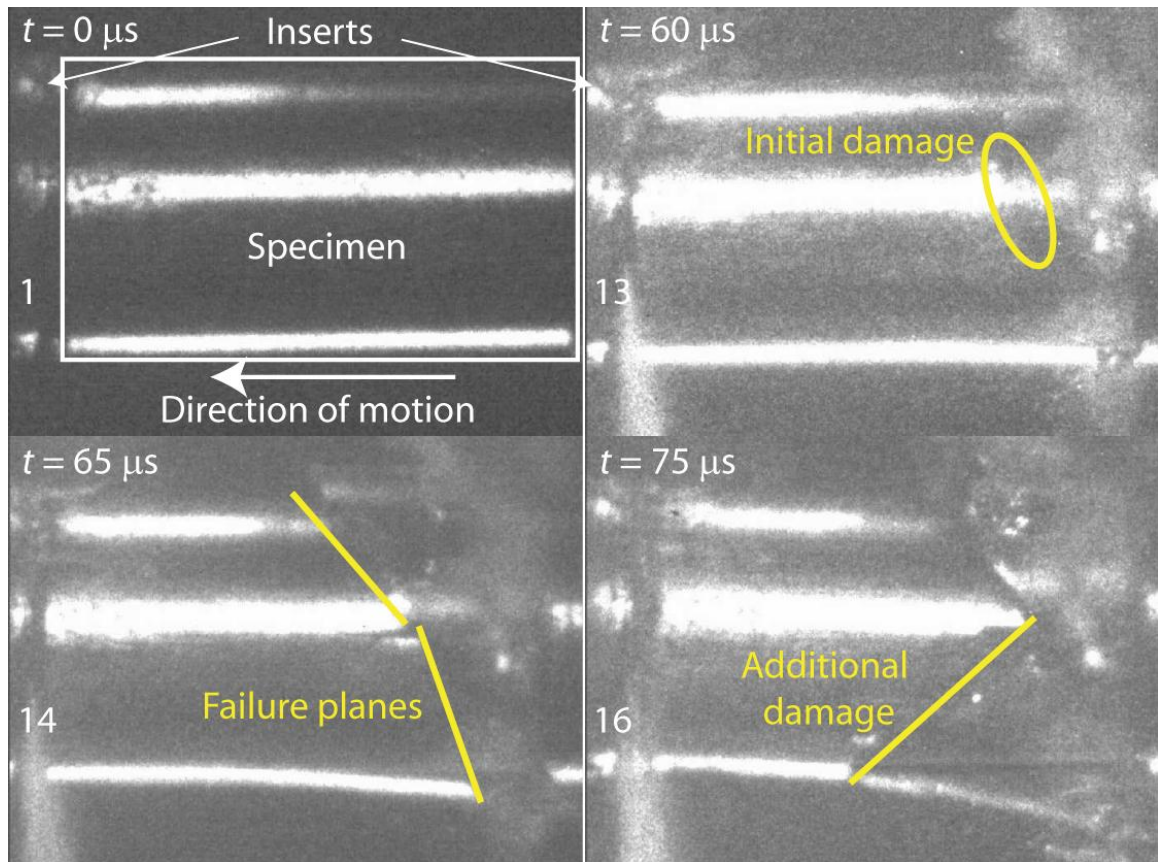


Figure 3.17 – High-speed camera images of annealed LM-1 ( $L/D = 2.0$ ) with the tapered inserts.

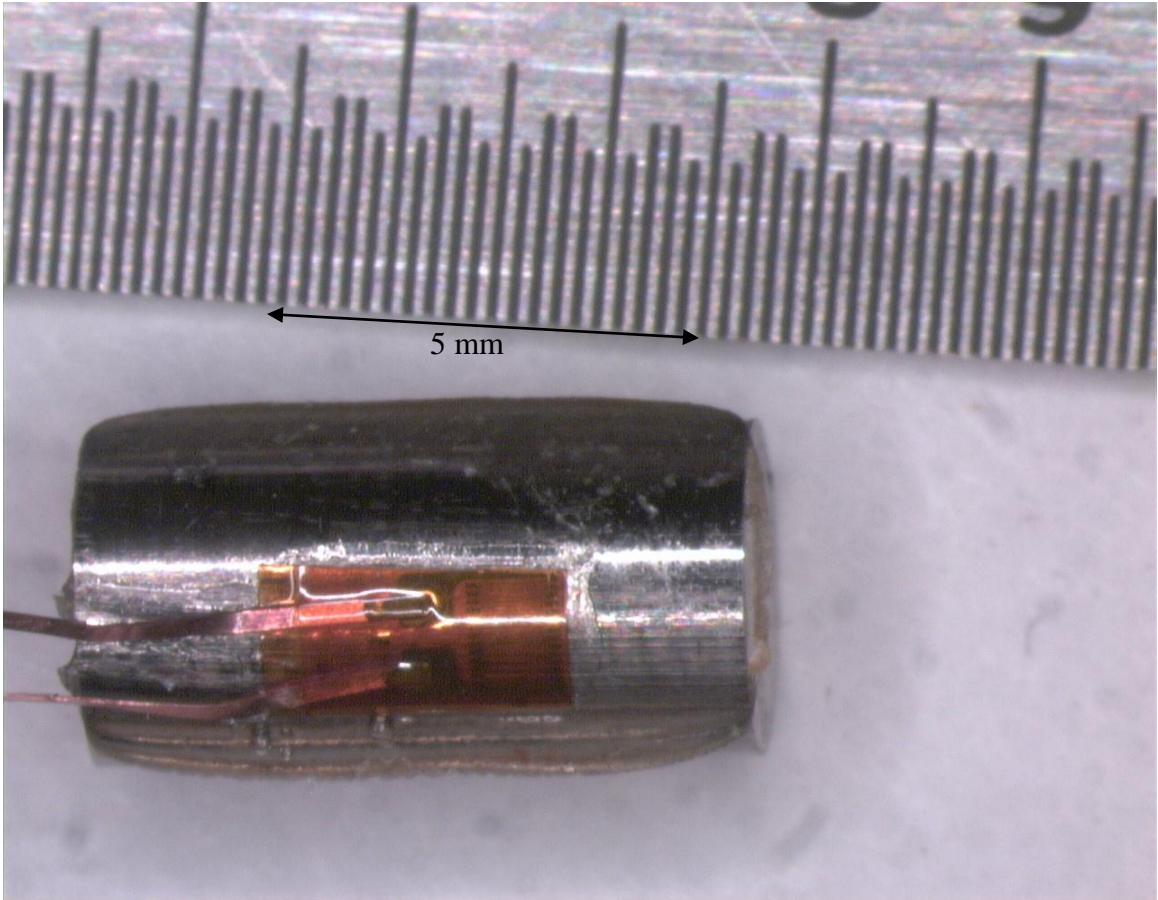


Figure 3.18 – Specimen with strain gage attached, prior to removal of epoxy and detachment of leads. The barreled appearance of the specimen is due to the epoxy on the specimen.

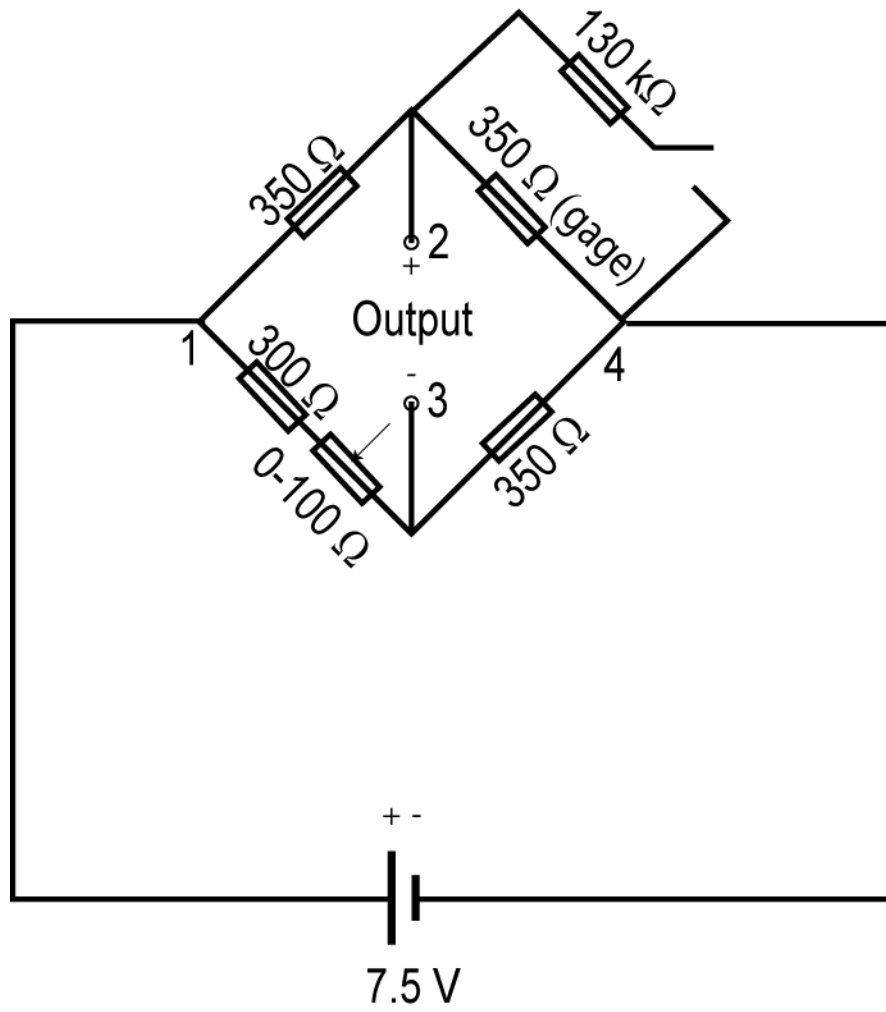


Figure 3.19 – Wheatstone bridge employed for the strain gage experiments in this study

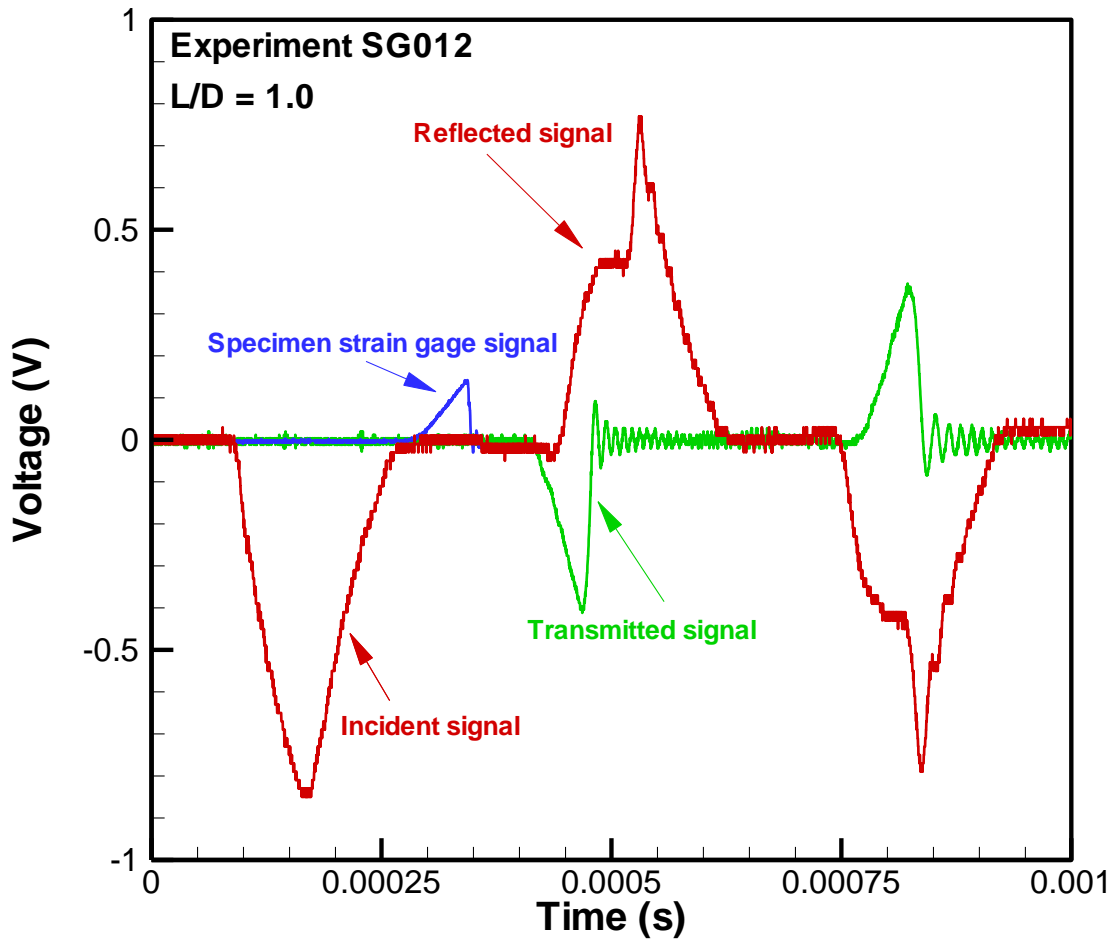


Figure 3.20 – Strain history signals from the strain gages mounted on the incident bar, transmitted bar, and specimen.

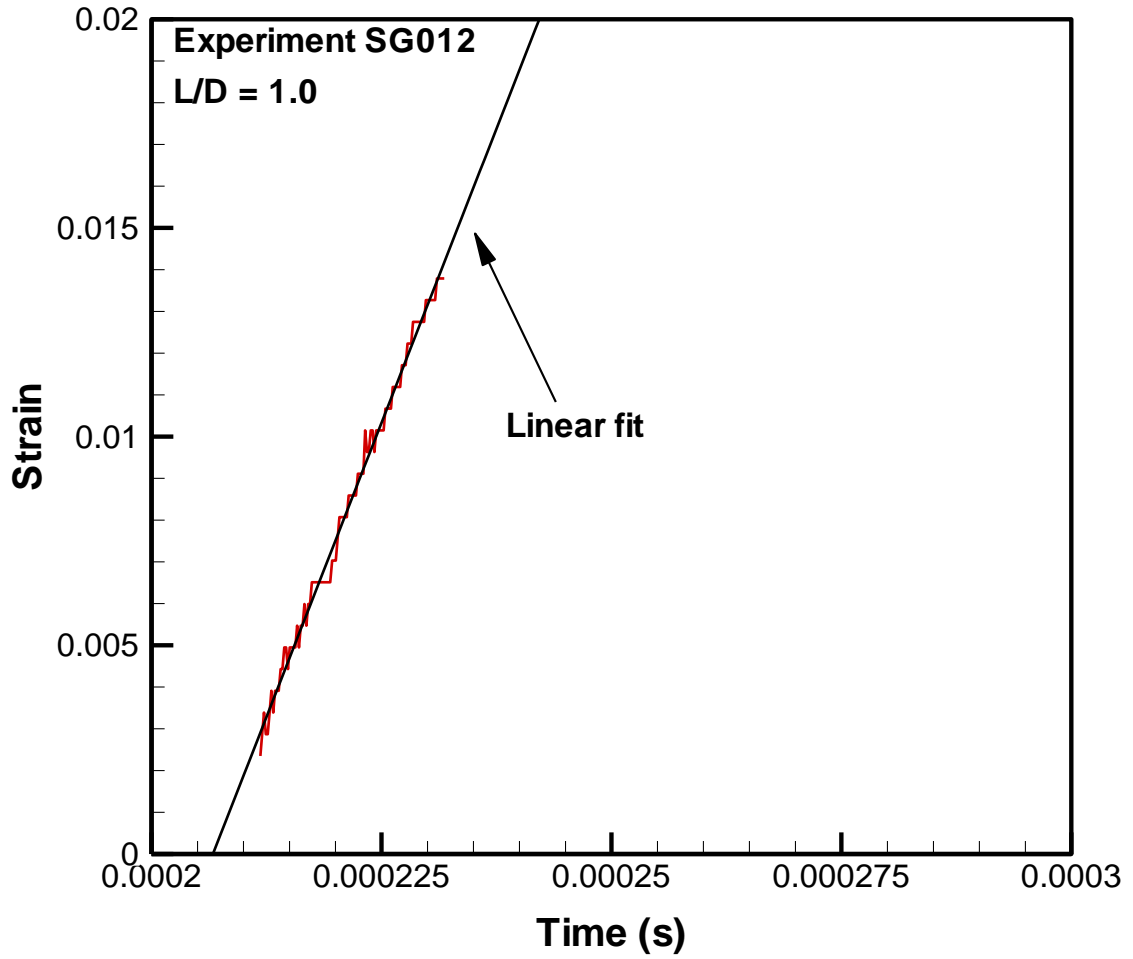


Figure 3.21 – Selected strain history as determined from the strain gage in Figure 3.20.

Based on the linear fit, the specimen is deforming under constant strain-rate (550/s) conditions.

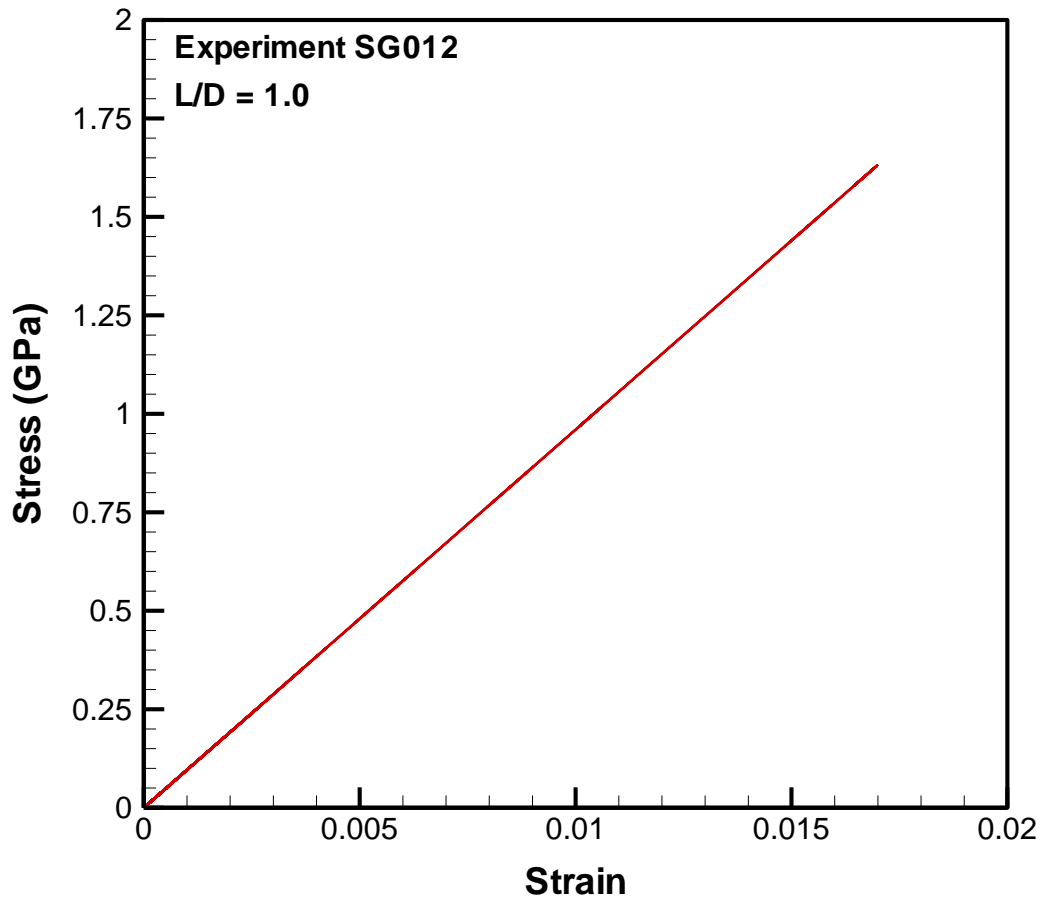


Figure 3.22 – Stress-strain curve constructed from the specimen strain gage signal in Figure 3.20.

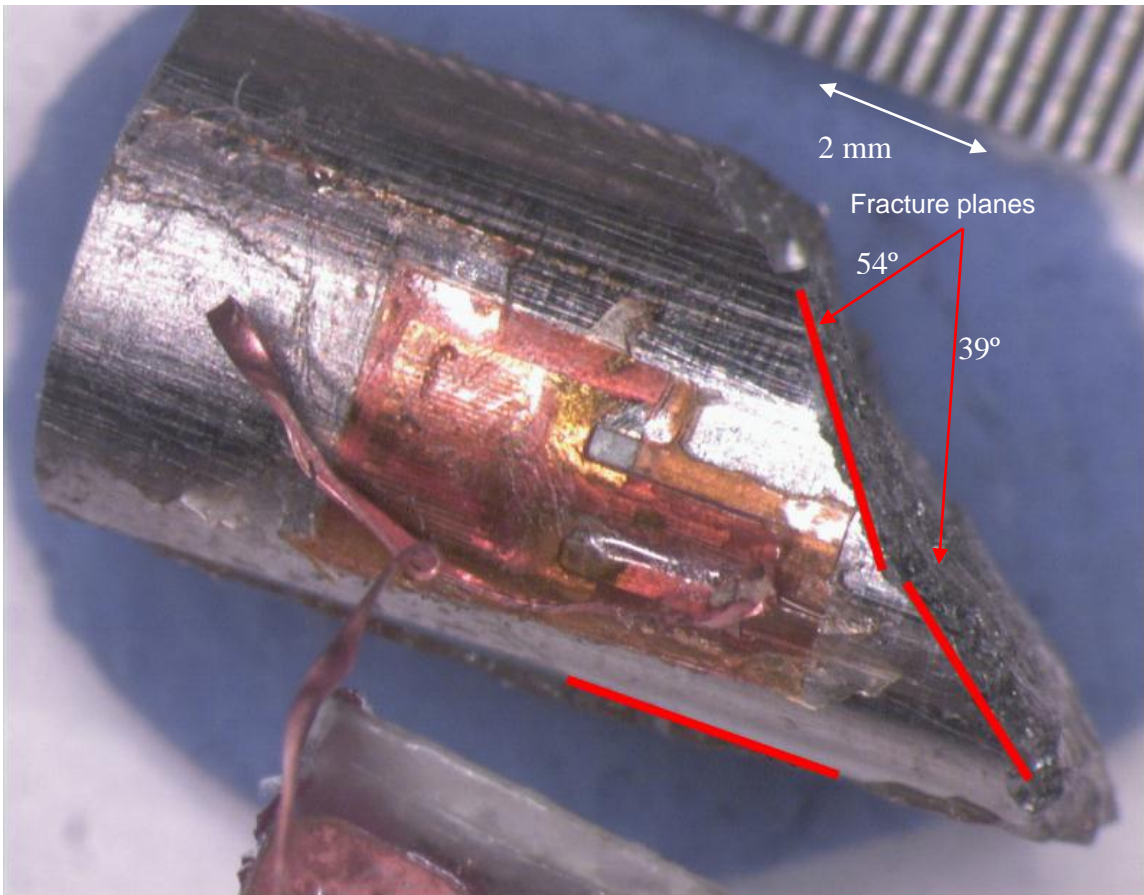


Figure 3.23 – Optical microscopy of as-cast specimen,  $L/D = 2.0$ , after testing. The strain gage is still adhered to the sample surface, and the fracture angles are noted here.

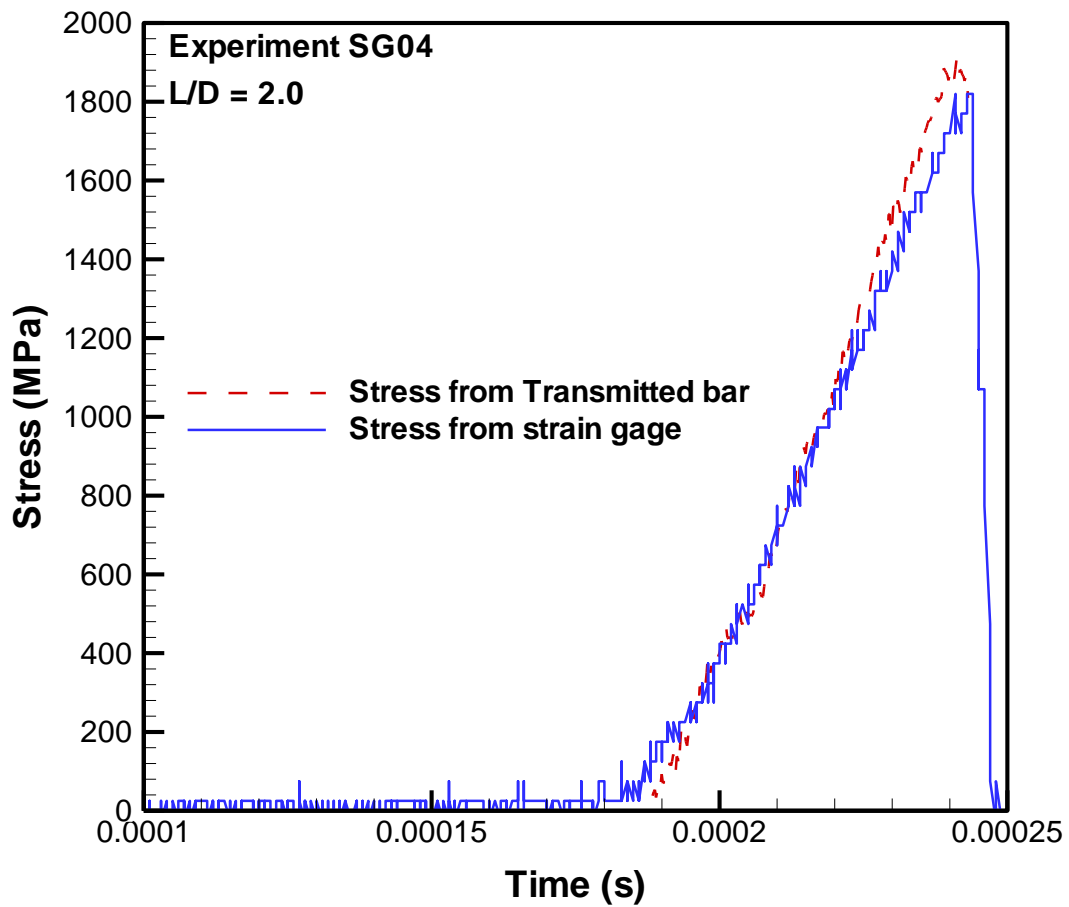


Figure 3.24 – Comparison of stress signals as determined from the transmitted bar and specimen strain gage

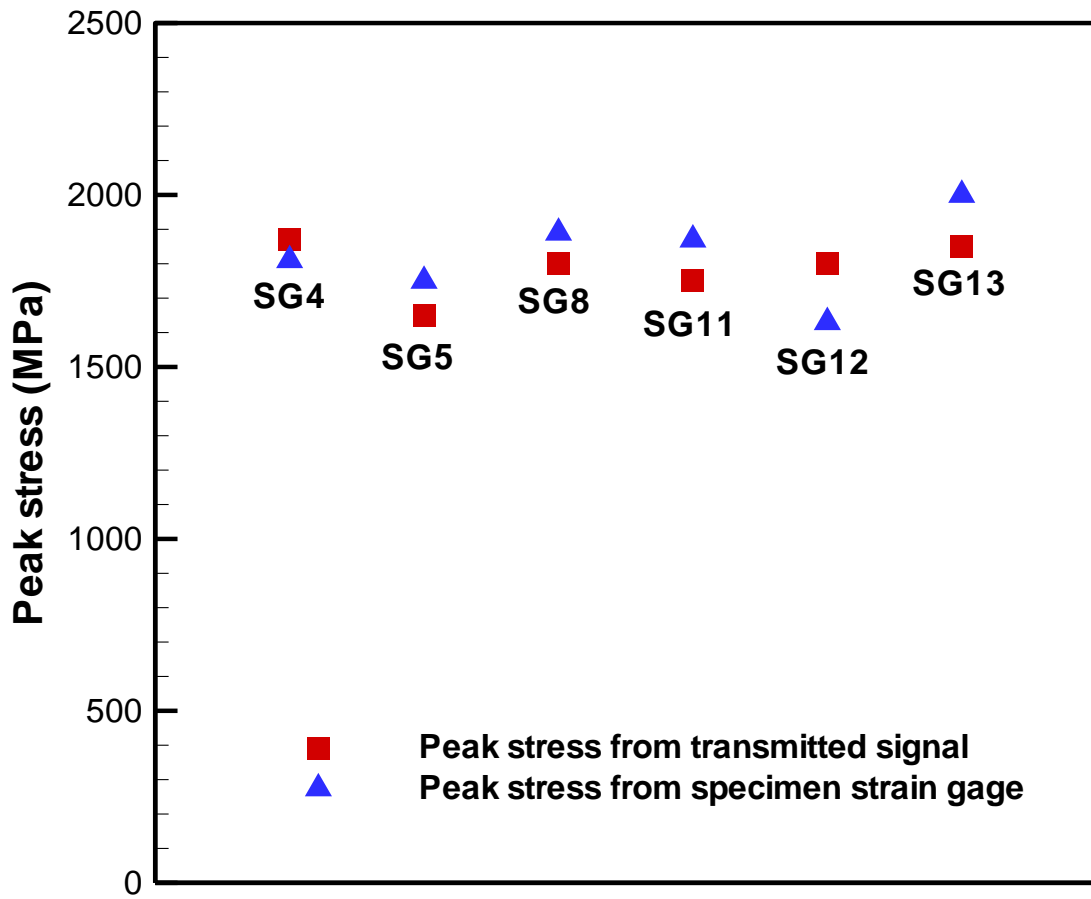


Figure 3.25 – Peak stresses as determined from transmitted and specimen strain gage signals

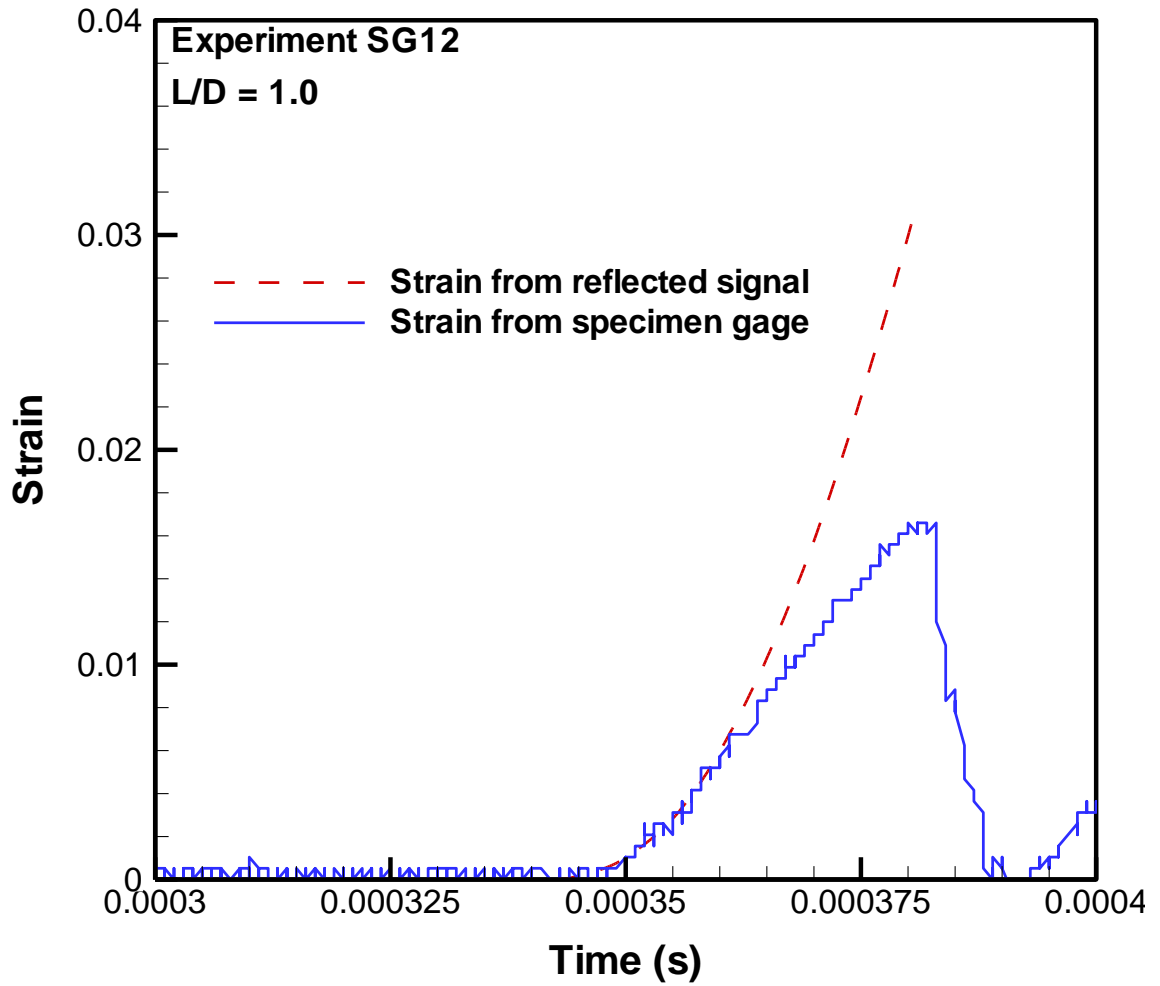


Figure 3.26 – Strain vs. time plots as determined from the reflected signal and from the specimen strain gage. The strain-rate calculated thusly (from the slope of the curve) is much higher than the actual strain-rate experienced by the specimen.

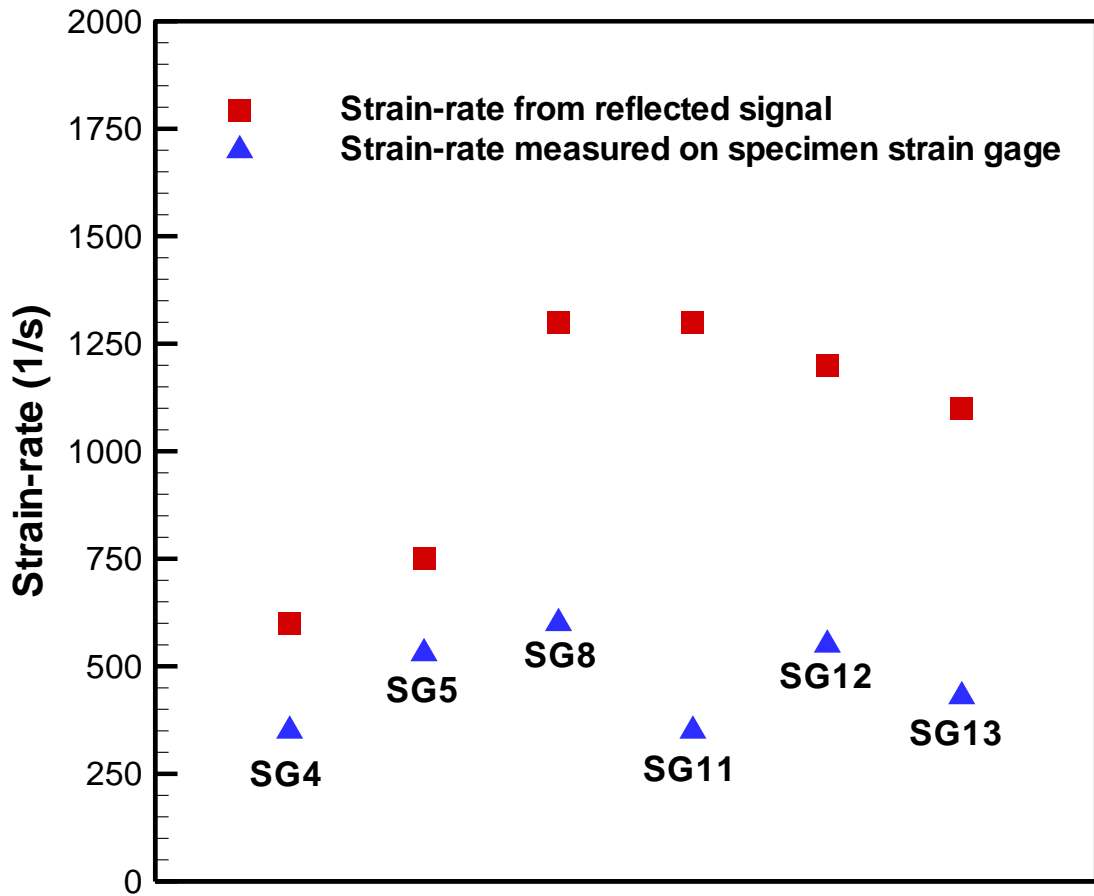


Figure 3.27 – Peak strain-rates as measured from the reflected signal compared to constant strain-rates as measured from the specimen strain gage

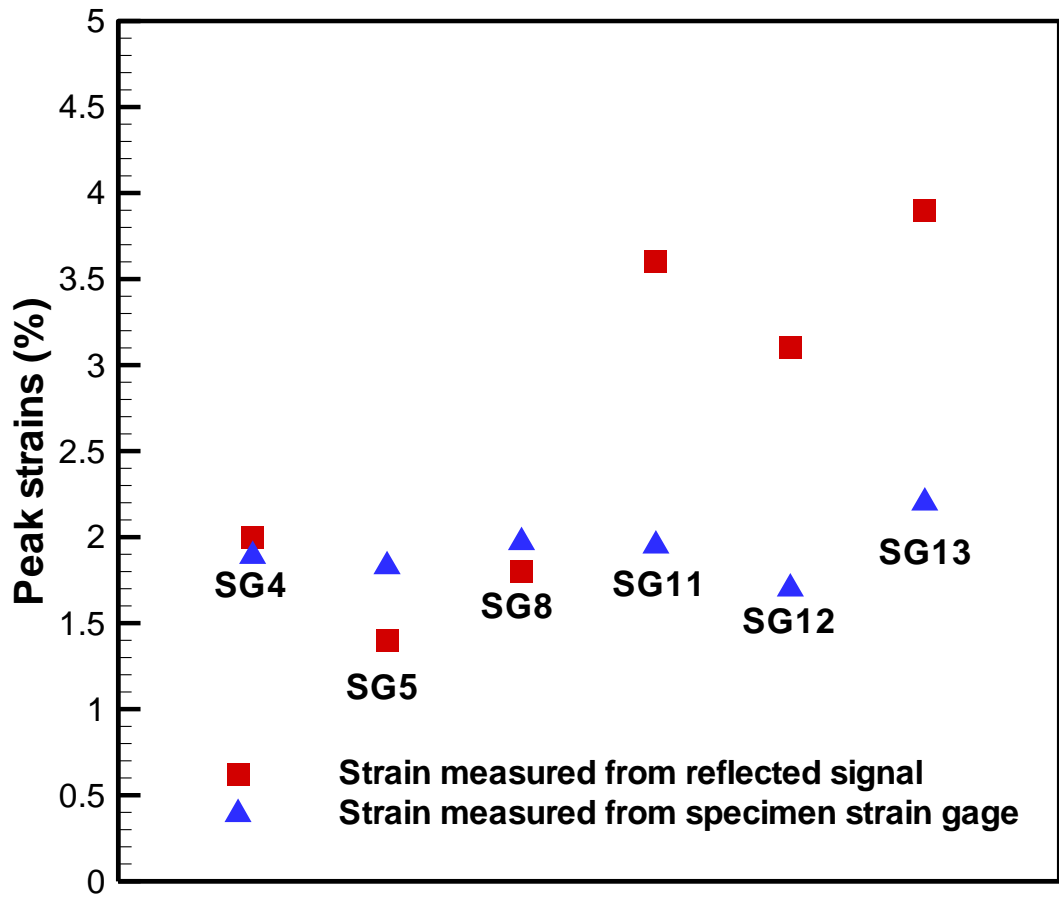


Figure 3.28 – Peak strains as measured from the reflected signal and specimen strain gage

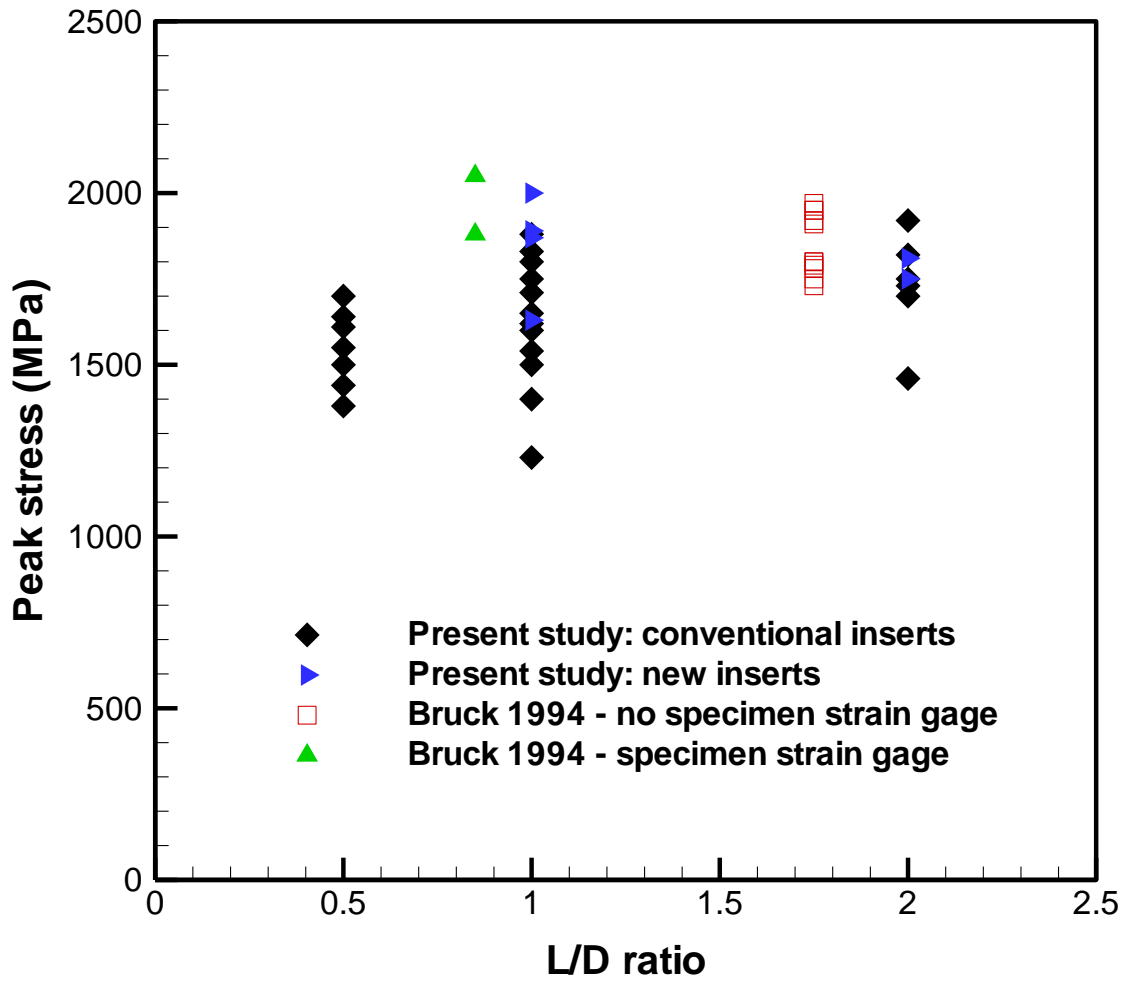


Figure 3.29 – Peak stress achieved by as-cast LM-1 specimens with both conventional and new inserts, with outlying data circled. Data from Bruck [20] are also included.

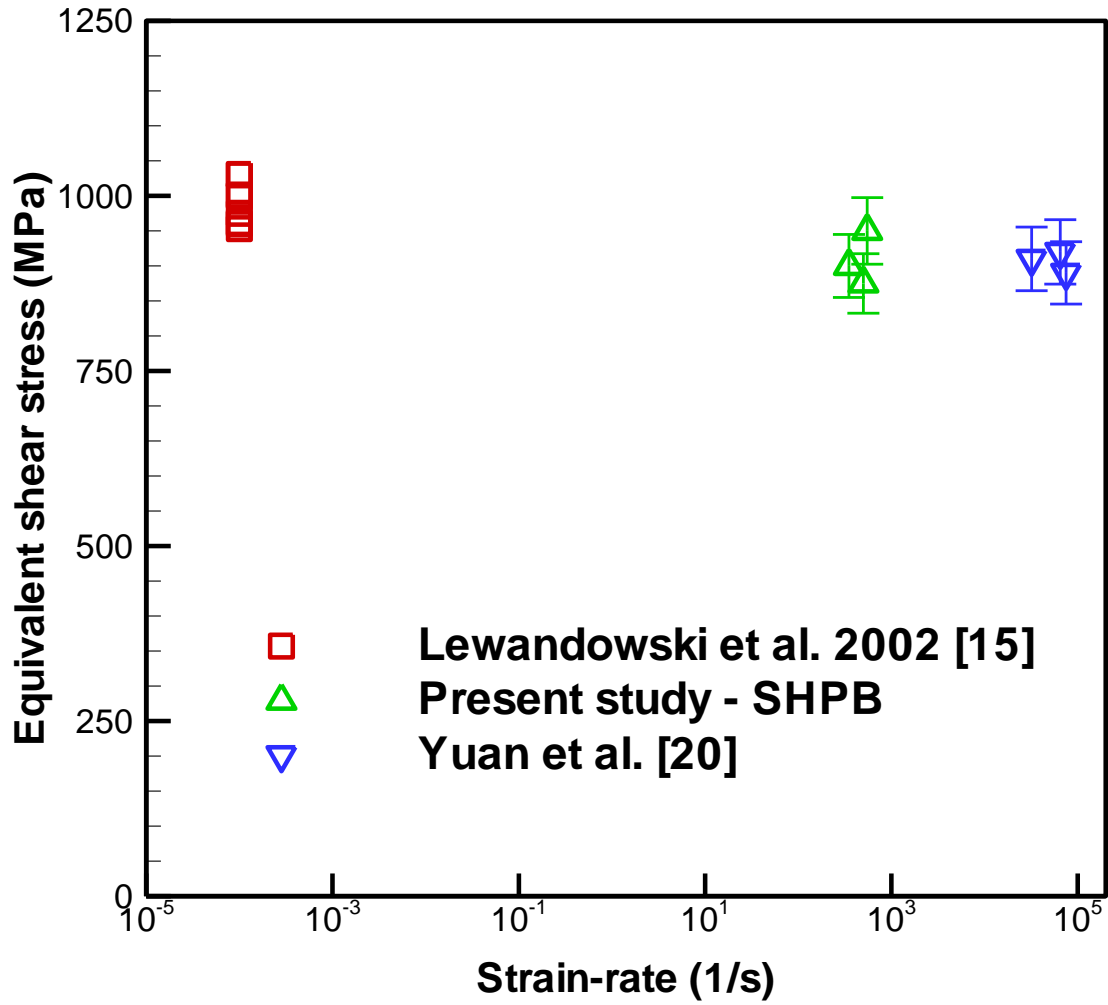


Figure 3.30 – Strain-rate sensitivity of LM-1 from a strain-rate of  $10^{-4}$ /s –  $10^5$ /s

## **Chapter 4: High Loading-Rate Fracture of LM-1**

### **4.1 Overview**

In recent years, bulk metallic glasses (BMGs) have been of significant scientific and technical interest due to their amorphous structure as well as a range of desirable mechanical properties, such as near-theoretical yield strength, large elastic strain, and high hardness. One specific BMG, LM-1, ( $Zr_{41.25}Ti_{13.75}Cu_{12.5}Ni_{10}Be_{22.5}$ , Liquidmetal Inc.), because of its low critical cooling rate (1 K/s) and large critical thickness (>10 mm), is an ideal candidate for bulk dynamic fracture testing [1].

In this work, the dynamic response of notched fully amorphous LM-1 is investigated to better understand fracture initiation and propagation in notched LM-1 specimens under high loading-rates. A number of studies have investigated the mechanical behavior of fatigue-precracked LM-1 specimens under quasi-static [2-9] and dynamic conditions [10, 11], and similar studies have been conducted on notched specimens under quasi-static conditions [2, 4-6, 12]. Details of these previous studies are provided in Section 4.2. Details of the experiments are provided in Section 4.3, and the wave propagation equations needed to interpret the data are derived in Section 4.4. The results of the experiments are provided in Section 4.5, and the implications of these results are discussed in Section 4.6.

### **4.2 Background and Motivation**

A number of studies have been performed on the fracture toughness of BMGs, and the work that has been conducted has primarily focused on Zr-based BMGs (specifically LM-1), because of their excellent glass forming ability. The low critical cooling rates (e.g. 1 K/s) allow for fully amorphous specimens in excess of 1 mm in thickness, and such sample sizes are necessary to ensure plane-strain conditions during the experiment for metallic glasses that exhibit high fracture toughness. A number of studies have focused on the fracture toughness of fatigue-precracked specimens under both low (e.g. 1 MPa m<sup>1/2</sup>/s) [2-7] and high (e.g. 10<sup>6</sup> MPa m<sup>1/2</sup>/s) [10, 11] loading-rates, while a smaller number of studies have focused on the fracture toughness of notched specimens under quasi-static loading [2, 4-6]. Work conducted by Lewandowski et al. [13] has indicated that fracture energy is highly dependent on the ratio of the shear modulus to the bulk modulus ( $\mu/B$ ); when this value is below 0.4, the fracture energy approaches 100 kJ/mm<sup>2</sup>, whereas above this value, the fracture energy approaches 0.001 kJ/mm<sup>2</sup>. (The value of  $\mu/B$  can be determined solely in terms of  $\nu$ , Poisson's ratio; the critical value of  $\nu$  in this case is approximately 0.32.)

The first notched fracture toughness experiments on LM-1 were conducted by Conner et al. [7] using two experimental setups to provide estimates of the fracture toughness. In the first setup, the LM-1 specimen was loaded under three-point bending, and the fracture toughness was calculated based on the load applied to the specimen and assuming linear elastic fracture mechanics, which is a good assumption based on the high yield strength exhibited in stress-strain curves from quasi-static experiments conducted in compression and the calculated size of the plastic zone relative to the sample dimensions

[6, 14]. The second experimental setup used coherent gradient sensing (CGS), which utilizes laser light, a mirror, and two gratings in order to determine out-of-plane displacements (through the presence of fringes) which can be related directly to the fracture toughness of the specimen. Results from the experiments show consistent values of  $K_Q$  (fracture toughness under mode-I loading) of about  $60 \text{ MPa m}^{1/2}$ , along with the presence of some crack branching in the specimen. The experiments were conducted under notched bending conditions; while the notch root radius of the specimen was not explicitly stated, a micrograph of the crack profile indicates a notch root radius of approximately  $100 \text{ }\mu\text{m}$  [7]. While the authors claim that this value of  $K_Q$  is the material constant  $K_{IC}$  given in the paper, a valid  $K_{IC}$  measurement requires the use of a fatigue precrack instead of a blunt notch; therefore, this value of  $K_Q$  likely overestimates the actual fracture toughness as shown later [5, 6] and would also explain the presence of crack branching.

Around the same time as the initial experiments by Conner et al., Gilbert et al. [9] conducted experiments on fatigue-precracked compact tension (CT) specimens of LM-1 as well as two annealed forms of LM-1 (633 K and 733 K). The observed fracture toughness of LM-1 was approximately  $55 \text{ MPa m}^{1/2}$ , and the annealed (633 K) and devitrified (733 K) LM-1 specimens exhibited fracture toughness of about  $1 \text{ MPa m}^{1/2}$ . While it was clear that the specimens were fatigue-precracked, it is less clear whether the dominant fracture was planar or if it had the same roughness characteristics as in the work by Conner et al. Subsequent work by Gilbert [8] showed significant out-of-plane

fracture and crack front bowing, partly attributed to residual stresses induced during processing.

A few years later, additional fracture toughness experiments under low loading-rates were conducted by Lowhaphandu et al. [5, 6] also utilizing three-point bending. Results from these experiments showed a much lower fracture toughness of about 18 MPa m<sup>1/2</sup>, an absence of crack front bowing, and a planar macroscopic fracture surface. More specimens were tested in this study -- the six specimens tested exhibited a scatter of less than 2 MPa m<sup>1/2</sup>, indicating a high degree of confidence in the measured fracture toughness. Unlike the work performed by Conner et al., the region below the notch was observed to be largely planar; the discrepancy between the two sets of results was attributed to the thicker sample size in Lowhaphandu's work (4-7 mm, instead of 2.2 mm), along with a possible difference in the notching technique. Additional experiments using a number of notch root radii (from 60 μm – 1 mm) show a dramatic increase in the value of the critical fracture toughness ( $K_{Ic}$ ) from 20 MPa m<sup>1/2</sup> (fatigue-precracked) to as high as 250 MPa m<sup>1/2</sup> (1 mm notch root radius) [2, 4, 6]. The large increase in the fracture toughness in the notched specimens is evidenced by the large increase in the degree of crack bifurcation in the specimens with the bluntest notches. Further experiments [2] indicate that increasing the stress-intensity rate  $\dot{K}$  from 0.2 MPa m<sup>1/2</sup>/s to 800 MPa m<sup>1/2</sup>/s had a negligible effect on the observed fracture toughness for both the fatigue-precracked and notched specimens.

Owen et al. [10] investigated dynamic fracture initiation in three-point bend specimens using a drop weight tower as well as an asymmetric impact configuration to generate mode II loading, and thus, substantial shearing in the specimen, in contrast to pure mode I conditions. The drop weight experiments indicate a large increase in the dynamic fracture toughness with loading rate, from  $60 \text{ MPa m}^{1/2}$  under quasi-static loading [7] to about  $200\text{-}250 \text{ MPa m}^{1/2}$  at crack tip loading rates of approximately  $10^7 \text{ MPa m}^{1/2}/\text{s}$ . Recent mixed-mode loading experiments have also suggested significant increases in toughness when loading is not strictly mode I [15].

Additional work has been conducted by Rittel and Rosakis [11], in which the results of dynamic three-point bend tests obtained by using two techniques – a drop-weight tower and a modified Split-Hopkinson Pressure Bar (MHPB) – were compared with those obtained by employing a short-beam dynamic fracture technique to verify its validity in testing specimens of LM-1. These results showed a large increase in the fracture toughness of LM-1 with loading-rate, from  $\sim 50 \text{ MPa m}^{1/2}$  ( $1 \text{ MPa m}^{1/2}/\text{s}$ ) to  $\sim 150 \text{ MPa m}^{1/2}$  ( $10^6 \text{ MPa m}^{1/2}/\text{s}$ ); however, substantial scatter ( $100 \text{ MPa m}^{1/2}/\text{s}$  above or below the stated fracture toughness) was present in the results at the higher loading-rates. Any effect of notch geometry in these specimens on the fracture toughness was observed to be negligible, although the effects of mode-mixity on the toughness were not evaluated.

From the previous experiments conducted, it is apparent that while there have been comparisons between the quasi-static and dynamic fracture response of precracked

LM-1 specimens, as well as the effects of changes in mode mixity, little work has been conducted to investigate the effects of crack tip loading-rate on the fracture toughness of notched LM-1. In addition, the previous experiments conducted focused primarily on three-point bending, which produces great demands on the ability to align the impactor with the notch, and small shifts in the impactor's alignment can produce substantial shear in the specimen, which has been shown to enhance the toughness values via the introduction of mixed-mode loading. The large increase in the observed fracture toughness with the application of shear, as shown by Owen et al. [10] and Varadarajan et al. [15], confirms the importance of alignment of the impactor and the notch. To that end, dynamic fracture experiments are conducted on notched samples of amorphous LM-1 using an instrumented Modified Split-Hopkinson Pressure Bar (MHPB) [16]. The experiments were conducted using four-point bend specimens; a high-speed camera was utilized to investigate dynamic crack initiation and propagation during the loading process. In these experiments, the load-point force versus time profiles at loading-rates in excess of  $10^6$  MPa m<sup>1/2</sup>/s were obtained. The high-speed camera images were matched to the force-versus-time profile to examine the sequence of the failure events leading to the catastrophic fracture of the specimen. Extensive scanning electron microscopy was also conducted to examine the fracture surfaces. Finally, a series of well-controlled stress wave loading experiments were conducted to induce pre-determined sub-critical levels of damage at the notch (without causing catastrophic failure of the LM-1 specimens), so as to better understand the damage initiation mechanisms at the notch in response to the dynamic bend loading.

### 4.3 Experimental Procedure

Plates of fully amorphous LM-1 of size (85 x 51 x 2.2) mm were received from Liquidmetal Inc, [2, 5, 6, 17]. These plates were cut to size (50.8 x 25.4 x 2.2) mm or (50.8 x 19.1 x 2.2) mm using a diamond saw; the specimen faces were ground to be flat and parallel. A notch with a root radius 110  $\mu\text{m}$  was machined using a wire saw (Buehler) to a depth of  $a/W = 0.5$ . A schematic of the specimen is shown in Figure 4.1. The stress intensity factor was calculated based on the following equation

$$K_Q = \frac{3Pl}{tW^2} \sqrt{\pi a} F(\alpha), \quad (4.4)$$
$$F(\alpha = \frac{a}{W}) = 1.122 - 1.121\alpha + 3.74\alpha^2 + 3.873\alpha^3 - 19.05\alpha^4 + 22.55\alpha^5$$

where  $K_Q$  is the stress intensity factor,  $t$  is the thickness of the specimen, and all other quantities are shown in Figure 4.1. Sample geometry and loading configurations were kept consistent with specifications followed by ASTM-399 when possible, although no ASTM standard currently exists for dynamic toughness measurements.

An instrumented Modified Hopkinson Pressure Bar (MHPB) was employed to perform experiments in four-point bending. As shown schematically in Figure 4.2, the MHPB consists of a gas gun, a striker bar (0.6 m), and an instrumented incident bar (2.3 m). The striker and incident bars are both made of 6061-T6 Al alloy. Semiconductor strain gages are placed diametrically opposite each other on the incident bar because of the low strains exhibited by the incident bar during the impact. The Wheatstone bridge is connected to a 15 V power supply, which is in turn connected to a differential amplifier

(Tektronix 5A22N). Data acquisition is performed by using a high-bandwidth oscilloscope (Tektronix 680C), running at 100 MHz. A copper pulse shaper (0.8 mm thick) was employed to ensure a ramp-like loading pulse. The ramp wave serves two purposes: it ensures that the specimen does not fracture during the rise time of the loading pulse, and it helps to minimize effects of wave dispersion.

The dynamic fracture experiments were conducted at impact velocities sufficient to induce fracture; however, an additional experiment was conducted at lower impact velocities to induce controlled sub-critical levels of damage in the notched specimens. In addition, a high-speed camera (Imacon 200) is employed to record the crack initiation and propagation events; images are taken at 50,000 frames per second (i.e. an interframe time of 20  $\mu$ s) with an exposure time of 4  $\mu$ s.

To perform four-point bend tests, a special fixture was prepared on the incident bar. The fixture, shown schematically in Figure 4.3, consists of a cylindrical aluminum tab (approximately 8 mm length by 19.05 mm diameter) with two slots, the centers of which are 12 mm apart, machined perpendicular to the loading surface. Each of the slots houses a loading pin of diameter 4 mm, which is press-fit to the slot. In addition, two hardened pins of diameter 4 mm are placed in between the specimen and a rigid support. The specimen is aligned carefully to ensure that the loading pins are equidistant from the rear support pins and that the loading pins are in full contact with the specimen prior to the experiment.

#### 4.4 Wave Propagation in the MHPB

A schematic time-distance ( $t$ - $x$ ) diagram for the wave propagation in the MHPB is shown in Figure 4.4, with each state (force and velocity) denoted. Prior to impact, both the striker (State 0) and incident (State 1) bars are unstressed, while the striker bar is propelled at a known velocity. Upon impact, compressive waves (State 2), the duration of which are dependent on the length of the striker (0.6 m) and the wave speed of the striker (5.1 km/s), are generated in both the striker and the incident bars. The compressive wave in the striker bar travels to the left and reflects from the free end of the bar as a release wave (State 3). The compressive wave in the incident bar travels to the right and arrives at the incident-bar and specimen interface; part of this wave is transmitted through to the specimen (State 4), while the rest is reflected back into the incident bar (State 5). In all of the experiments conducted, the impact velocity is controlled in order to ensure that both the striker and incident bars remain elastic throughout the duration of the experiment.

The various force and velocity states, in conjunction with a stress-particle velocity relationship, are given by

$$F_i(t) \pm \rho c_L A V_i(t) = \text{const, along } \frac{dx}{dt} = \mp c, \quad (4.5)$$

and can be utilized to obtain the specimen's load-displacement history from the measured strain history of the strain gage placed on the incident bar. In Equation (4.5),  $F_i(t)$  is the axial force in the bar for state  $i$ ,  $\rho$  is the bar density,  $c_L$  is the longitudinal wave speed,  $A$  is the area of the bar, and  $V_i(t)$  is the particle velocity for the state  $i$ . This equation, combined with the boundary and initial conditions ( $V_0 = V_{\text{impact}}$  (impact velocity),  $V_1 = 0$ ,

and  $F_0 = F_1 = 0$ ) can be applied to the striker and incident bars prior to and after the passage of the compressive waves, to give

$$F_2(t) = \frac{1}{2} \rho c_L A V_{\text{impact}} \quad \text{and} \quad V_2(t) = -\frac{F_2(t)}{\rho c_L A}. \quad (4.6)$$

Also, Equation (4.5) can be used to relate the forces and velocities at States 2 and 4 by the following relationship

$$F_4(t) = 2F_2(t) + \rho c_L A V_2(t), \quad (4.7)$$

which is along the forward characteristic, and a backward characteristic can also be used to relate the forces and velocities at States 3, 4, and 5 by

$$\begin{aligned} F_4(t) = F(t) &= F_2(t) - F_3(t) + F_5(t) \\ V_4(t) = V(t) &= \frac{F_5(t) - F_3(t) - F_2(t)}{\rho c_L A}. \end{aligned} \quad (4.8)$$

In Equation (4.8),  $F(t)$  is the load-point history on the specimen, while  $V(t)$  is the specimen's particle velocity. The displacement  $\delta$  can be determined by integrating the velocity over time, so that

$$\delta = \int_0^t V(t^*) dt^*. \quad (4.9)$$

Finally, since  $F_3(t)$  is the resultant of the loading and unloading waves in the striker bar (which remains elastic under the given experimental conditions),  $F_3(t) = 0$ ; thus, the load point force and the displacement are solely functions of  $F_2(t)$ , the incident signal, and  $F_5(t)$ , the reflected signal.

## 4.5 Results and Discussion

Table 4.1 summarizes the experiments conducted in the present study. It shows the experiment number, specimen dimensions, notch length, notch radius, and the impact velocity used in the particular experiment. Experiments Frac-1 and Frac-4 were conducted at a high enough impact velocity such that specimen fracture occurred catastrophically, experiment Frac-2 was conducted at a lower impact velocity to ensure recovery of the fracture specimen with damage concentrated at the notch region but without catastrophic failure, and experiment Frac-2B was conducted to reload the post-test damaged specimen recovered from Frac-2.

Results of a load-point force-versus-time curve and force-versus-displacement curve obtained from experiment Frac-1 are shown in Figures 4.5a and 4.5b, respectively. The force versus time curve shows the presence of distinct peaks; unstable crack propagation occurs at  $\sim 120 \mu\text{s}$ , when the load-point force reaches  $\sim 10 \text{ kN}$  (the highest peak), and the corresponding load point displacement is  $\sim 0.62 \text{ mm}$ . The force versus time curve shows additional crack initiation attempts at two prior peaks – one at  $\sim 3 \text{ kN}$  and the other at  $\sim 6 \text{ kN}$  – before attainment of the highest peak at  $\sim 10 \text{ kN}$ , which corresponds to an energy to fracture of  $2.60 \text{ J}$ . While the presence of multiple peaks suggests that the initial attempts to induce failure were unsuccessful due to shear-band driven blunting at the notch, the presence of multiple peaks justified the synchronization of the images from the high-speed camera with points on the force vs. time curve in the remaining experiments. Using Equation (4.4), the stress intensity factor corresponding to

the peak force is approximately  $112 \text{ MPa m}^{1/2}$ , while the previous peaks correspond to stress of intensities of  $35 \text{ MPa}^{1/2}$  (for the 3 kN peak) and  $68 \text{ MPa}^{1/2}$  (for the 6 kN peak).

Results of similar load-point force versus time and force versus displacement curves for experiment Frac-4 are shown in Figures 4.6(a) and 4.6(b), respectively. In addition, superimposed high-speed camera images have also been added in order to confirm when crack initiation (i.e. catastrophic failure) occurs. Once again, there are three distinct peaks in the force vs. time curve – the first at  $\sim 3 \text{ kN}$ , the second at  $\sim 6.5 \text{ kN}$ , and the third at  $\sim 8 \text{ kN}$ . The high-speed camera images confirm that crack initiation and subsequent propagation do not occur prior to the attainment of the highest peak in the force versus time curve. The energy at fracture is  $2.57 \text{ J}$ , and the corresponding fracture toughness is approximately  $129 \text{ MPa m}^{1/2}$ .

The fracture surfaces, shown in Figure 4.7, show evidence of fine-scale deformation bands (Figure 4.7(a, b)) as well as vein patterns and viscous flow (Figure 4.7(c, d)). In addition, careful optical imaging (at 10x magnification) and SEM imaging of the crack path in the specimen, shown in Figures 4.8a and 4.8b, respectively, show evidence of crack bifurcation, which is consistent with a material exhibiting such a high value of  $K_{Ic}$ . Images of the fracture surface, shown in Figure 4.9, detail a wide range of surface features exhibited by the fractured specimens. Just ahead of the notch is a short planar region [Figure 4.10], measuring about  $150\text{-}200 \mu\text{m}$  in length. Past this planar region is a larger region consisting of fine-scale veins [Figure 4.11] that are similar to those observed in other studies of compression and fracture specimens [5, 6, 9, 10, 12,

14, 18-21]. Halfway down the specimen width, the large veining region begins to smooth out, so that there is less roughness in the region, but further down there is another region consisting of large vein-like features with a roughness on the order of 500  $\mu\text{m}$ , as shown in Figure 4.12. Finally, as the crack reaches near the end of the specimen (commonly referred to as the overload region due to the very high stresses there), the crack deflection occurs, as shown by a “ridge” near the bottom of the specimen [Figure 4.13]. The presence of the large-veined region and “ridge” appear to be due to the extremely high stresses near the rear surface as the crack approaches the free surface at the end of the specimen.

Figure 4.14 shows a typical force-versus-time curve for an experiment in which catastrophic fracture did not occur. Once again, distinct peaks were observed at forces corresponding to  $\sim 4\text{kN}$  and  $\sim 8\text{ kN}$ , respectively. The corresponding stress intensity factor,  $K_Q$ , assuming fracture at  $\sim 8\text{kN}$ , is in excess of  $92\text{ MPa m}^{1/2}$ . However, SEM imaging of the specimen revealed the presence of very intricate crack-like patterns (deformation/shear bands) at and around the notch. One group of these bands occurs along the direction of the notch (Figure 4.15(a)) to a distance of approximately  $150\text{ }\mu\text{m}$  from the notch root; a second group of deformation bands, which can also be associated with this damage, is observed to be perpendicular to the first group of deformation bands (Figure 4.15(b)).

One way to explain the presence of some of the deformation features around the area of the notch is to consider slip-line field theory around the area of the notch, as it can

provide analytical solutions for materials undergoing largely perfectly plastic deformation. The slip-lines represent lines along which the shear stress has reached the critical stress required to yield the material in shear. In order to make use of the results of the slip line theory three key assumptions need to be satisfied: plane-strain deformation, quasi-static loading, and a material that obeys a non-hardening (perfectly-plastic) von Mises material model. In this regard, in the present study, inertial effects in the specimen are negligible by the time dynamic fracture initiation occurs due to multiple wave reflections in the specimen, and LM-1 has been observed to follow elastic perfectly-plastic and nearly rate-insensitive material behavior [22]. Separate investigations have also demonstrated nearly pressure-independent behavior of this BMG [3, 6, 15, 23-25].

The plastic zone  $r_p$ , defined as

$$r_p = \frac{1}{6\pi} \left( \frac{K_I}{\sigma_{YS}} \right)^2, \quad (4.10)$$

where  $K_I$  is the calculated fracture toughness in the experiments, and  $\sigma_{YS}$  is the yield strength of LM-1 (i.e. 2 GPa), is 0.13-0.18 mm, or about 6-8% of the thickness of the specimen. For a true plane-strain fracture experiment, the plastic zone size should be no more than 2% of the thickness of the specimen, according to ASTM-E399; all the other critical dimensions ( $a$ ,  $w-a$ ) in the specimens are at least 9 mm, and thus, much larger than the plastic zone size. Earlier work on both 4 mm thick and 7 mm thick BMG of identical chemistry showed little effect of these changes on the magnitude of toughness [6]. Nevertheless, the present experiments do not attain fully plane strain conditions.

Additional work that considers the use of slip-line theory was conducted by Flores and Dauskardt [12] on a similar BMG. In these experiments, single edge notched tension [SEN(T)] samples of LM-1 were tested under quasi-static loading conditions. Extensive blunting appeared to occur at the crack tip; the region in which the deformation bands were present was between 50 and 370  $\mu\text{m}$  – the sizes of the regions correspond to stress intensities of about 60 and 135  $\text{MPa m}^{1/2}$ , respectively. Both the SEN(T) specimens and the specimen for experiment Frac-1 clearly showed crack bifurcation; however, the resulting crack paths in the SEN(T) specimens are parallel to each other, while the two main cracks in Figure 4.8(a) diverge. This behavior may be explained simply due to the different types of loading to test the specimens as well as fracture which seeks the loading pins in the four-point bend experiments.

Another relationship that has been of particular interest is the size of the planar region in fracture samples when compared to the measured fracture toughness [26]. Previous work performed by Lowhaphandu et al. [6] on notched (60-250  $\mu\text{m}$  notch radius) LM-1 fracture samples under quasi-static conditions reveal a largely planar region of about 150 – 200  $\mu\text{m}$  ahead of the notch. The planar region ahead of the notch for experiment Frac-1, shown in Figure 4.10, also appears to be about 150-200  $\mu\text{m}$ . The similarities in the size of the planar region and the fracture toughness ( $\sim 105 \text{ MPa m}^{1/2}$ ) provide additional support for the rate-insensitivity of the toughness of LM-1.

Figure 4.16 shows the results from experiment Frac-2B, in which the initially impacted (and damaged) notched fracture specimen (Frac-2) is subsequently reloaded.

The re-loading of the specimen shows no reduction in the dynamic force necessary to cause catastrophic failure of the specimen, as seen in Figure 4.16(a); the load-point force on the specimen is in excess of 12 kN when unstable fracture occurs at  $\sim 120 \mu\text{s}$ . This is consistent with the observation that the initial damage does not adversely affect the fracture toughness of the specimen. The high-speed video again provides evidence of repeated attempts of crack initiation via shear banding and subsequent further opening and blunting of the notch due to the shear bands, as illustrated by the several peaks in the force versus time profile of the reloaded specimen. The energy required to induce unstable fracture, based on the force versus displacement curve (Figure 4.16(b)), is approximately 5.2 J. This clearly shows that the previously induced damage actually increases the energy required to fracture the specimen upon subsequent re-loadings. Such an increase in the energy required can be rationalized by considering the previous damage zone essentially increases the notch radius, much like with the process zones seen from Flores and Dauskardt's previous work [12]. In particular, the corresponding fracture toughness  $K_{Ic}$  for experiment Frac-2B ( $\sim 136 \text{ MPa m}^{1/2}$ ) is in good agreement with the expected fracture toughness that is suggested for a specimen with a notch radius of about 160-170  $\mu\text{m}$  [4], which closely approximates the radius of the damaged zone from Figure 4.15 (a) as well as the plane strain process zone size.

#### **4.6 Summary**

Dynamic fracture experiments were conducted on notched specimens of amorphous LM-1 using an instrumented modified Split-Hopkinson Pressure Bar (MHPB) to ensure four-point bending of the specimens. Based on the results of these experiments:

1. Force versus time curves show the presence of several peaks, and high-speed camera images synchronized to the curves show repeated instances of crack initiation followed by blunting.
2. The peak force at fracture corresponds to a fracture toughness of approximately  $110 \text{ MPa m}^{1/2}$ , similar to that under quasi-static conditions, which provides evidence of the strain-rate insensitivity of LM-1.
3. Additional experiments to induce sub-critical levels of damage in the specimens show extensive deformation banding extending 150 - 200  $\mu\text{m}$  outward from the notch.
4. SEM images indicate the presence of deformation bands, which are nominally perpendicular to each other and run both along the direction of the notch and perpendicular to it. They are consistent with previous experiments under quasi-static conditions and with the slip-line fields in front of notches in an elastic perfectly-plastic material. This is also consistent with the nominally pressure-independent behavior measured for this and similar materials.
5. Subsequent loading of the damaged specimen shows several attempts at crack initiation followed by blunting; the initial damage in the specimen increases the

energy needed to cause catastrophic failure of the specimen which is consistent with an increase in the effective notch radius due to the pre-existing damage.

6. The high toughness and relatively thin specimens tested in the present study produce non-plane strain conditions. While previous work has shown little effect on quasi-static toughness on going from 7 mm thick specimens to 4 mm thick specimens, the present samples are only 2.2 mm thick. Unfortunately, testing thicker samples is not possible under the current test configuration. Nonetheless, rate-insensitive behavior was recorded for these non-plane strain toughness measurements.

## References

1. Peker A., Johnson W.L. (1993) A highly processable metallic glass -  $Zr_{41.2}Ti_{13.8}Cu_{12.5}Ni_{10.0}Be_{22.5}$ . *Applied Physics Letters* **63**, 2342-2344.
2. Lewandowski J.J. (2001) Effects of Annealing and Changes in Stress State on Fracture Toughness of Bulk Metallic Glass. *Materials Transactions* **42**, 633-637.
3. Lewandowski J.J., Lowhaphandu P. (2002) Effects of hydrostatic pressure on the flow and fracture of a bulk amorphous metal. *Philosophical Magazine A* **82**, 3427-3441.
4. Lewandowski J.J., Shazly M., Nouri A.S. (2006) Intrinsic and extrinsic toughening of metallic glasses. *Scripta Materialia* **54**, 337-341.
5. Lowhaphandu P., Lewandowski J.J. (1998) Fracture toughness and notched toughness of bulk amorphous alloy: Zr-Ti-Ni-Cu-Be. *Scripta Materialia* **38**, 1811-1817.
6. Lowhaphandu P., Ludrosky L.A., Montgomery S.L., Lewandowski J.J. (2000) Deformation and fracture toughness of a bulk amorphous Zr-Ti-Ni-Cu-Be alloy. *Intermetallics* **8**, 487-492.
7. Conner R.D., Rosakis A.J., Johnson W.L., Owen D.M. (1997) Fracture toughness determination for a beryllium-bearing bulk metallic glass. *Scripta Materialia* **37**, 1373-1378.
8. Gilbert C., Schroeder V., Ritchie R. (1999) Mechanisms for fracture and fatigue-crack propagation in a bulk metallic glass. *Metallurgical and Materials Transactions A* **30**, 1739-1753.

9. Gilbert C.J., Ritchie R.O., Johnson W.L. (1997) Fracture toughness and fatigue-crack propagation in a Zr--Ti--Ni--Cu--Be bulk metallic glass. *Applied Physics Letters* **71**, 476-478.
10. Owen D.M., Rosakis A.J., Johnson W.L. (1999) Dynamic failure mechanisms in beryllium-bearing bulk metallic glasses. *Materials Research Society Symposium - Proceedings* **554**, 419.
11. Rittel D., Rosakis A.J. (2005) Dynamic fracture of beryllium-bearing bulk metallic glass systems: A cross-technique comparison. *Engineering Fracture Mechanics* **72**, 1905-1919.
12. Flores K.M., Dauskardt R.H. (1999) Enhanced toughness due to stable crack tip damage zones in bulk metallic glass. *Scripta Materialia* **41**, 937-943.
13. Lewandowski J.J., Wang W.H., Greer A.L. (2005) Intrinsic plasticity or brittleness of metallic glasses. *Philosophical Magazine Letters* **85**, 77-87.
14. Bruck H.A., Christman T., Rosakis A.J., Johnson W.L. (1994) Quasi-static constitutive behavior of  $Zr_{41.25}Ti_{13.75}Ni_{10}Cu_{12.5}Be_{22.5}$  bulk amorphous alloys. *Scripta Metallurgica et Materialia* **30**, 429-434.
15. Varadarajan R., Lewandowski J. (2010) Stress-State Effects on the Fracture of a Zr-Ti-Ni-Cu-Be Bulk Amorphous Alloy. *Metallurgical and Materials Transactions A* **41**, 1758-1766.
16. Martins C.F., Irfan M.A., Prakash V. (2007) Dynamic fracture of linear medium density polyethylene under impact loading conditions. *Materials Science and Engineering: A* **465**, 211-222.

17. Wesseling P., Lowhaphandu P., Lewandowski J. (2003) Effects of superimposed pressure on flow and fracture of two bulk metallic glass. *Mat. Res. Soc. Symp Proc.* **754**, 275-279.
18. Sunny G., Prakash V., Lewandowski J.J. (2007) Effects of annealing and specimen geometry on dynamic compression of a Zr-based bulk metallic glass. *Journal of Materials Research* **22**, 389-401.
19. Johnson W.L. (1996) Fundamental Aspect of Bulk Metallic Glass Formation in Multicomponent Alloys. *Materials Science Forum* **225-227**, 35-50.
20. Gilbert C.J., Ager Iii J.W., Schroeder V., Ritchie R.O., Lloyd J.P., Graham J.R. (1999) Light emission during fracture of a Zr--Ti--Ni--Cu--Be bulk metallic glass. *Applied Physics Letters* **74**, 3809-3811.
21. Gu X.J., Poon S.J., Shiflet G.J., Lewandowski J.J. (2010) Compressive plasticity and toughness of a Ti-based bulk metallic glass. *Acta Materialia* **58**, 1708-1720.
22. Sunny G., Yuan F., Prakash V., Lewandowski J. (2008) Effect of high strain rates on peak stress in a Zr-based bulk metallic glass. *Journal of Applied Physics* **104**, 093522.
23. Lewandowski J.J., Lowhaphandu P. (1998) Effects of hydrostatic pressure on mechanical behavior and deformation processing of materials. *International Material Reviews* **43**, 145-187.
24. Lowhaphandu P., Montgomery S.L., Lewandowski J.J. (1999) Effects of superimposed hydrostatic pressure on flow and fracture of a Zr-Ti-Ni-Cu-Be bulk amorphous alloy. *Scripta Materialia* **41**, 19-24.

25. Caris J., Lewandowski J.J. (2009) Pressure effects on metallic glasses. *Acta Materialia* **58**, 1026-1036.
26. Gu X.J., Poon S.J., Shiflet G.J., Lewandowski J.J. (2009) Ductile-to-brittle transition in a Ti-based bulk metallic glass. *Scripta Materialia* **60**, 1027-1030.

## Tables

Experiment name	Specimen length (mm)	Thickness (mm)	Width (mm)	Notch length (mm)	Notch radius ( $\mu\text{m}$ )	Impact velocity (m/s)
Frac-1	50.8	2.1	24.8	12.0	110	7.2
Frac-2	50.8	2.1	24.7	12.2	110	5.0
Frac-2B	50.8	2.1	24.7	12.2	110	9.5
Frac-4	50.8	2.1	18.7	9.35	110	8.4

Table 4.1 – Summary of fracture experiments conducted in the present study

## Figures

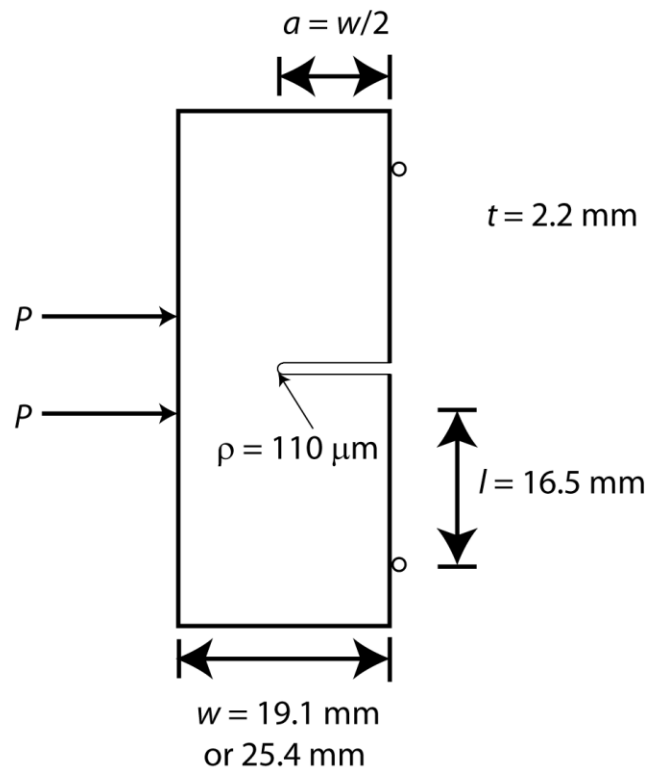


Figure 4.1 – Four-point bend specimen in the present study

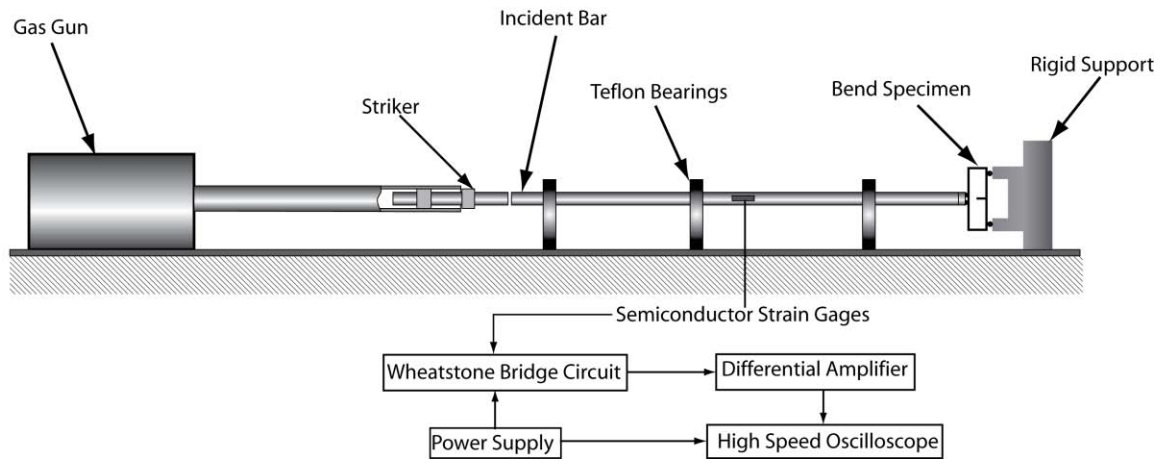


Figure 4.2 – Schematic of the MHPB for dynamic four-point bending

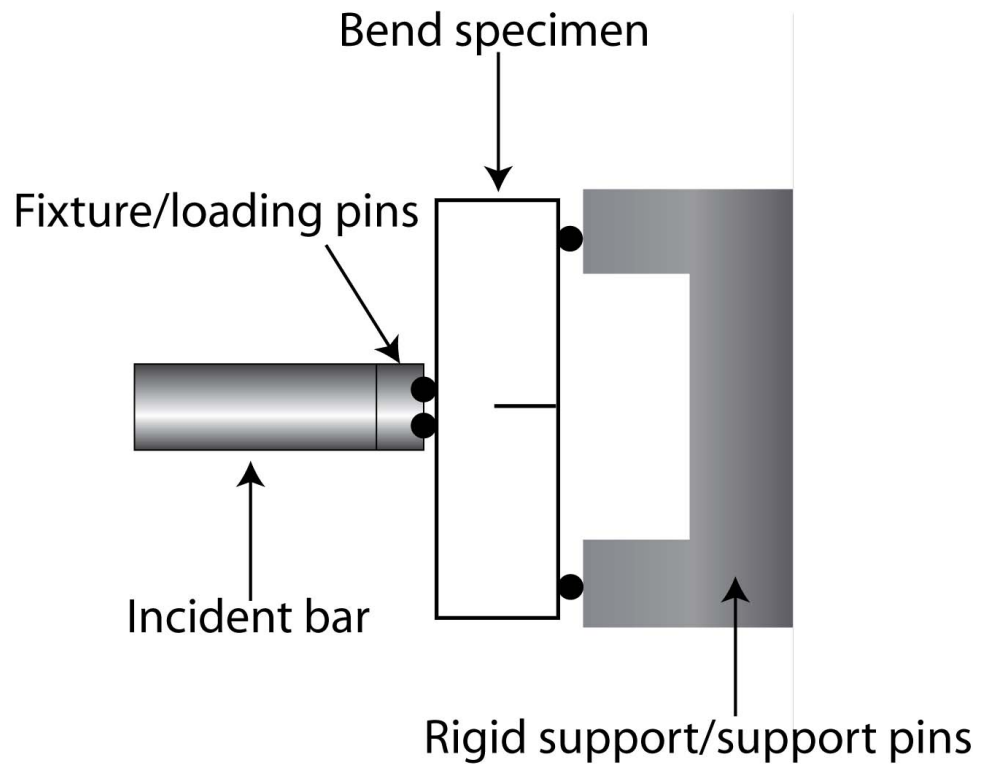


Figure 4.3 – Schematic of the fixture used for the dynamic four-point bending experiments

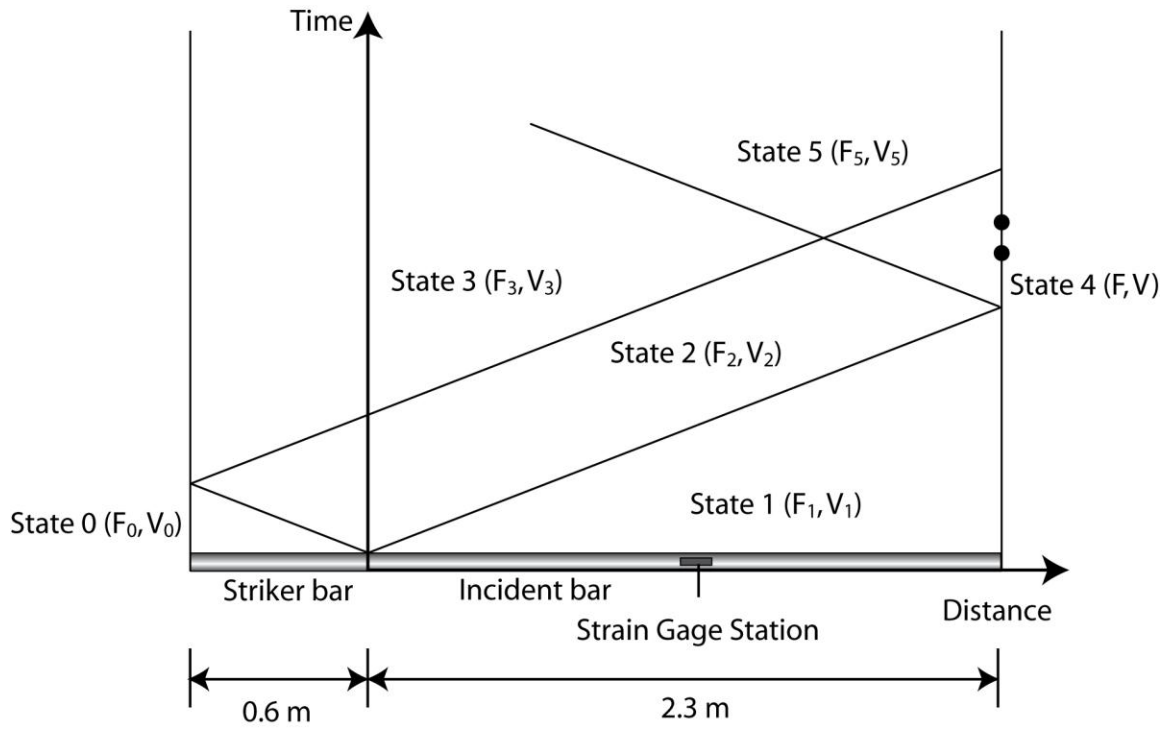
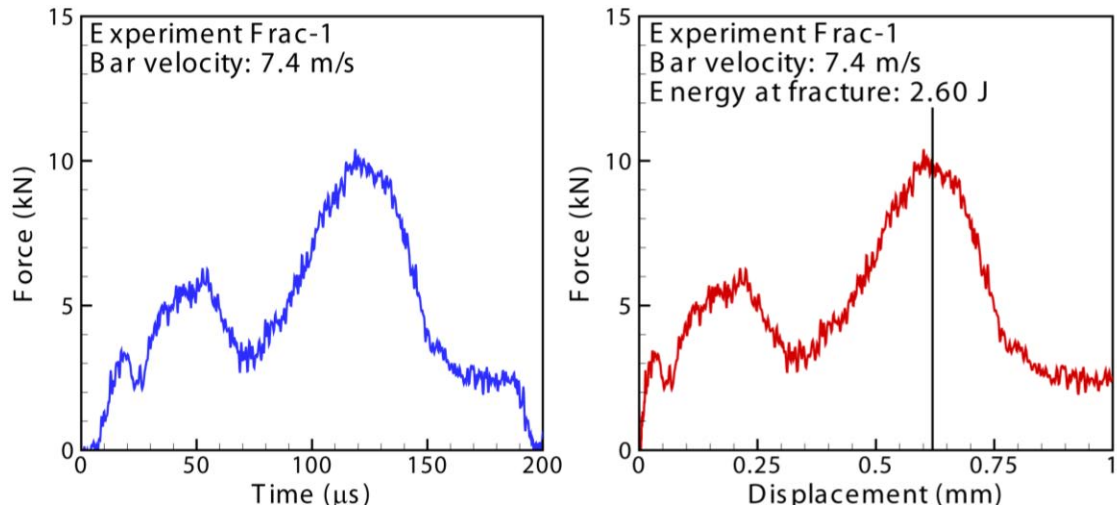


Figure 4.4 – Schematic time-distance ( $t-x$ ) diagram for wave propagation in the MHPB.



(a)

(b)

Figure 4.5 – (a) Force-versus-time curve for experiment Frac-1, (b) corresponding force-versus-displacement curve. Failure occurs at approximately 120  $\mu\text{s}$  after loading.

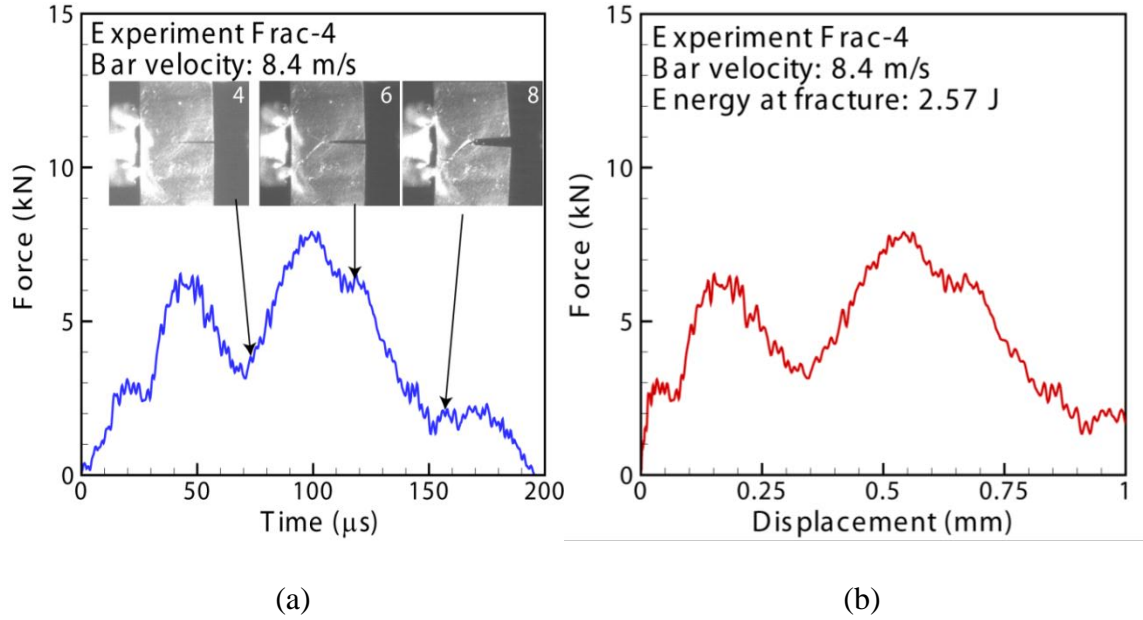
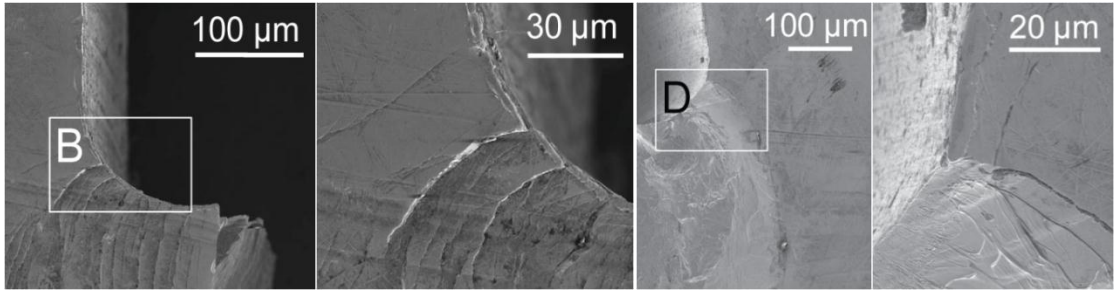


Figure 4.6 – (a) Force-versus-time curve for a typical dynamic fracture experiment, along with selected high-speed camera images, (b) corresponding force versus displacement curve; failure occurs at about 100  $\mu\text{s}$ .



(a)

(b)

(c)

(d)

Figure 4.7 –Typical fracture surfaces after a dynamic four-point bending experiment resulting in failure. (a) Left side fracture surface and (b) inset, showing evidence of fine-scale deformation/shear bands. (c) Right side fracture surface and (d) inset, showing evidence of viscous flow on the fracture surface.



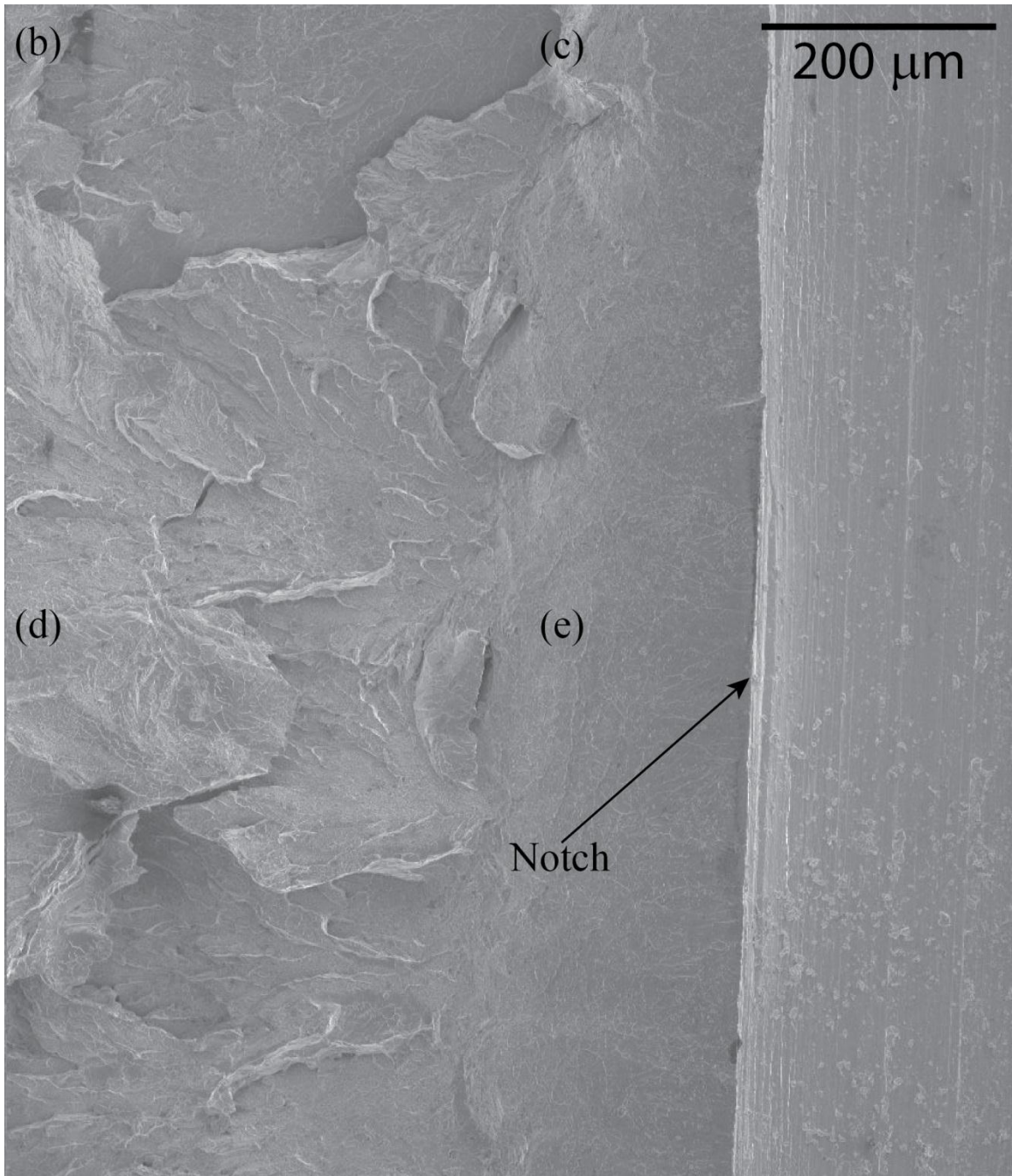
(a)

(b)

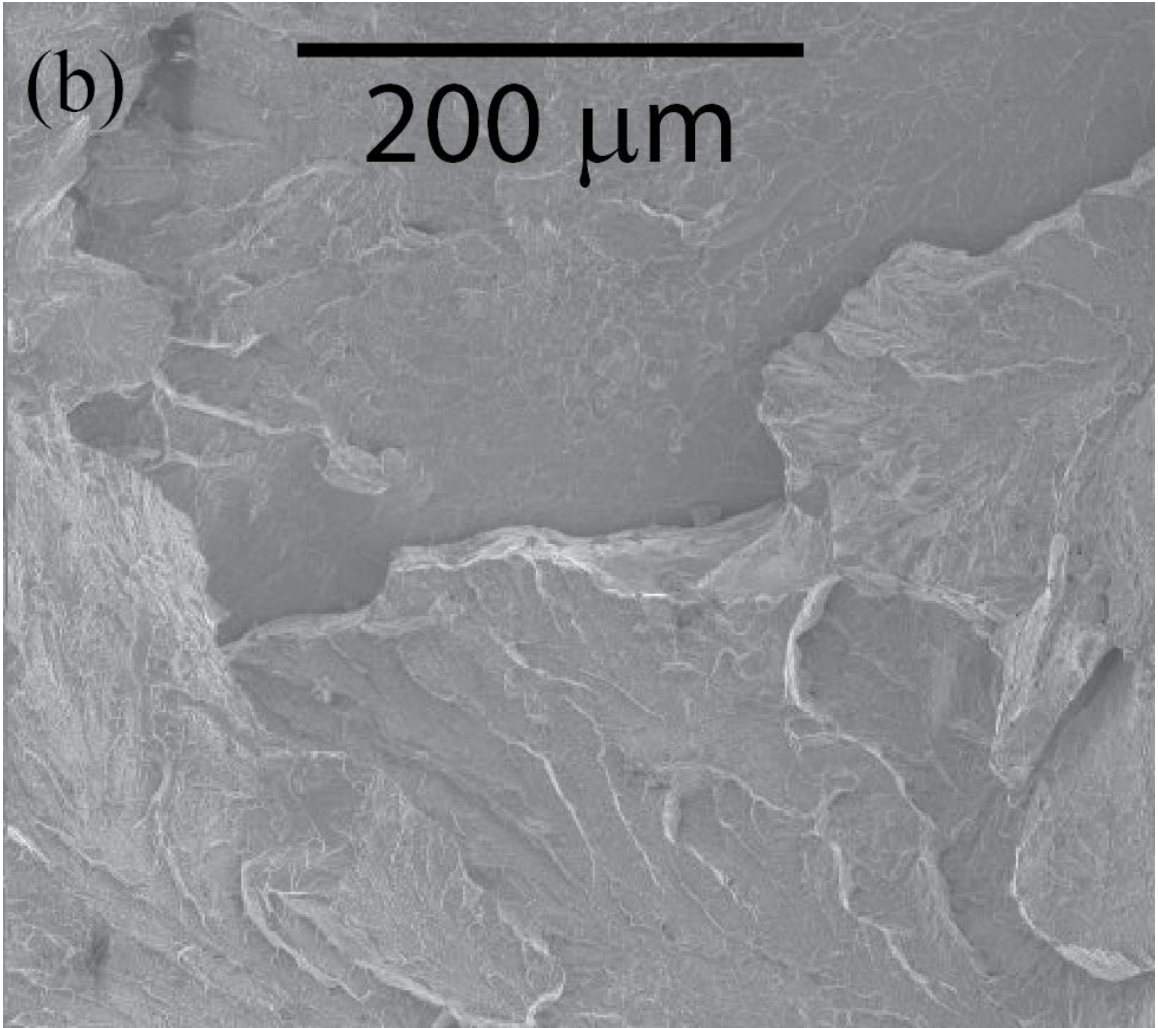
Figure 4.8 – Side views of fracture specimen: (a) Two resulting fractured plates at 10x optical magnification to show crack paths, and (b) SEM imaging for additional detail of (a). The notch is at the right of image (b).



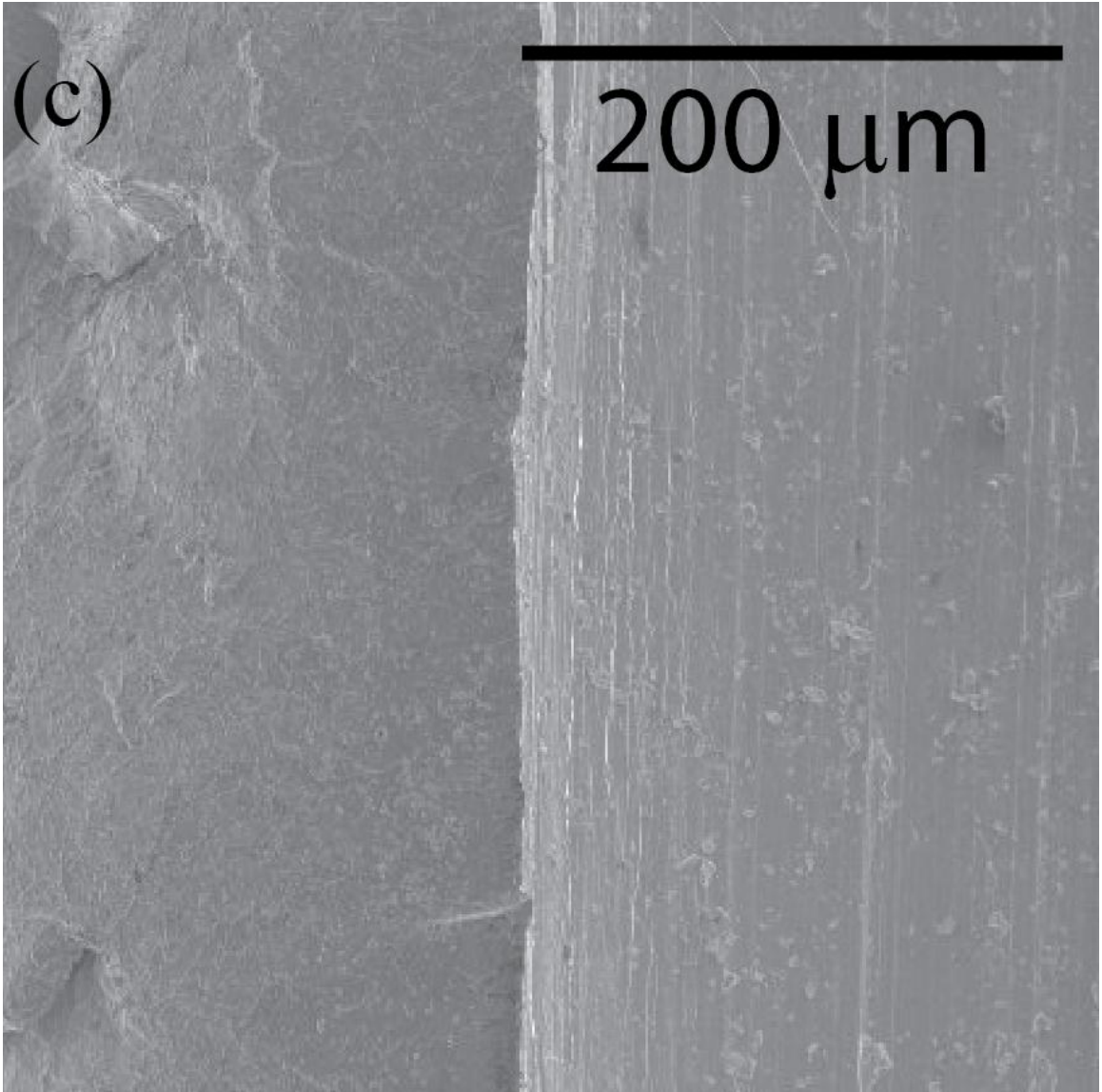
Figure 4.9 – Fracture surface of notched LM-1 specimen, with direction of failure propagation shown. The boxed regions B, C, D, and E refer to higher-magnification images for Figures 4.10, 4.11, 4.12, and 4.13, respectively.



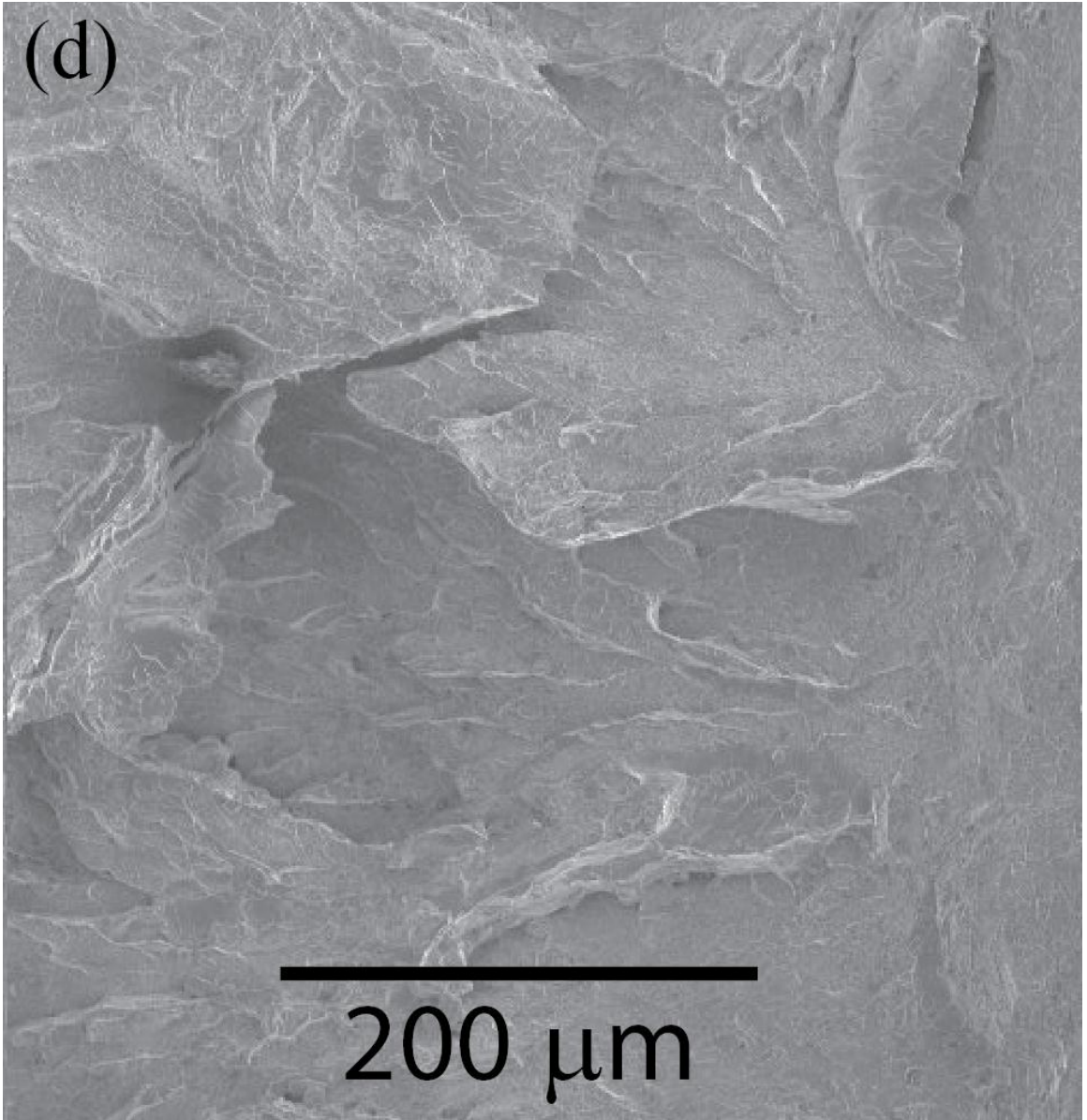
(a)



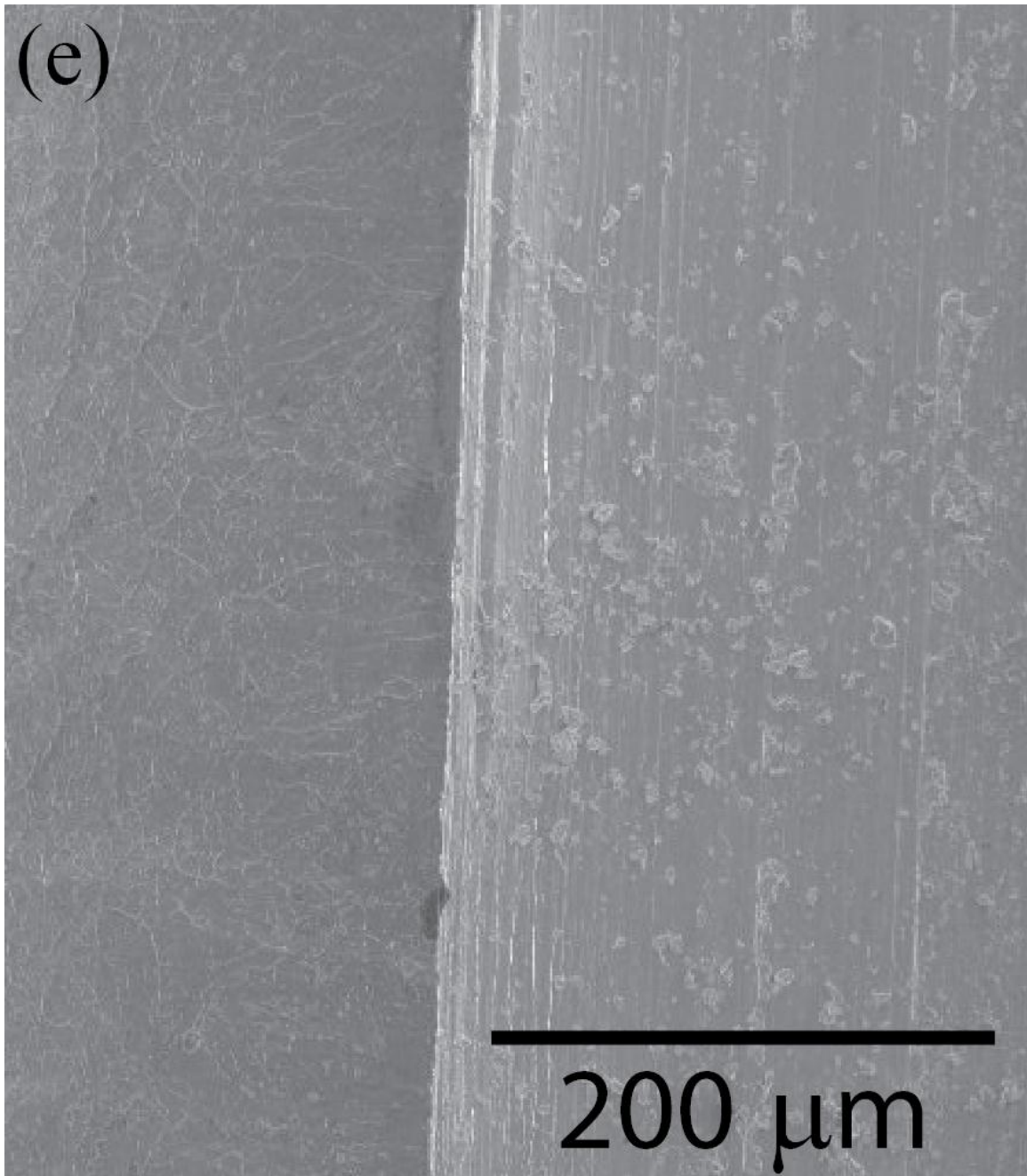
(b)



(c)

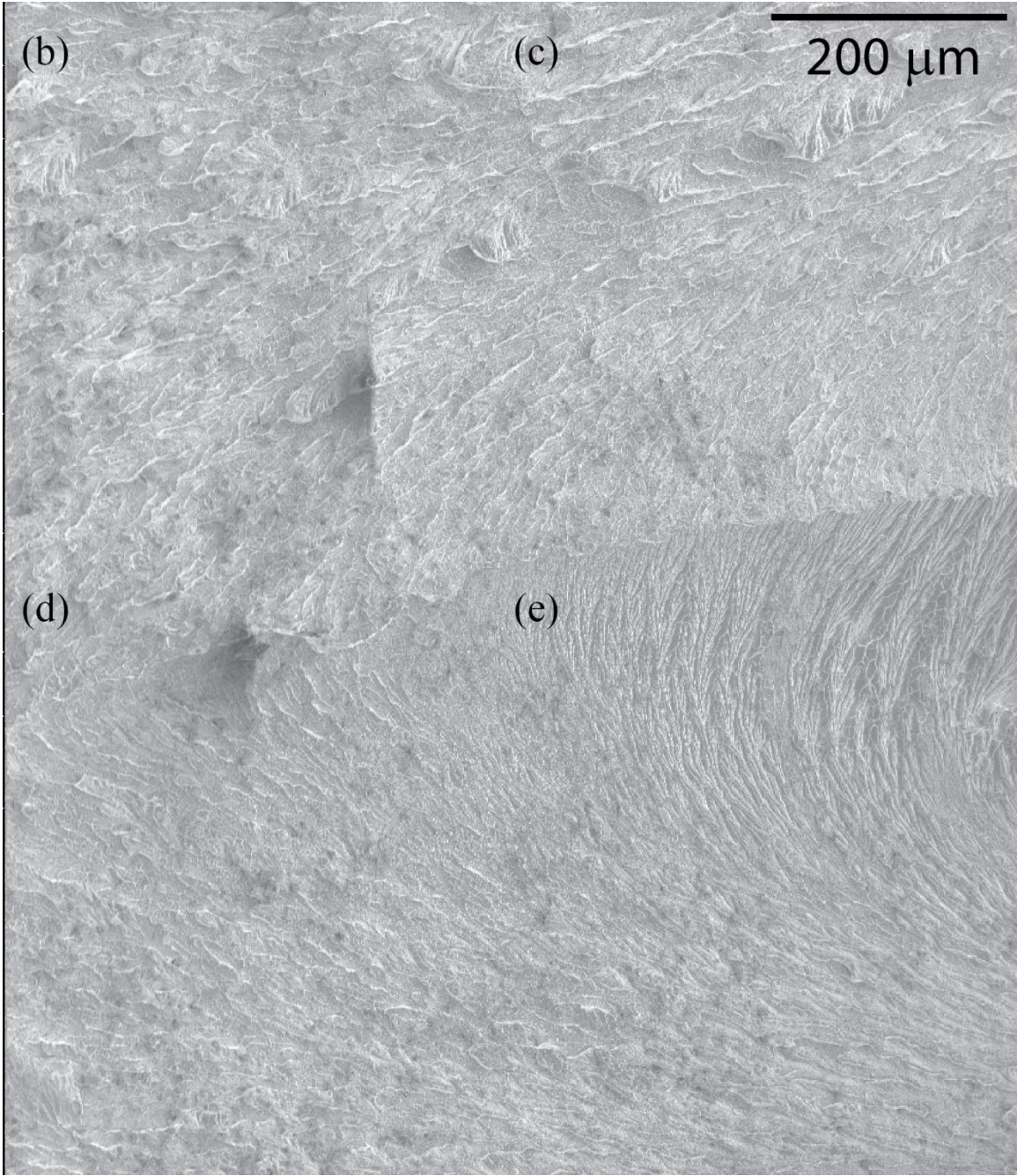


(d)

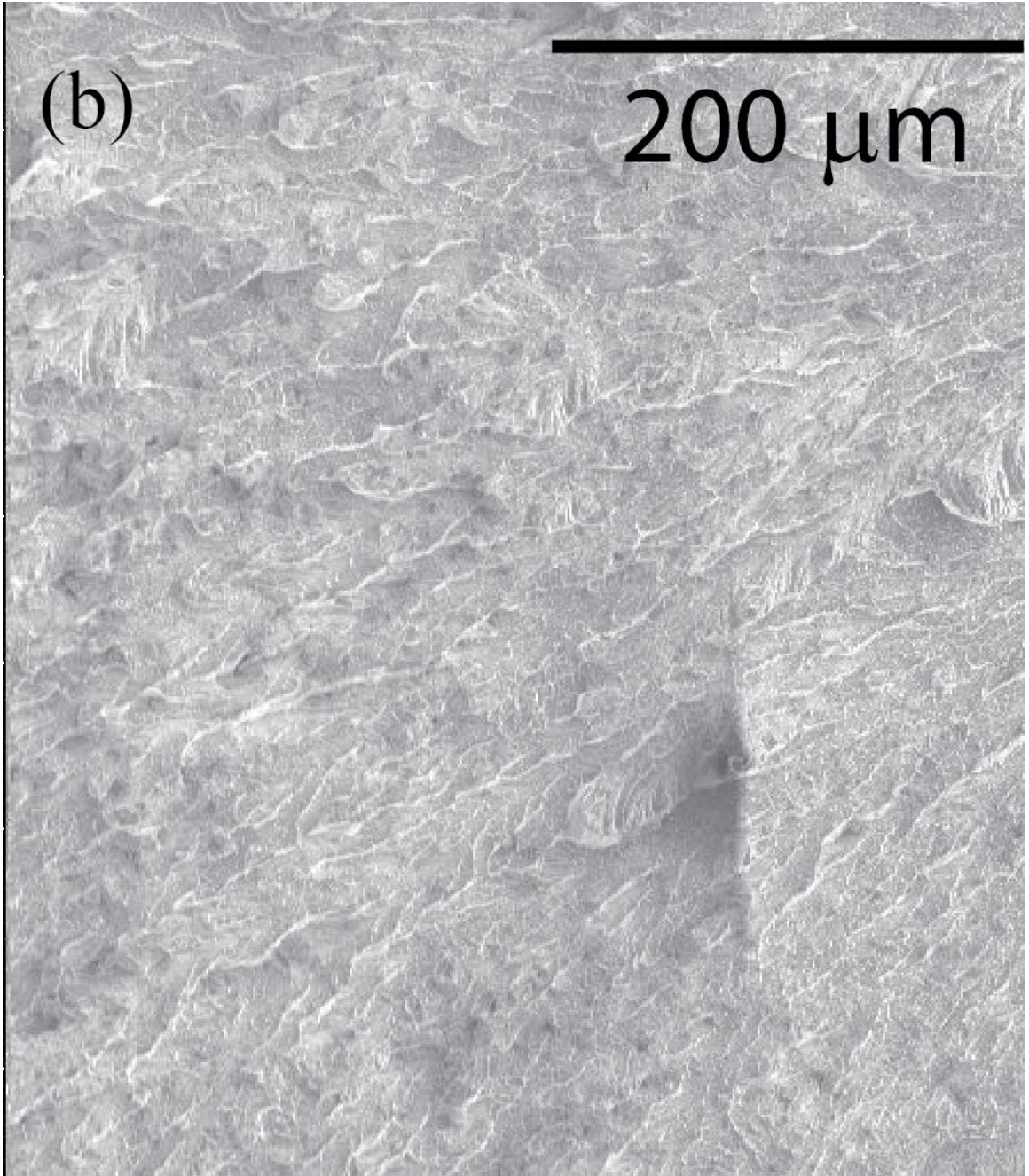


(e)

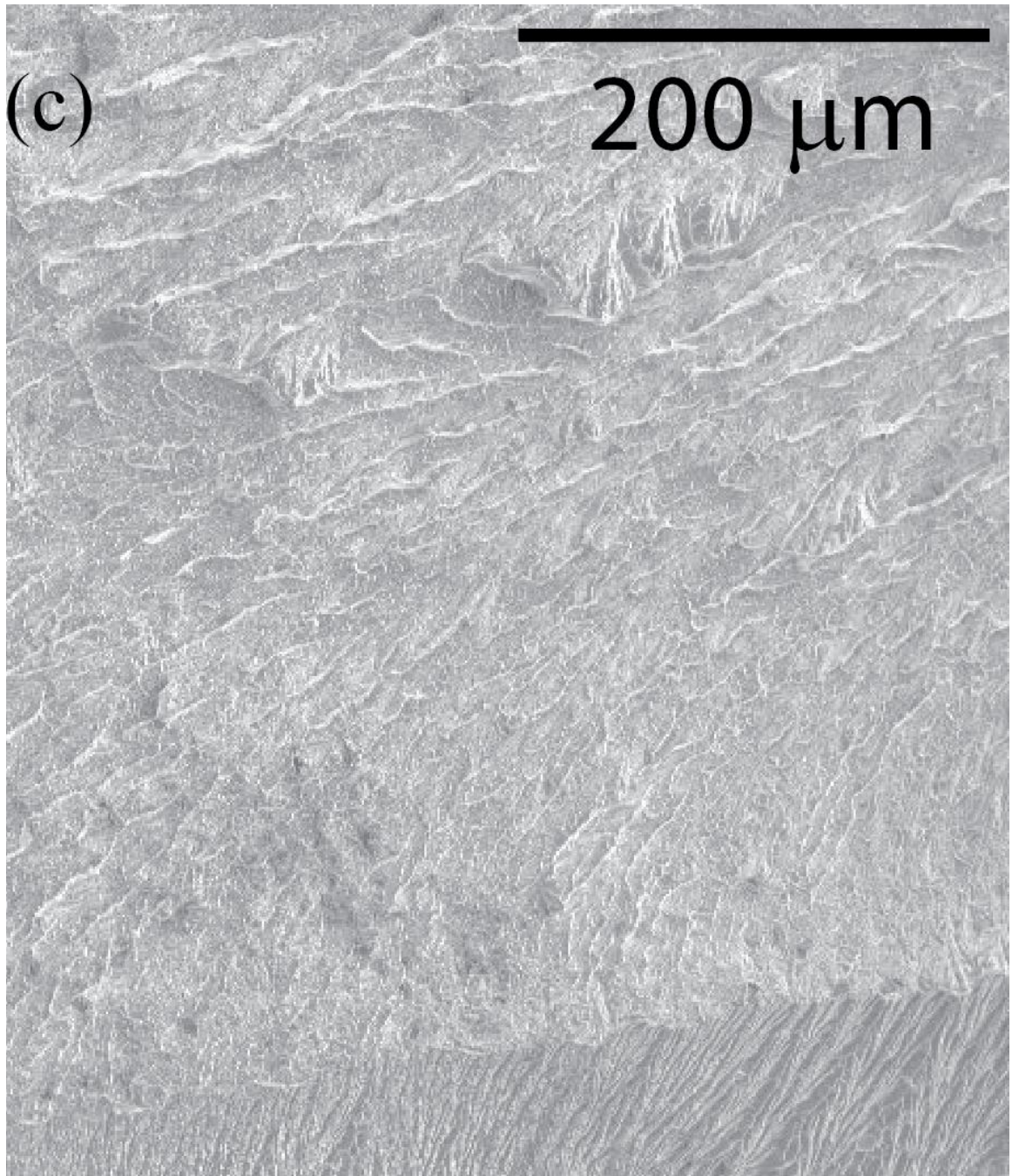
Figure 4.10 – (a) Fracture surface near the notch [indicated] in region B in Figure 4.9, (b) top left quadrant of Figure 4.10a, (c) top right quadrant of Figure 4.10a, (d) bottom left quadrant of Figure 4.10a, (e) bottom right quadrant of Figure 4.10a.



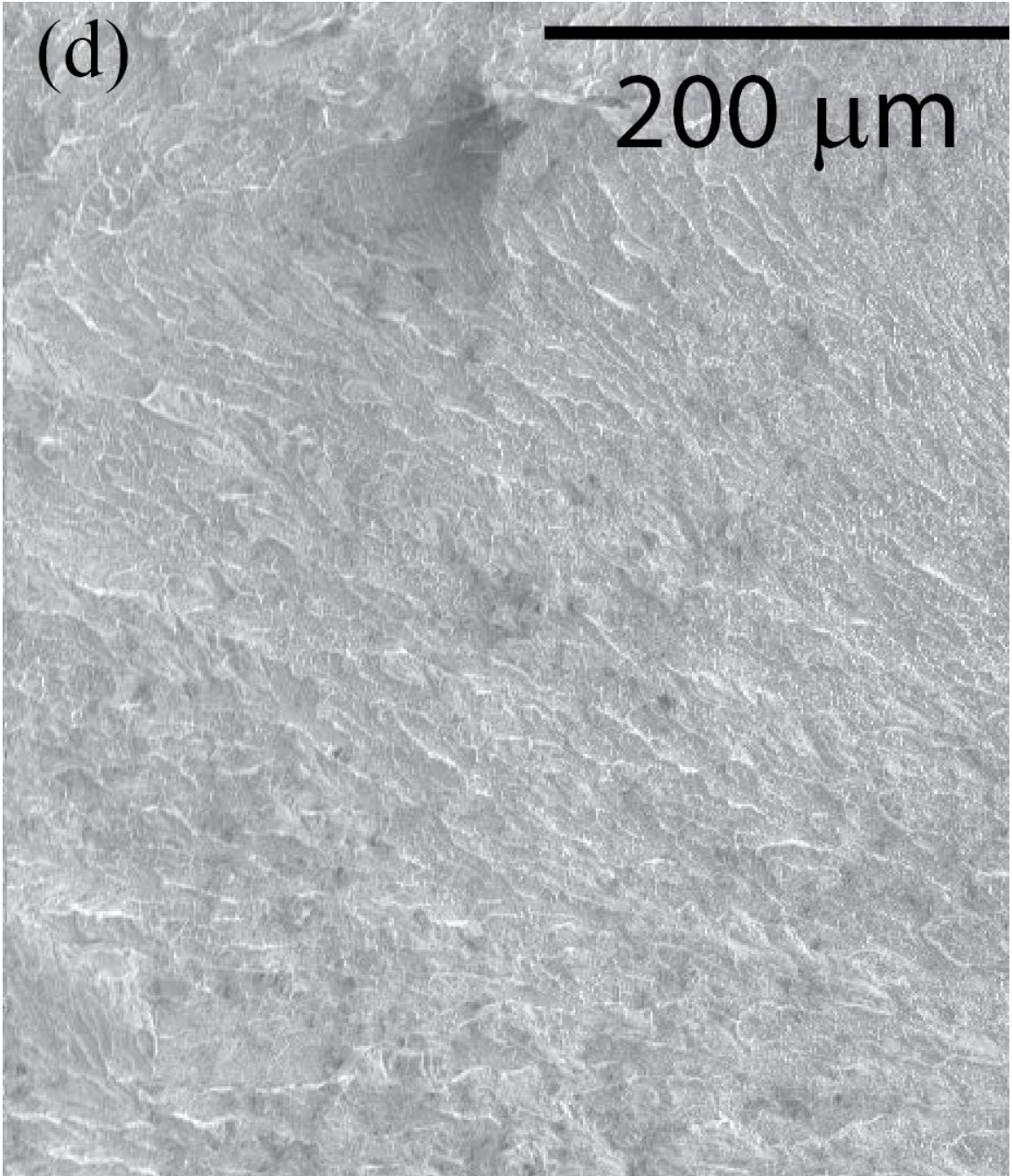
(a)



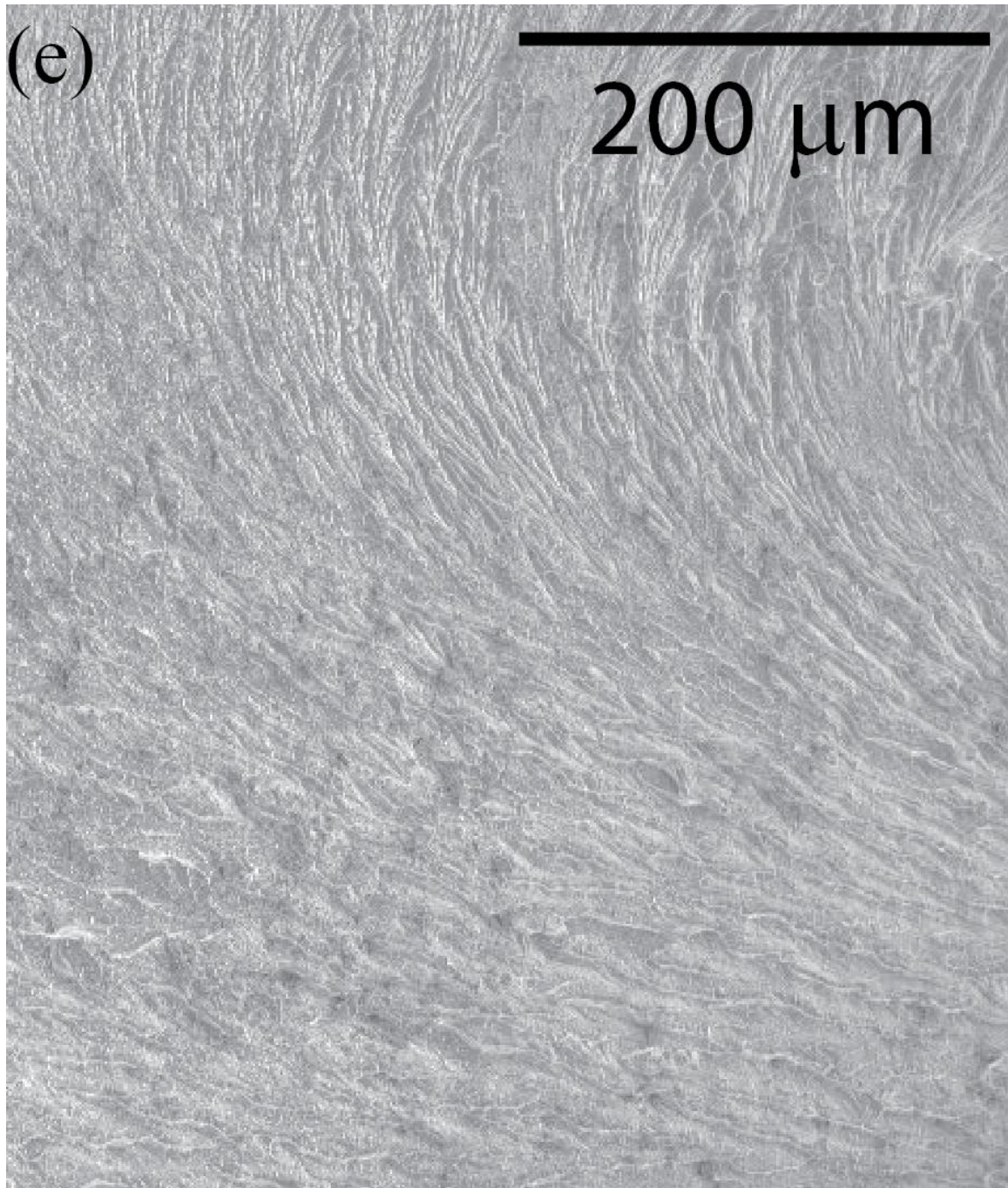
(b)



(c)

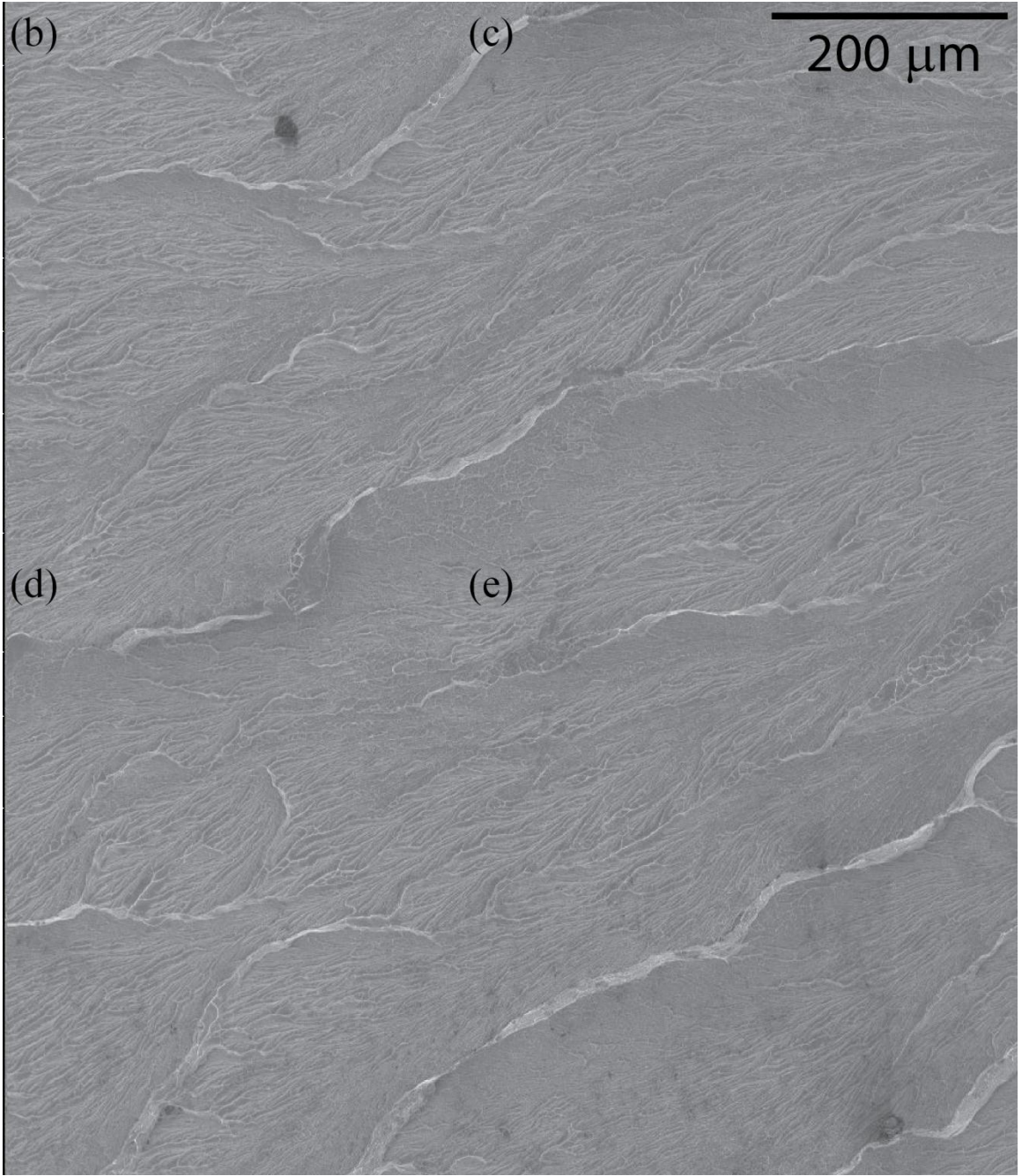


(d)

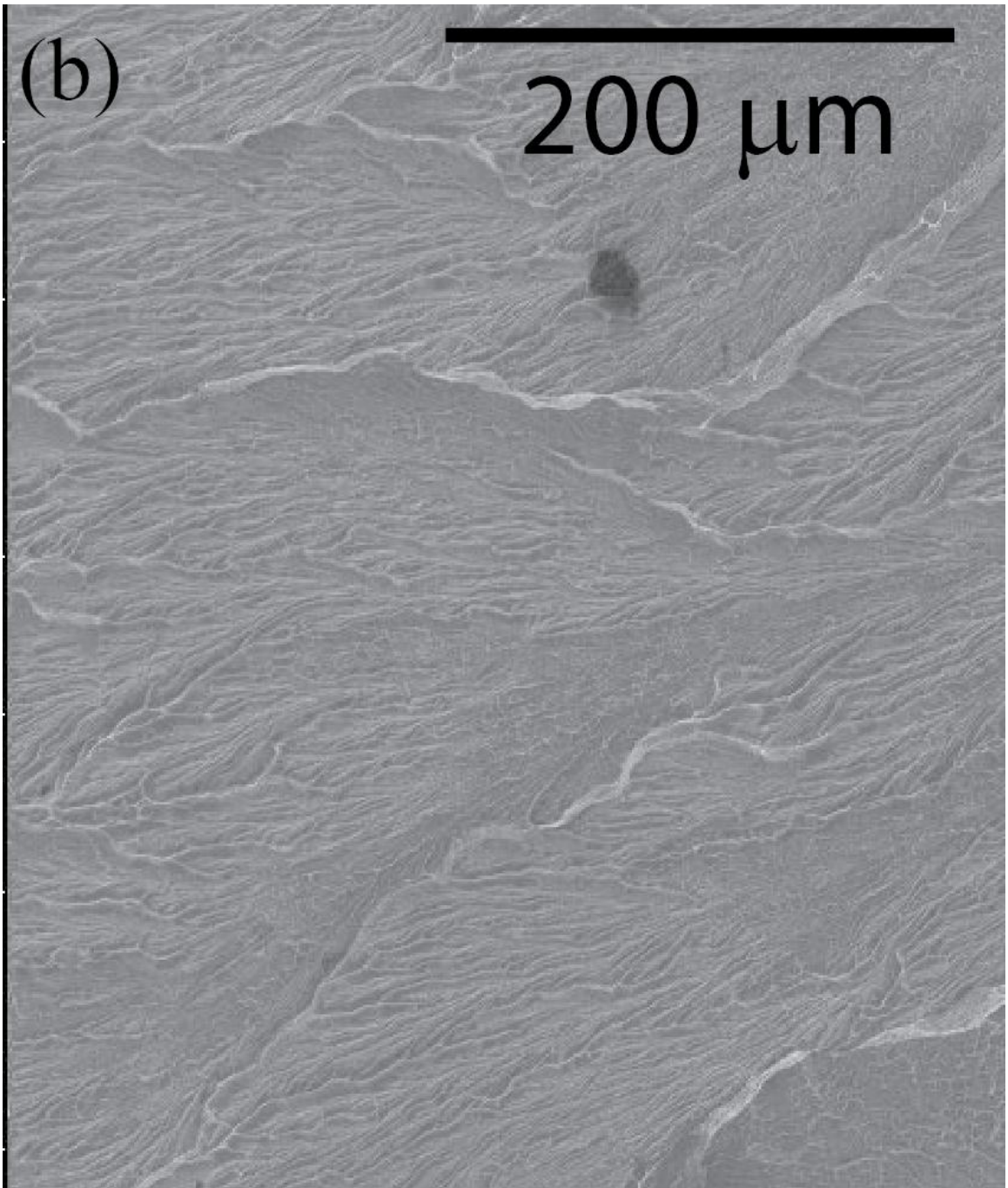


(e)

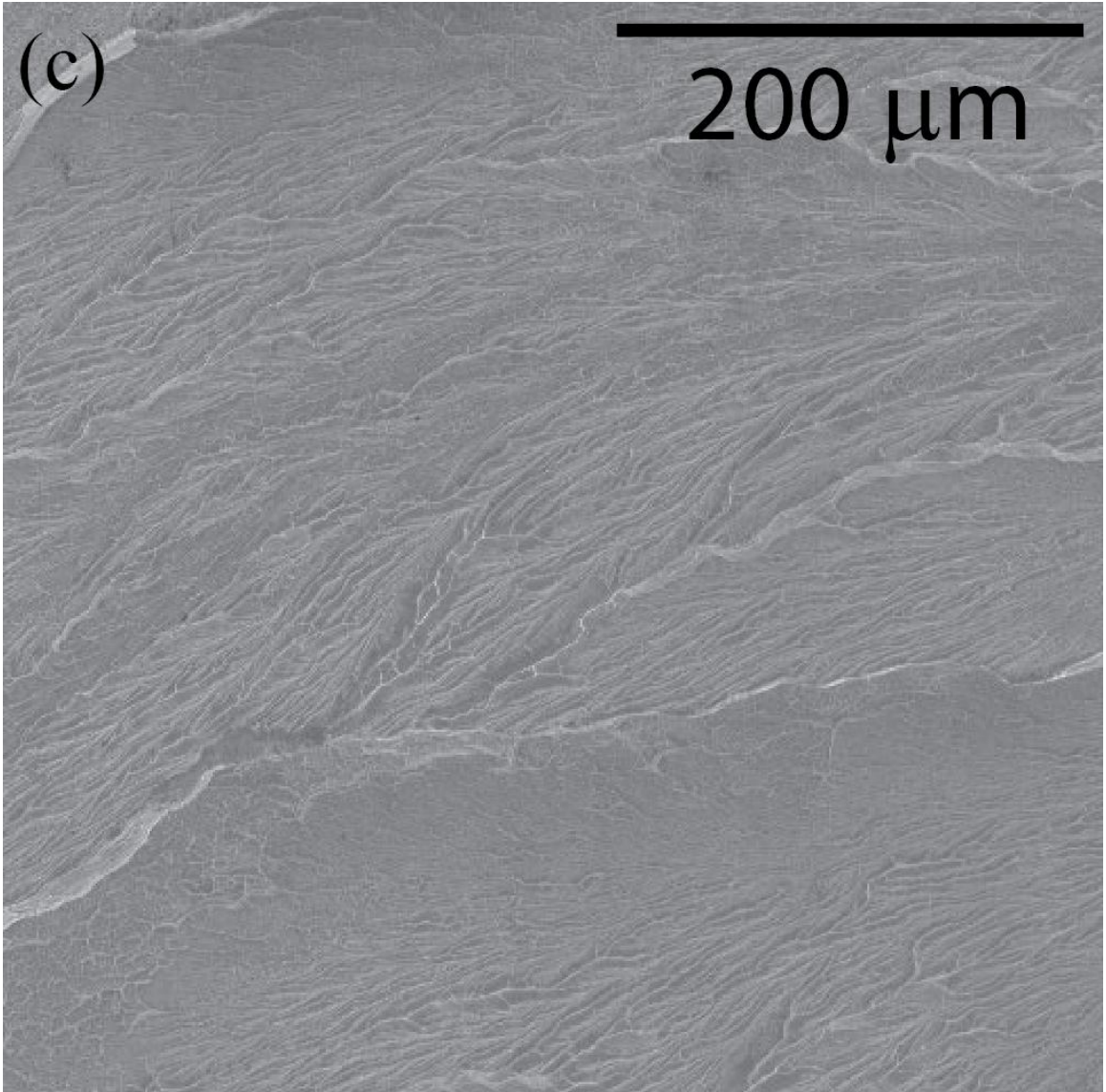
Figure 4.11 – (a) Fracture surface of region C from Figure 4.9, (b) top left quadrant of Figure 4.11(a), (c) top right quadrant, (d) bottom left quadrant, (e) bottom right quadrant.



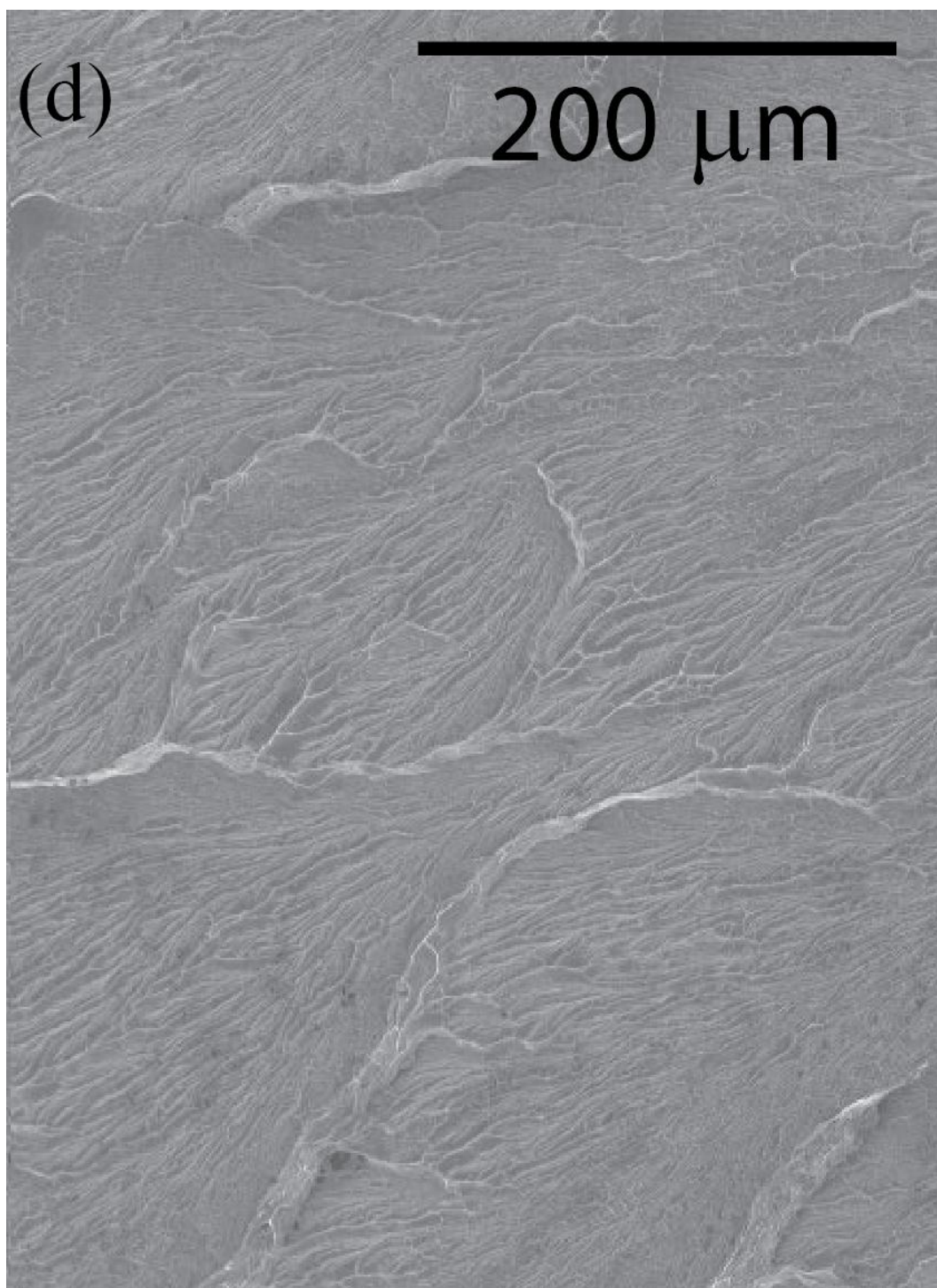
(a)



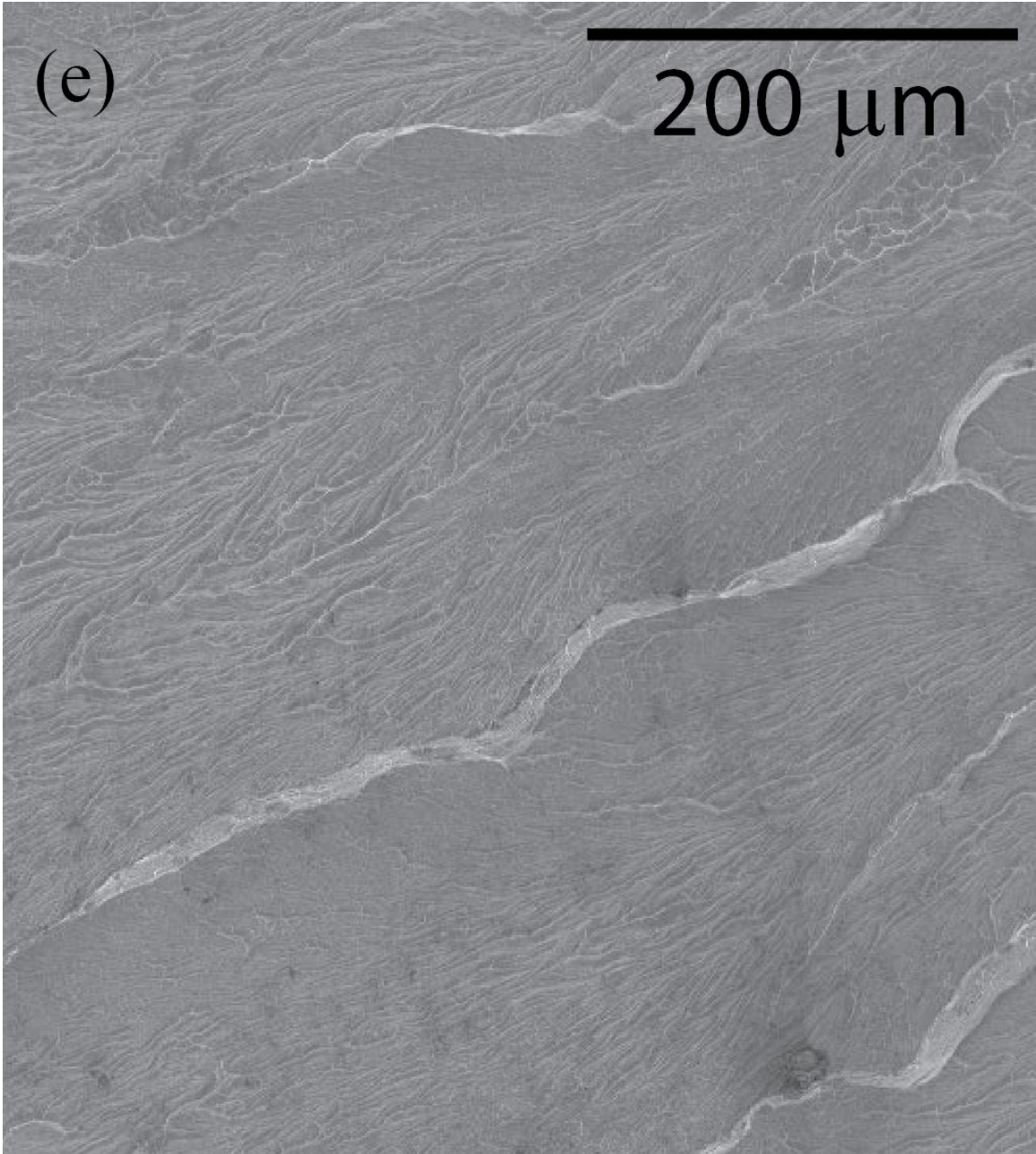
(b)



(c)

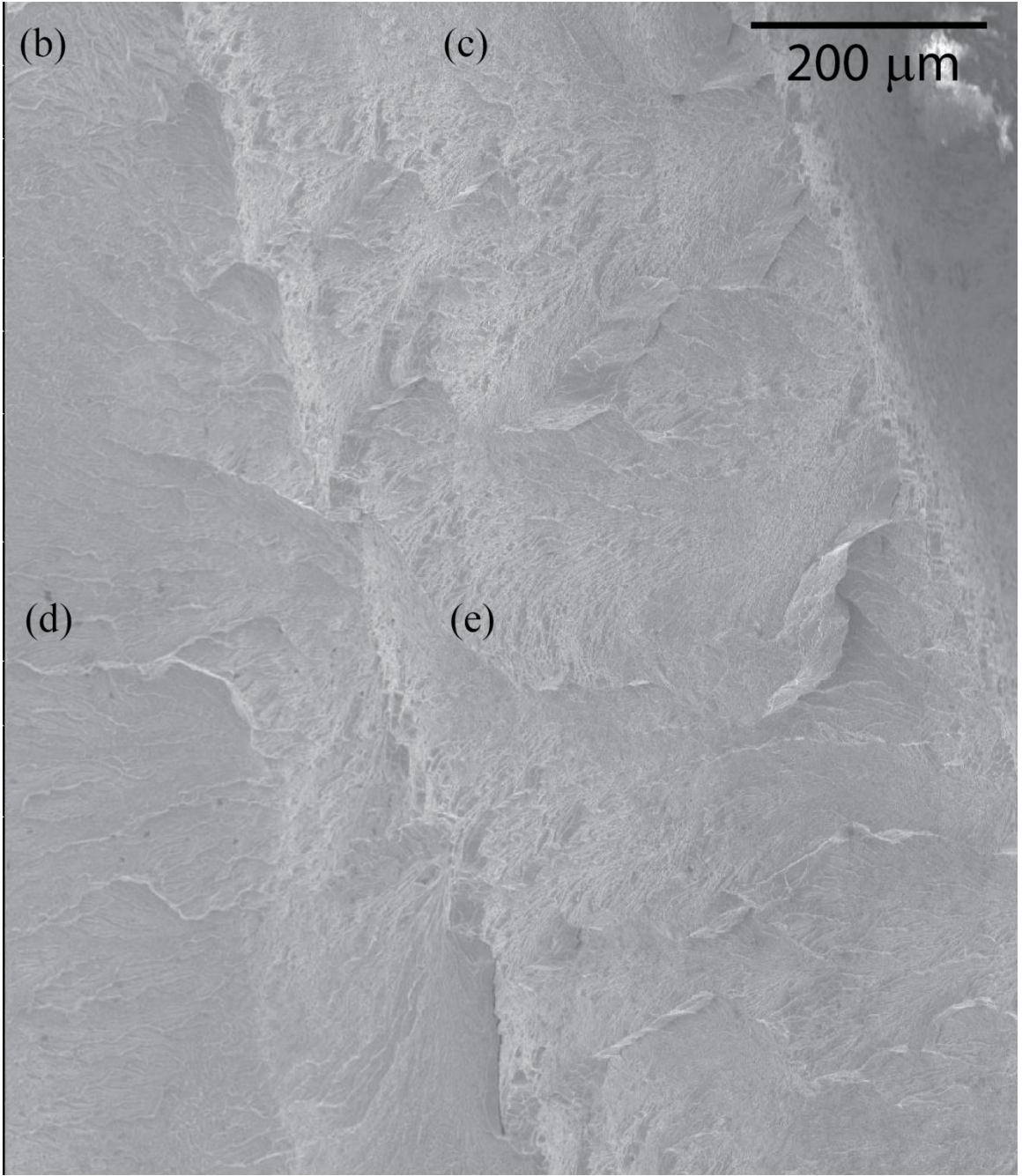


(d)

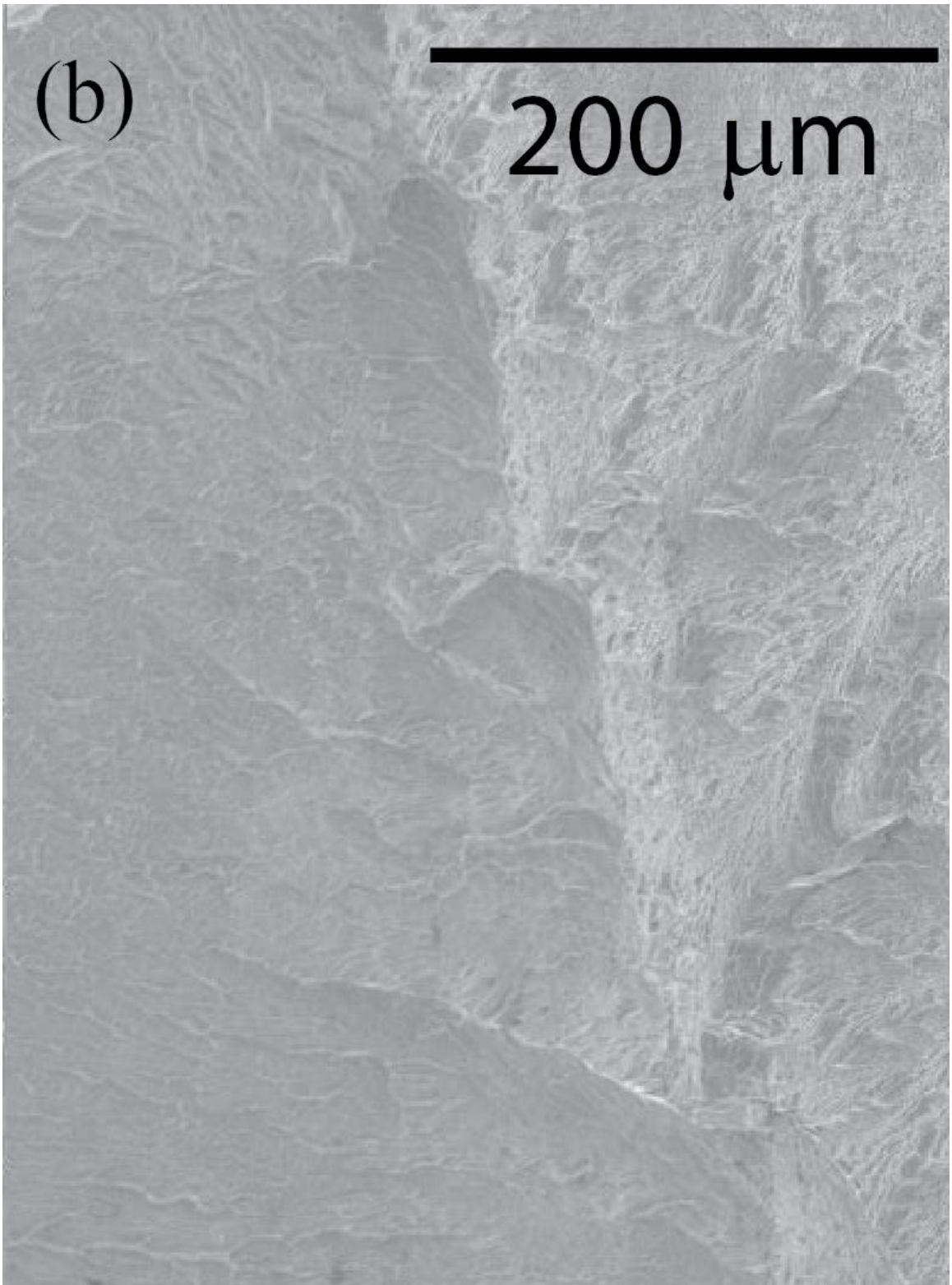


(e)

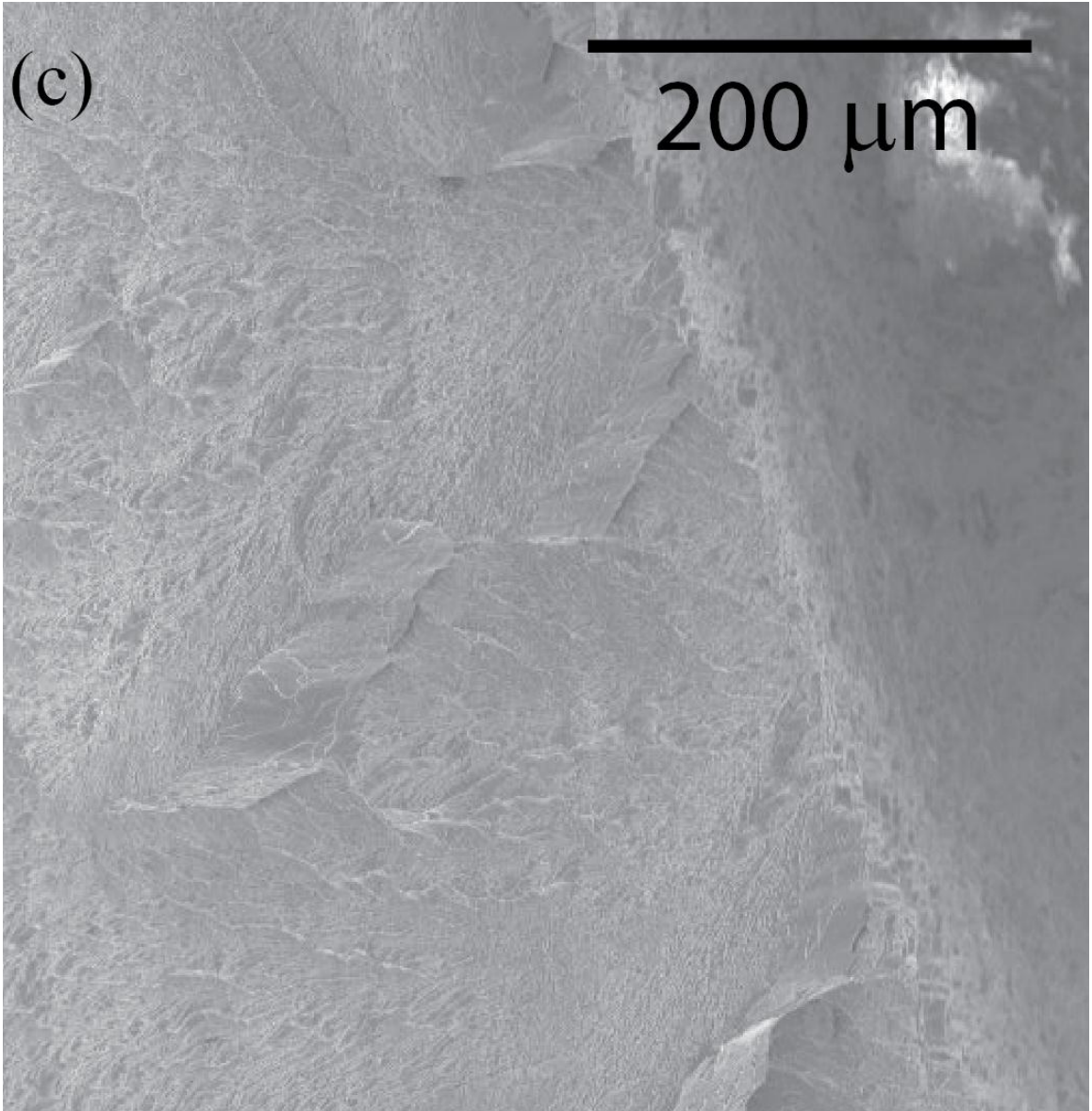
Figure 4.12 – (a) Fracture surface of region D from Figure 4.9, (b) top left quadrant of Figure 4.12(a), (c) top right quadrant, (d) bottom left quadrant, (e) bottom right quadrant.



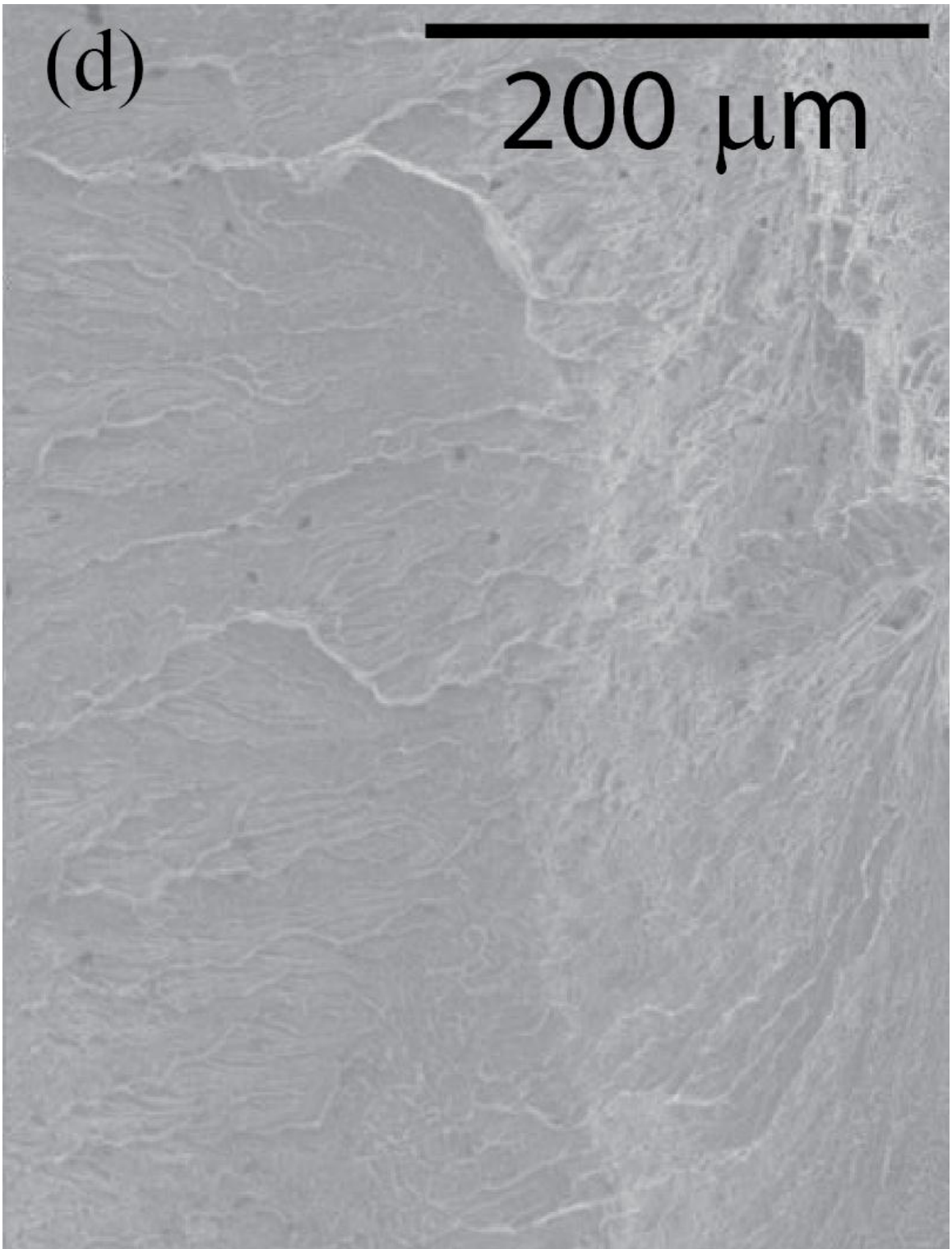
(a)



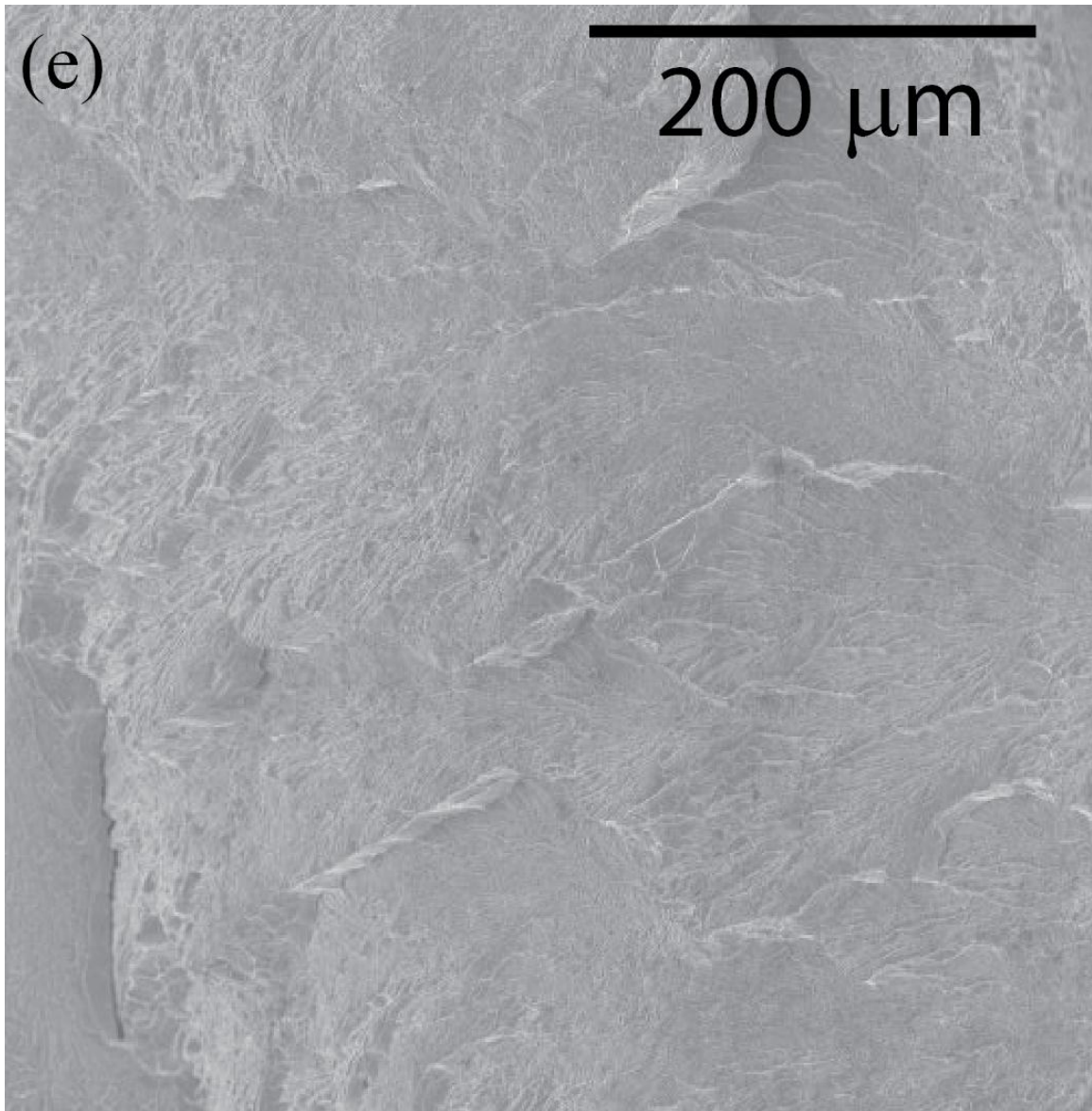
(b)



(c)



(d)



(e)

Figure 4.13 – (a) Fracture surface of region E (overload region) from Figure 4.9, (b) top left quadrant of Figure 4.13(a), (c) top right quadrant, (d) bottom left quadrant, (e) bottom right quadrant.

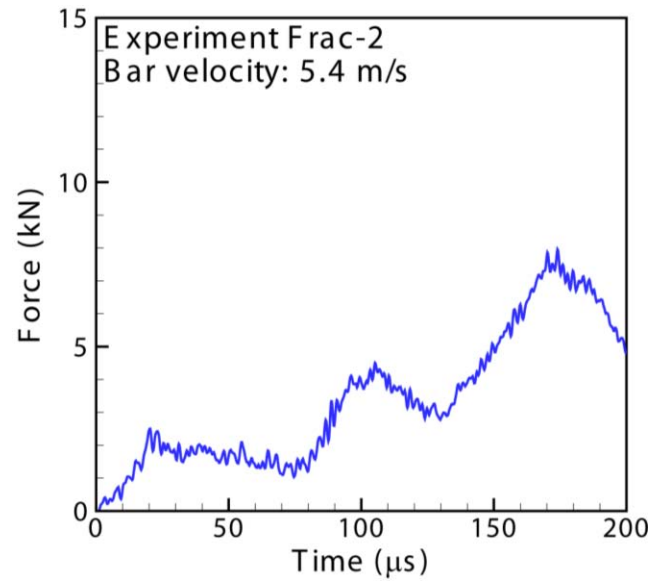
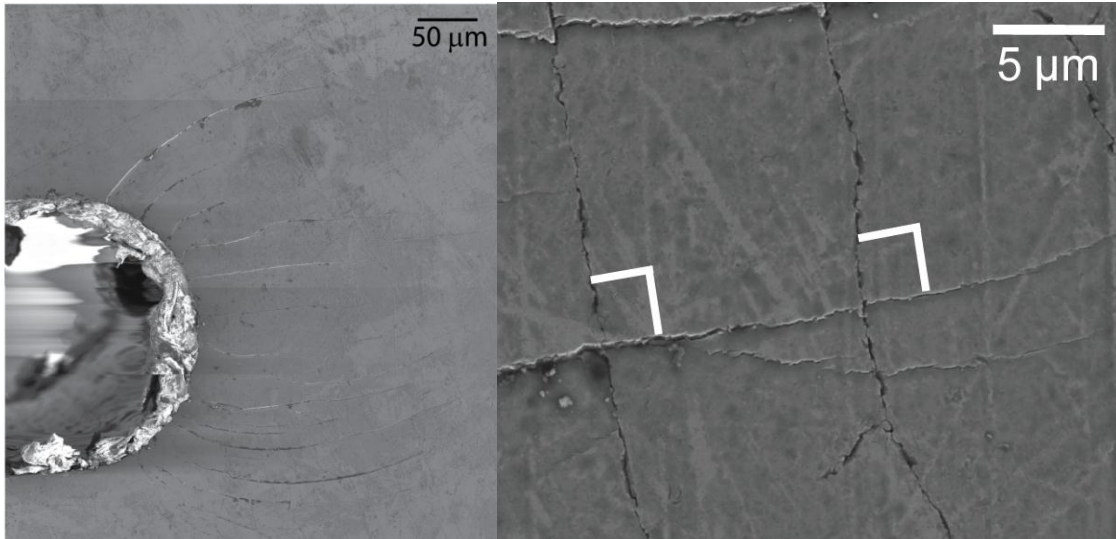


Figure 4.14 – Force-versus-time plot for a dynamic bending experiment in which failure did not occur



(a)

(b)

Figure 4.15 – SEM images after an experiment in which unstable fracture did not occur.

Fine scale deformation bands are present both (a) along the notch direction and (b) perpendicular to the notch. Note that the bands intersect at  $90^\circ$  to each other.

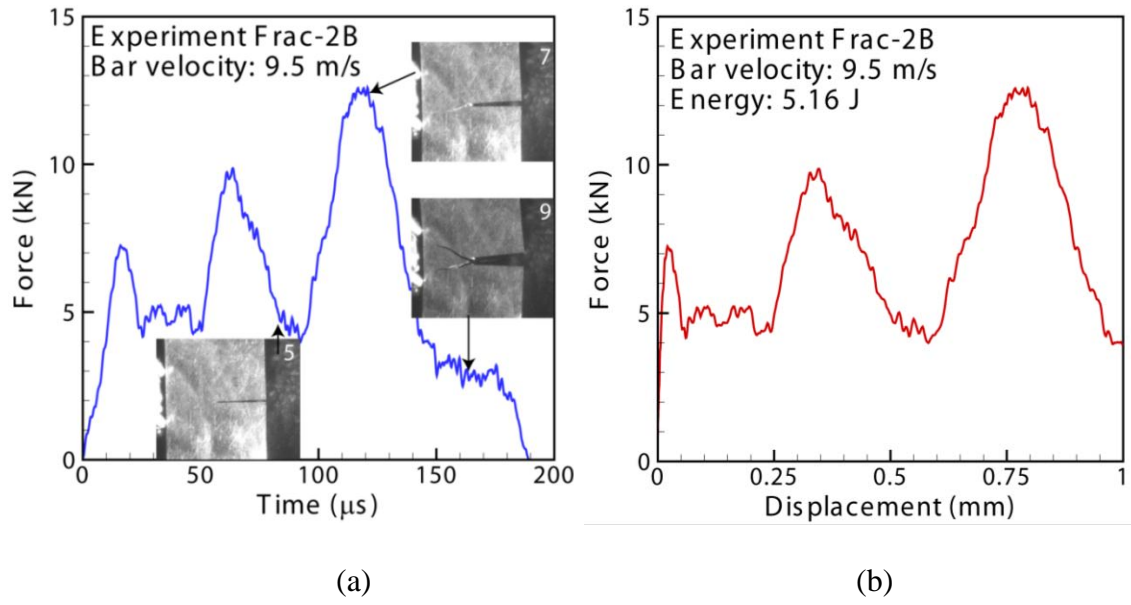


Figure 4.16 – Results from subsequent loading of initially damaged LM-1 sample: (a) force-versus-time curve with selected high-speed images, (b) corresponding force-versus-displacement curve, with failure at 120  $\mu\text{s}$ .

## ***Chapter 5: Literature Review of Hydroxy Terminated PolyButadiene (HTPB) and HTPB-based Particulate Composites***

### **5.1 Overview**

The loading response of composites has been of substantial scientific and technical interest because the presence of two dissimilar materials can provide attractive multifunctional properties, such as relatively high strength and stiffness with a low density. Typically, these composites consist of relatively hard and strong particles within a softer matrix; this arrangement allows the composite to take advantage of some of the high strength and modulus of the particles while also taking advantage of the plastic deformation allowed from the matrix. Such an arrangement may increase the amount of energy required to induce failure in some systems (such as with tungsten in LM-1), but the arrangement may also decrease the amount of energy (such as with silicon carbide in aluminum). In addition, careful selection of both the particles and the matrix can ensure that the resulting material has desirable properties, such as increased specific strength or specific modulus. Many classes of composites have taken advantage of the interplay between the particles and the matrix, such as metal matrix composites (e.g. increased specific modulus), ceramic matrix composites (e.g. increased damage tolerance), polymer composites (e.g. increased strength and stiffness), and even natural materials, such as engineered wood. However, the large majority of composites are anisotropic, because the particles (e.g., fibers) themselves often have preferred orientations.

Particulate composites are a particularly interesting class of composites because they may exhibit increased strength while preserving the isotropic nature of the resulting composite. One reason for this interest is application-driven, as energetic materials are essentially particulates with a polymer binder [1-4]. Understanding particulate composites is essential to gain insight into the response of energetic materials to mechanical loading. A second reason for this interest is the fact that the presence of the particles can provide as much as a tenfold increase in the strength of the composite while keeping a similar density to the original polymer. The motivation for the increase in the strength comes from the polymer having such a low peak stress [1-5] and Young's Modulus compared to the particles (e.g. 0.5 MPa and 5 MPa, respectively, for the polymer binder, ~100 MPa – 5 GPa and 5-500 GPa, respectively, for the particles). In addition, because the binder can support more strain than the particles, the overall strain is higher than if only the particles are present. However, to understand the particulate composite, an understanding of both the polymer binder itself, as well as the effects of the particles on the binder, is essential.

In this chapter, a background of one such polymer binder, hydroxyl-terminated polybutadiene (HTPB), is presented in Section 5.2. This discussion is expanded to consider the mechanical properties of the HTPB binder, an important material in the current study, in Section 5.3. A study of previous literature on the mechanical properties of HTPB-containing particulate composites is presented in Section 5.4, and this will put the scope of the current study, shown in Section 5.5, into context.

## 5.2 HTPB Binder Background

The HTPB binder is typically comprised of several components. Among the components are the HTPB pre-polymer, a material in the polyurethane family that contains one hydroxyl (-OH) group at each end; an isocyanate, an organic compound that contains at least one  $\text{-N=C=O}$  functional group; and an additive that is used to either extend the resulting polymer chains or to promote cross-linking or bonds between individual units in the polymer. Additional components used to create the polymer include catalysts (often, but not always, metal compounds). In this section, the HTPB, isocyanate, and chain extenders, and their roles in the properties of the binder will be discussed. In addition, information on the physical properties of the polymer as well as the structure-property relationships will be presented.

### 5.2.1 HTPB pre-polymer

The HTPB pre-polymer, as stated earlier, is largely a polymerized chain of butadiene molecules ( $\text{C}_4\text{H}_6$ ) [6]; at the ends of the chain are hydroxyl units (OH). The first polymerization reaction that results in the HTPB pre-polymer, an intermediate product which can be further polymerized, is shown in Figure 5.1. Crosslinking of the pre-polymer occurs when the hydroxyl units are not aligned in a linear fashion; this crosslinking leads to a higher functionality of the hydroxyl group (i.e. more reaction sites for covalent bonds). The number of butadiene molecules and hydroxyl units determines the molecular weight, thus also the ultimate tensile strength and durability of the polymer; lower molecular weights (due to fewer butadiene molecules in the polymer chain) typically lead to higher tensile strength and durability because more of the HTPB reacts

with the isocyanate which is needed to complete the urethane reaction [7]. The various degrees of crosslinking and the range in molecular weights of HTPBs (500-3500) lead to the existence of a variety of HTPBs, which are either viscous liquids or slightly waxy solids.

### *5.2.2 Isocyanates*

Isocyanates play a very important role in determining the nature of the resulting polymer, and several types of isocyanates have been developed to provide specific properties to the HTPB polymers. These isocyanates, which contain the  $-N=C=O$  functional group, react quite readily with other substances, which include water, alcohols/polyols (like HTPB), and amides. They are often so reactive that an excess of isocyanate will produce a further reaction with the intermediate product, thus producing a separate polymer. They come in three general forms – aromatic, aliphatic, and cycloaliphatic. Aromatic isocyanates, which contain hybrids of single and double bonds (much like benzene), are generally the most reactive of the three [6, 7]. Aliphatic isocyanates and cycloaliphatic isocyanates (which do not contain these hybrid bonds) are less reactive, but they are sometimes used when the end product has specific requirements, such as transparency and UV stability.

### *5.2.3 Chain extenders and crosslinkers*

The third major component of HTPB polymers can be either a chain extender or a cross-linker. The chain extender is a low molecular-weight reactant whose function is to connect the various prepolymer links. A number of chain extenders are either diols or

triols, units containing two or three alcohol groups, respectively, or amines. These chain extenders are often considered the “hard segments” to the “soft segments” of the HTPB polymer, and thus slightly increase the glass transition temperature of the resulting polymer and increase the strength of the polymer by increasing the number of hydrogen bonds and covalent bonds. However, these chain extenders (particularly diols) can also be slow to react with the pre-polymer, thus necessitating the use of a catalyst to speed up the reaction process. Alternatively, the “hard segments” can also be used as cross-linkers, in order to increase the strength and stiffness of the resulting structure; however, their presence (especially triols) can reduce those properties by reducing the molecular weight of the structure [8]. In particular, an excess amount of diol can increase the degree of reaction with the pre-polymer, thus increasing the functionality of the hydroxyl groups and increasing the amount of cross-linking present in the polymer. While the polymers are often classified by their average functionality, even a polymer with an average functionality close to 2.0 can have pockets of extensive cross-linking [6].

#### *5.2.4 Additional components*

Because of the slow reaction rate between chain extenders/cross-linkers and the HTPB prepolymer, additional components can be important in the preparation of the polymer. One of the most common ingredients is a catalyst that is used to speed up the reaction. Typically, the catalyst contains one or more metallic compounds, but tin catalysts, particularly stannous octoate, have been particularly effective when trying to perform the urethane reaction [7] which is needed to produce the HTPB polymer. Reactivity rates of isocyanates and hydroxyl units suggest that the presence of stannous

octoate (concentration of 0.1-0.3%) provides a two order of magnitude increase in the reaction rate, and the addition of amine catalysts (concentration of 0.2-0.5%) to the tin catalyst provides another tenfold increase in the reaction rate. On the other hand, the use of amines by themselves (concentration of 0.1%) provides roughly a 50-fold increase in the reaction rate compared to the uncatalyzed polymer, which may be useful when wanting to ensure complete reaction is delayed somewhat. Plasticizers, such as isodecyl perlargonate (IDP), soften the polymer, reduce the glass transition temperature (thereby increasing the range of temperatures in which it acts like a rubbery polymer), and increase the amount of strain needed to induce damage in the polymer.

#### *5.2.5 Physical properties*

HTPB polymers, because of the relatively large amount of “soft segments,” are rubbery polymers. Therefore, their glass transition temperatures are quite low (typically -40 to -60°C), even with the presence of the diols that are used to connect the HTPB prepolymer units. In addition, they exhibit a very high resiliency and can almost fully recover even when an 80% strain is applied. However, they also exhibit a very low modulus of elasticity as well as a low density (~0.9 g/cc), which means they are very low impedance materials and provide challenges in testing. They also exhibit low strength (~1 MPa) under quasi-static conditions, although this can vary depending on processing conditions.

While the elasticity and strength of HTPB polymers are generally quite low, there are several ways to alter the physical properties of the HTPB polymers. One of the most

important factors in determining the physical properties is the amount of HTPB and the amount of chain extenders in the polymer. Because the chain extenders have a relatively high glass transition temperature compared to the HTPB, a reduction in the chain extenders reduces the strength and modulus of the resulting polymer and increases the ultimate tensile strength. Another factor related to improving the mechanical properties of the HTPB polymer is the molecular weight; an increased molecular weight will increase both the strength and modulus. Higher intermolecular forces [6] and chain stiffness [9], particularly due to the presence of aromatic chains, also increase the hardness and melting point of the polymer. The presence of crystallinity plays a substantial role in the mechanical properties of the polymer; there is a positive correlation between the crystallinity of the polymer and the hardness, modulus, and strength. Finally, cross-linking, particularly in the presence of crystallinity, has fairly complex results [10, 11]. In amorphous polymers, the strength increases, but when there is some limited crystallinity in the polymer, a small amount of cross-linking reduces the regularity and alignment of the previously crystalline polymer, thus reducing the modulus of the polymer; increased amounts of cross-linking increase the modulus until the polymer molecules can no longer move and the polymer becomes rigid.

### **5.3 Mechanical Properties of the HTPB Polymer**

In the past, a number of experiments have been conducted on various HTPB polymers, which vary by the concentrations of HTPB, isocyanates, chain extenders, and catalysts. These experiments can be grouped into low strain-rate experiments (below 100/s), which are either quasi-static experiments or dynamic mechanical analyzer (DMA)

experiments, or high strain-rate experiments, in which a Split-Hopkinson Pressure Bar (SHPB) or gas gun is employed. In this section, papers that have investigated strain-rate effects will be discussed in order to provide an understanding of the current body of literature on HTPB polymers.

### *5.3.1 Low strain-rate mechanical properties*

Among the first set of experiments conducted on HTPB polymers at quasi-static strain-rates were those conducted by Blumenthal et al. [5]. Quasi-static experiments were conducted in compression for the HTPB-based polymer to understand the effects of both temperature and strain-rate on the mechanical properties (modulus of elasticity and strength) of an HTPB-based polymer. This polymer consisted of approximately 47% HTPB monomer, 47% plasticizer (IDP), and 6% isophorone di-isocyanate (IPDI), along with small amounts (<1% by weight) of antioxidant and catalyst, and it was cooled down with liquid nitrogen spray to facilitate machining. The quasi-static experiments were conducted at temperatures ranging from -40°C to 22°C at a strain-rate of  $10^{-3}$ /s, and strain measurements were conducted using crosshead displacements as well as specimen extensometer measurements. Results showed that the temperature dependence on the flow stress (at 10% strain) of the HTPB polymer was much stronger at lower temperatures than at room temperature; from -20°C to 20°C, the flow stress was constant at approximately 0.1 MPa, while at -50°C, the flow stress increased to 0.25 MPa.

Another study was conducted by Siviour et al. [12] on a slightly different HTPB polymer. While few details are present, it appears that the polymer was 33% plasticizer

(dioctyl sebatate) and the HTPB and isocyanate make up roughly the remaining 67% of the polymer. In this set of experiments, DMA sweeps were conducted between  $-100^{\circ}\text{C}$  and  $-30^{\circ}\text{C}$ , and by varying the frequency from 1-100 Hz, the effective strain-rates were varied from  $4.8 \times 10^{-3}/\text{s}$  to  $4.8 \times 10^{-1}/\text{s}$ . Based on the results from the DMA experiments, which provide information about the flexural modulus of the polymer, along with the glass transition temperature exhibited at the different strain-rates, a flow stress of about 80 MPa (corresponding to 10% strain) was suggested for temperatures about  $-70^{\circ}\text{C}$ , which was the approximate glass transition temperature at a strain-rate of 3000/s. This flow stress was extrapolated by making several assumptions: the glass transition temperature and the flexural modulus would exhibit the same dependence on strain-rate as was observed in the DMA sweeps, the polymer acts in a linear elastic manner, and that the modulus of the polymer can be directly determined from the SHPB experiments. Siviour et al. [12] state that an increase in the loading-rate by one order of magnitude increases the glass transition temperature by about 3.6 K. However, the extrapolated values of stress are dependent on a largely constant modulus of elasticity throughout the 10% strain, which is not consistent with typical polymer behavior.

### *5.3.2 High strain-rate mechanical properties*

In addition to the quasi-static experiments on the HTPB polymer, Blumenthal et al. [5] conducted additional experiments on the SHPB for temperatures from  $-55^{\circ}\text{C}$  to  $22^{\circ}\text{C}$  to examine the effects of strain-rate in the HTPB polymer. In these experiments, 8 mm diameter HTPB specimens ( $L/D = 0.4$ ) were tested at strain-rates of  $\sim 2500/\text{s}$  using a AZ31B magnesium alloy bar; the magnesium alloy bar was employed in order to

maximize the strain in the bars, and therefore, the resolution of the resulting signal. One key issue brought up in this set of experiments was the time required for the sample to reach equilibrium; comparison of the one-wave (transmitted signal) and two-wave (incident and reflected signal) calculations showed that equilibrium conditions did not occur in the polymer until approximately 5% strain had accumulated. In addition, it is apparent that there are still significant variations in the one-wave analysis (a variation of 0.25 MPa, compared to a flow stress of about 0.5 MPa at 10% strain). The dispersive nature of the HTPB polymer appears to be the cause of this noise, although alignment issues cannot be ruled out. Results from these experiments suggest a slight temperature dependence from -20°C to 20°C (decrease of flow stress from 0.6 MPa to 0.5 MPa), but that temperature dependence becomes much more substantial at -40°C (flow stress of 1.8 MPa). At all temperatures, there was strong strain-rate sensitivity (over 6 orders of magnitude of strain-rate, the flow stress increased between four-fold and eight-fold), and the flow stress is being used in lieu of a peak stress because specimen failure did not occur.

In a similar way, Siviour et al. [12] conducted experiments employing the SHPB at strain-rates of approximately 3000/s in order to compare to the earlier DMA results. Experiments were conducted on 5.6 mm and 9.8 mm diameter specimens ( $L = 2$  mm in both cases), and these specimens were prepared using a cork borer attached to a drill press operating at a high angular velocity and a slow feed rate (although details of the speed and feed rates are not present in the paper). Lubrication in these experiments was achieved by the use of paraffin wax, and a wide range of temperatures (-80°C - 20°C)

were achieved by the use of an environment chamber and helium gas. Because of the cooling of the bars, Inconel and magnesium alloy bars were used for the lower ( $< -20^{\circ}\text{C}$ ) and higher temperature experiments, respectively, as these two materials exhibit little variation in mechanical properties in the temperature range of the study. In addition, polyvinylidene fluoride gages were utilized on the front and the back of the specimen to ensure that the front and back stresses were equal in order to assure equilibrium of the specimen [13]. Results of the experiments suggest a glass transition between  $-40^{\circ}\text{C}$  and  $-60^{\circ}\text{C}$  based on the tenfold increase in the flow stress at 10% strain (from 4 MPa to 40 MPa) and a transition from strain-hardening to essentially elastic-plastic behavior, and further experiments showed that the glass transition temperature is closer to  $-45^{\circ}\text{C}$ , in agreement with DMA extrapolation which suggested a change in the glass transition temperature from  $-70^{\circ}\text{C}$  to  $-48^{\circ}\text{C}$  as the effective strain-rates were increased by roughly six orders of magnitude. Further cooling (to  $-80^{\circ}\text{C}$ ) shows another increase in the flow stress (to 100 MPa) but a transition to strain softening after the peak stress is reached, and more brittle behavior was observed.

Millett et al. [1] conducted plate-impact experiments to determine the Hugoniot of two different HTPB binder formulations (one proprietary, one containing roughly 88% HTPB, 12% IPDI, and 0.05% tin catalyst, but no plasticizer). Experiments to measure the Hugoniot were performed by casting a 10 mm plate of HTPB between a 1 mm cover plate (either dural or copper) and a 12 mm polycarbonate backing to form the target assembly, while the same material from the cover plate was used for the flyer. Manganin stress gages were placed in between the cover plate and the HTPB, as well as between the

HTPB and the polycarbonate backing, in order to measure the shock velocities at 2 different points in the material. Additional experiments were conducted for recovery of the HTPB specimens; these samples were 20 mm in diameter and 4 mm in thickness, and momentum trapping was used to prevent lateral release waves in the HTPB. In these experiments, a very limited amount of relaxation occurred in the samples after equilibrium was reached, but over the impact stresses of interest (0.24-2.4 GPa), there was no Hugoniot elastic limit (HEL) present. In addition, comparison of the shock velocity vs. particle velocity lines shows that HTPB 2 exhibits a higher shock velocity at zero particle velocity along with a lower dependence of the particle velocity on the shock velocity, both of which are consistent with the observation that HTPB 2 is stiffer (which is expected, as HTPB 1 has plasticizer, but HTPB 2 does not). Recovery experiments conducted at impact stresses of 0.8 GPa and 1.5 GPa revealed no substantial change in the glass transition (evident from the differential scanning calorimetry scans) nor a change in the amount of toluene it is capable of absorbing over a sufficiently long time to produce steady state conditions.

#### **5.4 Mechanical Properties of the HTPB Composites**

While the HTPB polymers are extremely compliant, the addition of any crystalline material increases the strength and the stiffness of the composite while still preserving some measure of ductility in the resulting composite. In addition, because the crystalline material is typically in small particles (e.g. 25-300  $\mu\text{m}$  in diameter), the resulting isotropy of the composite is largely preserved. However, the size of the particles in the composite often dictates the resulting strength of the composite, and the

strain-rate sensitivity of the polymer plays a role in determining the strain-rate sensitivity of the composite.

#### *5.4.1 Low strain-rate*

Among the first quasi-static experiments conducted on an HTPB composite was that performed by Blumenthal et al. [5] on PBXN-110. In these experiments, 19 mm diameter specimens ( $L/D = 0.5$ ) were tested under strain-rates of 0.01/s or 0.1/s, but no lubrication was used in these experiments. Experiments were conducted at  $-15^{\circ}\text{C}$ ,  $22^{\circ}\text{C}$ , and  $50^{\circ}\text{C}$  in order to understand the effects of temperature as well. Decreases in temperature were shown to increase the maximum stress, the modulus, and the strain exhibited by the samples, but less drastically than, for example, Siviour's HTPB samples, which is consistent with the assertion that the temperatures at which the experiments were conducted were much higher than the glass transition temperature ( $-89^{\circ}\text{C}$ ). In addition, preparation methods appeared to have some effect on the strain (hand-cored samples exhibited lower strains than samples prepared using a core punch mounted in a press) and modulus (hand cored samples exhibited higher moduli).

Additional quasi-static experiments were conducted on a polymer-bonded sugar (PBS) by Siviour et al. [12]. Experiments were conducted on 10 mm diameter samples ( $L/D = 0.5$ ) of QRX030 PBS, which consists of 66% sugar crystals (50% having a particle size between 250 and 375  $\mu\text{m}$ ) and 34% HTPB binder at room temperature. The effects of strain-rate at the quasi-static level were examined by performing experiments at  $2 \times 10^{-3}/\text{s}$ , and temperature dependence was determined by conducting additional

experiments in a DMA (effective strain-rates of  $2 \times 10^{-3}/s$ ,  $2 \times 10^{-2}/s$ , and  $2 \times 10^{-1}/s$ ). The room temperature quasi-static experiments showed a peak stress of approximately 0.5 MPa, followed by a drop-off in stress to about 0.3 MPa between 15% strain and 30% strain. In this region, there appeared to be a change in the optical properties from off-white and translucent to white and opaque in this drop-off region. DMA results show the presence of two components of the glass transition; one was present at  $-78^{\circ}\text{C}$  (strain rate of  $2 \times 10^{-3}/s$ ) and appeared to rise approximately 5.5 K as the strain-rate was increased by an order of magnitude, while the other was present at about  $-20^{\circ}\text{C}$  and appeared to rise approximately 9 K for each order of magnitude increase in strain-rate. Additional examination was performed using X-ray tomography, in which a number of scans are produced at different cross-sections in order to view virtual “slices” of the specimen without having to perform additional preparation of the sample. X-ray tomography shows substantial debonding of QRX030; that debonding was shown to precede strain-softening that is present in the quasi-static experiments. However, it does not appear that alterations in the crystals (change of shape, size, or fracture) occurred in the PBS.

#### *5.4.2 High strain-rate*

One early work that focused on the high strain-rate behavior of an HTPB composite containing glass beads, plastic beads, and aluminum was performed by Kawata et al. [14]. In this work, high strain-rate tests were performed using a specialized dynamic tensile impact system, different from the SHPB. In this apparatus, rubber ropes were stretched using a worm wheel, and a pin is placed that holds an anvil (which contains a cutout the size of the specimen to prevent compressive loading). When the pin

is released, the ropes accelerate the anvil towards the specimen, thus generating a compressive pulse in the impact block; this pulse is reflected back through the impact block as a tensile pulse which propagates through the specimen. The results from these experiments show that the peak stress in the specimen was approximately 8 MPa, four times that of the specimens tested under quasi-static conditions, with a strain-at-failure of approximately 40%, compared to 60% in the quasi-static experiments. Several details of the experiment cause concern: first, equilibrium conditions in the specimen are not addressed, either through a constant strain-rate or through the matching of the front and back stresses; second, while calculations are made on the elastic modulus of the polymer, the specimen will not be in a state of equilibrium and the elastic modulus calculated will not necessarily be the dynamic elastic modulus.

One key work that focuses on the high strain-rate behavior of an HTPB composite is that of Blumenthal et al. [15]. In this work, SHPB experiments were conducted at a variety of temperatures ( $-55^{\circ}\text{C} - 22^{\circ}\text{C}$ ) on 6.4 diameter cylindrical samples ( $L/D = 0.5$ ) of PBXN-110 to examine the strain-rate sensitivity of the material and the effect of specimen preparation (hand-coring vs. precision-coring). Results from the experiments indicate a strong temperature-dependence on the peak stress of the material; the peak stresses at  $-55^{\circ}\text{C}$  were about 25 MPa, compared to about 5 MPa at  $22^{\circ}\text{C}$ . The results also indicate that failure did not occur in any specimens, nor were there any significant signs of damage in the tested material. Comparison of the hand-cored and precision-cored samples suggested that there was not a substantial effect on preparation; however, the

large scatter present at lower temperatures (e.g., 13 MPa at  $-40^{\circ}\text{C}$ ) suggests that the wide range of crystals present may have had an effect on uniformity of material properties.

In addition to the variety of quasi-static experiments conducted by Siviour et al. [12] on the PBS, additional high strain-rate experiments were conducted using the SHPB to examine the stress-strain response and material behavior of 6 mm and 8 mm diameter samples ( $L/D = 0.5$ ) of QRX030 at 2000-3000/s for temperatures from  $-100^{\circ}\text{C}$  to  $20^{\circ}\text{C}$ . Once again, there appears to be a strong temperature dependence on the high strain-rate experiments, particularly when reducing the temperature from  $-20^{\circ}\text{C}$  (corresponding to a flow stress of 10 MPa) to  $-40$  and  $-60^{\circ}\text{C}$  (corresponding to flow stresses of 20 and 50 MPa, respectively), suggesting that the glass transition point for this material is in the neighborhood of  $-30^{\circ}\text{C}$ . While there appears to be some strain hardening above the glass transition temperature, the strain hardening is virtually zero for temperatures of  $-40^{\circ}\text{C}$ . The rapid fall in the stress-strain curve for temperatures below  $-60^{\circ}\text{C}$  suggests that brittle behavior may dominate at such temperatures, as well. However, the lack of strain softening suggests that debonding plays less of a role at high strain-rate. In contrast, the high strain-rates, combined with the low temperatures, appear to lead to brittleness of the binder. High-speed video, not present in this paper, would be useful in confirming whether brittle specimen failure occurred under these conditions. Particle-particle interaction was suggested as another possible cause of the change in flow and fracture behavior in the high strain-rate experiments at  $-80^{\circ}\text{C}$ . Earlier work [13] has shown that increasing the median particle size from  $160\ \mu\text{m}$  –  $710\ \mu\text{m}$  in a different HTPB

composite has also been shown to contribute to the presence of a distinct yield point, but it also reduces the flow stress of the composite and increases its strain-rate sensitivity.

A similar study on an HTPB binder simulant was performed by Drodge et al. [16] utilizing the SHPB. Experiments were conducted between  $-100^{\circ}\text{C}$  and  $50^{\circ}\text{C}$  on 8 mm and 10 mm diameter samples of a simulant containing both HTPB and sugar. All of the bars employed in the experiments are Inconel, and no pulse shaper was used; the presence of both of these likely added additional noise to the resulting stress-strain signals. In addition, digital image correlation was conducted on the PBS samples using a Hadland Ultra-8 high-speed camera to view the sample at various stages of deformation. Experiments conducted showed the presence of a glass transition between  $-50^{\circ}\text{C}$  and  $-35^{\circ}\text{C}$ , as evidenced by the increased peak stress (from 20 MPa to 45 MPa) and the presence of what appears to be “strain-softening”. The peak stress of the simulant was 80 MPa at  $-80^{\circ}\text{C}$ , but there appeared to be a reduction at lower temperatures. Weakening of the simulant, according to the authors, was due to stress localization, but no further information was provided that would verify such behavior. In addition, line laser measurements and corresponding volume calculations showed that dilatation was present during compression; the lack of barreling, verified through the high-speed camera images, suggests that the dilatation was due to mesoscale damage. This is in agreement with the suggestion that stress localization is occurring in these composites.

Additional experiments were conducted by Drodge and Proud [17] on HTPB/sugar simulant in order to separate the effects of particle-particle spacing and

particle size, as previous work conducted by Balzer et al. [18] suggested that the flow stress of HTPB/ammonium perchlorate composites was proportional to the inverse square root of both particle size and particle-particle spacing. To decouple these two factors, SHPB experiments were conducted on two groups of composites – one varying the percentage of sugar by weight while fixing the particle distribution (thus varying the particle-particle spacing), and the other varying the particle distributions while fixing the particle-particle spacing. Room temperature SHPB experiments were conducted on 8 mm diameter specimens ( $L/D = 0.625$ ); magnesium AZ91 bars were employed to reduce noise effects. Results from the experiments show that the flow stress at 10% strain increased approximately linearly as the median particle size increases from 150  $\mu\text{m}$  to 500  $\mu\text{m}$  but decreased as the particle-particle spacing increases. Further analysis shows that there is a positive correlation between the flow stress and the fill fraction, but it is apparent that there are competing mechanisms when trying to predict the flow stress of these composites.

Little work has been conducted on HTPB composites under shock loading, but work has been conducted by Millett and Bourne to determine the Hugoniot of a plastic bonded explosive, two sugar simulants, and three simulants containing glass beads [2]. One of the simulants contains sugar crystals of 160  $\mu\text{m}$  (1.35 g/cc); the other contains crystals of 16  $\mu\text{m}$  particle size (1.31 g/cc). Both of these simulants are less dense than the explosive (1.58 g/cc) or pure sugar (1.48 g/cc). The three glass beads simulants were 60% soda-lime glass beads by weight and consisted of 30  $\mu\text{m}$  beads, 300  $\mu\text{m}$  beads, or a combination of the two (1.40 g/cc). The experimental setup is similar to that from the

shock loading experiments on HTPB (plate-impact experiments, dural/copper flyers, sugar/simulant cast into cups of 80 mm diameter and 11 mm thickness, manganin gages on both the front and back faces of the explosive/simulant). Stress vs. time profiles from the manganin gages reveal that the coarse grained simulant and the sugar exhibited substantial noise; the fine-grained simulant and the explosive exhibited very little noise in comparison. Stress vs. particle velocity curves comparing the sugar, explosive, and the two simulants show that the explosive exhibits behavior most similar to the fine-grained composite; similar curves also show that the soda-lime glass beads simulants exhibit stresses 2-3 times as high as that of the explosive. However, the particle size of the explosive crystals are primarily 30-300  $\mu\text{m}$ , which is much larger than the fine-grained composite; the authors clearly state that this means that the model simulant must be chosen carefully and that the relationship between the mechanical properties and the microstructural behavior must be approached carefully.

## **5.5 Scope of the present study**

While sugar is generally utilized to prepare the HTPB simulants, there are a number of papers that have investigated the effects of the addition of glass beads to produce polymer composites. Besides the work conducted by Millett et al. [2], three sets of experiments, have investigated the addition of glass beads under high strain-rate conditions. Work by Cardoso et al. [19] investigated the effect of adding glass bubbles to a polyester binder. While the peak stress increased under SHPB loading when the glass bubbles were added, the size scale of the glass spheres played a key role; while the largest spheres ( $> 100 \mu\text{m}$  in diameter) broke, smaller spheres either were intact or pulled

out of the composite. Finally, plate-impact experiments conducted by Yuan et al. [20] examined the effects of weave size of two glass-reinforced polymer composites (GRPs), one with a 5 mm weave size, the other with a 1.25 mm weave size. The difference in the spall strengths between the tighter weave and the coarser weave were quite substantial. The coarser weave GRP exhibited a spall strength of 45 MPa at an impact stress of 200 MPa, and this fell to 0 MPa at an impact stress of 600 MPa; on the other hand, the tighter weave exhibited a spall strength of 120 MPa at an impact stress of 300 MPa and a spall strength of 70 MPa at an impact stress of 2300 MPa.

While there has been some work conducted on the rate sensitivity of HTPB polymers and composites, the degree to which this rate sensitivity has been investigated at high strain-rates is limited. For a PBXN-110 composite previously tested by Joshi [21], an increase in the strain-rate from 1700/s to 3500/s increases the peak stress from 5 MPa to over 40 MPa. In addition, the literature that has been cited show a wide variety of HTPB polymers and composites that have been tested, so comparisons between HTPBs from different investigators will not entirely address the degree of rate sensitivity. To that end, chapter 6 will be separated into two parts. First, the experimental approach and results from SHPB compression experiments on HTPB polymer between 500/s and 4000/s will be detailed. Second, results from SHPB compression experiments on an HTPB composite with glass beads will be discussed.

## References

1. Millett J.C.F., Bourne N.K. (2004) The shock Hugoniot of a plastic bonded explosive and inert simulants. *Journal of Physics D: Applied Physics* **37**, 2613-2617.
2. Millett J.C.F., Bourne N.K., Akhavan J., Milne A.M. (2005) The response of soda-lime glass-hydroxyterminated polybutadiene composites to shock loading. *Journal of Applied Physics* **97**, 043524-043527.
3. Millett J.C.F., Deas D., Bourne N.K., Montgomery S.T. (2007) The deviatoric response of an alumina filled epoxy composite during shock loading. *Journal of Applied Physics* **102**, 063518-063516.
4. Millett J.C.F., et al. (2005) The equation of state of two alumina-filled epoxy resins. *Journal of Physics D: Applied Physics* **38**, 930.
5. Blumenthal W.R., Thompson D.G., Cady C.D., Gray G.T., III, Idar D.J. (2002) Compressive Properties of PBXN-110 and its HTPB-Based Binder as a Function of Temperature and Strain Rate. *12th International Detonation Symposium San Diego, CA, August 11-16, 2002.*
6. Szycher M. (1999) *Szycher's Handbook of Polyurethanes*, CRC Press, Boca Raton, FL.
7. Hillstrom W.W. (1988) Elastometric binders and bonding agents for desensitization of explosives. Aberdeen, MD.
8. Haska S.B., Bayramli E., Pekel F., Özkar S. (1997) Mechanical properties of HTPB-IPDI-based elastomers. *Journal of Applied Polymer Science* **64**, 2347-2354.

9. Mulliken A.D., Boyce M.C. (2006) Mechanics of the rate-dependent elastic-plastic deformation of glassy polymers from low to high strain rates. *International Journal of Solids and Structures* **43**, 1331-1356.
10. Manjari R., Pandureng L.P., Somasundaran U.I., Sriram T. (1994) Structure–property relationship of HTPB-based propellants. III. Optimization trials with varying levels of diol–triol contents. *Journal of Applied Polymer Science* **51**, 435-442.
11. Wingborg N. (2002) Increasing the tensile strength of HTPB with different isocyanates and chain extenders. *Polymer Testing* **21**, 283-287.
12. Siviour C.R., Laity P.R., Proud W.G., Field J.E., Porter D., Church P.D., Gould P., Huntingdon-Thresher W. (2008) High strain rate properties of a polymer-bonded sugar: their dependence on applied and internal constraints. *Proceedings of the Royal Society A: Mathematical, Physical and Engineering Science* **464**, 1229-1255.
13. Siviour C.R., Gifford M.J., Walley S.M., Proud W.G., Field J.E. (2004) Particle size effects on the mechanical properties of a polymer bonded explosive. *Journal of Materials Science* **39**, 1255-1258.
14. Kawata K., Chung H.-L., Itabashi M. (1994) Dynamic mechanical behavior of HTPB dummy composite propellant. *Advanced Composite Materials* **3**, 163-175.
15. Gray III G.T., Blumenthal W.R., Idar D.J., Cady C.M. (1998) Influence of temperature on the high-strain-rate mechanical behavior of PBX 9501. *The tenth American Physical Society topical conference on shock compression of condensed matter*, Amherst, Massachusetts (USA),

16. Drodge D.R., Addiss J.W., Williamson D.M., Proud W.G. (2007) Hopkinson bar studies of a PBX simulant. *15th International American Physical Society Conference on Shock Compression of Condensed Matter*, Hilo, HI, July 24-29, 2007.
17. Drodge D.R., Proud W.G. (2009) The effects of particle size and separation on PBX deformation. *16th International American Physical Society Conference on Shock Compression of Condensed Matter*, Nashville, TN, June 28 - July 3, 2009.
18. Balzer J.E., Siviour C.R., Walley S.M., Proud W.G., Field J.E. (2004) Behaviour of ammonium perchlorate-based propellants and a polymer-bonded explosive under impact loading. *Proceedings of the Royal Society of London. Series A: Mathematical, Physical and Engineering Sciences* **460**, 781-806.
19. Cardoso R.J., Shukla A., Bose A. (2002) Effect of particle size and surface treatment on constitutive properties of polyester-cenosphere composites. *Journal of Materials Science* **37**, 603-613.
20. Yuan F., Tsai L., Prakash V., Rajendran A.M., Dandekar D.P. (2007) Spall strength of glass fiber reinforced polymer composites. *International Journal of Solids and Structures* **44**, 7731-7747.
21. Joshi V.S., Lee R.J. (2002) Resolving Mechanical Response of Plastic Bonded Explosives at High Strain-Rate Using Split Hopkinson Pressure Bar. *Shock Compression of Condensed Matter - 2001: 12th APS Topical Conference*, Atlanta, Georgia (USA),

## Figures

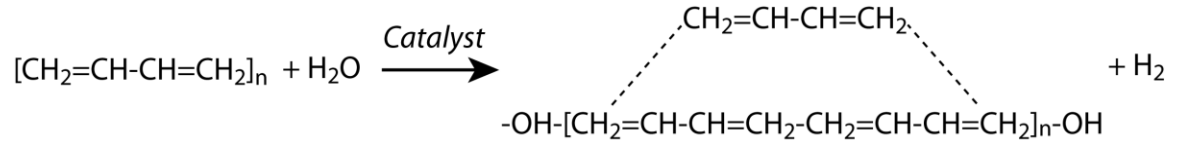


Figure 5.1 – Mechanism for synthesis of HTPB pre-polymer (prior to addition of isocyanates and plasticizer), which allows for the possibility of cross-linking.

## ***Chapter 6 - High Strain-Rate Compression of an HTPB polymer and its Particulate Composite***

### **6.1 Overview**

As noted in Chapter 5, there has been substantial interest in understanding the mechanical behavior of polymer-bonded explosives (PBXs) under high strain-rates [1-4]. PBXs consist of explosive crystals cast in a polymer binder, and their mechanical properties vary greatly depending on factors such as the solid explosive used, properties of the binder, and volume fractions of the crystals and binder in the PBX. The key to a PBX is the polymer coating that bonds the explosive granules into a solid, stable mass. Plastic bonding decreases sensitivity to initiation, but does not eliminate it. The choice of polymer and bonding technique involve both careful design, and continued verification through the processing, storage, and testing phases. A PBX that is too brittle can sustain damage or initiate during normal handling, and it can succumb to extreme temperature swings or thermal shocks. On the other hand, a PBX that is too soft may be susceptible to creep and may lack dimensional stability or strength. A number of previous investigations have focused on the initiation of PBXs due to explosive loading [1-6], however, in these studies the mechanical response (i.e. stress-strain behavior) of the explosive was not investigated. Understanding the high strain-rate behavior of the explosive is key to determine its sensitivity for initiation from mechanical impulses. The difficulty in preparing explosive samples and the high costs of conducting experiments with said samples, make the use of particulate composites, which simulate the structure of the PBX, of considerable interest.

In this chapter, the high strain-rate compression response of both the HTPB polymer and its associated particulate composite are investigated. Section 6.2 details experimental challenges that need to be addressed while testing these soft materials, including modifications to the SHPB to conduct testing on soft materials. In Section 6.3, details of specimen preparation for both the HTPB polymer and the simulant are provided. In Section 6.4, results from the SHPB experiments on both the HTPB polymer and the simulant as well as possible reasons for the observed rate-sensitivity in these materials are discussed.

## 6.2 Experimental Challenges in Testing “Soft” Polymers with the SHPB

The derivation of the governing relations between stress and strain in the specimen and the measured strains in the incident and transmitted bars was provided in Chapter 2 [7]. The key equations relating the stress and strain in the specimen to the strains in the incident and transmitted bars are provided here again for convenience

$$\dot{\varepsilon}_s(t) = -\frac{2c_0}{l_s} \varepsilon_R(t) \quad (6.1)$$

$$\varepsilon_s(t) = -\frac{2c_0}{l_s} \int_0^t \varepsilon_R(\tau) d\tau \quad (6.2)$$

$$\sigma_s(t) = \frac{F_1}{A_s} = \frac{F_2}{A_s} = E\varepsilon_T(t). \quad (6.3)$$

In Equations (6.1) - (6.3),  $\dot{\varepsilon}$  refers to the engineering strain-rate,  $\varepsilon$  refers to the engineering strain, and  $\sigma$  refers to the engineering stress in the specimen. All of these are

a function of the time,  $t$ ;  $L$  refers to the specimen length;  $c_0$  is the wave speed in the incident and transmitted bars;  $F_1$  and  $F_2$  are the stresses in front and back impact faces of the specimen, respectively;  $A$  is the area; and  $E$  is the Young's Modulus of the bar. The subscript  $R$  refers quantities related to the reflected pulse, the subscript  $T$  refers to quantities related to the transmitted pulse, and the subscript  $s$  refers to quantities related to the specimen. These equations also assume that the specimen is in a state of stress equilibrium.

The testing of soft materials in the SHPB has been studied by a number of investigators [7-9]. There are a number of challenges that are present when testing soft samples, including large difference in impedance between the bars and the specimens tested and the very small peak stresses (in some cases, less than 1 MPa) in the specimens. These challenges will be discussed in more detail in the following section.

### *6.2.1 Equilibrium considerations*

One of the most common issues in testing soft materials is the low density and low wave speed in these materials due to their low stiffness (for rubbery polymers, this can be two orders lower than in metals). This, in turn, leads to a much lower longitudinal mechanical impedance of the specimens, which can drastically increase the time necessary for equilibrium conditions to be reached in the specimen. As noted earlier, the minimum time required for equilibrium in the specimen is  $\pi$  round-trip transit times [7]; therefore, the time necessary for the specimen to reach equilibrium, i.e.  $t_{eq}$ , can be expressed as

$$t_{eq} = \frac{2\pi l_s}{c_s}. \quad (6.4)$$

For rubbery polymers, the bar wave speed is typically on the order of 1 km/s when compared to about 5 km/s for aluminum and steel; therefore, the time required for stress equilibrium is about five times as long for the polymer specimens (for a given specimen length) compared to steel or aluminum specimens. This necessitates the use of shorter specimens, and this approach has been advocated by other authors [9, 10], even if the L/D ratio is less than 0.5.

The shorter the specimen (for a given diameter), the more likely that radial (interfacial friction) effects will play a role in the SHPB experiment. For this reason, proper lubrication of the specimens to ensure minimal interfacial friction is essential; previous experiments have suggested either the use of molybdenum disulfide grease or petroleum jelly. In addition, other specimen configurations have been suggested, such as an annular specimen by Song and Chen [11]; however, the very low stresses (as will be shown in the next section) make reductions in area deleterious to the ability of accurately resolving the transmitted signals, and therefore, the overall stress profile of the specimen.

Additional methods have been used to determine whether a specimen is in equilibrium. Pulse shaping, discussed in Section 2.2, is a common one and has been utilized extensively in the testing of hard and soft materials [8, 10, 12]. The type of pulse shaper used is typically dependent on what desired strain-rate profile is needed (for example, a constant engineering strain-rate or a constant true strain-rate). Another method that has been popular is the comparison of the back stress ( $F_2$ , also used for a

one-wave analysis) and the front stress ( $F_1$ ) to determine whether equilibrium conditions exist in the specimen [8-11, 13, 14]; this comparison is called a two-wave analysis, while only the back stress is considered in a one-wave analysis. This method has been used as a standard for determining whether soft materials are in equilibrium. However, it can be difficult to get accurate measurements of when the incident, reflected, and transmitted pulses reach the strain gage, and slight variations (due to either noise in electronic components connected to the strain gages or changes in the start of the pulse) can lead to large variations in the front stress. For this reason, while the front and back stresses become largely equal after the specimen exhibits some true strain (usually 5%), the oscillations in the stress-strain curve can be substantially larger than the stress, especially for the softer materials.

### *6.2.2 Stress measurements*

One of the greatest difficulties in generating reliable stress-strain data in soft materials has been the relatively low level stresses supported by these materials. Engineering metals and ceramics, with yield strengths in excess of 100 MPa, are typically fairly easy to test in the SHPB because the corresponding transmitted bar strain gage signal (which are directly proportional to the stress in the specimen) are on the order of 0.25-1%, which can be easily measured with conventional foil gages. However, peak stresses in rubbery polymers and soft biomaterials are closer to 1 MPa [8, 9, 11, 13, 15], corresponding to transmitted bar strains (assuming a steel transmitter bar) of less than 0.01%, which are difficult to detect with a conventional foil strain gage.

The use of semiconductor strain gages to measure the incident and transmitted bar strain signals has been the method of choice to circumvent the aforementioned problems [8, 10, 11]. Compared with foil gages, which have a gage factor (defined as the percentage change in resistance divided by the percentage change in strain) of about 2, semiconductor strain gages have a gage factor of about 140, thus allowing for strains of less than 0.01% to be detected in the transmitted bar. However, when testing soft materials, the use of semiconductor strain gages (and other piezoresistive gages, such as quartz gages [11]) may not be enough to resolve meaningful stress-strain data by itself.

Two other methods are commonly used to improve the resolution of the stress-strain data generated in the SHPB experiments. The first method is to change the material used for the striker, incident, and transmitted bars. While steel bars were used in the SHPB compression experiments on LM-1, aluminum [10, 11, 16] and magnesium [9, 13-15, 17] bars have been more common when testing softer materials, because the reduced value of  $E$  ensures that the transmitted bar exhibits about 3-5 times as much strain as a corresponding steel bar would. Another method that has been used with some success is a tubular transmitter bar, as suggested by Chen and Song [8, 11]. By reducing the area of the transmitter bar, the corresponding strain in the transmitter bar is increased thus increasing the resolution of the stress measurements. This increase is typically by a factor of about 2-3, depending on the wall thickness of the tubular bar.

## **6.3 Experimental Procedure**

### *6.3.1 Materials and specimen preparation*

Both HTPB polymer (binder) and composite containing HTPB polymer and glass beads (simulant) were received from Eglin AFB, FL. Both the polymer and the composite were cast as three rods of diameter 25.4 mm (1 inch) and length 300 mm (12 inches), as well as three larger rods of diameter 76 mm (3 inches) and length 300 mm (12 inches). The ingredients of the binder and simulant are shown in Table 6.1.

Two different techniques were used to prepare specimens for testing. The first method, shown in Figure 6.1, consisted of placing the 25 mm diameter rod inside a 43 mm diameter PVC tube (McMaster, wall thickness 6 mm). A two-part epoxy was prepared and poured so that it filled the area between the rod and the PVC tube, and this epoxy was left to dry overnight. The resulting structure was then cut into roughly 4 mm thick disks using a Buehler high-speed saw. Specimens were prepared by coring the disks with the use of a dermal punch; the resulting specimens were roughly 8 mm diameter, although all of them were measured in order to compensate for slight changes in coring technique. This method was largely effective for preparing specimens for the simulant, but the low density of the binder ( $\sim 970 \text{ kg/m}^3$ ) led to the binder floating on top of the epoxy. The second method consisted of cutting parallel slices of roughly 2-4 mm thickness perpendicular to the circular face of the binder using a sharp knife. The resulting strips were then cored using the same 8 mm dermal punch, and the resulting specimens were measured.

### *6.3.2 Experimental technique*

In light of the challenges of SHPB testing of rubbery polymers, several modifications to the SHPB experiments were implemented. A schematic of the modifications to the SHPB is shown in Figure 6.2. The first modification is to employ a shorter, tubular aluminum transmitter bar (Al6061-T6, McMaster-Carr) of outer diameter 19.05 mm, wall thickness 1.65 mm, and length 0.9 m. The reduction in area of this aluminum bar thus increases the strain measurement in the transmitted signal by a factor of 2.5. The striker bar (0.6 m) and incident bar (1.8 m) are both made of solid aluminum, and, unlike the LM-1 experiments, there are no inserts present (due to the low stresses exhibited by the binder and simulant). In addition, the gain selected for the amplifier was set at 100, as the amplitude of the signals is generally fairly small, even with the modifications present in the experiment, and further increases in the amplifier gain proportionally increased the noise, thus providing no improvement to the signal quality. Once again, semiconductor strain gages (Kulite, gage factor 140) were placed on the bar, diametrically opposite to each other, to measure the small strains in both the incident and transmitter bars. These gages, of resistance  $\sim 1.1 \text{ k}\Omega$ , were connected to Wheatstone bridges, which were in turn connected to 15 volt power supplies. Petroleum jelly was used between the specimen and the incident bar and transmitted bar surfaces to reduce friction at the specimen-bar interfaces, and both bar interfaces were cleaned carefully using acetone to remove any glass beads that might be present from the simulant experiments.

Information (material, geometry, and calculated impact velocity) about the experiments conducted on both the binder and the simulant are shown in Table 6.2.

Calculations of the stress-strain curves were performed using the same in-house MATLAB program discussed in Chapter 2, but high-frequency noise was filtered out above 100 kHz (corresponding to the filtering used by the differential amplifier). A representative signal of the raw data and the true stress vs. true strain and true strain-rate vs. true strain profiles, are shown in Figure 6.3 and 6.4, respectively. For the sake of clarity in the figure, the transmitted signal in Figure 6.3 is amplified by a factor of 10. The small signal in the transmitted bar (due to the generally low stresses in the binder and simulant) implies that as long as the incident signal reaches a constant value, the reflected signal, and therefore, the engineering strain-rate in the specimen, will be constant for the majority of the experiments. The observed increase in the true strain-rate as strain increases in the experiments is due to the fact that the engineering strain-rate is constant, and because

$$\dot{e} = \frac{\dot{\varepsilon}}{1 + \varepsilon}, \quad (6.5)$$

where  $\dot{e}$  is the true strain-rate. Because  $\dot{\varepsilon}$ ,  $\dot{e}$ , and  $\varepsilon$  are negative (as these are compression tests), the true strain-rate will increase while the engineering strain-rate is remains constant.

## 6.4 Results and Discussion

### 6.4.1 Binder study

The stress-strain curves from the experiments in the present study are shown in Figure 6.5. A very high strain-rate sensitivity is apparent from the stress-strain curves; experiments conducted at 600/s exhibit a peak stress of less than 1 MPa. In addition, the

total strain accumulated in the specimens generally increases as the strain-rate increases, up to 3000/s. However, as the strain-rate is increased above 3000/s, the peak stress achieved in the binder increases to 10-35 MPa and the strain accumulated at failure drops from about 20-25% to about 10%; this strain increases somewhat as the strain-rate is increased to 4000/s. Not surprisingly, the increase in the strain-rate also leads to a marked increase in the slope of the initial part of the stress-strain curve. In three of the experiments (Bin33, Bin34, and Bin35) the specimen fractured into at least two pieces; in Bin33 and Bin35, the resulting specimen fractured into two or three pieces, while in Bin34 (the highest strain-rate at 4000/s), the sample fractured into multiple pieces. In the remaining experiments, the specimen remained intact after the experiment. Photographs of the intact and broken post-test specimens are shown in Figure 6.6.

One of the interesting results from this set of experiments is the degree of rate sensitivity of the HTPB polymer, as evidenced from the stress vs. strain-rate plot in Figure 6.7; the enhanced strain-rate sensitivity of the polymer appears to come into effect at  $\sim 2100/s$ , as shown in Figure 6.8. These results are in agreement with those obtained by Blumenthal et al. [9] on a slightly different composition of the HTPB, where they observed a roughly six-fold increase in the true stress at 10% strain as the strain-rate was increased from 0.01/s to 2500/s. It is worth noting that processing does play a substantial role in the mechanical properties of the HTPB polymer, since isocyanates, chain extenders, and catalysts, which can vary based on the different formulations, can provide changes in the peak stresses achieved, sometimes in excess of an order of magnitude. Similar transitions in rate-sensitivity has been shown in other polymers, such as

polycarbonate [18, 19]. Mehta performed quasi-static, SHPB, and plate-impact pressure-shear experiments on polycarbonate (PC), and from his experiments, there was a transition in rate-sensitivity at  $\sim 300/s$ . Mulliken, who utilized DMA experiments, quasi-static experiments, and SHPB experiments, established the strain-rate at which the strain-rate sensitivity of PC increases substantially ( $\sim 100/s$ ) and connected that to the strain-rate at which the  $\beta$ -transition begins to play a role in the mechanical response of PC. Likewise, additional experiments were conducted by Song and Chen [20] on an EPDM rubber at strain-rates ranging from 600/s to 5000/s; a transition in strain rate-sensitivity occurs at approximately 2000/s as well; the strain-rate sensitivity above 2000/s is approximately one order of magnitude higher than the rate-sensitivity below 2000/s. The stark transition in strain rate-sensitivity is similar to that seen in the current study; this is not unexpected as HTPB is a rubbery polymer rather than a glassy polymer such as PC.

While there clearly is a connection between strain-rate and temperature sensitivity in polymers, it is unlikely that the enhanced strain-rate sensitivity above 2100/s is solely due to the coupled nature of the strain-rate and temperature. DMA experiments and SHPB experiments conducted by Siviour [13] indicate the presence of substantial temperature dependence as well as strain-rate dependence on the mechanical behavior of the HTPB polymer. As shown in Figure 6.9, while the room temperature specimens exhibited peak stresses of less than 1 MPa, the specimens tested at  $-80^{\circ}\text{C}$  exhibited peak stresses of 100 MPa. Local fracture was also observed to occur during the specimen loading as well. In addition, Figure 6.10(a) shows the shift in the glass transition temperature of the HTPB polymer as the strain-rate is increased (based on the DMA

experiments). The shift in temperature with strain-rate (approximately 4 °C/decade of strain-rate) implies that the glass transition temperature of the HTPB polymer for the SHPB experiments at 2000/s would be approximately -42°C. The rapid increase in stress with decreasing temperature at -40°C, as seen from Figure 6.10(b), clearly supports the presence of a glass transition temperature near approximately -40°C for the HTPB, which would be roughly the same for the experiments conducted in the present study.

As noted before, most of the post-test (impacted) specimens recovered in the present study were largely intact, except in three cases (Experiment Bin33, 3200/s; Experiment Bin34, 4000/s; Experiment Bin35, 3050/s), where the specimen fractured into at least two pieces. The photographs, shown in Figure 6.6 (c) and (d), provide clear evidence of axial splitting that occurs in the specimens, even though the experiments are being performed at room temperature. While there has been little investigation of the micro-flaws necessary for axial splitting, it is likely that these are introduced during the casting process. This failure mode in the HTPB polymer is different from LM-1, where specimen failure (using the conventional inserts) was due to high stresses near the specimen-insert interface in conjunction with a substantial stress concentration. Therefore, the inserts discussed in Chapter 3 are not necessary for these experiments. More careful laser confocal microscopy, discussed further elsewhere [21] shows that the failed HTPB polymer specimens also exhibit evidence of tearing, as shown in Figure 6.11a (Experiment Bin35, 3050/s), in contrast to the pristine surfaces shown in Figure 6.11b. This behavior is again consistent with axial splitting, because while the faces are loaded in compression, tensile strains are present perpendicular to the loading direction

(i.e. parallel to the specimen faces). The presence of axial splitting is common in brittle materials [22, 23], such as rocks and ceramics, that are not under confinement stress. This is due to the presence of microflaws in these brittle materials, which foster the nucleation of tensile cracks which are oriented roughly in the direction of axial compression. However, unlike in brittle materials, where the fracture surfaces are largely flat, the fracture surface of the polymer specimens also exhibits evidence of tearing and other non-planar features. Some evidence of vein-like features, also seen in LM-1 [24-28], is shown in Figure 6.11.

#### *6.4.2. Simulant Study*

The stress-strain curves from the SHPB experiments conducted on the simulant are shown in Figure 6.12. The experiments in this part of the study were conducted at strain-rates between 300/s and 3000/s to understand the strain-rate sensitivity over an order of magnitude of strain-rates. The peak stresses in the simulants increase substantially with strain-rate; the peak stress at 310/s was approximately 0.6 MPa, compared to 6 MPa at a strain-rate of 2900/s. However, the peak stresses appear to level off as the strain-rate reaches approximately 700/s; the peak stress corresponding to this strain-rate is approximately 3.5 MPa, more than half of the maximum peak stress attained in this study. Unlike in the binder study, none of the specimens failed due to axial splitting, and all of the samples appeared to be largely intact, although in a number of cases, the specimens retained some of the applied compressive deformation. For the experiments conducted at higher strain-rates, more glass beads appeared to separate (decohesion at the particle matrix interface) from the simulant during the experiment.

A couple factors can help explain why there is a reduction in rate sensitivity in the simulant compared to the HTPB polymer. The first is that none of the simulant specimens showed failure by axial splitting, unlike the binder counterparts. The second factor is due to the composition of the simulant. In the current simulant, approximately 87% of the specimen (by weight) consists of glass beads, and as such, there are numerous interfaces between the glass beads and the polymer binder. These interfaces provide locations for delamination of the glass beads from the polymer binder, and they also provide the possibility for other defects to be present. Both of these mechanisms can inhibit the ability of the simulant to undergo additional stress, thus limiting the rate-sensitivity of the simulant.. Due to their small and varying size, the glass beads were not tested for strain-rate sensitivity, but previous studies on ceramics and other materials [29, 30] clearly show that while there is still strain-rate sensitivity, it is much lower (10-15% per 10-fold increase in strain-rate) compared to the binder (as much as 1000+% per 10-fold increase in strain-rate). Both of these reasons provide a rationalization for why the strain-rate sensitivity of the simulant is so much lower than for the binder.

Laser confocal microscopy of the simulants show some of the large glass beads during the high strain-rate loading. However, it does not appear that, from the laser confocal microscopy, that the large glass bead in Figure 6.13, corresponding to experiment Si18, is broken. Instead, it seems that additional smaller particles may be obscuring parts of the largest glass beads. In addition, some of the intact smaller glass spheres can also be seen, but some of them appear to be obscured by larger particles in

the vicinity. The degree to which delamination of the smaller glass beads occurs in the simulant is inconclusive, as smaller glass beads on the surface of the specimen were removed between the impact and the optical microscopy due to transfer of the specimen. Similar reinforcement size effects on fracture and decohesion have been reported in metal matrix composites, as well [31-33].

## **6.5 Summary**

In this chapter, SHPB compression experiments were conducted on both an HTPB polymer (binder) and its corresponding polymer composite (simulant). The low stresses and stiffness exhibited by the binder and the simulant provided substantial challenges in specimen preparation and accurate measurement of the stress-strain curves. However, the use of a hollow aluminum transmitter bar and semiconductor gages provide the ability to accurately measure the stresses exhibited by the binder and the simulant. Some of the conclusions that can be made from the results of the current study are as follows:

1. The HTPB polymer exhibits a transition in rate-sensitivity at approximately 2100/s.
2. Above approximately 3000/s, the binder becomes much more susceptible to axial splitting, and the specimens at still higher strain-rates fracture into multiple fragments. While there is a shift in the glass transition temperature for the HTPB polymer, that shift in temperature does not the rapid accumulation of stress and the associated axial cracking, as the expected glass transition temperature of the

HTPB polymer in the SHPB experiment is about  $-40^{\circ}\text{C}$ , and damage is occurring well in excess of that temperature.

3. The fracture surfaces of the HTPB polymer clearly show tearing that is consistent with the axial splitting phenomenon. This tearing is not present in the pristine samples.
4. The simulant exhibits a lower strain-rate sensitivity than the binder; the peak stress achieved by the binder is 0.5 MPa at 300/s and ~6 MPa at 3000/s.
5. Unlike the binder, the simulant does not appear to be susceptible to axial splitting at the highest strain-rates; the post-test specimens appear to remain cylindrical and largely intact. However, both fracture of the larger particles and delamination of smaller particles from the matrix is inconclusive based on laser confocal microscopy.

## References

1. Bat`kov Y.V., Fishman N.D., Novikov S.A. (1983) Investigation of shear stress on a shock front in solid high explosives (HE). *Combust., Explos. Shock Waves (Engl. Transl.)*; Translated from *Fizika Goreniya i Vzryva, May 1983* **19**, 357-359.
2. Bat`kov Y.V., Novikov S.A., Pogorelov A.P., Sinitsyn V.A., Khabarov I.P. (1983) Investigation of the influence of specimen diameter on the explosive transformation development behind a weak nonstationary shock front. *Combust., Explos. Shock Waves (Engl. Transl.)*; Translated from *Fizika Goreniya i Vzryva, May 1983* **19**, 359-360.
3. Boyle V., Frey R.B., Blake O. (1989) Combined pressure shear ignition of explosives. *Proceedings of the Ninth Symposium (International) on Detonation*, Portland, OR, August 28 - September 1, 1989.
4. Frey R.B. (1980) The Initiation of Explosive Charges by Rapid Shear. Aberdeen, MD.
5. Jordan J.L., Dorgan R.J., Nixon M.E., Dick R.D. (2007) Initiation of Polymer Bonded Explosive (PBXN-110) by Combined Shock and Shear Loading. *15th APS Topical Conference on Shock Compression of Condensed Matter*, Waikoloa, HI,
6. Tarver C.M., Hallquist J.O., Erickson L.M. (1985) Modeling short pulse duration shock initiation of solid explosives. United States,

7. Gray G.T. (2000) Classic split-Hopkinson pressure bar testing. *American Society for Materials Handbook* (8<sup>th</sup> ed.), American Society for Materials International, Materials Park, OH, 462-476
8. Chen W., Zhang B., Forrestal M. (1999) A split Hopkinson bar technique for low-impedance materials. *Experimental Mechanics* **39**, 81-85.
9. Blumenthal W.R., Thompson D.G., Cady C.D., Gray G.T., III, Idar D.J. (2002) Compressive Properties of PBXN-110 and its HTPB-Based Binder as a Function of Temperature and Strain Rate. *12th International Detonation Symposium* San Diego, CA, August 11-16, 2002.
10. Shukla A., Ravichandran G., Rajapakse Y.D.S., Chen W.W., Song B. Dynamic Characterization of Soft Materials. *Dynamic Failure of Materials and Structures* ed.), Springer US, 1-28
11. Song B., Chen W.W. (2005) Split Hopkinson pressure bar techniques for characterizing soft materials. *Latin American Journal of Solids and Structures* **2**, 113-152.
12. Frew D., Forrestal M., Chen W. (2002) Pulse shaping techniques for testing brittle materials with a split Hopkinson pressure bar. *Experimental Mechanics* **42**, 93-106.
13. Siviour C.R., Laity P.R., Proud W.G., Field J.E., Porter D., Church P.D., Gould P., Huntingdon-Thresher W. (2008) High strain rate properties of a polymer-bonded sugar: their dependence on applied and internal constraints. *Proceedings of the Royal Society A: Mathematical, Physical and Engineering Science* **464**, 1229-1255.

14. Joshi V.S., Lee R.J. (2002) Resolving Mechanical Response of Plastic Bonded Explosives at High Strain-Rate Using Split Hopkinson Pressure Bar. *Shock Compression of Condensed Matter - 2001: 12th APS Topical Conference*, Atlanta, Georgia (USA),
15. Siviour C.R., Gifford M.J., Walley S.M., Proud W.G., Field J.E. (2004) Particle size effects on the mechanical properties of a polymer bonded explosive. *Journal of Materials Science* **39**, 1255-1258.
16. Chen W., Subhash G., Ravichandran G. (1994) Evaluation of ceramic specimen geometries used in split-Hopkinson pressure bar. *Dymat Journal* **1**, 193-210.
17. Gray III G.T., Blumenthal W.R., Idar D.J., Cady C.M. (1998) Influence of temperature on the high-strain-rate mechanical behavior of PBX 9501. *The tenth American Physical Society topical conference on shock compression of condensed matter*, Amherst, Massachusetts (USA),
18. Mulliken A.D., Boyce M.C. (2006) Mechanics of the rate-dependent elastic-plastic deformation of glassy polymers from low to high strain rates. *International Journal of Solids and Structures* **43**, 1331-1356.
19. Mehta N. (2003) *Pressure and strain rate dependency of flow stress of glassy polymers under dynamic loading*. Ph.D. Thesis, Case Western Reserve University
20. Song B., Chen W. (2003) One-dimensional dynamic compressive behavior of EPDM rubber. *Journal of Engineering Materials and Technology, Transactions of the ASME* **125**, 294-301.
21. Hovis D.B., Heuer A.H. (2010) The use of laser scanning confocal microscopy (LSCM) in materials science. *Journal of Microscopy* **240**, 173-180.

22. Horii H., Nemat-Nasser S. (1986) Brittle Failure in Compression: Splitting, Faulting and Brittle-Ductile Transition. *Philosophical Transactions of the Royal Society of London. Series A, Mathematical and Physical Sciences* **319**, 337-374.
23. Chen W., Ravichandran G. (1996) An experimental technique for imposing dynamic multiaxial-compression with mechanical confinement. *Experimental Mechanics* **36**, 155-158.
24. Lewandowski J.J., Shazly M., Nouri A.S. (2006) Intrinsic and extrinsic toughening of metallic glasses. *Scripta Materialia* **54**, 337-341.
25. Lewandowski J.J., Wang W.H., Greer A.L. (2005) Intrinsic plasticity or brittleness of metallic glasses. *Philosophical Magazine Letters* **85**, 77-87.
26. Lowhaphandu P., Ludrosky L.A., Montgomery S.L., Lewandowski J.J. (2000) Deformation and fracture toughness of a bulk amorphous Zr-Ti-Ni-Cu-Be alloy. *Intermetallics* **8**, 487-492.
27. Xi X.K., Zhao D.Q., Pan M.X., Wang W.H., Wu Y., Lewandowski J.J. (2005) Fracture of Brittle Metallic Glasses: Brittleness or Plasticity. *Physical Review Letters* **94**, 125510.
28. Flores K.M., Dauskardt R.H. (1999) Enhanced toughness due to stable crack tip damage zones in bulk metallic glass. *Scripta Materialia* **41**, 937-943.
29. Sarva S., Nemat-Nasser S. (2001) Dynamic compressive strength of silicon carbide under uniaxial compression. *Materials Science and Engineering A* **317**, 140-144.
30. Shazly M., Prakash V., Lerch B. (2006) *High strain-rate compression of ice*, National Aeronautics and Space Administration, Cleveland, OH.

31. Lewandowski J.J., Liu C., Hunt Jr W.H. (1989) Effects of matrix microstructure and particle distribution on fracture of an aluminum metal matrix composite. *Materials Science and Engineering: A* **107**, 241-255.
32. Singh P., Lewandowski J. (1993) Effects of heat treatment and reinforcement size. *Metallurgical and Materials Transactions A* **24**, 2531-2543.
33. Vaidya A.R., Lewandowski J.J. (1996) Effects of SiCp size and volume fraction on the high cycle fatigue behavior of AZ91D magnesium alloy composites. *Materials Science and Engineering A* **220**, 85-92.

## Tables

Ingredient	Binder weight %	Simulant weight %
R45 (HTPB)	44.909	5.61
IDP	44.834	5.61
Lecithin	5.605	0.70
Ethyl 702	0.400	0.05
DBTDL	0.060	0.10
Glass beads: 25-40 $\mu\text{m}$		21.80
Glass beads: 300-400 $\mu\text{m}$		65.60
IPDI	4.192	0.53

Table 6.1 – Ingredients in binder and simulant. The binder weight percentages are generally eight times as much as the simulant because the glass beads comprise about 87% of the simulant.

Experiment	Length (mm)	Diameter (mm)	Bar velocity (m/s)
Bin33	2.64	7.84	7.9
Bin34	2.51	7.64	9.6
Bin35	2.67	7.55	8.1
Bin36	3.01	7.72	7.7
Bin38	2.29	7.30	5.2
Bin41	2.37	7.71	6.5
Bin43	2.2	7.61	4.3
Bin44	2.09	7.72	4.3
Bin45	2.12	7.65	3.3
Bin46	2.33	7.68	1.5
Si6	5.07	7.83	5.1
Si7	5.28	7.77	3.7
Si8	5.74	7.81	1.8
Si10	5.62	7.78	2.4
Si12	5.42	7.75	3.5
Si13	5.38	7.80	3.2
Si14	5.10	7.71	2.4
Si16	4.13	7.74	3.0
Si18	4.64	7.79	5.9
Si19	5.01	7.8	7.3
Si20	2.85	7.75	7.9

Table 6.2 – Specimen length and diameter, along with bar velocity, for the HTPB and simulant experiments in the current study. Experiments starting with Bin are for the HTPB polymer (binder), while experiments starting with Si are for the HTPB polymer composite (simulant).

Figures

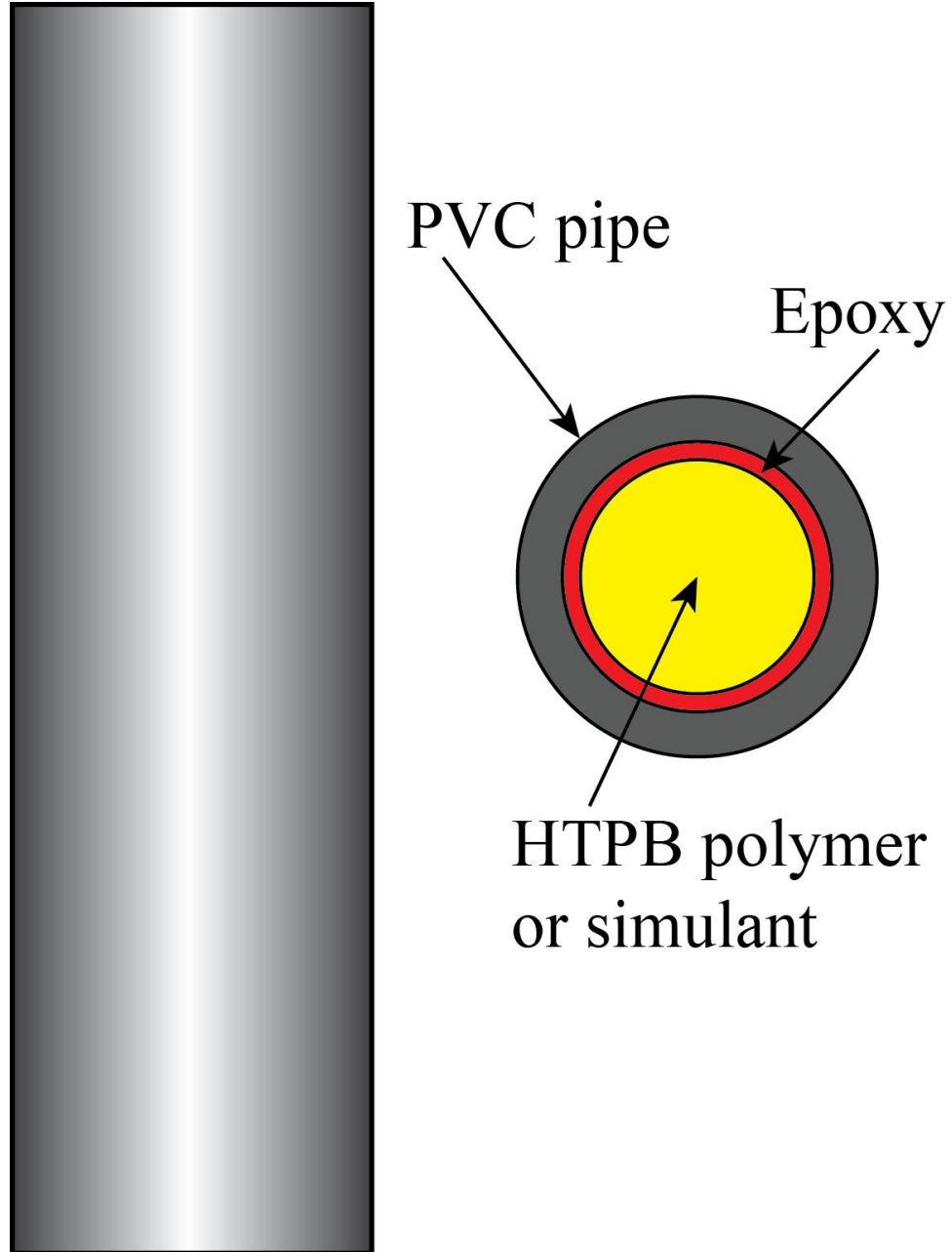


Figure 6.1 – Schematic of one technique utilized to prepare SHPB specimens in the current study. The resulting structure was cut into 4-6 mm thick disks and specimens were cored from the disks.

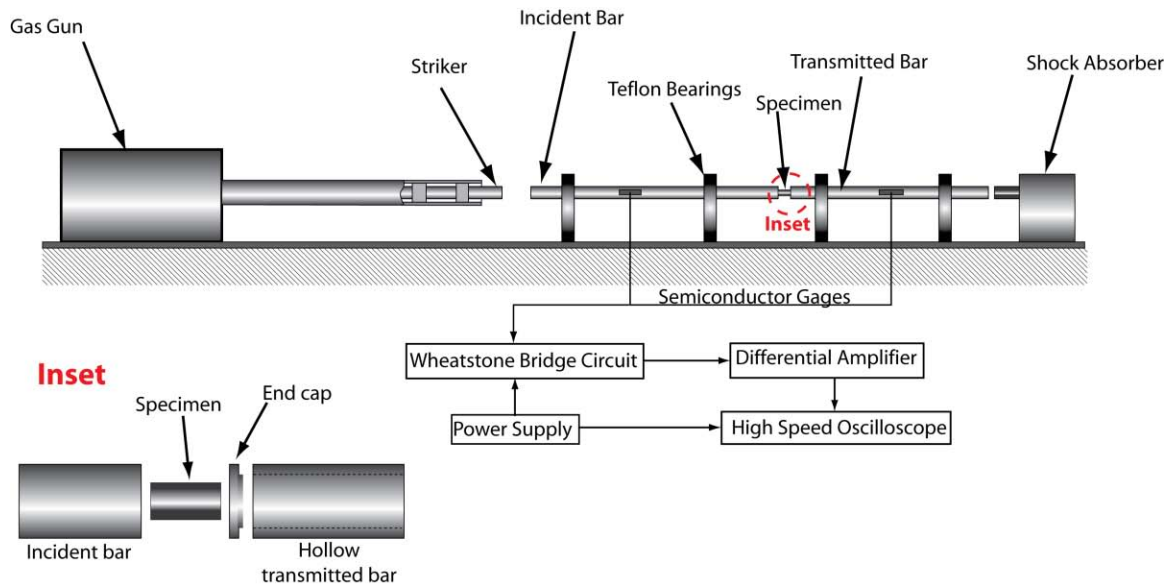


Figure 6.2 – Schematic of SHPB employed in experiments in the current study, with an exploded inset provided to show the end cap and hollow transmitted bar.

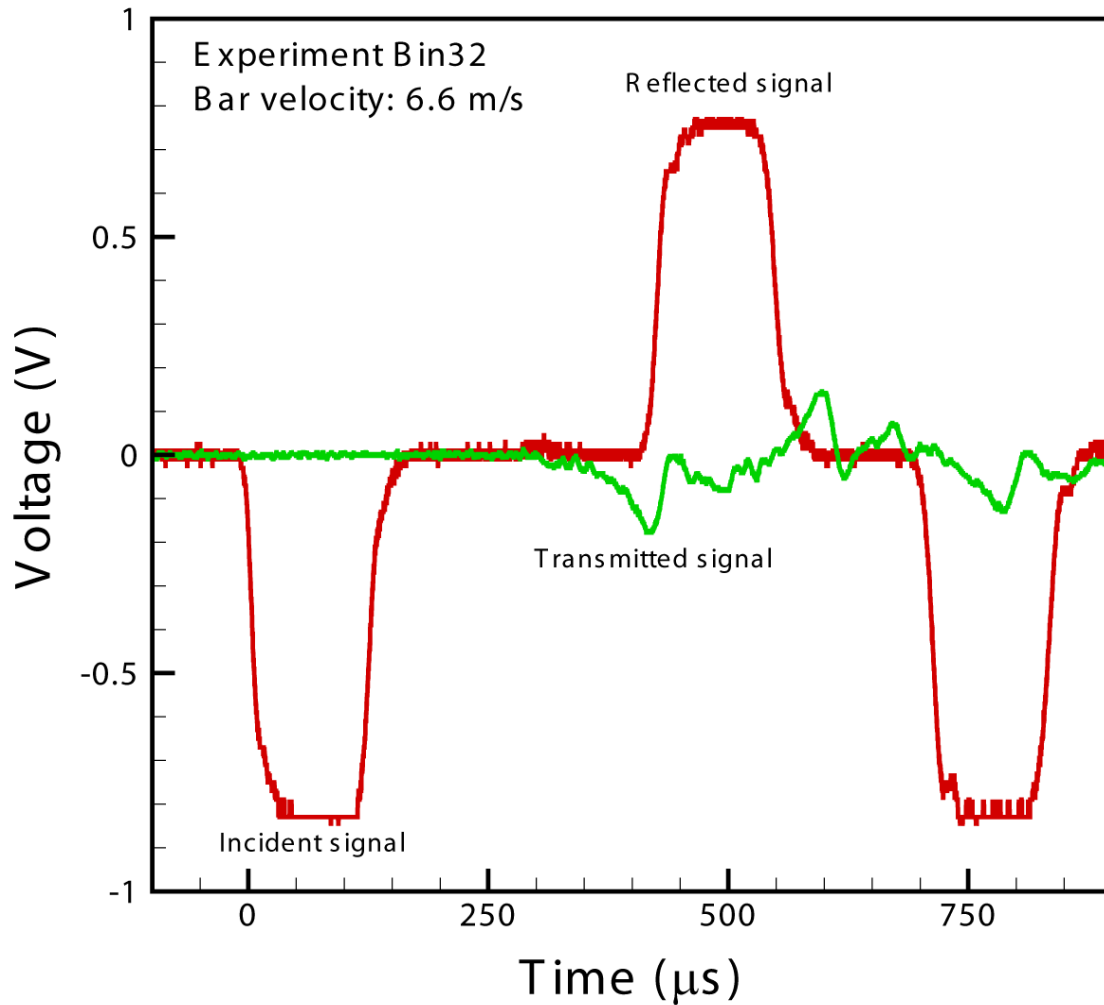


Figure 6.3 – Raw data from a representative experiment on the SHPB binder. The incident signal and reflected signal are the actual size, but the transmitted signal in this experiment is amplified by a factor of 10 to ensure figure clarity.

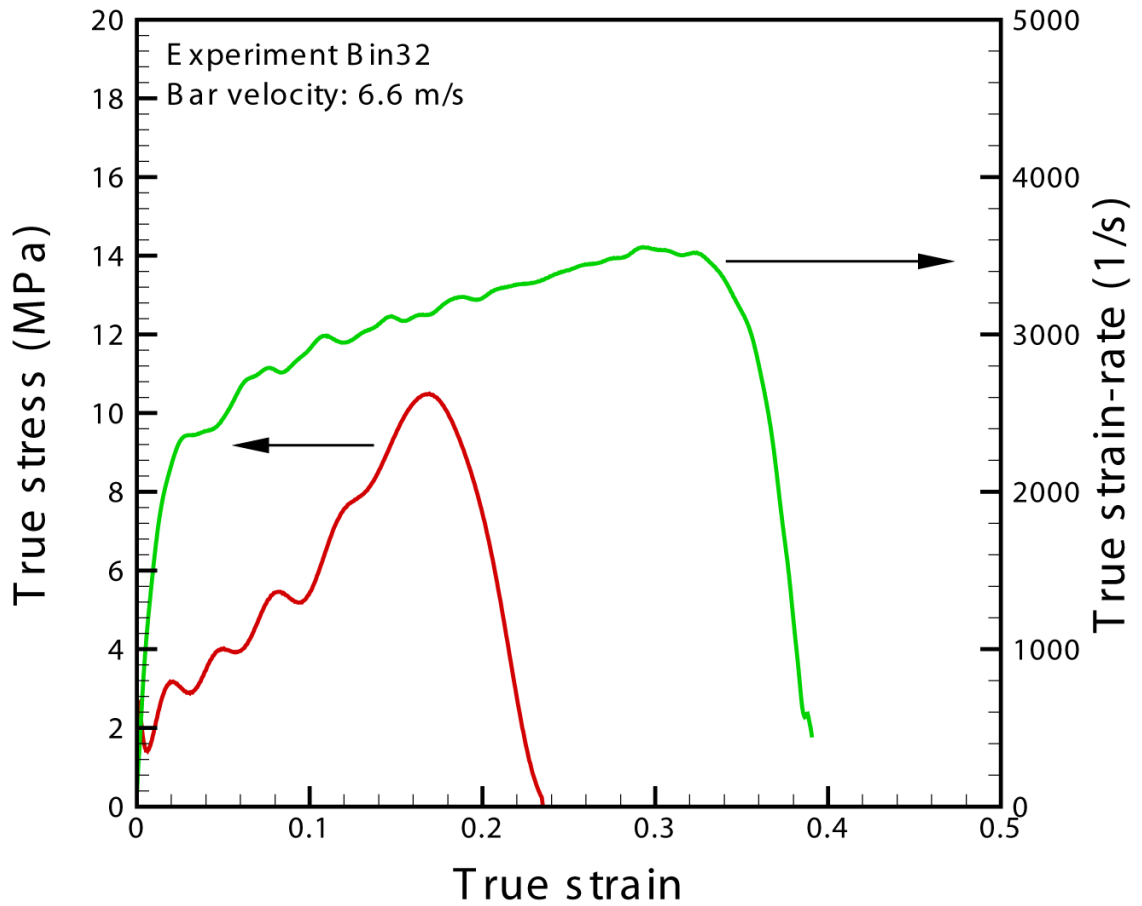


Figure 6.4 – Representative true stress vs. true strain (red) and true strain-rate vs. true strain curves corresponding to the data from Figure 6.3. The increase in the true strain-rate is solely because the true strain increases with time.

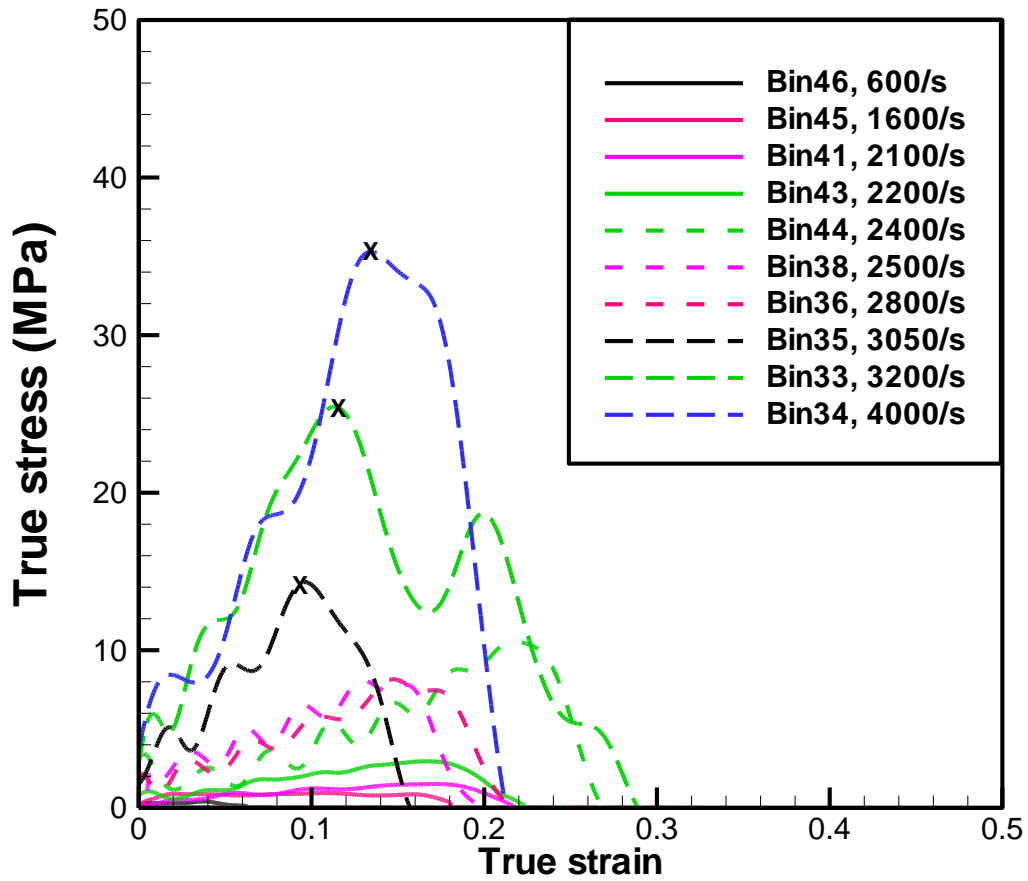


Figure 6.5 – Stress-strain curves in the present study for experiments conducted on the HTPB polymer. In three experiments (Bin33, Bin 34, Bin35) X denotes the likely location of failure.

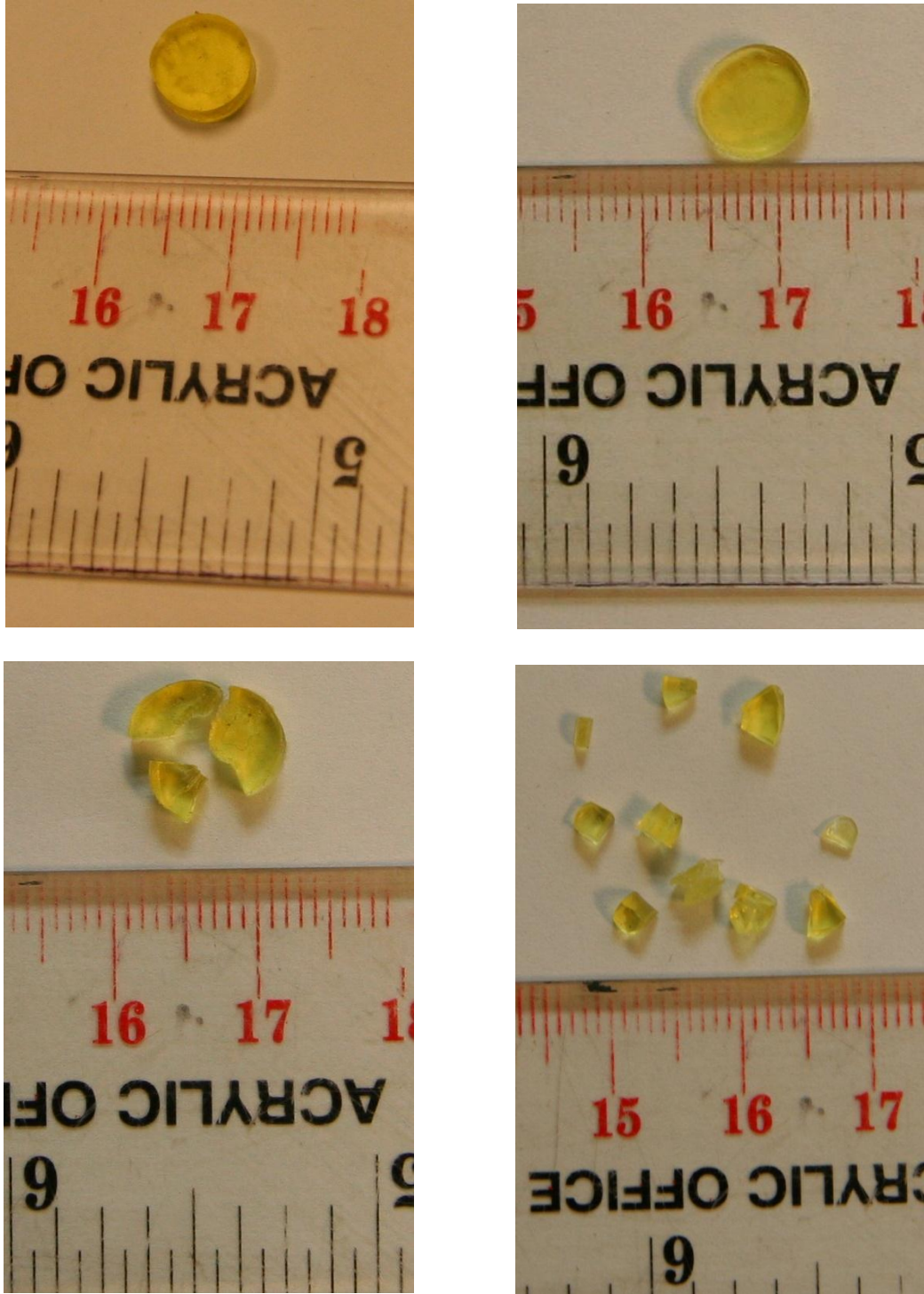


Figure 6.6 – Images of four post-test specimens: (a) Bin41, (b) Bin38, (c) Bin35, and (d) Bin34. They are in order of increasing strain-rate, and they show a transition from (a, b) largely uniform deformation to (c) axial splitting to (d) multiple fragmentation.

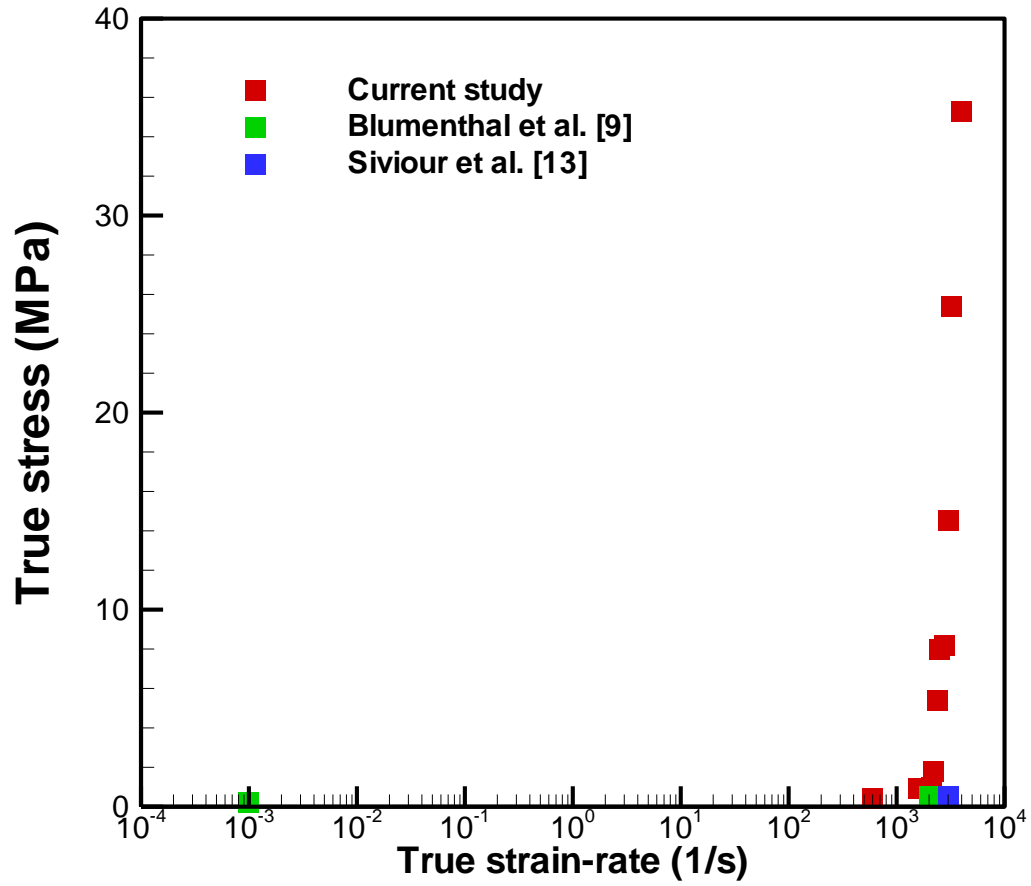


Figure 6.7 – Peak stress of the HTPB polymer as a function of strain-rate in the current study, as well as in two previous studies.

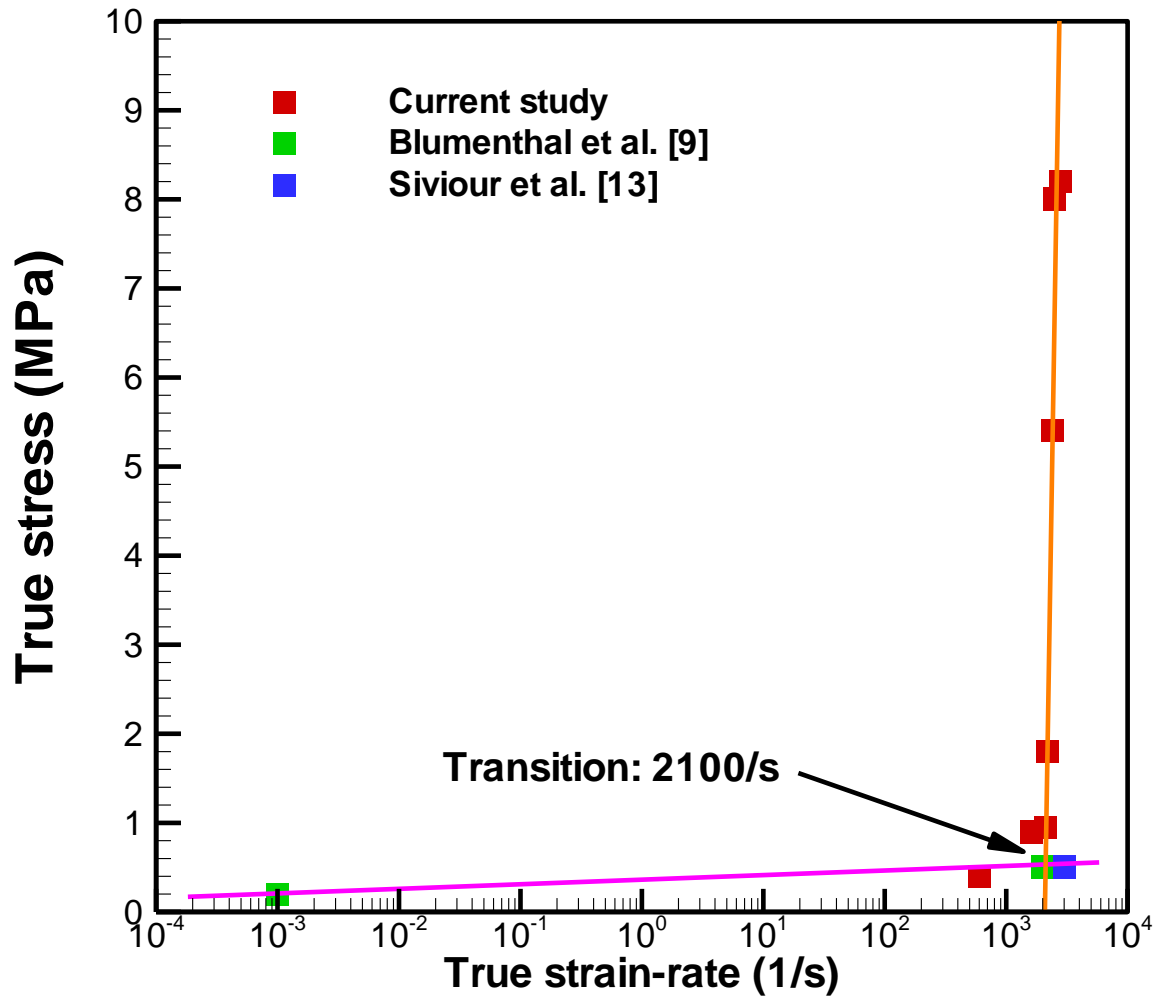


Figure 6.8 – Magnified view of Figure 6.7 to locate the approximate strain-rate for the transition from low strain-rate sensitivity to high strain-rate sensitivity at 2100/s.

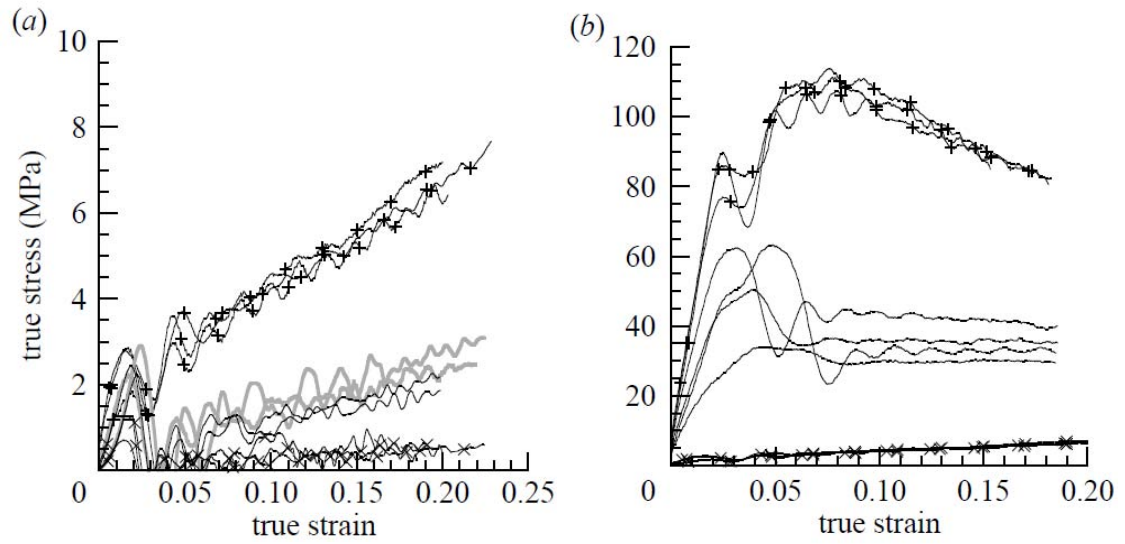


Figure 6.9 – Stress-strain curves at 3000/s for HTPB from a previous study by Siviour [13] for (a) temperatures of  $-40^{\circ}\text{C}$  and above, and (b) for temperatures of  $-40^{\circ}\text{C}$  and below. The curves show an increase in the peak stress from 1 MPa at room temperature (crosses, figure a) to 100 MPa at  $-80^{\circ}\text{C}$  (plus signs, figure b).

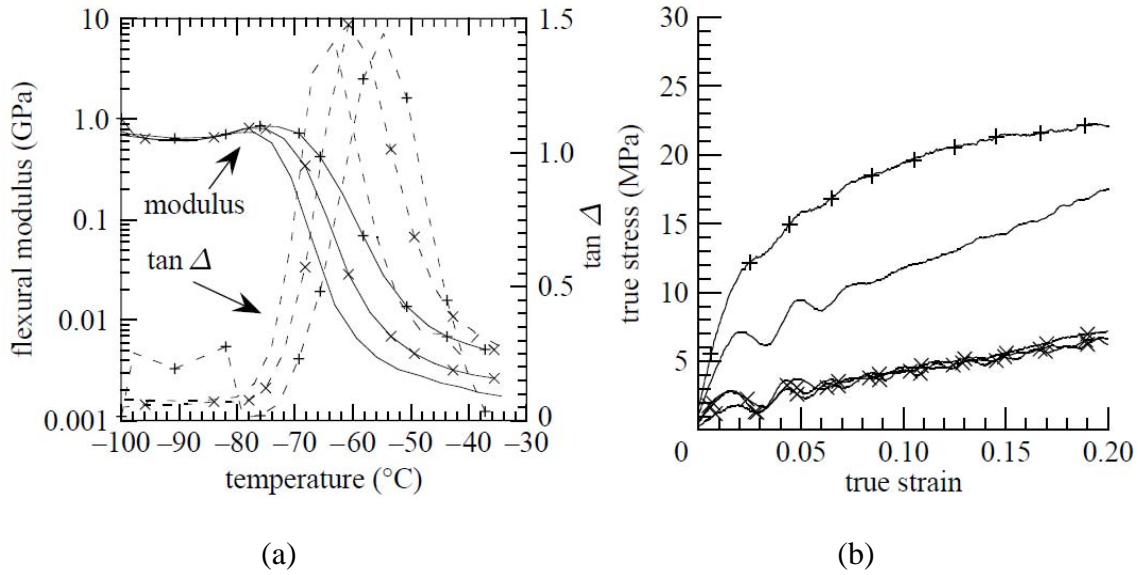
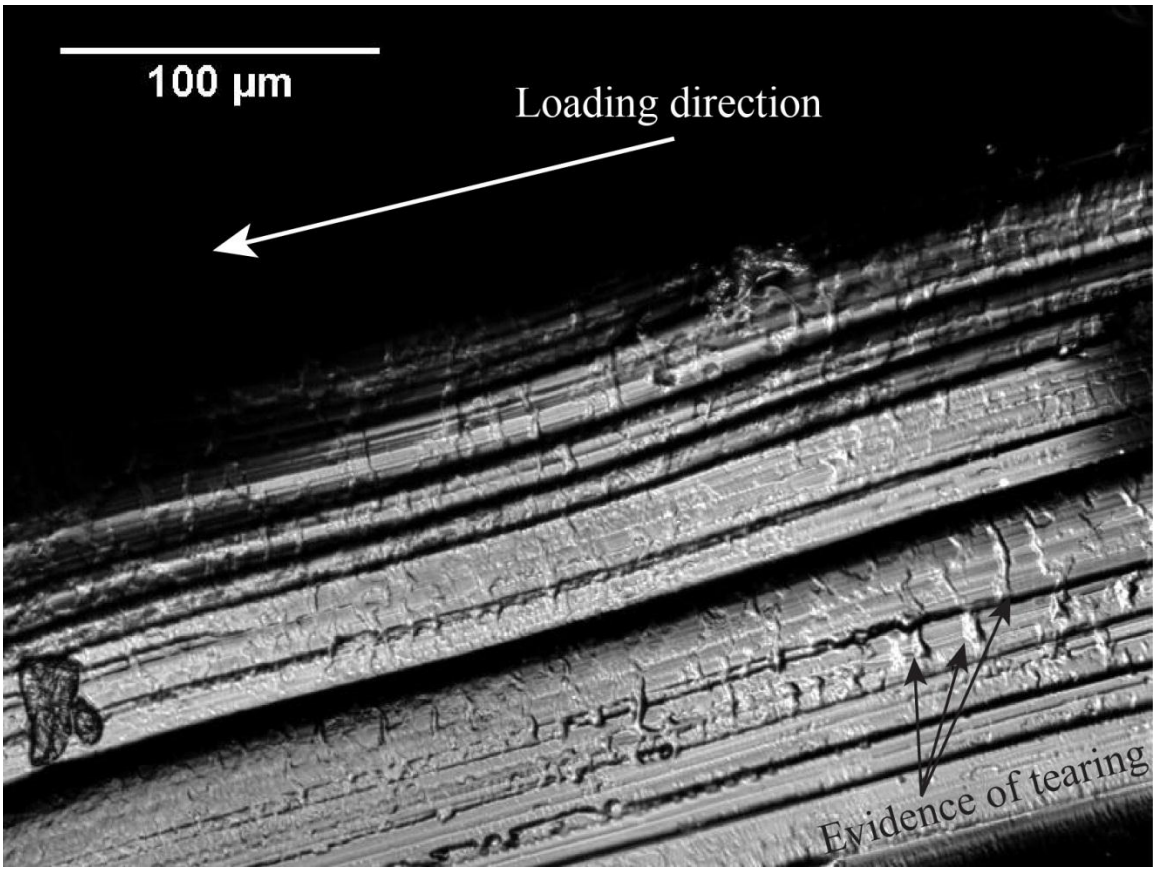
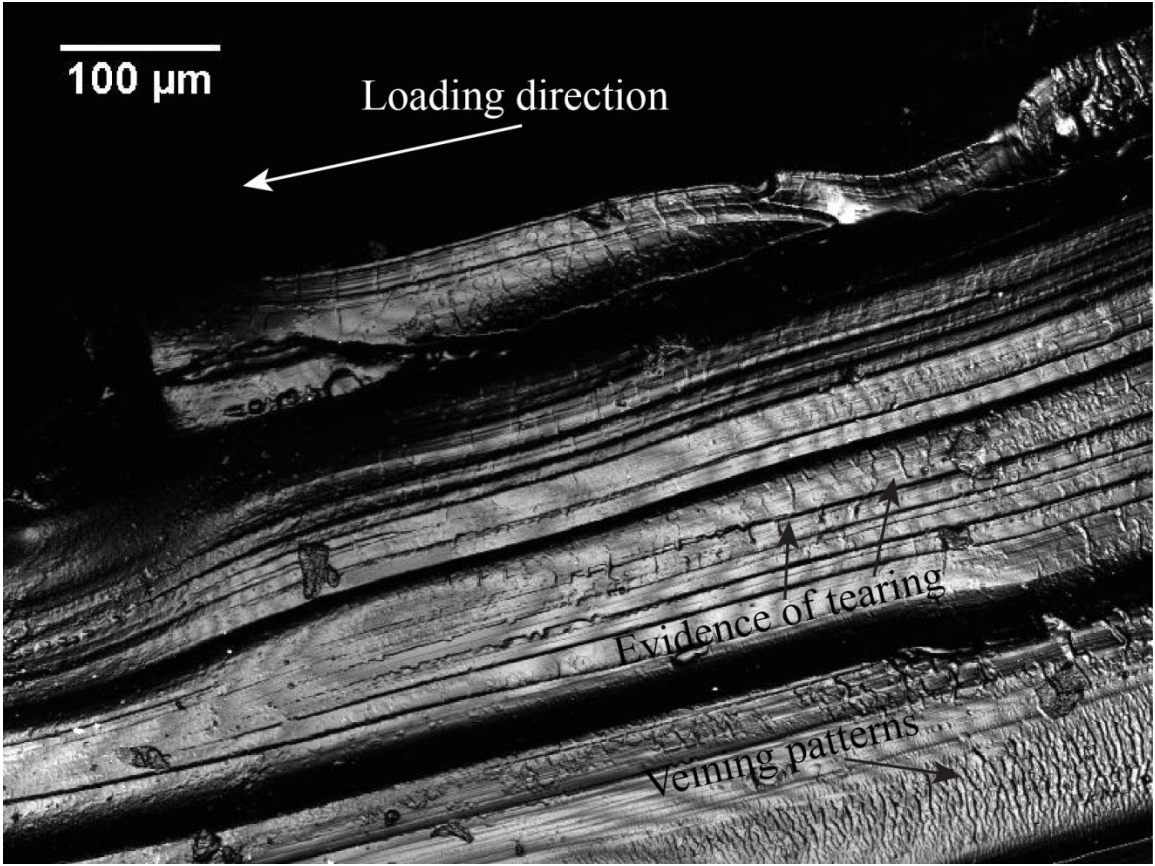


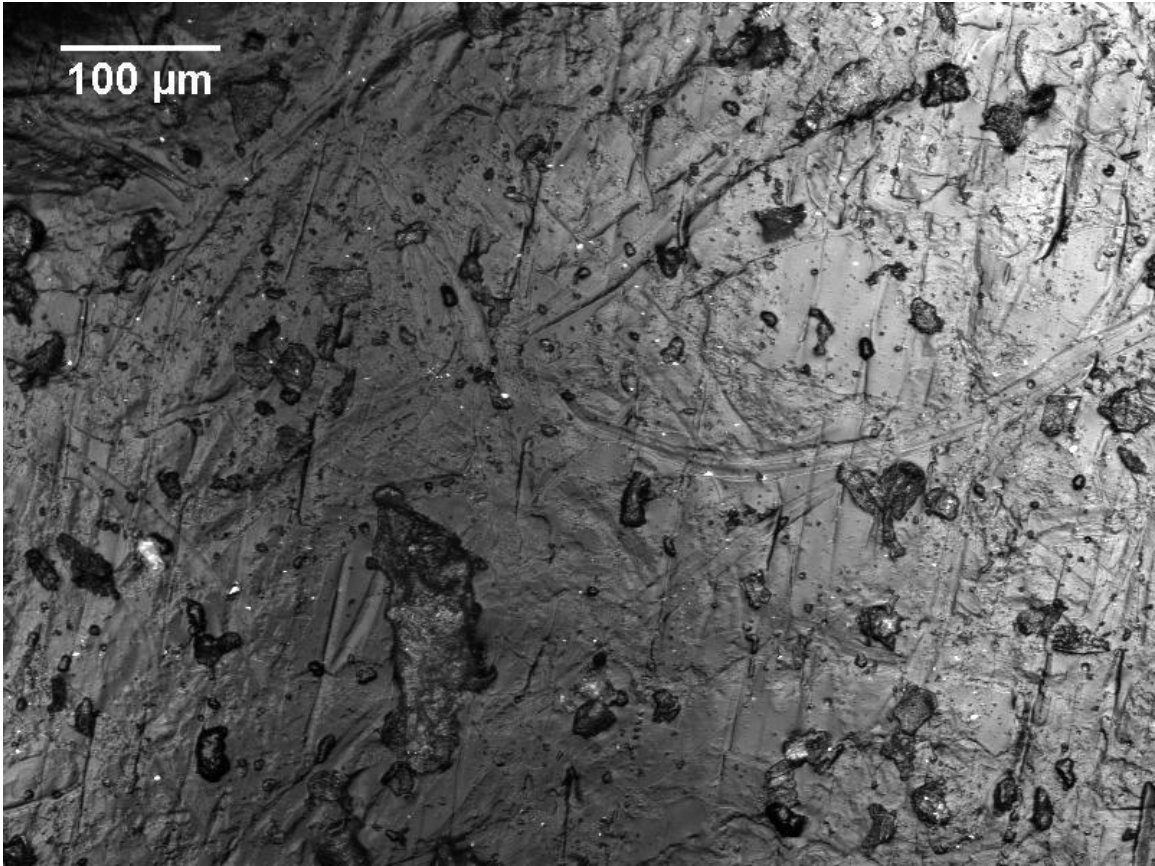
Figure 6.10 – (a) DMA traces from Siviour [13] showing a shift in the peak in loss modulus ( $\tan \Delta$ ) as strain-rate increases from 0.005/s [no symbols] to 0.5/s [plus signs], thus an increase in the glass transition temperature by about 4  $^{\circ}\text{C}$ /decade of strain-rate, implying a glass transition temperature of -42 $^{\circ}\text{C}$  for a strain-rate of 3000/s, and (b) true stress- true strain curves at -40 $^{\circ}\text{C}$  (crosses), -45 $^{\circ}\text{C}$  (solid line), and -51 $^{\circ}\text{C}$  (plus signs), providing clear evidence of the rapid increase in stress below the glass transition temperature.



(a)



(b)



(c)

Figure 6.11 – Laser confocal microscopy images of (a, b) failed HTPB polymer [Experiment Bin35, 3050/s), imaged along the fracture surface and with loading direction labeled, and (c) pristine HTPB polymer after specimen preparation, with loading direction into the plane of the paper. Figure 6.11a clearly shows tearing of the HTPB polymer during axial splitting, while Figure 6.11b also shows what appears to be a veining pattern that is also associated with tearing.

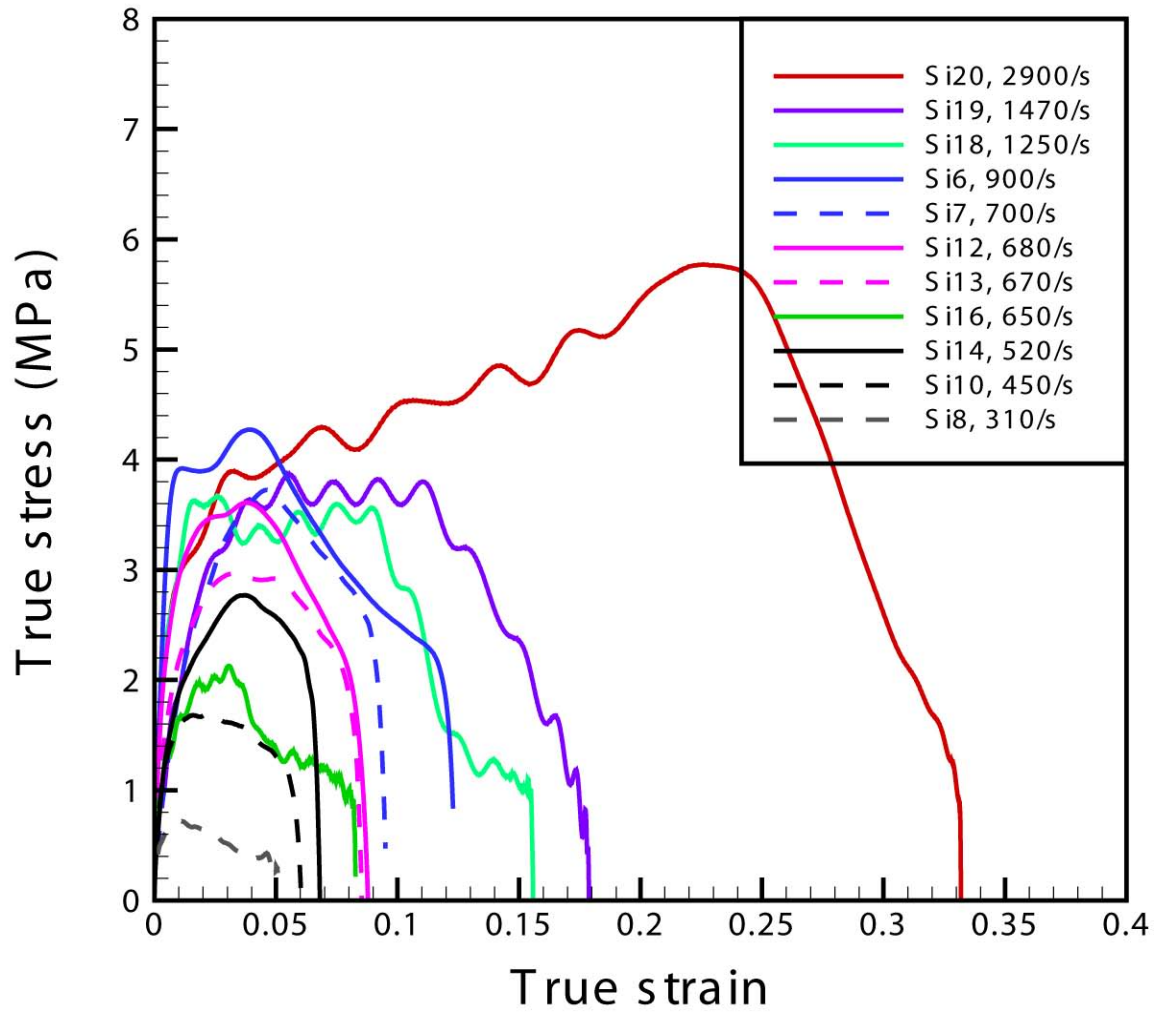


Figure 6.12 – True stress vs. true strain curves for SHPB experiments conducted on the simulant in the present study.

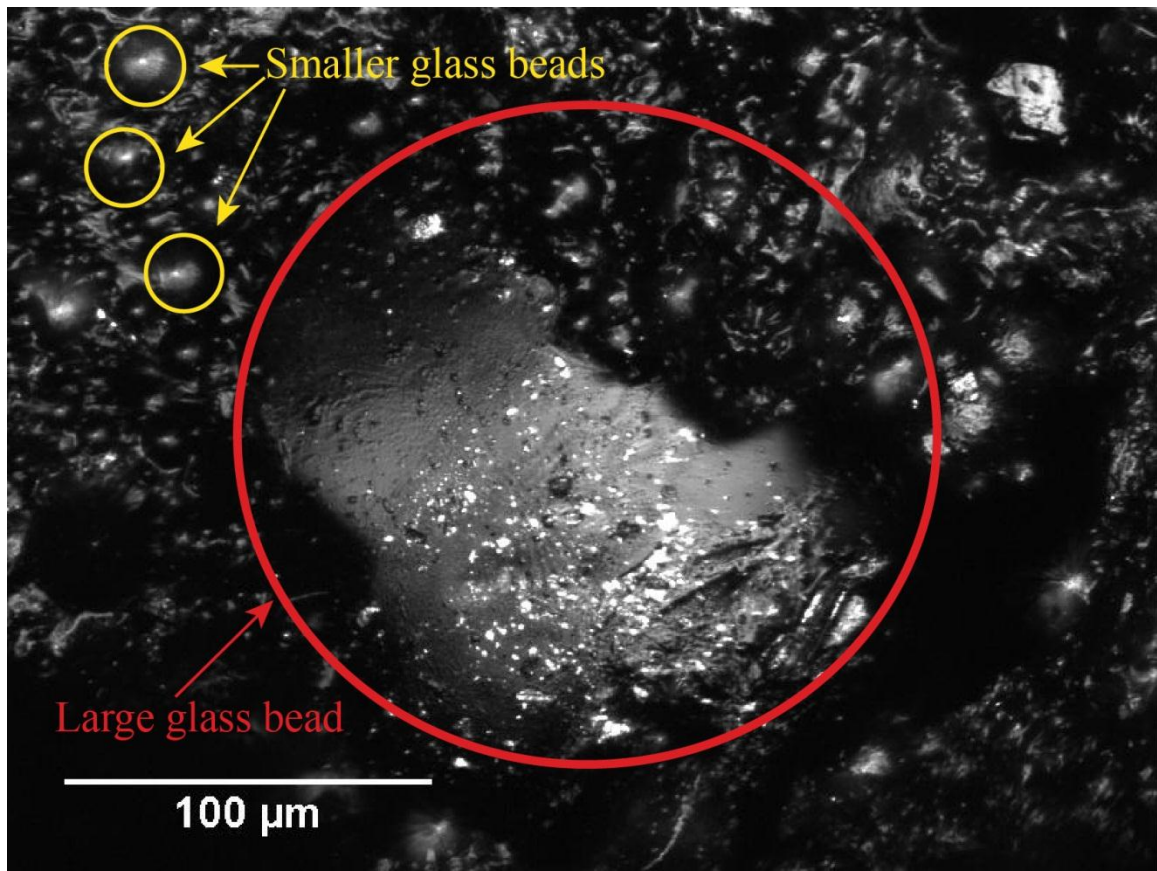


Figure 6.13 – Laser confocal microscopy of simulant (Experiment Si18, 1250/s), showing a large (e.g. 300  $\mu\text{m}$  diameter) particle, likely partially obscured by other smaller particles. Smaller particles (e.g. 25-40  $\mu\text{m}$  diameter) appear to be left intact.

## **Chapter 7 – Conclusions and Future Work**

### **7.1 Summary and Conclusions**

#### *7.1.1 High strain-rate compression of LM-1*

Because of its amorphous nature, LM-1, a Zr-based BMG, exhibits a very high yield strength (e.g. 2 GPa) and an elastic strain limit (i.e. 2%) under quasi-static loading conditions. However, the behavior of as-cast (i.e., amorphous) LM-1 under high strain-rate loading conditions has been studied by relatively few researchers. Almost all of the previous studies were performed on a narrow range of specimen  $L/D$  ratios, and the results of these tests show differing observations on the rate sensitivity of the BMG. In addition, the behavior of annealed, i.e. embrittled, LM-1 has not, to the author's knowledge, been previously characterized under high strain-rate loading.

In the present study, in order to understand better the dynamic behavior of LM-1, high strain-rate (i.e.  $10^2$ - $10^4$ /s) compression tests were performed on as-cast (i.e. amorphous) and annealed LM-1 using the SHPB. These tests were primarily designed to investigate the effects of  $L/D$  ratio and annealing treatment on the dynamic response of LM-1. Experiments were first conducted using the conventional SHPB configuration with cylindrical maraging steel inserts, but the stress concentration present in the specimen necessitated a change to a new tapered insert, as discussed in Section 2.6. An ultra high-speed camera was also employed to perform in-situ recordings of the deformation and failure processes of LM-1.

From the results of the experiments conducted using the conventional SHPB configuration, it is observed that the as-cast LM-1, appears to exhibit a slight reduction in the peak stress as  $L/D$  is decreased, but with an increase in the apparent strain. Both of these behaviors are particularly noticeable as the  $L/D$  ratio is decreased to 0.5. Failure of the as-cast LM-1 appears to be dominated by a single shear plane, which, with the conventional inserts, initiates at the specimen-insert interface. However, the fracture behavior appears to be dependent on the specimen  $L/D$  ratio; in-situ video verified that specimens with  $L/D = 1.0$  and  $2.0$  exhibit catastrophic failure by slip along the fracture plane, but as  $L/D$  is reduced, fracture by slip along multiple shear planes is observed which is followed by consolidation of the resulting fractured pieces (fragments) of the specimen. These two behaviors provide evidence that the conventional (i.e. cylindrical) inserts demonstrate significant geometrical ( $L/D$ ) effects in the flow and fracture behavior of as-cast LM-1. On the other hand, annealed LM-1 exhibits a slightly higher peak stress than the as-cast LM-1, with a higher strain-to-failure. This “apparent” increase in the strain-to-failure is partly due to the change in flow/fracture behavior that occurs as a result of the annealing process. Instead of the highly localized mode of shear fracture (along a single macroscopic plane) in the as-cast specimens, failure in the annealed specimens is accompanied by extensive fragmentation of the specimen. The fragmentation is observed to initiate at the specimen-insert interface, perhaps because of the stress concentration that is present with the cylindrical inserts. Also, because of the relatively violent and extensive fragmentation of the specimen, very little consolidation of the fragments occurs, even for specimens with  $L/D = 0.5$ , and the geometrical effects that are present in the as-cast LM-1 are not observed.

The reduction in the peak stress to failure with lower  $L/D$ , the failure of the LM-1 specimens at the specimen-insert interface, and the consolidation of the broken fragments of the as-cast LM-1 for small  $L/D$  ratios (e.g. 0.5) provide evidence for the presence of stress concentrations in the LM-1 specimens under dynamic compressive loading using the conventional SHPB. In order to better understand the issue and alleviate such effects during the dynamic loading process, finite element simulations using LS-DYNA were performed on several insert geometries to determine the state of stress and time for equilibrium in the impacted specimens. Both cylindrical and conical inserts exhibited considerable stress concentrations at the specimen-insert interface during the early part of the dynamic loading, and thus, an inhomogeneous state of stress was developed within the specimens; however, in the simulations, a dogbone specimen was suggested to promote relatively homogenous conditions as well as failure initiation in the gage section. In this way, conversion of the dogbone ends to maraging steel reduced the likelihood of premature failure of the ends and promoted a homogeneous, uniaxial stress state within the specimen. This conversion to dogbone ends does not adversely affect the ability for the specimen to reach a state of stress equilibrium prior to failure, based on the simulations. In addition, the new inserts allow smaller diameter specimens to be tested, thus ensuring that fully amorphous specimens can be tested. However, because the inserts are not of a constant diameter, strain gages attached directly on the specimen was proposed to ensure accurate dynamic stress-strain measurements.

Two groups of experiments were performed with the new tapered inserts. First, as-cast and annealed specimens were tested with the new experimental setup but without strain gages. An ultra high-speed camera was again employed to provide in-situ recordings of the deformation and failure process of the LM-1 specimens. Second, strain gages were attached to as-cast LM-1 specimens prior to testing in order to determine the elastic stress-strain response. In-situ video revealed that specimens clearly failed in the gage section during testing and the as-cast LM-1 exhibited more than one fracture plane, compared to the single fracture plane exhibited when conventional inserts were utilized, while the behavior of the annealed LM-1 revealed initial failure in the gage section, followed by extensive fragmentation. In addition, by attaching strain gages directly on the specimen, the peak strains and stresses achieved by the as-cast LM-1 were characterized, and a large constant strain-rate region was exhibited. While the new tapered inserts introduced wave dispersion, this appeared to have little effect on the transmitted signal; however, the strains and strain-rates calculated from the reflected signal were found to be well in excess of those experienced by the specimen. One reason for the large error is due to the fact that the strain-rates measured by the incident signal take into account the compression of the specimen as well as the maraging steel inserts and the elastic deformation of the inserts, which need to be accounted for in the sample strain-rate and strain analysis. Finally, the as-cast LM-1 specimens appear to be relatively insensitive to both strain-rate and  $L/D$  ratio, unlike the specimens tested with conventional inserts, and the use of the new tapered inserts reveals higher peak stresses achieved by the samples of as-cast LM-1. This rate-insensitive behavior of LM-1 is consistent with additional work that has been performed by others over a strain-rate range from  $10^{-4}/s - 10^5/s$ .

### *7.1.2 Dynamic fracture of LM-1*

In addition to the SHPB compression experiments, a series of dynamic fracture experiments were conducted using four-point bend specimens to expand previous investigations on notched fracture toughness of LM-1 from quasi-static to dynamic loading rates. In order to conduct these experiments, the aluminum transmitted bar typically employed for dynamic fracture experiments was modified by adding an additional short aluminum cylinder with two grooves which was fastened to the transmitted bar, and two hardened pins were placed inside the grooves to apply the loading. The four-point bend loading fixture was chosen as it ensures a constant bending moment at and near the notch tip and prevents any effects from mixed-mode loading present in three-point bend fracture test geometries that have been suggested to produce artificially high toughness values in LM-1. In addition, high-speed in-situ video is taken of the LM-1 and synchronized to the force vs. time curves to determine accurately when catastrophic failure of the specimen occurs.

Results from the first two notched experiments show a fracture toughness of approximately  $120 \text{ MPa m}^{1/2}$ , which, when compared to the previous quasi-static studies on notched LM-1 (110  $\mu\text{m}$  notch root radius), confirms that the fracture toughness is insensitive to strain-rate, consistent with the compression experiments. Moreover, the force vs. time curves indicate multiple fracture initiation and arrest events leading to the large scale blunting of the notch tip prior to catastrophic failure of the specimen. The fracture surface, shown for convenience in Figure 7.1(a), is largely planar until

approximately 150  $\mu\text{m}$  past the notch, as can be seen in Figure 7.1(b), after which crack bifurcation and dense veining on the fracture surfaces is evident. This dense veining, seen in Figure 7.1(c) smooths out about halfway down the specimen but another region containing large vein-like regions and substantial roughness ( $\sim 500 \mu\text{m}$ ) [Figure 7.1(d)] past this region prior to crack deflection near the specimen surface [Figure 7.1(e)].

An additional experiment was conducted at stress levels below the threshold for catastrophic fracture initiation in order to induce sub-threshold controlled damage in the vicinity of the notch in the four-point bend LM-1 fracture specimen (the stress intensity factor for this experiment was approximately  $90 \text{ MPa m}^{1/2}$ ). By studying the deformed region ahead of the notch tip, it was expected to better understand the mechanisms of damage and failure that precede catastrophic fracture initiation in LM-1. Subsequent SEM imaging of the post-test near-notch tip region clearly showed the presence of multiple deformation/shear bands emanating approximately 150  $\mu\text{m}$  from the notch root. Higher magnification shows the presence of a second group of bands that is perpendicular to the first. These deformation/shear bands are largely consistent with the slip-line fields (planes of maximum shear) near a notch, and are, to the author's knowledge, the first example of the slip-line fields in an otherwise intact LM-1 specimen. Reloading of the previously damaged LM-1 specimen shows an increase in the force required to cause catastrophic specimen failure, and the force vs. time curves again clearly show multiple attempts at catastrophic failure along with corresponding blunting. The corresponding fracture toughness of  $136 \text{ MPa m}^{1/2}$  is in good agreement with the expected fracture toughness for a specimen with a notch radius of about 160-170  $\mu\text{m}$ ,

which closely approximates the radius of the damaged zone from Figure 4.11 (a) as well as the plane strain process zone size.

### *7.1.3 High strain-rate compression of HTPB polymer (binder) and its composite (simulant)*

High strain-rate compression experiments were conducted on an HTPB polymer and its corresponding glass beads-filled polymer composite in order to investigate their strain-rate sensitivity. In order to conduct these experiments, the steel striker and incident bars in the original experiments were replaced with aluminum bars, and the steel transmitted bar typically employed in the SHPB was replaced with a hollow aluminum transmitter bar attached to an end cap. The modifications to the SHPB ensured that stresses as low as 1 MPa could be measured accurately during the high strain-rate loading process, which is of great importance because previous studies have shown that the peak stress of HTPB is on the order of 1 MPa. In addition, smaller length-to-diameter ratios (e.g. 0.25-0.75) were utilized to ensure that stress equilibrium was attained in the binder and the simulant.

Results from the experiments on the binder and simulant both show substantial rate-sensitivity, but the manner in which the rate sensitivity manifests itself is quite different in the two materials. In the binder, as the strain-rate increased from 600/s to 4000/s, the peak stress achieved in the specimen increased from 0.5 MPa to approximately 35 MPa. Moreover, as the strain-rate was increased, a greater level of damage was present in the post-test (impacted) binder specimens. At a strain-rate of

approximately 3100/s, the specimens were observed to fracture into at least two pieces, and clear evidence of axial splitting was present. At the highest strain-rate (4000/s), the resulting specimen fragmented into approximately 10 pieces. This behavior was consistent with previous observations that the glass transition temperature appears to increase as the strain-rate increases. In addition, the degree of rate sensitivity at these strain-rates is substantially higher than HTPBs previously investigated at quasi-static strain-rates. The simulant specimens did not show the same degree of rate sensitivity; the peak stress increased from 0.5 MPa at 300/s to approximately 6 MPa at 2900/s. This is most likely because the high stresses generated in the simulant cannot be accommodated; thus, decohesion of the bead from the binder can occur at any of the numerous interfaces between the glass beads and the polymer binder due to the large volume fraction of glass beads (approximately 85%) in the specimen. In addition, the larger particles (e.g. 200-400  $\mu\text{m}$  diameter) can also fracture and will tend to do so before the smaller particles (e.g. 25-40  $\mu\text{m}$ ).

## **7.2 Future Work**

### *7.2.1 Composites incorporating LM-1*

The increase in the apparent strain for specimens with small  $L/D$  ratios accompanied by extensive shear banding can be of great scientific and technical interest in the design of novel high-energy absorption composite structures. The extensive shear banding that is present in as-cast LM-1 may provide a very effective mechanism for energy absorption in high-rate applications, particularly in the confined state. On the other hand, the extensive fragmentation that is present in annealed LM-1 provides a

different (but still very potent) energy absorption mechanism in the material due to diffusion of the primary crack front. Both methods of energy absorption, either by themselves or coupled with the large plasticity present in other materials such as Al alloys, may be useful for the development of lightweight, high-energy absorption materials. In addition, high-rate 2-D and 3-D imaging with both high spatial (e.g.  $< 10\ \mu\text{m}$ ) and temporal (e.g.  $> 10^5$  frames/sec) resolutions can be utilized for full-field, real-time measurements of failure in these composites under various loading conditions.

### *7.2.2 Temperature rise in BMGs*

Local increases in temperature during and after testing have been of interest to researchers experimenting with BMGs. While it appears that temperature rise is not a precursor to shear fracture/failure observed in as-cast BMG, local temperature rises due to shear fracture and subsequent slip may affect the performance of other material constituents in a typical BMG-composite. To this end, along with the measurement of the stress and the strain fields, methods of detecting temperature rise with high spatial and temporal resolution have been of interest. Two primary methods have been considered – infrared detectors and coatings – and if either method can be used for dynamic testing, it can provide a better understanding of the strain-rate effects on temperature behavior for a much wider strain-rate regime than is presently available.

While there have been a number of experiments that have discussed temperature rise during and after fracture for high strain-rate compression of LM-1, all of the experiments either have taken an analytical approach or require specimen failure. Both of

these approaches have flaws because any calculations that require specimen failure include both the energy from the specimen and the energy involved with the creation of the fracture surfaces (as well as any sliding that occurs, given the role that shear plays in failure of BMGs). A recent investigation has used high spatial-resolution fusible coatings on the surface of fracture specimens; the temperature that is reached can be determined by examining whether the coating melts after the experiment. However, the high loading-rate fracture experiments of LM-1 clearly show that catastrophic failure does not occur; therefore, the sliding of surfaces against each other do not occur because the only damage that is present is from the bands along slip-lines (planes of maximum shear). Such an experiment could be combined with the fusible coating to clearly investigate whether temperature rise and not the sliding present during and after specimen failure is the cause for the veining patterns present on the surfaces.

### *7.2.3 Additional tests with new inserts*

The use of tapered inserts is not restricted to LM-1. Such inserts may be of interest in both the quasi-static and dynamic testing of other low strain-to-failure materials, such as other bulk metallic glasses, ceramics and rocks, as the stress concentrations present in these materials provide similar difficulties in testing. For most ceramics, however, inserts of a higher compressive strength than maraging steel, such as tungsten carbide inserts, must be machined. Such inserts are being used for quasi-static testing of Fe-based BMGs exhibiting hardness approaching 12 GPa, as the maraging steel inserts would likely yield and fail prior to failure of the Fe-based BMG. In addition,

recent dynamic testing using the maraging steel inserts led to the inserts being sheared off prior to specimen failure.

#### *7.2.4 Failure of HTPB polymer and simulant*

From the experiments conducted in the current study, it is clear that understanding the presence of defects in the HTPB polymer are key to gaining insight into what defects are causing axial splitting to occur in the HTPB polymer for strain-rates above 3000/s. Surprisingly, while there have been papers that have examined the high strain-rate response of HTPB [1, 2], as well as under shock loading conditions [3, 4], the amount of analysis into the microstructure (especially the defects) present in HTPB is relatively sparse. In addition, because many types of HTPB polymer are present, the defects caused by casting in one formulation may be different from those in another formulation. Some additional shock experiments have been done on HTPB-glass composites [5], but like in the current study, the degree to which delamination and particle fracture occur are largely inconclusive. Shock experiments conducted above the Hugoniot Elastic Limit would be helpful in determining the degree to which these two mechanisms play a role in flow and fracture of the HTPB simulant.

#### *7.2.5 Effects of compression and shear in HTPB*

One area of substantial interest is the understanding of the effects of combined pressure and shear on rubbery polymers, such as HTPB, and polymer composites. While a number of investigations have been performed on the high strain-rate response of HTPB and HTPB composites, the role of shear in understanding the mechanical

properties of both of these is quite limited. Bridgman [6] postulated that shear could have important effects in the ignition of some related explosives, and explosively driven shock-shear experiments have been performed [7-9]; unfortunately, these experiments were solely to look at the resulting reaction, not mechanical properties. Chhabildas and Kipp [10] conducted pressure-shear experiments using a y-cut quartz that would generate stress waves in two directions because longitudinal waves cannot propagate along the y-axis, while Cowperthwaite and Gupta [11] conducted oblique-impact experiments using manganin gages embedded in the target to be able to vary the amount of shear imposed on the specimen. Mehta [12] conducted two types of plate-impact pressure-shear experiments on polycarbonate (while not a rubbery polymer, this is the first study on pressure-shear impact of polymers), one incorporating a sudden pressure drop, and noted that strain-hardening is present throughout the entire loading process, except for when the pressure suddenly drops. In that case, the shear stress falls, reaches a plateau, and then strain hardening continues. This is in stark contrast to the strain-softening that is observed as one of the phases of loading in the SHPB experiments. Still other experiments determined shear strength by calculating it from normal stresses obtained during shock-loading experiments.

One possible avenue for further research comes from recent modifications done on the SHPB to ensure combined compression-and-shear loading by replacing the end cap with an end cap inclined at 45°, thus ensuring that the shear and compressive stresses applied are similar. This particular method would allow direct comparison to SHPB compression experiments on the binder and the simulant, but the work that has been

conducted to this point has been limited. Another method to investigate strain-rate effects further (i.e. to  $10^5/s$ ) is the plate-impact pressure-shear experiment. The challenge in this experiment is to prepare a uniformly thin specimen (75  $\mu\text{m}$  thickness, 75 mm diameter), but spin coating has been postulated as a method that can be used to achieve the required thickness.

## References

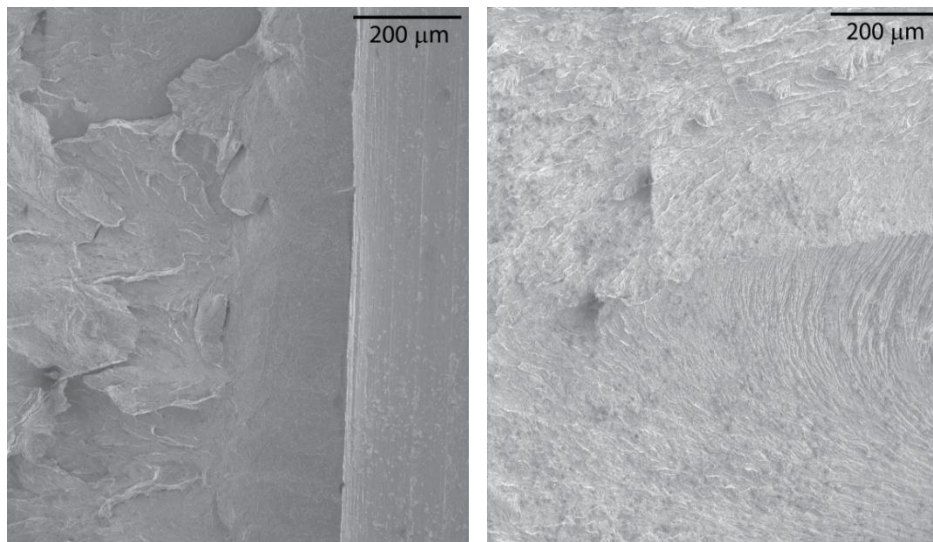
1. Blumenthal W.R., Thompson D.G., Cady C.D., Gray G.T., III, Idar D.J. (2002) Compressive Properties of PBXN-110 and its HTPB-Based Binder as a Function of Temperature and Strain Rate. *12th International Detonation Symposium* San Diego, CA, August 11-16, 2002.
2. Siviour C.R., Laity P.R., Proud W.G., Field J.E., Porter D., Church P.D., Gould P., Huntingdon-Thresher W. (2008) High strain rate properties of a polymer-bonded sugar: their dependence on applied and internal constraints. *Proceedings of the Royal Society A: Mathematical, Physical and Engineering Science* **464**, 1229-1255.
3. Bourne N.K., Gray G.T. (2005) Soft-recovery of shocked polymers and composites. *Journal of Physics D: Applied Physics* **38**, 3690.
4. Millett J.C.F., Bourne N.K., Akhavan J. (2004) The response of hydroxy-terminated polybutadiene to one-dimensional shock loading. *Journal of Applied Physics* **95**, 4722-4727.
5. Millett J.C.F., Bourne N.K., Akhavan J., Milne A.M. (2005) The response of soda-lime glass-hydroxyterminated polybutadiene composites to shock loading. *Journal of Applied Physics* **97**, 043524-043527.
6. Bridgman P.W. (1935) Effects of High Shearing Stress Combined with High Hydrostatic Pressure. *Physical Review* **48**, 825-847.
7. Boyle V., Frey R.B., Blake O. (1989) Combined pressure shear ignition of explosives. *Proceedings of the Ninth Symposium (International) on Detonation*, Portland, OR, August 28 - September 1, 1989.

8. Frey R.B. (1980) The Initiation of Explosive Charges by Rapid Shear. Aberdeen, MD.
9. Cart E.J., Lee R.J., Gustavson P.K., Coffey C.S., Sutherland G.T. (2004) The Role of Shear in Shock Initiation of Explosives. *AIP Conference Proceedings* **706**, 925-928.
10. Chhabildas L.C., Kipp M.E. (1985) Pressure-shear loading of PBX-9404. *Proceedings of the Eighth Symposium (International) on Detonation*, Albuquerque, NM, July 15-19, 1985.
11. Cowperthwaite M., Gupta Y.M. (1985) Investigation of shear-induced reaction in composition B3. *4th International American Physical Society Conference on Shock Compression of Condensed Matter*, Spokane, WA, July 1985.
12. Mehta N. (2003) *Pressure and strain rate dependency of flow stress of glassy polymers under dynamic loading*. Ph.D. Thesis, Case Western Reserve University

## Figures

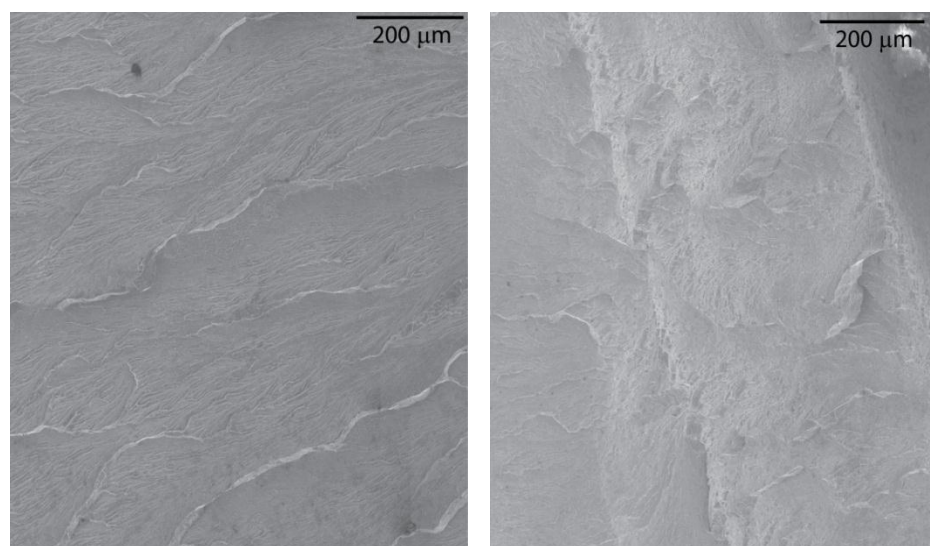


(a)



(b)

(c)



(d)

(e)

Figure 7.1 – (a) Fracture surface of the specimen from experiment Frac-1, with notch at right and arrow showing the direction of crack propagation, (b) inset near the notch showing a planar zone, (c) inset showing the presence of vein patterns, (d) inset showing a second stepped region with coarser veins, and (e) inset showing the overload region.

## Bibliography

1. Argon A.S. (1979) Plastic deformation in metallic glasses. *Acta Metallurgica* **27**, 47-58.
2. Balzer J.E., Siviour C.R., Walley S.M., Proud W.G., Field J.E. (2004) Behaviour of ammonium perchlorate-based propellants and a polymer-bonded explosive under impact loading. *Proceedings of the Royal Society of London. Series A: Mathematical, Physical and Engineering Sciences* **460**, 781-806.
3. Bat`kov Y.V., Fishman N.D., Novikov S.A. (1983) Investigation of shear stress on a shock front in solid high explosives (HE). *Combust., Explos. Shock Waves (Engl. Transl.)*; Translated from *Fizika Goreniya i Vzryva, May 1983* **19**, 357-359.
4. Bat`kov Y.V., Novikov S.A., Pogorelov A.P., Sinitsyn V.A., Khabarov I.P. (1983) Investigation of the influence of specimen diameter on the explosive transformation development behind a weak nonstationary shock front. *Combust., Explos. Shock Waves (Engl. Transl.)*; Translated from *Fizika Goreniya i Vzryva, May 1983* **19**, 359-360.
5. Blumenthal W.R., Gray G.T., III (1989) Characterizations of shock-loaded aluminum-infiltrated boron carbide cermets. *Proceedings of the American Physical Society Topical Conference, Albuquerque, NM, August 14-17, 1989*.
6. Blumenthal W.R., Gray G.T., III (1989) Structure-property characterization of a shock-loaded boron carbide-aluminum cermet. *International conference on mechanical properties of materials at high rates of strain, Oxford, UK, March 20, 1989*.

7. Blumenthal W.R., Thompson D.G., Cady C.D., Gray G.T., III, Idar D.J. (2002) Compressive Properties of PBXN-110 and its HTPB-Based Binder as a Function of Temperature and Strain Rate. *12th International Detonation Symposium* San Diego, CA, August 11-16, 2002.
8. Bourne N.K., Gray G.T. (2005) Soft-recovery of shocked polymers and composites. *Journal of Physics D: Applied Physics* **38**, 3690.
9. Boyle V., Frey R.B., Blake O. (1989) Combined pressure shear ignition of explosives. *Proceedings of the Ninth Symposium (International) on Detonation*, Portland, OR, August 28 - September 1, 1989.
10. Bridgman P.W. (1935) Effects of High Shearing Stress Combined with High Hydrostatic Pressure. *Physical Review* **48**, 825-847.
11. Bruck H.A., Christman T., Rosakis A.J., Johnson W.L. (1994) Quasi-static constitutive behavior of  $Zr_{41.25}Ti_{13.75}Ni_{10}Cu_{12.5}Be_{22.5}$  bulk amorphous alloys. *Scripta Metallurgica et Materialia* **30**, 429-434.
12. Bruck H.A., Rosakis A.J., Johnson W.L. (1996) The dynamic compressive behavior of Beryllium bearing bulk metallic glasses. *Journal of Materials Research* **11**, 503-511.
13. Cardoso R.J., Shukla A., Bose A. (2002) Effect of particle size and surface treatment on constitutive properties of polyester-cenosphere composites. *Journal of Materials Science* **37**, 603-613.
14. Caris J., Lewandowski J.J. (2009) Pressure effects on metallic glasses. *Acta Materialia* **58**, 1026-1036.

15. Cart E.J., Lee R.J., Gustavson P.K., Coffey C.S., Sutherland G.T. (2004) The Role of Shear in Shock Initiation of Explosives. *AIP Conference Proceedings* **706**, 925-928.
16. Chen H.S., Kimerling L.C., Poate J.M., Brown W.L. (1978) Diffusion in a Pd-Cu-Si metallic glass. *Applied Physics Letters* **32**, 461-463.
17. Chen W., Ravichandran G. (1996) An experimental technique for imposing dynamic multiaxial-compression with mechanical confinement. *Experimental Mechanics* **36**, 155-158.
18. Chen W., Subhash G., Ravichandran G. (1994) Evaluation of ceramic specimen geometries used in split-Hopkinson pressure bar. *Dymat Journal* **1**, 193-210.
19. Chen W., Zhang B., Forrestal M. (1999) A split Hopkinson bar technique for low-impedance materials. *Experimental Mechanics* **39**, 81-85.
20. Chhabildas L.C., Kipp M.E. (1985) Pressure-shear loading of PBX-9404. *Proceedings of the Eighth Symposium (International) on Detonation*, Albuquerque, NM, July 15-19, 1985.
21. Chree C. (1889) The Equations of an Isotropic Elastic Solid in Polar and Cylindrical Coordinates, Their Solution and Applications. *Transactions of the Cambridge Philosophical Society* **14**, 251-369.
22. Conner R.D., Rosakis A.J., Johnson W.L., Owen D.M. (1997) Fracture toughness determination for a beryllium-bearing bulk metallic glass. *Scripta Materialia* **37**, 1373-1378.

23. Cosculluela A., Cagnoux, J., Collombet, F. (1991) Uniaxial compression of alumina: structure, microstructure, and strain rate. *Journal de Physique IV* **1**, C3-109 - C103-116.
24. Couque H., Albertini C., Lankford J. (1993) Failure mechanisms in a unidirectional fibre-reinforced thermoplastic composite under uniaxial, in-plane biaxial and hydrostatically confined compression. *Journal of Materials Science Letters* **12**, 1953-1957.
25. Cowperthwaite M., Gupta Y.M. (1985) Investigation of shear-induced reaction in composition B3. *4th International American Physical Society Conference on Shock Compression of Condensed Matter*, Spokane, WA, July 1985.
26. Davies E.D.H., Hunter S.C. (1963) The dynamic compression testing of solids by the method of the split Hopkinson pressure bar. *Journal of the Mechanics and Physics of Solids* **11**, 155-179.
27. Davies R.M. (1948) A critical study of the Hopkinson pressure bar. *Philosophical Transactions of the Royal Society of London, Series A* **240**, 375-457.
28. Dieter G.E. (1976) *Mechanical Metallurgy*, McGraw Hill, Inc., New York, NY.
29. Donovan P.E. (1988) Compressive deformation of amorphous Pd<sub>40</sub>Ni<sub>40</sub>P<sub>20</sub>. *Materials Science and Engineering* **98**, 487-490.
30. Drodge D.R., Addiss J.W., Williamson D.M., Proud W.G. (2007) Hopkinson bar studies of a PBX simulant. *15th International American Physical Society Conference on Shock Compression of Condensed Matter*, Hilo, HI, July 24-29, 2007.

31. Drodge D.R., Proud W.G. (2009) The effects of particle size and separation on PBX deformation. *16th International American Physical Society Conference on Shock Compression of Condensed Matter*, Nashville, TN, June 28 - July 3, 2009.
32. Flores K.M., Dauskardt R.H. (1999) Enhanced toughness due to stable crack tip damage zones in bulk metallic glass. *Scripta Materialia* **41**, 937-943.
33. Follansbee P.S. (1985) The Hopkinson Bar. *American Society for Materials Handbook* (2nd ed.), Materials Park, OH, 198-203
34. Frew D., Forrestal M., Chen W. (2002) Pulse shaping techniques for testing brittle materials with a split Hopkinson pressure bar. *Experimental Mechanics* **42**, 93-106.
35. Frey R.B. (1980) *The Initiation of Explosive Charges by Rapid Shear*. Aberdeen, MD.
36. Gilbert C.J., Ager III J.W., Schroeder V., Ritchie R.O., Lloyd J.P., Graham J.R. (1999) Light emission during fracture of a Zr--Ti--Ni--Cu--Be bulk metallic glass. *Applied Physics Letters* **74**, 3809-3811.
37. Gilbert C.J., Ritchie R.O., Johnson W.L. (1997) Fracture toughness and fatigue-crack propagation in a Zr--Ti--Ni--Cu--Be bulk metallic glass. *Applied Physics Letters* **71**, 476-478.
38. Gilbert C., Schroeder V., Ritchie R. (1999) Mechanisms for fracture and fatigue-crack propagation in a bulk metallic glass. *Metallurgical and Materials Transactions A* **30**, 1739-1753.

39. Gray G.T. (2000) Classic split-Hopkinson pressure bar testing. *American Society for Materials Handbook* (8<sup>th</sup> ed.), American Society for Materials International, Materials Park, OH, 462-476
40. Gray III G.T., Blumenthal W.R., Idar D.J., Cady C.M. (1998) Influence of temperature on the high-strain-rate mechanical behavior of PBX 9501. *The tenth American Physical Society topical conference on shock compression of condensed matter*, Amherst, Massachusetts (USA),
41. Gu X.J., Poon S.J., Shiflet G.J., Lewandowski J.J. (2009) Ductile-to-brittle transition in a Ti-based bulk metallic glass. *Scripta Materialia* **60**, 1027-1030.
42. Gu X.J., Poon S.J., Shiflet G.J., Lewandowski J.J. (2010) Compressive plasticity and toughness of a Ti-based bulk metallic glass. *Acta Materialia* **58**, 1708-1720.
43. Haska S.B., Bayramli E., Pekel F., Özkaz S. (1997) Mechanical properties of HTPB-IPDI-based elastomers. *Journal of Applied Polymer Science* **64**, 2347-2354.
44. Hillstrom W.W. (1988) Elastometric binders and bonding agents for desensitization of explosives. Aberdeen, MD.
45. Hopkinson B. (1914) A Method of Measuring the Pressure Produced in the Detonation of High Explosives or by the Impact of Bullets. *Philosophical Transactions of the Royal Society of London, Series A* **213**, 437-456.
46. Horii H., Nemat-Nasser S. (1986) Brittle failure in compression: splitting, faulting and brittle-ductile transition. *Philosophical Transactions of the Royal Society of London. B* **319**, 337.

47. Hovis D.B., Heuer A.H. (2010) The use of laser scanning confocal microscopy (LSCM) in materials science. *Journal of Microscopy* **240**, 173-180.
48. Hufnagel T.C., Jiao T., Xing L.Q., Ramesh K.T. (2002) Deformation and failure of  $Zr_{57}Ti_5Cu_{20}Ni_8Al_{10}$  bulk metallic glass under quasi-static and dynamic compression. *Journal of Materials Research* **17**, 1441-1445.
49. Inoue A. (1998) *Bulk Amorphous Alloys: Preparation and Fundamental Characteristics*, Trans Tech Publications, Zurich.
50. Inoue A., Nakamura Y., Nishiyama N., Masumoto T. (1992) Mg-Cu-Y Bulk Amorphous Alloys with High Tensile Strength Produced by a High-Pressure Die Casting Method. *Materials Transactions JIM* **33**, 937-945.
51. Inoue A., Zhang T., Masumoto T. (1990) Production of Amorphous Cylinder and Sheet of  $La_{55}Al_{25}Ni_{20}$  Alloy by a Metallic Mold Casting Method. *Materials Transactions JIM* **31**, 425-428.
52. Johnson W.L. (1996) Fundamental Aspect of Bulk Metallic Glass Formation in Multicomponent Alloys. *Materials Science Forum* **225-227**, 35-50.
53. Jordan J.L., Dorgan R.J., Nixon M.E., Dick R.D. (2007) Initiation of Polymer Bonded Explosive (PBXN-110) by Combined Shock and Shear Loading. *15th APS Topical Conference on Shock Compression of Condensed Matter*, Waikoloa, HI,
54. Joshi V.S., Lee R.J. (2002) Resolving Mechanical Response of Plastic Bonded Explosives at High Strain-Rate Using Split Hopkinson Pressure Bar. *Shock Compression of Condensed Matter - 2001: 12th APS Topical Conference*, Atlanta, Georgia (USA),

55. Kawata K., Chung H.-L., Itabashi M. (1994) Dynamic mechanical behavior of HTPB dummy composite propellant. *Advanced Composite Materials* **3**, 163-175.
56. Klement W., Willens R.H., Duwez P. (1960) Non-crystalline Structure in Solidified Gold-Silicon Alloys. *Nature* **187**, 869-870.
57. Kolsky H. (1949) An investigation of the mechanical properties of materials at very high rates of loading. *Proceedings of the Physical Society, Section B* **62**, 676-700.
58. Kui H.W., Greer A.L., Turnbull D. (1984) Formation of bulk metallic glass by fluxing. *Applied Physics Letters* **45**, 615-616.
59. Lankford J. (1977) Compressive strength and microplasticity in polycrystalline alumina. *Journal of Materials Science* **12**, 791-796.
60. Lewandowski J.J. (2001) Effects of Annealing and Changes in Stress State on Fracture Toughness of Bulk Metallic Glass. *Materials Transactions* **42**, 633-637.
61. Lewandowski J.J., Liu C., Hunt Jr W.H. (1989) Effects of matrix microstructure and particle distribution on fracture of an aluminum metal matrix composite. *Materials Science and Engineering: A* **107**, 241-255.
62. Lewandowski J.J., Greer A.L. (2006) Temperature rise at shear bands in metallic glasses. *Nature Materials* **5**, 15-18.
63. Lewandowski J.J., Lowhaphandu P. (1998) Effects of hydrostatic pressure on mechanical behavior and deformation processing of materials. *International Material Reviews* **43**, 145-187.

64. Lewandowski J.J., Lowhaphandu P. (2002) Effects of hydrostatic pressure on the flow and fracture of a bulk amorphous metal. *Philosophical Magazine A* **82**, 3427-3441.
65. Lewandowski J.J., Shazly M., Nouri A.S. (2006) Intrinsic and extrinsic toughening of metallic glasses. *Scripta Materialia* **54**, 337-341.
66. Lewandowski J.J., Wang W.H., Greer A.L. (2005) Intrinsic plasticity or brittleness of metallic glasses. *Philosophical Magazine Letters* **85**, 77-87.
67. Love A.E.H. (1927) *A Treatise on the Mathematical Theory of Elasticity*, Cambridge University Press, Cambridge, UK.
68. Lowhaphandu P., Lewandowski J.J. (1998) Fracture toughness and notched toughness of bulk amorphous alloy: Zr-Ti-Ni-Cu-Be. *Scripta Materialia* **38**, 1811-1817.
69. Lowhaphandu P., Ludrosky L.A., Montgomery S.L., Lewandowski J.J. (2000) Deformation and fracture toughness of a bulk amorphous Zr-Ti-Ni-Cu-Be alloy. *Intermetallics* **8**, 487-492.
70. Lowhaphandu P., Montgomery S.L., Lewandowski J.J. (1999) Effects of superimposed hydrostatic pressure on flow and fracture of a Zr-Ti-Ni-Cu-Be bulk amorphous alloy. *Scripta Materialia* **41**, 19-24.
71. Lu J., Ravichandran G., Johnson W.L. (2003) Deformation behavior of the  $Zr_{41.2}Ti_{13.8}Cu_{12.5}Ni_{10}Be_{22.5}$  bulk metallic glass over a wide range of strain-rates and temperatures. *Acta Materialia* **51**, 3429-3443.
72. Manjari R., Pandureng L.P., Somasundaran U.I., Sriram T. (1994) Structure–property relationship of HTPB-based propellants. III. Optimization trials with

- varying levels of diol–triol contents. *Journal of Applied Polymer Science* **51**, 435-442.
73. Martins C.F., Irfan M.A., Prakash V. (2007) Dynamic fracture of linear medium density polyethylene under impact loading conditions. *Materials Science and Engineering: A* **465**, 211-222.
74. Mehta N. (2003) *Pressure and strain rate dependency of flow stress of glassy polymers under dynamic loading*. Ph.D. Thesis, Case Western Reserve University
75. Millett J.C.F., Bourne N.K., Akhavan J. (2004) The response of hydroxy-terminated polybutadiene to one-dimensional shock loading. *Journal of Applied Physics* **95**, 4722-4727.
76. Millett J.C.F., Bourne N.K., Akhavan J., Milne A.M. (2005) The response of soda-lime glass-hydroxyterminated polybutadiene composites to shock loading. *Journal of Applied Physics* **97**, 043524-043527.
77. Millett J.C.F., Deas D., Bourne N.K., Montgomery S.T. (2007) The deviatoric response of an alumina filled epoxy composite during shock loading. *Journal of Applied Physics* **102**, 063518-063516.
78. Millett J.C.F., et al. (2005) The equation of state of two alumina-filled epoxy resins. *Journal of Physics D: Applied Physics* **38**, 930.
79. Mulliken A.D., Boyce M.C. (2006) Mechanics of the rate-dependent elastic-plastic deformation of glassy polymers from low to high strain rates. *International Journal of Solids and Structures* **43**, 1331-1356.
80. Nathenson D.I. (2006) *Experimental Investigation of High-Velocity Impacts on Brittle Materials*. Ph.D. Thesis, Case Western Reserve University

81. Owen D.M., Rosakis A.J., Johnson W.L. (1999) Dynamic failure mechanisms in beryllium-bearing bulk metallic glasses. *Materials Research Society Symposium - Proceedings* **554**, 419.
82. Peker A., Johnson W.L. (1993) A highly processable metallic glass -  $Zr_{41.2}Ti_{13.8}Cu_{12.5}Ni_{10.0}Be_{22.5}$ . *Applied Physics Letters* **63**, 2342-2344.
83. Pilkey W.D. (1997) *Peterson's Stress Concentration Factors*, John Wiley and Sons, New York, NY.
84. Pochhammer L. (1876) Uber Fortplanzungsgeschwindigkeiten kleiner Schwingungen in einem unbergrenzten isotropen Kreiszyylinder (On the propagation velocities of small oscillations in an infinite isotropic circular cylinder). *Journal fur der reine und angewandte Mathematick* **81**, 324-326.
85. Rittel D., Rosakis A.J. (2005) Dynamic fracture of beryllium-bearing bulk metallic glass systems: A cross-technique comparison. *Engineering Fracture Mechanics* **72**, 1905-1919.
86. Sarva S., Mulliken A.D., Boyce M.C. (2006) The mechanics of large-strain inhomogeneous deformation of polymeric materials under dynamic loading conditions. *Journal de Physique IV* **134**, 95-101.
87. Shazly M. (2005) *Dynamic Deformation and Failure of Gamma-Met PX at Room and Elevated Temperatures*. Ph.D. Thesis, Case Western Reserve University
88. Shazly M., Prakash V., Lerch B. (2006) *High strain-rate compression of ice*, National Aeronautics and Space Administration, Cleveland, OH.

89. Shukla A., Ravichandran G., Rajapakse Y.D.S., Chen W.W., Song B. Dynamic Characterization of Soft Materials. *Dynamic Failure of Materials and Structures* ed.), Springer US, 1-28
90. Singh P., Lewandowski J. (1993) Effects of heat treatment and reinforcement size. *Metallurgical and Materials Transactions A* **24**, 2531-2543.
91. Siviour C.R., Gifford M.J., Walley S.M., Proud W.G., Field J.E. (2004) Particle size effects on the mechanical properties of a polymer bonded explosive. *Journal of Materials Science* **39**, 1255-1258.
92. Siviour C.R., Laity P.R., Proud W.G., Field J.E., Porter D., Church P.D., Gould P., Huntingdon-Thresher W. (2008) High strain rate properties of a polymer-bonded sugar: their dependence on applied and internal constraints. *Proceedings of the Royal Society A: Mathematical, Physical and Engineering Science* **464**, 1229-1255.
93. Song B., Chen W. (2003) One-dimensional dynamic compressive behavior of EPDM rubber. *Journal of Engineering Materials and Technology, Transactions of the ASME* **125**, 294-301.
94. Song B., Chen W.W. (2005) Split Hopkinson pressure bar techniques for characterizing soft materials. *Latin American Journal of Solids and Structures* **2**, 113-152.
95. Spaepen F. (1977) A microscopic mechanism for steady state inhomogeneous flow in metallic glasses. *Acta Metallurgica* **25**, 407-415.

96. Subhash G., Dowding R.J., Kecskes L.J. (2002) Characterization of uniaxial compressive response of bulk amorphous Zr-Ti-Cu-Ni-Be alloy. *Materials Science and Engineering A* **334**, 33-40.
97. Subhash G., Ravichandran G. (2000) Split-Hopkinson pressure bar testing of ceramics. *American Society for Materials Handbook* (8<sup>th</sup> ed.), American Society for Metals International, Materials Park, OH, 497-504
98. Subhash G., Zhang H., Li H. (2003) Thermodynamic and mechanical behavior of Hafnium-/Zirconium-based bulk metallic glasses. *Proceedings of the International Conference on Mechanical Behavior of Materials (ICM-9)*, Geneva, Switzerland, May 25-29, 2003.
99. Szycher M. (1999) *Szycher's Handbook of Polyurethanes*, CRC Press, Boca Raton, FL.
100. Tarver C.M., Hallquist J.O., Erickson L.M. (1985) Modeling short pulse duration shock initiation of solid explosives. United States,
101. Telford M. (2004) The case for bulk metallic glass. *Materials Today* **7**, 36-43.
102. Sunny G., Prakash V., Lewandowski J.J. (2007) Effects of annealing and specimen geometry on dynamic compression of a Zr-based bulk metallic glass. *Journal of Materials Research* **22**, 389-401.
103. Sunny G., Yuan F., Prakash V., Lewandowski J. (2008) Effect of high strain rates on peak stress in a Zr-based bulk metallic glass. *Journal of Applied Physics* **104**, 093522.
104. Tracy C.A. (1987) A Compression Test for High Strength Ceramics. *Journal of Testing and Evaluation* **15**, 14-19.

105. Vaidya A.R., Lewandowski J.J. (1996) Effects of SiCp size and volume fraction on the high cycle fatigue behavior of AZ91D magnesium alloy composites. *Materials Science and Engineering A* **220**, 85-92.
106. Varadarajan R., Lewandowski J. (2010) Stress-State Effects on the Fracture of a Zr-Ti-Ni-Cu-Be Bulk Amorphous Alloy. *Metallurgical and Materials Transactions A* **41**, 1758-1766.
107. Wesseling P., Lowhaphandu P., Lewandowski J. (2003) Effects of superimposed pressure on flow and fracture of two bulk metallic glass. *Mat. Res. Soc. Symp Proc.* **754**, 275-279.
108. Wingborg N. (2002) Increasing the tensile strength of HTPB with different isocyanates and chain extenders. *Polymer Testing* **21**, 283-287.
109. Xi X.K., Zhao D.Q., Pan M.X., Wang W.H., Wu Y., Lewandowski J.J. (2005) Fracture of Brittle Metallic Glasses: Brittleness or Plasticity. *Physical Review Letters* **94**, 125510.
110. Yang B., Liu C., T., Nieh T G., Morrison M., L., Liaw P., K., Buchanan R., A. (2006) Localized heating and fracture criterion for bulk metallic glasses. *Journal of Materials Research* **21**, 915-922.
111. Yuan F., Prakash V., Lewandowski J.J. (2007) Spall strength and Hugoniot elastic limit of a Zirconium-based bulk metallic glass under planar shock compression. *Journal of Materials Research* **22**, 402-411.
112. Yuan F., Prakash V., Lewandowski J.J. (2010) Shear yield and flow behavior of a zirconium-based bulk metallic glass. *Mechanics of Materials* **42**, 248-255.

113. Yuan F., Tsai L., Prakash V., Rajendran A.M., Dandekar D.P. (2007) Spall strength of glass fiber reinforced polymer composites. *International Journal of Solids and Structures* **44**, 7731-7747.
114. Zhang T., Inoue A., Masumoto T. (1991) Amorphous Zr-Zr-Al-TM (TM=Co, Ni, Cu) Alloys with Significant Supercooled Liquid Region of over 100 K. *Materials Transactions JIM* **32**, 1005-1010.
115. Zhang Y., Greer A.L. (2006) Thickness of shear bands in metallic glasses. *Applied Physics Letters* **89**, 071907-071903.
116. Zhang Y., Stelmashenko N.A., Barber Z.H., Wang W.H., Lewandowski J.J., Greer A.L. (2007) Local Temperature Rises during Mechanical Testing of Metallic Glasses. *Journal of Materials Research* **22**, 419-427.
117. Zhang Z.F., He G., Eckert J., Schultz L. (2003) Fracture Mechanisms in Bulk Metallic Glassy Materials. *Physical Review Letters* **91**, 045505.
118. Zhou F., Molinari J.-F., Ramesh K.T. (2005) A cohesive model based fragmentation analysis: effects of strain rate and initial defects distribution. *International Journal of Solids and Structures* **42**, 5181-5207.
119. Zhuang S., Lu J., Ravichandran G. (2002) Shock wave response of a zirconium-based bulk metallic glass and its composite. *Applied Physics Letters* **80**, 4522-4524.

DISTRIBUTION LIST  
AFRL-RW-EG-TR-2011-053

\*Defense Technical Info Center  
8725 John J. Kingman Rd Ste 0944  
Fort Belvoir VA 22060-6218

AFRL/RWME (6)  
AFRL/RWOC-1 (STINFO Office)